Probing the Mantle Cargo of Kimberlites – A Geochemical Investigation of Different Mineral Components and Evaluation of their Potential as Petrogenetic and Exploration Tools

by

Yannick Bussweiler

A thesis submitted in partial fulfillment of the requirements for the degree of

Doctor of Philosophy

Department of Earth and Atmospheric Sciences

University of Alberta

Abstract

This thesis applies microanalytical tools to the geochemical investigation of different mineral components in the volcanic rock kimberlite. This work significantly advances the application of one of these tools, deep UV (193 nm) laser ablation inductively coupled plasma mass spectrometry (LA-ICP-MS), to the investigation of the most common mineral in kimberlite and the upper mantle – olivine. The investigation is focused on, but not limited to, samples from the Lac de Gras kimberlite field in the Central Slave Craton, Canada. The overall aim is to further illuminate the applicability of clinopyroxene, garnet, and olivine as petrogenetic and exploration indicator minerals using advanced analytical techniques of electron microprobe microanalysis (EPMA), quantitative evaluation of minerals by scanning electron microscopy (QEMSCAN), laser ablation inductively coupled plasma mass spectrometry (LA-ICP-MS), and secondary ion mass spectrometry (SIMS).

One petrogenetic topic of interest is the formation of megacrysts, large (> 1 cm) crystals commonly found in kimberlites. Cr-diopside clinopyroxene and Cr-pyrope garnet megacrysts from Lac de Gras kimberlites, Slave Craton, Canada, are investigated. Based on their large crystal size and compositional overlap with lherzolitic phases, the samples can be classified as Cr-rich megacrysts, constituting the first report of such megacrysts in Lac de Gras kimberlites. While trace element systematics and Sr isotope isotopes suggest a genetic link to kimberlite-like melts, a strictly cognate relationship is ruled out, based on evidence for disequilibrium with the transporting kimberlite. Instead, an older metasomatic origin is adopted for their formation, presumably linked to precursor kimberlite melts that stalled at mantle depths and reacted with the wall rocks.

The Cr-rich megacrysts also contain fully crystallized former melt inclusions. A detailed petrographical and geochemical study suggests that these polymineralic inclusions constitute an early snapshot of the transporting kimberlite melt which infiltrated the megacrysts during ascent. Within Cr-diopsides, polymineralic inclusions are dominated by calcite and olivine and are commonly surrounded by reaction rims with abundant fluid inclusions (CO_2-rich). This mineralogy appears to record long-proposed decarbonation reactions that may play an important role in the evolution of calcite-bearing kimberlites, such as:

diopside + dolomite (melt) = olivine + calcite + CO_2.

In examining new applications of olivine geochemistry using LA-ICP-MS to kimberlite evolution and mantle studies, it is necessary to develop a strict protocol for the measurement of trace elements in olivines. Comparative experiments reveal a more pronounced and complex beam-size dependent inter-element fractionation behavior for olivine that requires careful optimization of ablation parameters and calibration strategies. Methods developed in this thesis have been externally verified in laboratories at the University of Melbourne and at the Geological Survey of Canada. A main conclusion of this study is that matrix-matched calibration is necessary in order to avoid inaccuracies caused by calibration and fractionation effects, especially when using small (< 100 μm) laser spot sizes. Thus, an important output of this study is the characterization of appropriate olivine standards for matrix-matched LA-ICP-MS calibration.

The development of a fast and accurate method for analyzing trace elements in olivine opens up new possibilities to pinpoint the different origins of olivine in kimberlite and to explore its potential as a petrogenetic indicator mineral and as a possible diamond exploration tool. Using

natural samples, this investigation presents new trace element discriminators to distinguish between olivines derived from spinel- and garnet-peridotites.

Using the high-pressure, high-temperature experiments performed by Brey et al. (1990), it is possible to derive the first experimental calibration of the Al-in-olivine thermometer at upper mantle conditions and hence evaluate the empirical thermometer of De Hoog et al. (2010). Al measurements in the experiments are performed at high spatial resolution (~8 μm) by SIMS, including SIMS mapping in order to investigate element distribution in the experiments. Based on Al concentrations in the experimental olivines, an improved and simplified calibration of the Al-in-olivine geothermometer applicable to garnet peridotites can be derived. Evaluation of this thermometer against olivine from natural garnet peridotites indicates that it may be the most reliable geothermometer currently available for garnet harzburgites.

Preface

This thesis contains four separate manuscripts based on the findings of Y.B.'s Ph.D. research supervised by Prof. Graham Pearson.

A modified version of Chapter 2 has been published as: *Bussweiler, Y., Stone, R.S., Pearson, D.G., Luth, R.W., Stachel, T., Kjarsgaard, B.A. and Menzies, A., 2016. The evolution of calcite-bearing kimberlites by melt-rock reaction: evidence from polymineralic inclusions within clinopyroxene and garnet megacrysts from Lac de Gras kimberlites, Canada. Contributions to Mineralogy and Petrology, 171(7), pp.1-25*. Y.B. collected the samples, conducted most of the analytical work, and wrote the paper. R. S. Stone and her thesis supverisor R.W. Luth provided crucial input for interpretation of the data. D.G. Pearson, T. Stachel, and B.A. Kjarsgaard supervised the research project and provided valuable discussions and manuscript edits. A. Menzies conducted QEMSCAN® analysis at the Universidad Católica del Norte, Antofagasta, Chile.

Chapter 3 constitutes a separate study on the same samples as in Chapter 2. Y.B. conducted the analytical work and wrote the paper. D.G. Pearson, T. Stachel, and B.A. Kjarsgaard provided valuable discussions and manuscript edits. The manuscript has not yet been submitted.

A modified version of Chapter 4 has been published as: *Bussweiler, Y., Brey, G.P., Pearson, D.G., Stachel, T., Stern, R.A., Hardman, M.F., Kjarsgaard, B.A., Jackson, S.E., 2017. The aluminum-in-olivine thermometer for mantle peridotites – Experimental versus empirical calibration and potential applications. Lithos, 272-273, pp. 301-314*. Y.B. performed sample preparation and most of the analytical work and wrote the paper. G.P. Brey provided the samples and helped to edit the manuscript. R.A. Stern was instrumental in setting up the analytical routine for SIMS. M.F. Hardman helped with statistical analysis of the data. B.A. Kjarsgaard and S.E. Jackson provided additional LA-ICP-MS data. D.G. Pearson and T. Stachel supervised the project and provided valuable discussions and manuscript edits.

Chapter 5 constitutes a concerted effort between the University of Alberta, the University of Melbourne, and the Geological Survey of Canada to improve LA-ICP-MS methods for the analysis of olivine. Y.B. conducted the analytical work at the University of Alberta and wrote the manuscript. A. Giuliani and A. Greig conducted analytical work at the University of Melbourne. B.A. Kjarsgaard and S.E. Jackson conducted analytical work at the Geological Survey of Canada. Y. Luo assisted with LA-ICP-MS at the University of Alberta and provided valuable comments. The manuscript has not yet been submitted.

Acknowledgements

This thesis would not have materialized without the advice, assistance, and support of a lot of people.

First and foremost, I would like to thank my supervisor Prof. Graham Pearson for accepting me as a PhD student in his Arctic Resources Laboratory research group. I am very grateful for the opportunity to work on kimberlites in this excellent research environment with this excellent group of people. I would like to thank Graham for always being available for expert advice, not only on my PhD research. I am also thankful for being given the opportunity to gain an extra amount of experience in laser ablation besides my main research objectives. Specifically, thanks for letting me laser so many diamonds in half.

Next, I would like to thank Prof. Thomas Stachel for providing additional guidance, sample material, and pointed feedback to my different research projects. In particular, discussions with Thomas about kimberlite petrology and geothermobarometry were immensely helpful. Thanks also for tolerating me in the diamond group lunch meetings. I kindly thank Dr. Bruce Kjarsgaard for providing plenty of feedback to my research from an external perspective. I am also grateful for Bruce's crucial advice on how to wrap up a thesis with Graham. Prof. Robert Luth is thanked for shedding some light onto the obscure field of thermodynamics. I also appreciate the various discussions with Bob about kimberlite formation from the angle of experimental petrology. I would like to thank Prof. Gerhard Brey for lending me his original experimental samples and letting me "reassemble" them by violently cutting and drilling them apart.

The team at Diavik Diamond Mines, in particular Yuri Kinakin and Gus Fomradas, are thanked for letting me collect samples while getting a glimpse of the life at a diamond mine. With outside temperatures of down to -40°C it was literally a cool experience. Juanita Bellinger is thanked for providing additional sample material from Diavik.

I am greatly indebted to the excellent team of staff at EAS. Dr. Andrew Locock is thanked for assistance with EPMA and very helpful mineralogical advice. I thank Dr. Sarah Woodland for providing help with a lot of things – basically everything from plasma tuning to mailing samples. Dr. Yan Luo is thanked for sharing her expertise in LA-ICP-MS. Dr. Chiranjeeb Sarkar is thanked for help with column chemistry and SIMS. At this point I would also like to thank Prof. Larry Heaman for putting us up in his lab for doing Sr columns. Dr. Richard Stern is thanked for

assistance with SIMS and developing the analytical method for measuring Al in olivine. I thank Katie Hogberg for assistance with sample preparation, i.e. spending many hours cutting, mounting, and polishing experimental olivine samples. Finally, I would like to thank Martin von Dollen for his excellent sample preparation and for fulfilling many small important tasks on the spot.

Thanks go out to all of my fellow grad students in EAS, especially the original Tory crew including Janina, Laura, Léanne, Mandy, Rebecca, Dave, and Pedro for many scientific and not so scientific conversations. I am also grateful to my old and new Canadian friends, including the Mayfield crew and my band – metal drumming turned out to be a great way to stay balanced during my PhD.

Last but not least, I would like to thank my family and friends overseas for staying in touch (even without Facebook). My parents are thanked for their continuous support and for their understanding that studying rocks is important and requires moving across the ocean. I would like to thank my brother for great vacations in California. And finally, I thank Julia for being my major source of motivation and inspiration.

Table of Contents

List of Figures

Chapter 1

Chapter 2

Chapter 3

Chapter 4

Chapter 5

List of Tables

To enhance readability all data tables are included in the Appendix.

1. Introduction

The overarching theme of this thesis is the application of new micro-analytical techniques to the volcanic rock kimberlite and its diverse mantle cargo. The investigation is focused on (but not limited to) samples from the Lac de Gras kimberlite field in the Central Slave Craton, Canada. The geochemistry of clinopyroxene and garnet megacrysts – as well as fully crystallized melt inclusions within them – and of olivine is studied to unlock new insights into processes of kimberlite formation and mantle sampling. The findings of this thesis may provide new useful tools for kimberlite exploration and diamond potential evaluation.

The kimberlites of the Lac de Gras field classify as archetypal or group I kimberlites (Nowicki et al. 2004; Kjarsgaard et al. 2009). This group is defined as "volatile-rich (dominantly CO_2), potassic, ultrabasic rocks commonly exhibiting a distinctive inequigranular texture resulting from the presence of a characteristic suite of megacryst/macrocryst minerals (including olivine, pyrope garnet, diopside clinopyroxene, phlogopite, ilmenite, and monticellite) in a fine-grained groundmass of olivine together with one or more of the following primary minerals: monticellite, phlogopite, perovskite, spinel, apatite, and serpentine" (Mitchell 1995, page 15).

Group I kimberlites are almost exclusively found within ancient sections of continental crust (cratons) and have the deepest origin (> 150 km) of any type of magma found on Earth (Mitchell 1986). By entraining mantle xenoliths and transporting them to the Earth's surface, kimberlites can sample the entire subcontinental lithospheric mantle (SCLM). Studies on xenoliths from kimberlites have revealed a wealth of information on the structure and chemical composition of the SCLM (see reviews by Pearson et al. 2003; Griffin et al. 2009). Typically, the SCLM records a multi-stage evolution characterized by initial melt depletion to high degrees early in Earth's history, followed by varying degrees of re-fertilization by infiltrating fluids and melts (Carlson et al. 2005; Griffin et al. 2009). The exact nature of the re-fertilizing melts is still a matter of debate. It has been proposed that re-fertilization, characterized by introduction of clinopyroxene (and to a lesser extent garnet) into depleted cratonic mantle, may be linked to kimberlite-like melts (Simon et al. 2003).

The general processes of mantle depletion and re-fertilization resulted in the commonly observed lithologies in the SCLM beneath the Slave Craton: Shallow layers tend to be dominated by

harzburgite (olivine, garnet, orthopyroxene), representing a very depleted rock type, whereas deeper layers are dominated by lherzolite (olivine, garnet, orthopyroxene, clinopyroxene), representing a more fertile rock type (Griffin et al. 1999; Menzies et al. 2004). Both of these rocks are peridotites, implying an olivine-rich mineralogy. An olivine-free rock type in the SCLM is eclogite (garnet, clinopyroxene) which is generally assumed to constitute old oceanic crust which became incorporated as lenses by subduction (Jacob 2004).

The exact origin and nature of primary kimberlite melt are still a matter of scientific debate. This includes the magmatic evolution path that kimberlites follow from the upper mantle to the low-pressure mineral assemblage observed in the crust. The search for primary kimberlite melt(s) is complicated by the entrainment of, and reaction with, xenocrysts and xenoliths spanning the entire lithosphere, and by post-emplacement alteration processes (Mitchell 1986; Mitchell 1995; Price et al. 2000; Kopylova et al. 2007; Sparks et al. 2009; Kjarsgaard et al. 2009). Researchers are currently debating whether the primary kimberlite is carbonatitic (Dawson 1971; Dawson and Hawthorne 1973; Russell et al. 2012; Kamenetsky and Yaxley 2015; Kamenetsky 2016), a carbonated silicate melt (e.g., Nielsen and Sand 2008; Brey et al. 2008), or a highly saline carbonatite (e.g., Kamenetsky et al. 2012). Another outstanding issue is the generation of calcite-dominated kimberlites observed in the crust, given that the vast majority of experimental evidence suggests that a primary melt formed from the melting of a peridotitic source must produce Mg-rich carbonate, namely dolomite (e.g., Wyllie and Huang 1975; Dalton and Presnall 1998a).

1.1. The Mantle Cargo of Kimberlites

During kimberlite ascent and eruption, the sampled mantle xenoliths tend to disaggregate into separate xenocrysts as a function of the respective rock strength (Brett et al. 2015). In addition, crustal xenoliths can become incorporated into the magma, so that upon emplacement kimberlite constitutes a hybrid rock with both xenocrystic (non-cognate) and phenocrystic (magma-related or cognate) mineral components in a fine-grained groundmass (Mitchell 1986). Distinguishing the origin of the different mineral components is not always straightforward. This is especially true for the minerals studied here: clinopyroxene, garnet, and olivine are all represented in different SCLM lithologies (e.g., eclogites and peridotites) and may further belong to the so-called megacryst suite, which is assumed to be of high-pressure magmatic origin. Olivine, the

dominant mineral in kimberlites, can further crystallize from the magma over a large pressure interval (polybaric crystallization). This thesis builds on a number of previous studies in trying to further pinpoint the origin of these mineral components in kimberlites.

1.1.1. Megacrysts

Megacrysts are large crystals (> 1 cm, up to ~20 cm) typically found in kimberlites (Nixon and Boyd 1973; Mitchell 1986; Mitchell 1995). Common mineral phases include garnet, clinopyroxene, olivine, and ilmenite. Based on their mineral compositions, megacrysts can be divided into a Cr-poor and a Cr-rich suite, with the more common Cr-poor suite being characterized by lower Cr contents and higher Fe and Ti contents compared to equivalent peridotite phases (Harte 1983). Megacrysts of the Cr-rich suite are enriched in Cr and depleted in Fe and Ti and thus chemically indistinguishable from their peridotite equivalents, i.e. lherzolitic phases (Eggler et al. 1979).

In traditional genetic models, megacrysts are assumed to crystallize from a fractionating magma at depths of 150-200 km at the base of the lithosphere (Harte 1983), or even in a sublithospheric seismic low velocity zone (Boyd and Nixon 1973). The Cr-poor suite is thought to crystallize within the magma chamber, whereas Cr-rich megacrysts are seen as products of chemical interaction at low fluid/wall rock ratios with the surrounding mantle. The chemical nature of the proposed megacryst magma and its relationship to the transporting kimberlite are an ongoing matter of debate (Mitchell 1995; Bell and Moore 2004; Moore and Belousova 2005). Here, we present new data on large crystals of clinopyroxene and garnet from Lac de Gras kimberlites that classify them as Cr-rich megacrysts (Chapter 3). We propose a model in which they may have formed from older kimberlite pulses that stalled at variable depths within the lithospheric mantle.

Megacrysts can contain fully crystallized melt inclusions, so-called polymineralic inclusions (Haggerty and Boyd 1975). Here, it will be demonstrated that these inclusions probably do not represent the primary kimberlite melt or the megacryst magma, as previously assumed. Instead, they appear to reveal reactions between mantle minerals and kimberlite melt during ascent that may have important consequences for kimberlite evolution, especially for the formation of calcite-bearing kimberlites (Chapter 2). Such decarbonation reactions have been anticipated for quite some time based on experimental studies (see Mitchell 1995, page 324), however, they have rarely been reported in natural xenolith samples.

1.1.2. Olivine

Olivine constitutes the major mineral component in kimberlites and is characterized by a diverse nature with different populations. In order to distinguish these different populations, spatially resolved analyses are necessary as it has been found that olivine in kimberlite can record complex growth histories, with cores having different origins than the rims (Fedortchouk and Canil 2004; Kamenetsky et al. 2008; Brett et al. 2009; Bussweiler et al. 2015). To some extent, the different origins become apparent when plotting NiO content against Mg# (Mg/(Mg+Fe)), see Figure 1-1. Compared to typical MORB olivine, which shows a differentiation trend of gradually decreasing NiO with decreasing Mg#, the majority of olivine cores from kimberlite fall into a relatively narrow field of high NiO and a range of Mg# from about 0.89 to 0.94 (Figure 1-1). These cores are now interpreted to be dominantly xenocrystic cores originating from the disaggregation of mantle peridotites (Kamenetsky et al. 2008; Brett et al. 2009; Bussweiler et al. 2015; Howarth and Taylor 2016). The xenocrystic cores are commonly overgrown by a second type of olivine which follows a trend of decreasing NiO at nearly constant Mg# (Figure 1-1). This trend has been attributed to crystallization of olivine from the kimberlite melt onto pre-existing cores from different origins (Kamenetsky et al. 2008; Brett et al. 2009; Bussweiler et al. 2015; Howarth and Taylor 2016). Data for olivine from xenolith studies (e.g., Menzies et al. 2004) and diamond inclusion studies (e.g., Stachel et al. 2003; Donnelly et al. 2007) from the Lac de Gras area are in general agreement with the hybrid character of olivine from kimberlite, and this seems to hold true for different locations.

However, there are “oddities” which are not easily explained by this two-step model. One example is olivine from so-called polymict mantle breccias that are interpreted as remnants of failed kimberlites (Lawless et al. 1979; Höfer et al. 2009; Giuliani et al. 2014). Olivine found in the matrix of polymict breccias, plots at lower Mg# and NiO than the field of the xenocrystic cores (Figure 1-1). Another still enigmatic group of olivines found in kimberlites are associated with the megacryst suite (e.g., Gurney et al. 1979). Especially the more Fe-rich group of Cr-poor megacrysts has no counterpart in peridotitic xenoliths (Figure 1-1). Interestingly, the latest data reported by Moore and Costin (2016) appear to follow the MORB differentiation trend of olivines.

In order to confidently resolve these different groups and get a better understanding of their respective proportions in different kimberlite pipes, it would be extremely useful to investigate

their trace element signatures by LA-ICP-MS. Unfortunately, so far such studies have been hindered by analytical challenges. For example, the magmatic overgrowths on xenocrystic cores are often too thin to be analyzed reliably (e.g., Bussweiler et al. 2015). One aim of this study is to improve analytical protocols for LA-ICP-MS on olivines (Chapter 5). An important pillar of this undertaking is the characterization of natural olivine standards for matrix-matched calibration.

1.1.3. Al-in-Olivine Thermometry

The fact that recent studies have suggested that a large proportion of olivines in kimberlite (i.e. their cores) are mantle xenocrysts opens up new applications for the use of olivine as an indicator mineral. For example, olivine from till samples or mineral concentrates can be treated as a representative mantle sample of a given kimberlite. This mantle sample, of course, excludes olivine-free lithologies, such as eclogite, that may have great importance for diamond potential.

One promising application is the Al-in-olivine thermometer for mantle peridotites which has been calibrated empirically by De Hoog et al. (2010). This geothermometer has great potential to improve techniques to evaluate the mantle sampling characteristics of a given kimberlite. However, the empirical calibration has only been tested on a limited suite of samples and an experimental verification is still lacking. Moreover, there is no satisfying discussion of the analytical challenges associated with the determination of Al (and other trace elements) in olivine. Here, an experimental calibration of the Al-in-olivine thermometer for garnet peridotites is presented, based on the original high-temperature, high-pressure experiments by Brey et al. (1990) (Chapter 4).

1.2. Research Objectives

The research objectives of this thesis can be summarized as follows:

- Geochemical investigation of polymineralic inclusions in clinopyroxene and garnet megacrysts from Lac de Gras kimberlites to shed light on processes of kimberlite evolution (Chapter 2)
- Geochemical investigation of the above host megacrysts (Cr-diopside and Cr-pyrope) to the polymineralic inclusions to better understand the formation of megacrysts in the SCLM and their relationship to kimberlites (Chapter 3)
- Test and improve the Al-in-olivine thermometer for garnet peridotites by calibration against experimental samples and explore its potential applications to diamond exploration (Chapter 4)
- Discuss the analytical challenges associated with LA-ICP-MS on olivine and improve analytical protocols, including the characterization of natural olivine standards for matrix-matched calibration (Chapter 5)

1.3. Figures

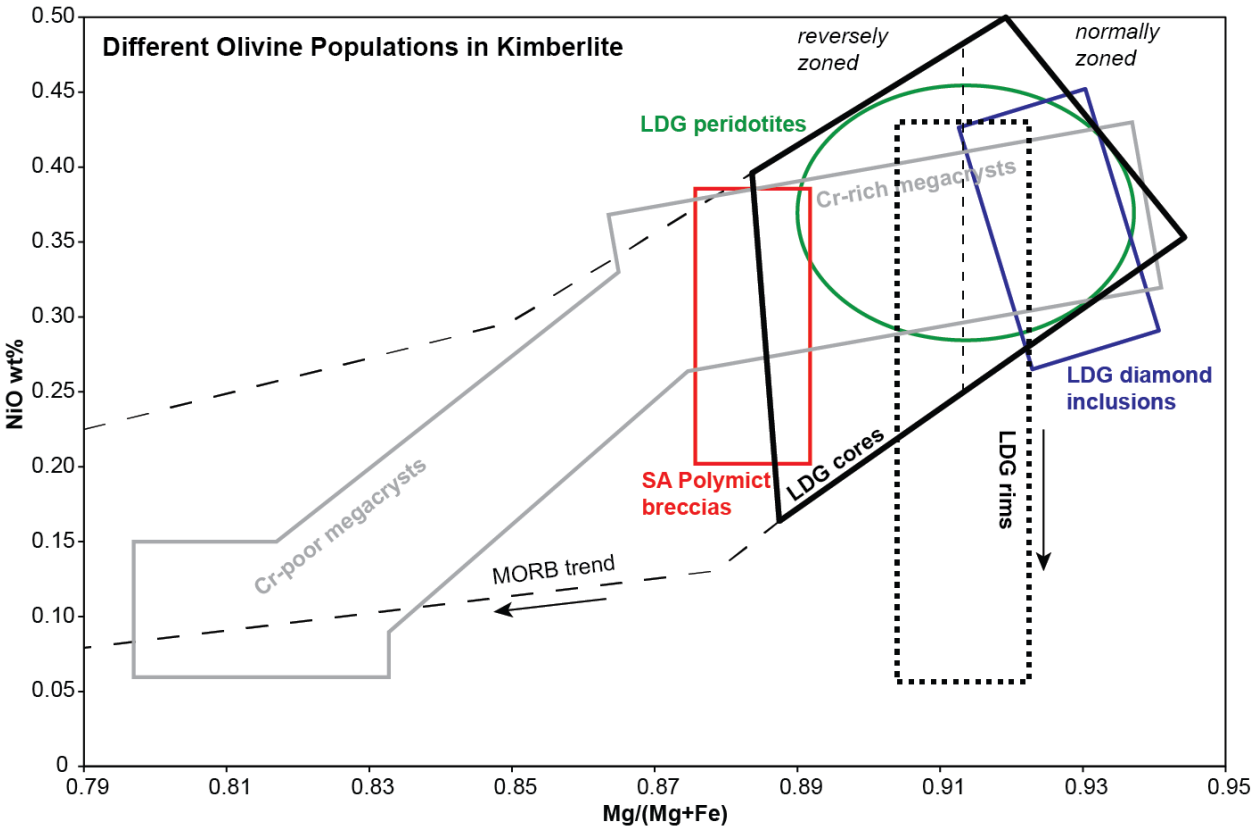

Figure 1-1: NiO vs. Mg# (Mg/(Mg+Fe)) plot showing different olivine populations present in kimberlite. Simplified fields are based on data for Lac de Gras (LDG) kimberlite olivine core and rim analyses (Bussweiler et al. 2015), LDG olivine inclusions in diamond (Stachel et al. 2003; Donnelly et al. 2007), LDG peridotites (Menzies et al. 2004), olivine from polymict breccias from Bultfontein, South Africa (Giuliani et al. 2014), and Cr-poor and Cr-rich megacrysts from the Colossus kimberlite, Zimbabwe (Moore and Costin 2016).

2. The Evolution of Calcite-Bearing Kimberlites by Melt-Rock Reaction – Evidence from Polymineralic Inclusions within Clinopyroxene and Garnet Megacrysts from Lac de Gras Kimberlites, Canada

Y. Bussweiler*[a], R.S. Stone[a], D.G. Pearson[a], R.W. Luth[a], T. Stachel[a], B.A. Kjarsgaard[b], A. Menzies[c]

[a)] Department of Earth and Atmospheric Sciences, University of Alberta, 126 ESB, Edmonton, AB T6G 2E3, Canada

[b)] Geological Survey of Canada, 601 Booth Street, Ottawa, ON, Canada K1A 0E8

[c)] Department of Geological Sciences, Universidad Católica del Norte, Antofagasta, Chile

*Corresponding author at: Department of Earth and Atmospheric Sciences, University of Alberta, 126 ESB, Edmonton, AB T6G 2E3, Canada. Tel.: +1 780 492 3265; fax:+1 780 492 2030. E-mail address: bussweil@ualberta.ca (Y. Bussweiler)

2.1. Acknowledgements

This study forms part of Y.B.'s Ph.D. research funded through D.G.P's Canada Excellence Research Chair. Y.B. is grateful for a University of Alberta Doctoral Recruitment Scholarship. The staff at Diavik Diamond Mine, especially Yuri Kinakin and Gus Fomradas, are thanked for generously allowing access to drill core for sampling. Juanita Bellinger at Rio Tinto is thanked for providing additional concentrate samples. The authors wish to acknowledge the support of CISEM (Centro de Investigación y Servicios Mineralógicos), Universidad Católica del Norte, Antofagasta, Chile for providing QEMSCAN® analytical time. At the University of Alberta, Sarah Gleeson is thanked for access to the fluid inclusion microscopy stage, Andrew Locock for assistance with EPMA, Yan Luo for assistance with LA-ICP-MS, and Chiranjeeb Sarkar for assistance with Sr column chemistry and TIMS. We are grateful to Vadim Kamenetsky for his constructive and insightful review and for kindly allowing us to use Figure 2-2d. We also thank Dante Canil for a very helpful review and Tim Grove for the editorial handling.

2.2. Abstract

Megacrystic (> 1 cm) clinopyroxene (Cr-diopside) and garnet (Cr-pyrope) xenocrysts within kimberlites from Lac de Gras (Northwest Territories, Canada) contain fully crystallized melt inclusions. These "polymineralic inclusions" have previously been interpreted to form by necking down of melts at mantle depths. We present a detailed petrographical and geochemical investigation of polymineralic inclusions and their host crystals to better understand how they form and what they reveal about the evolution of kimberlite melt. Genetically, the megacrysts are mantle xenocrysts with peridotitic chemical signatures indicating an origin within the lithospheric mantle (for the Cr-diopsides studied here ~4.6 GPa, 1015 °C). Textural evidence for disequilibrium between the host crystals and their polymineralic inclusions (spongy rims in Cr-diopside, kelyphite in Cr-pyrope) is consistent with measured Sr isotopic disequilibrium. The preservation of disequilibrium establishes a temporal link to kimberlite eruption. In Cr-diopsides, polymineralic inclusions contain phlogopite, olivine, chromite, serpentine, and calcite. Abundant fluid inclusion trails surround the inclusions. In Cr-pyropes, the inclusions additionally contain Al-spinel, clinopyroxene, and dolomite. The major and trace element compositions of the inclusion phases are generally consistent with the early stages of kimberlite differentiation trends. Extensive chemical exchange between the host phases and the inclusions is indicated by enrichment of the inclusions in major components of the host crystals, such as Cr_2O_3 and Al_2O_3. This chemical evidence, along with phase equilibria constraints, supports the proposal that the inclusions within Cr-diopside record the decarbonation reaction: dolomitic melt + diopside → forsterite + calcite + CO_2, yielding the observed inclusion mineralogy and producing associated (CO_2-rich) fluid inclusions. Our study of polymineralic inclusions in megacrysts provides clear mineralogical and chemical evidence for an origin of kimberlite that involves the reaction of high pressure dolomitic melt with diopside-bearing mantle assemblages producing a lower pressure melt that crystallizes a calcite-dominated assemblage in the crust.

2.3. Keywords

Kimberlite; Cr-rich Megacrysts; Polymineralic Inclusions; Melt Inclusions; Decarbonation Reaction; Kimberlite Evolution

2.4. Introduction

Despite over 100 years of research on kimberlites, the nature and origin of their primary melt(s) and their magmatic evolution path to the observed low pressure mineral assemblages remain controversial and elusive issues. The entrainment of, and reaction with, xenoliths and xenocrysts spanning the entire lithosphere greatly complicates the search for the primary kimberlite melt, and the picture is further obscured by post-emplacement alteration (Mitchell 1986; Mitchell 1995; Price et al. 2000; Kopylova et al. 2007; Sparks et al. 2009; Kjarsgaard et al. 2009). Two of the key issues in kimberlite research that are still debated are: 1) Whether the primary kimberlite is carbonatitic (Dawson 1971; Dawson and Hawthorne 1973; Russell et al. 2012; Kamenetsky and Yaxley 2015; Kamenetsky 2016), a carbonated silicate melt (e.g., Nielsen and Sand 2008; Brey et al. 2008), or a highly saline carbonatite (e.g., Kamenetsky et al. 2012); and: 2) The mechanism for generating the calcite-bearing kimberlites observed in the crust – all experimental evidence suggests that a primary melt formed from the melting of a peridotitic source must produce Mg-rich carbonate, namely dolomite (e.g., Wyllie and Huang 1975; Dalton and Presnall 1998a).

The idea that kimberlites start off as end-member carbonatites that then react with mantle phases, mostly orthopyroxene (opx), to create a more Si- and Mg-rich melt has recently gained ground following experimental studies (Russell et al. 2012; Kamenetsky and Yaxley 2015). However, so far attention has focused on opx dissolution as a dominant process in kimberlite magma evolution and eruption from the base of the lithosphere, although this has not yet been validated through experiments at upper mantle conditions (e.g., Sokol et al. 2016; Stone and Luth 2016), and could be reproduced only for a limited pressure range (Kamenetsky and Yaxley 2015). Here, we focus on the reaction of early high pressure kimberlite melt with clinopyroxene (cpx) and garnet (grt), manifest as solidified melt inclusions within kimberlite-hosted xenocrysts from the Lac de Gras kimberlite field (including the Diavik and Ekati diamond mines). Using reconstructed bulk compositions of these inclusions that trace extensive reaction with the host xenocrysts, we try to further constrain the possible nature of kimberlite melt at depth. Most importantly, we present evidence for reactions between the ascending melt and mantle minerals that lead to the eventual low pressure calcite-dominated mineralogy of kimberlites emplaced in the crust.

2.4.1. Polymineralic Inclusions in Kimberlite Xenocrysts

This study focuses on polymineralic inclusions (composed of multiple discrete mineral phases) that represent crystallized melt inclusions trapped in kimberlite megacryst phases (cpx and grt). Such polymineralic inclusions, also referred to as "spheroids" or "globules", have been reported to occur in a range of different megacryst minerals from kimberlites in different localities worldwide since the mid 1970s. Commonly reported phases in such inclusions are: phlogopite, olivine, carbonates (dominantly calcite), spinel, and serpentine. Haggerty and Boyd (1975) first described polymineralic inclusions in olivine megacrysts from the Monastery kimberlite in South Africa and interpreted them as early kimberlite melt with an immiscible sulphide liquid. Schulze (1985), studying inclusions in grt and cpx megacrysts, adopted this interpretation and extended it to propose that the trapped kimberlite melt may also constitute the magma from which the hosts crystallized. More recent studies of melt inclusions in Cr-diopside from the Diavik Diamond Mine in the Slave Craton, Canada, established a link to carbonatitic melts not in equilibrium with the host phases (van Achterbergh et al. 2002). In follow-up studies on the same samples, melt differentiation towards more silicate-rich melts was proposed, based on the observation of two end-member types of inclusions; carbonate-rich and more silicate-rich (van Achterbergh et al. 2004). Araújo et al. (2009) challenged the need for different inclusion end-members and stated that the spectrum of melt inclusions could "have formed through melt differentiation after wall–rock interaction and fractionation from melts with kimberlitic composition". The presence of pure calcite in the inclusions has previously been attributed to disequilibrium unmixing and quenching in the final stages of kimberlite emplacement (van Achterbergh et al. 2004). Pivin et al. (2009) reported similar polymineralic inclusions within grt megacrysts in kimberlites from the Democratic Republic of Congo, and tentatively interpreted them as products of destabilization of an unknown original phase due to metasomatism.

2.5. Geological Setting

The Archean Slave Craton forms the north-western part of the Canadian Shield and is exposed in the Northwest Territories and Nunavut (e.g., Kusky 1989; Padgham 1992). The Slave Craton formed by tectonic accretion of a pre-3 Ga nucleus in the west to a Neoarchean juvenile arc in the east, creating a north-south trending suture (e.g., Davis et al. 1996). Collisional events in the Paleoproterozoic led to the formation of the Thelon-Taltson and Wopmay orogens that now partially surround the craton (e.g., Isachsen and Bowring 1994). The Slave Craton hosts multiple

kimberlite fields with various emplacement ages ranging from Cambrian to Eocene (e.g., Creaser et al. 2004; Heaman et al. 2004). The central Lac de Gras (LDG) kimberlite field, which contains the Diavik and Ekati diamond mines, was principally active from 75 to 45 Ma (Cretaceous to Eocene) (Sarkar et al. 2015).

The LDG field is located east of the inferred craton suture (Figure 2-1). Its kimberlite pipes define a 100 km by 200 km northwest-trending zone (Lockhart et al. 2004). The generally small pipes (2-12 ha surface area) intrude into metamorphosed Archean basement rock and are overlain by Quaternary glacial deposits (Fedortchouk and Canil 2004; Nowicki et al. 2004). For a detailed description of Diavik and Ekati kimberlites, the reader is referred to Moss et al. (2008) and Nowicki et al. (2004), respectively. The geochemistry of the LDG kimberlite field has been discussed in detail by Kjarsgaard et al. (2009). We studied inclusion-bearing xenocrysts from the Diavik and Ekati kimberlites (Figure 2-1), where Cr-diopside hosted polymineralic inclusions are common.

2.6. Analytical Methods

Polished thin sections of megacrysts, some with surrounding kimberlite, were prepared avoiding the use of water, to prevent the dissolution of inclusion material. Samples with abundant and well-preserved inclusions were selected for imaging in back-scattered electron (BSE) mode using a scanning electron microscope (SEM) in the Canadian Centre for Isotopic Microanalysis (CCIM).

Major and minor element analyses of megacrysts and inclusion phases were collected in multiple analytical sessions by wavelength dispersive X-ray spectroscopy (WDS) using a JEOL 8900 electron probe microanalyzer (EPMA) at the University of Alberta. Analytical conditions and secondary standard results for the different minerals are given in the Appendix (A2.1. and A2.2.). Trace element analyses for phlogopite were obtained by laser inductively coupled plasma mass spectrometry (LA-ICP-MS) at the CCIM Arctic Resources Laboratory, University of Alberta, using a RESOlution 193 nm ArF excimer laser ablation system coupled to a Thermo Scientific ELEMENT XR 2 mass spectrometer. Measuring conditions and secondary standard results are given in the Appendix (A2.3. and A2.4.). LA-ICP-MS data reduction was performed using the Iolite software (Paton et al. 2011).

To obtain modal compositions of the inclusions, six megacrysts of cpx and seven of grt from the Point lake kimberlite, Ekati, were selected for automated mineralogical analysis using QEMSCAN® at the Universidad Católica del Norte, Chile. A detailed description of this technique is given in Ayling et al. (2011) and the operating conditions for these analyses were similar to those in Menzies et al. (2015). EPMA compositions were used in the elemental bulk calculations using mass balance.

Strontium isotopes were measured by thermal ionization mass spectrometry (TIMS) at the CCIM Arctic Resources Laboratory using a Thermo Scientific TRITON-Plus mass spectrometer. Carbonates in the inclusions were dissolved directly with 6N HCl. Host megacrysts were crushed and clear fragments were picked, undergoing two cleaning cycles (in 6N HCl at 120°C overnight, and rinsed in MQ water). The crystal fragments were dissolved in a mixture of HF and HNO_3. Column chemistry procedures to separate Sr from other potentially interfering elements are described by Sarkar et al. (2015). A drop of H_3PO_4 was added to the sample solution before drying down at 90 °C. $TaCl_5$ was added as an activator to the sample solution, which was then loaded to Re filaments. Two analyses of the NBS987 standard yielded a $^{87}Sr/^{86}Sr$ ratio of 0.71027 with a standard error of 0.00001. No corrections were made to the measured data.

2.7. Results

2.7.1. Megacryst Hosts

The cpx and grt samples in this study commonly exceed 1 cm in size and thus are megacrysts in a non-genetic sense (Mitchell 1986).

Cpx megacrysts were collected directly from drill core at the Diavik Diamond Mine. The host kimberlite is coherent (hypabyssal) kimberlite from the A154-North pipe containing abundant fresh olivine, plus ilmenite and grt megacrysts, and calcite of different textural populations. The cpx megacrysts are generally veined/fractured but often contain zones where the cpx has a fresh, clear appearance (Figure 2-2a-c). Some cpx megacrysts show signs of post-emplacement reaction with the host kimberlite in the form of embayments or reaction rinds (brownish discoloration of the surrounding kimberlite, Figure 2-2a). Calcite segregations within the host kimberlite were often observed in direct contact with cpx megacrysts (Figure 2-2b). Four cpx megacrysts (> 2 cm in size) containing abundant inclusions were selected for further analysis.

Diavik grt samples were obtained from ~1 cm mineral concentrates (Figure 2-2e). Their original spatial relationship to the kimberlite is unclear, however, some grains have attached remnants of the host kimberlite (kimberlite rinds). Grt crystals in this study have different genetic origins, as suggested by a color range from orange (eclogitic or low-Cr megacrystic) to red (lherzolitic or high-Cr megacrystic) and purple (harzburgitic) (Figure 2-2e) (McLean et al. 2007). Polymineralic inclusions are most common in red grt grains (lherzolitic or high-Cr megacrystic). A total of 14 separate grt grains with inclusions were analyzed.

Megacryst minerals from the Point lake and Wolverine kimberlite pipes, located on the Ekati Mine claim block, were also examined. Both cpx and grt were obtained from mineral concentrates (> 6 mm) and are likely to represent fragments of even larger crystals. A total of nine cpx grains and 17 grt grains from Point lake were found to contain inclusions. From the Wolverine sample suite, three cpx grains and six grt grains with inclusions were selected.

2.7.1.1. Classification and Thermobarometry

The majority of the cpx and grt mineral hosts to the polymineralic inclusions classify as Cr-diopside and Cr-pyrope, respectively (see Appendix A2.5. for EPMA analyses). Their Cr-rich compositions may suggest a genetic link to the Cr-rich megacryst suite, first documented by Eggler et al. (1979). To obtain P-T estimates of equilibration for Cr-diopside megacrysts, the single cpx thermobarometer of Nimis and Taylor (2000) was used in combination with the compositional filters suggested by Grütter (2009). This exercise yielded temperatures averaging around 1015°C and pressures around 4.6 GPa (Appendix A2.6.).

2.7.2. Polymineralic Inclusions

Polymineralic inclusions can be very abundant, especially in cpx, with up to 10 inclusions observed in single sample sections (Figure 2-2c) (see also van Achterbergh et al. 2002; 2004). In total, 80 polymineralic inclusions have been found and imaged in 20 cpx grains, and 51 inclusions in 29 grt grains. Polymineralic inclusions are usually rounded and up to 2 mm in diameter (Figure 2-2). Depending on whether their mineralogy is carbonate- or silicate-rich, they appear brownish-white or dark in thin section. The inclusions are generally located where veins/fractures with abundant fluid inclusions converge in the host grain (Figure 2-2d, f). Optical microscopy and preliminary Raman spectroscopy indicate that the fluid inclusions are CO_2-rich (Gleeson, S.A., pers. comm.). Larger inclusions along these trails are often filled by phlogopite,

calcite, and/or serpentine indicating that the veins are genetically related to the polymineralic inclusions (Figure 2-2d, f). Hence, the polymineralic inclusions strictly are secondary in nature, as defined by Roedder (1984). However, although the veins occasionally connect to the host kimberlite (where preserved) the appearance of polymineralic inclusions and kimberlite is markedly different (Figure 2-2f). Some megacryst grains contain dark blebs close to grain edges that are in direct contact with the host kimberlite (Figure 2-2b). On the basis of similar mineralogy to the host kimberlite groundmass, the blebs most likely represent late-stage kimberlite melt that infiltrated the grain rims.

It is important to distinguish polymineralic inclusions from other mineral inclusions. For example, cpx megacrysts can contain rounded inclusions of fresh olivine. In grt crystals (especially purple grains) mineral inclusions of olivine are common but often pervasively altered (Figure 2-2e). The resulting alteration assemblage is remnant olivine, with serpentine, calcite, and Ni-rich sulphide (vaesite or pentlandite). The proportion of secondary calcite that replaces olivine can exceed 50%, so that altered olivine inclusions in grt can be mistaken for carbonate-rich polymineralic inclusions (described below).

2.7.2.1. Mineralogy of Inclusions in Clinopyroxene

Polymineralic inclusions in cpx are commonly surrounded by a reaction rim containing abundant micro-inclusions (Figure 2-3a-c). EPMA element distribution maps (Figure 2-4) show that these rims are enriched in Ca, and depleted in Al and Na (also see Figure 2-9). The maps further highlight the presence of phlogopite, calcite, and serpentine in the micro-inclusions. Inside polymineralic inclusions, common phases are calcite, phlogopite, serpentine/chlorite, olivine, and chromite (Figure 2-3a-c). Two end-member inclusion types are distinguished based on the groundmass mineralogy of the inclusions. The groundmass can be composed entirely of calcite, which may display bright and dark zones in BSE images (Figure 2-3a). Alternatively, the groundmass is comprised of hydrated Mg-Fe-silicates (serpentine or chlorite) often with a distinctive vermicular texture (Figure 2-3c). In such inclusions calcite appears as small euhedral crystals or as blebs. In intermediate inclusions calcite can have a colloform texture (Figure 2-3b). Based on the observation that inclusions may either contain a calcite-rich or a serpentine/chlorite-rich groundmass, a division into ‘carbonate-rich’ and ‘silicate-rich’ inclusions, as proposed by van Achterbergh et al. (2004), is justified.

2.7.2.2. Mineralogy of Inclusions in Garnet

Phases observed in polymineralic inclusions in grt megacrysts are the same as those within cpx megacrysts, but further include Al-rich cpx, Al-spinel, and Ni-sulphides (vaesite or pentlandite) (Figure 2-3d-f). Al-spinels can have chromite cores, evident in BSE images as bright inner zones. Phlogopite crystals commonly line the inclusion walls. Importantly, carbonates within polymineralic inclusions in grt can be more Mg-rich (dolomite and Mg-calcite) as well as calcite (Figure 2-3e). Alteration rims showing an enrichment/depletion of the host grt around inclusions are absent. Instead, inclusions are surrounded by grt dissolution features akin to kelyphite rims usually observed at the grt-kimberlite interface (e.g., Canil and Fedortchouk 1999). Analyzing these kelyphite zones using energy dispersive X-ray spectroscopy (EDS) with a defocused electron beam yielded similar spectra to those of pristine grt. Both silicate-rich and carbonate-rich groundmasses are present, the latter being less frequent. Hence, a distinction into 'carbonate-rich' and 'silicate-rich' end-members also seems practical for polymineralic inclusions in grt megacrysts.

Polymineralic inclusions in both host phases can contain accessory apatite and sulfides. Representative QEMSCAN® maps of the end-member inclusion types in Cr-diopside and Cr-pyrope are shown in Supplementary Figure 1 (here Figure 2-14).

2.7.3. Mineral Chemistry of Inclusion Phases

2.7.3.1. Olivine

Within polymineralic inclusions from both Cr-diopside and Cr-pyrope megacrysts, olivine appears as typically euhedral, oblate to elongate crystals comprising up to 25% of the inclusion area. Individual olivine crystals are compositionally homogenous, whereas significant compositional variation can be observed among different inclusions (Appendix A2.7.). Olivine also occurs as single-phase mineral inclusions in some Cr-pyrope and in Cr-diopside megacrysts. For comparison, olivine in kimberlite rinds attached to megacryst hosts was also analyzed.

Olivine compositions from polymineralic inclusions and as mineral inclusions in grt and cpx are compared to LDG kimberlite olivine core and rim data (Figure 2-5). The LDG kimberlitic olivine data can be divided into two main trends: 1) cores with high NiO (and low CaO) at variable Mg/(Mg+Fe) (Mg#), and 2) rims with decreasing NiO (and increasing CaO) at relatively

constant Mg# (arrow in Figure 2-5a) (e.g., Fedortchouk and Canil 2004; Brett et al. 2009; Bussweiler et al. 2015).

Olivines in kimberlite rinds attached to cpx and grt hosts plot along the expected trends for LDG kimberlite olivine. In contrast, olivines within the polymineralic inclusions are distinguished by lower NiO and higher MnO, CaO, and Cr_2O_3 contents with decreasing Mg# (Figure 2-5). Olivines from polymineralic inclusions in Cr-pyrope megacrysts have lower NiO, CaO, and Cr_2O_3 and higher MnO compared to those in cpx megacrysts. Viewed together, olivines from inclusions in the two hosts define a trend of decreasing NiO and Mg# that diverges off the olivine rim trend in kimberlites (Figure 2-5a). A similar trend has been documented for megacrystic olivine in kimberlites and attributed to crystallization from a magma at depth (Boyd 1974).

Single phase olivine inclusions all plot in the field for olivine from LDG peridotite xenoliths (Figure 2-5d) and partially overlap with compositions of olivines included in diamond (Stachel et al. 2003; Donnelly et al. 2007). Thus, altered olivine mineral inclusions in grt megacrysts, which can mimic polymineralic inclusions in terms of mineralogy, are easily distinguished by the chemical composition of remnant olivine, for example by their high NiO and Mg#.

2.7.3.2. Phlogopite

Phlogopite (Appendix A2.8.) occurs in nearly all polymineralic inclusions, comprising up to 25% of the inclusion area within Cr-diopside, and up to 50% of the inclusion area in Cr-pyrope. Phlogopite is usually homogeneous, but crystals zoned in Cr_2O_3 are observed. Phlogopite also occurs as single-phase mineral inclusions, and as intergrowths with other mineral inclusions.

Major element compositions of phlogopite in polymineralic inclusions fall into the range of kimberlitic phlogopite, but define a more restricted window in Mg# space (0.85 - 0.94; Figure 2-6a). Phlogopite in polymineralic inclusions is further distinguished by higher Cr_2O_3 and more restricted TiO_2. Such elevated Cr contents have been observed in phlogopite from the Snap Lake kimberlite, NWT (Kopylova et al. 2010). Importantly, compared to global carbonatite- and kimberlite-derived phlogopite compositions (Reguir et al. 2009), the phlogopite data from polymineralic inclusions fall into the kimberlite field (Figure 2-6d), suggesting that the polymineralic inclusions considered to be ‘carbonate-rich’ are in fact also of kimberlitic lineage.

Compositional differences among phlogopite in polymineralic inclusions are controlled by the host crystal rather than kimberlite pipe or inclusion type; phlogopite in polymineralic inclusions in Cr-pyrope has higher Cr_2O_3 (up to 4.5 wt.%) and slightly lower Mg# (~0.90) than phlogopite in polymineralic inclusions in Cr-diopside (Figure 2-6). Phlogopite in polymineralic inclusions in Cr-pyrope also has higher Al_2O_3 contents and extends to higher Na_2O (Appendix A2.8.). BaO contents in phlogopite are relatively low in inclusions from either host phases, usually < 0.5 wt.% (0.2 wt.% on average), but tend to be higher in inclusions in Cr-pyrope (up to ~1.4 wt.%) (Appendix A2.8.). Phlogopite as single mineral inclusions, as megacrystic intergrowths (with grt, olivine and diopside), or cores of zoned phlogopite have significantly lower Cr_2O_3 contents.

Halogen contents in phlogopite were generally low (mostly F < 0.5 wt.%, Cl < 0.1 wt.%) (Appendix A2.8.). The highest F concentration (0.86 wt.%) was measured in a phlogopite in a 'carbonate-rich' inclusion in Cr-diopside from Diavik. The highest Cl concentration (0.13 wt.%) was measured in a megacrystic phlogopite intergrown with Cr-pyrope from Diavik.

Giuliani et al. (2016) performed a detailed investigation of phlogopite from the Bultfontein kimberlite, South Africa. Compared to their compositional fields for groundmass phlogopite (late crystallization) and high Ti-Cr cores (crystallization at depth), the trace element composition of phlogopite in polymineralic inclusions are low in Zr, Ba, and Mn while extending to Cr-rich compositions and are thus clearly more similar to phlogopite crystallizing at depth (Figure 2-6d-f; Appendix A2.9.).

2.7.3.3. Carbonates

Carbonate forms the groundmass in 'carbonate-rich' end-member inclusions. In intermediate to 'silicate-rich' inclusions carbonate is present as distinct crystals with colloform texture, as blebs, or as euhedral phenocrysts. Compositional zoning, evident as darker and brighter areas in BSE images, is common. Most analyzed carbonates are calcite with < 1.0 wt.% MgO; rarely calcite contains up to 5.0 wt.% MgO (Appendix A2.10.). Within 'silicate-rich' inclusions in Cr-pyrope megacrysts, dolomite (up to ~22 wt.% MgO) is present. FeO contents are generally low in calcite (< 0.5 wt.%) but are higher in dolomite (up to ~4.5 wt.%).

All analyzed carbonates in polymineralic inclusions plot within the reported compositional range of kimberlitic carbonates in terms of Ca# (Ca/(Ca+Mg+Fe)) and SrO contents (e.g., Armstrong et al. 2004) (Figure 2-7a). In polymineralic inclusions, calcite has generally low SrO (< 1.0

wt.%). Higher SrO concentrations are restricted to bright zones (in BSE images) in either the groundmass of 'carbonate-rich' inclusions in Cr-diopside or zoned single crystals in 'silicate-rich' inclusions in Cr-pyrope. Dolomite within inclusions in Cr-pyrope also has low SrO contents (< 0.5 wt.%) and thus overlaps dolomite compositions in kimberlite. Carbonates in polymineralic inclusions, especially in 'silicate-rich' inclusions in Cr-pyrope, extend to higher MnO contents than kimberlitic calcite (Figure 2-7b).

2.7.3.4. Chromite and Spinel

Chromite occurs in all polymineralic inclusions, whereas Cr-rich Al-spinel only occurs in polymineralic inclusions in Cr-pyrope. No clear compositional differences were found between 'carbonate-rich' and 'silicate-rich' inclusions (Appendix A2.11.).

Kimberlite chromite data show a trend of decreasing Cr# and increasing Ti contents at relatively constant Fe# (Fe/(Fe+Mg)), which is referred to as "magmatic spinel trend 1" according to the terminology of Mitchell (1986, 1995). The less common "magmatic trend 2" is characterized by Fe-enrichment prior to an increase in Ti contents, which has been tentatively attributed to preceding crystallization of phlogopite (Mitchell 1995).

Chromites in polymineralic inclusions classify as titanian-magnesian-chromite (TIMAC, Mitchell (1986)) and overlap core compositions of chromite found in the kimberlite groundmass (Figure 2-8). Such chromites are characteristic for kimberlites and are not present in carbonatites (Mitchell 1986). Chromites in polymineralic inclusions generally lie at the beginning of the two differentiation trends (Figure 2-8). Analyses of chromites in polymineralic inclusions in Cr-diopsides, and some analyses in Cr-pyropes, plot along the beginning of magmatic trend 2 (Figure 2-8b). This Fe-enrichment is in accordance with the abundant presence of phlogopite in the polymineralic inclusions. Co-crystallization of olivine may also play a role in Mg-depletion, as evident in the olivine differentiation trend (Figure 2-5a).

Cr-rich Al-spinels within inclusions in Cr-pyrope are characterized by low TiO_2 contents (usually < 2.0 wt.%). Such spinels have no counterpart in the groundmass of LDG kimberlites (Armstrong et al. 2004; Roeder and Schulze 2008). However, some Cr-rich Al-spinels were found to contain cores of chromite. Such zoned spinels may also be the cause for mixed analyses of relatively low Cr# and elevated TiO_2 contents (Figure 2-8c).

Spinel in peridotitic mantle xenoliths (coarse spinel-grt peridotites from Jericho) overlaps spinel in polymineralic inclusions in Cr# vs. Fe# space but can be distinguished by lower TiO_2 (Kopylova et al. 1999).

2.7.3.5. Serpentine and Chlorite

Serpentine/chlorite (Appendix A2.12.) is present in most polymineralic inclusions. In 'carbonate-rich' inclusions, serpentine (Mg-rich) commonly replaces olivine, and chlorite (Al-bearing) replaces phlogopite. In 'silicate-rich' inclusions, an intergrowth of serpentine and chlorite forms the groundmass and can display a characteristic vermicular texture.

Serpentine in kimberlites is defined by a broad range in Mg# (~0.80 - 0.95) and mostly has low Al_2O_3 contents (< 1.0 wt.%). However, Al_2O_3 concentrations up to ~8.0 wt.% have been reported in the literature (e.g., Mitchell, 1986). Serpentine within inclusions in Cr-diopsides from LDG lies at the high-Mg# end and extends to Al_2O_3 contents of up to ~5.0 wt.%, whereas serpentine within polymineralic inclusions in Cr-pyrope can have even higher Al_2O_3 contents (up to ~9.0 wt.%) (Supplementary Figure 2, here Figure 2-15). Serpentine associated with altered olivine inclusions in Cr-pyrope has intermediate Mg# and Al_2O_3 contents, and low Cr_2O_3 and TiO_2 contents.

2.7.3.6. Clinopyroxene in Polymineralic Inclusions

Cpx is only present in polymineralic inclusions within Cr-pyrope hosts and occurs exclusively in 'silicate-rich' inclusions. Cpx in polymineralic inclusions generally classifies as Al-rich, Cr-bearing augite and less commonly diopside (Appendix A2.13.). It is chemically distinct from the Cr-diopside megacrysts hosts and the modified cpx in the alteration rims around the polymineralic inclusions (Figure 2-9). There is some compositional overlap between cpx in inclusions in Cr-pyrope and the global cpx megacryst trend, for example in Mg# and TiO_2 contents. However, cpx in inclusions is more enriched in Cr_2O_3, Al_2O_3, and CaO, and has significantly lower Na_2O contents than typical cpx megacrysts (Figure 2-9). Most prominently, cpx in inclusions has higher MnO contents (clustering around 0.3 wt.%) than all other cpx populations (Figure 2-9f).

2.7.4. Strontium Isotopes

Sr isotopes were measured for 'carbonate-rich' inclusions and their Cr-diopside and Cr-pyrope hosts. Because Rb concentrations were generally very low (commonly below detection limits), the measured ratios were not corrected for radiogenic ingrowth of Sr since kimberlite eruption.

Inclusions in Cr-diopside have $^{87}Sr/^{86}Sr$ ratios of 0.7049 to 0.7053, whereas inclusions in Cr-pyrope are more radiogenic (0.7061 to 0.7071; Figure 2-10). If a previous analysis of carbonate-rich globules in Cr-diopside megacrysts by van Achterbergh et al. (2002) is included, there is overlap in the range of Sr isotopic values of the inclusions in the two hosts. Compared to groundmass calcite from the Jos kimberlite, Somerset Island (Malarkey et al. 2010), signatures of 'carbonate-rich' inclusions in both host minerals are less radiogenic than those of late-stage kimberlitic calcite that is presumed to be affected by increased crustal contamination experienced by kimberlite melts during ascent plus subsequent low-T hydrothermal alteration. But there is overlap (Figure 2-10) with a population of "early" kimberlitic calcite, interpreted to be the product of magmatic crystallization (Malarkey et al. 2010).

Except for the most radiogenic 'carbonate-rich' inclusion in Cr-pyrope, the Sr signatures of the inclusions overlap with those of LDG kimberlites (Tappe et al. 2013). The host kimberlite (Diavik A154) has the most radiogenic signature of all LDG kimberlites and is slightly more radiogenic (0.70619) than inclusions in Cr-diopsides. The relatively radiogenic character has been previously attributed to derivation from a fertile peridotite domain within an otherwise highly depleted domain in the convecting upper mantle (Tappe et al. 2013). However, since LDG kimberlite isotope ratios were obtained from bulk samples, their more radiogenic Sr may be influenced by sampling of late-stage crustal components. The latter scenario seems plausible, because Sr isotope signatures measured in LDG perovskites - an early crystallizing phase in kimberlites - are lower (~0.70424) and have a narrower range (Sarkar et al. 2015).

Importantly, the Sr isotope ratios of the LDG host megacrysts are significantly lower than those of their inclusions, indicating isotopic disequilibrium, as found also by van Achterbergh et al. (2002). In addition, it can be noted that the difference in Sr ratios between inclusion and host is smaller for Cr-diopside than for Cr-pyrope (Figure 2-10).

2.7.5. Reconstructed Bulk Compositions of Polymineralic Inclusions

Major element bulk compositions of polymineralic inclusions were reconstructed using modal proportions obtained with QEMSCAN® or EPMA element maps and mineral compositions measured with EPMA. The overall uncertainty of the reconstructed bulk compositions is thus a function of 1) the uncertainty of the modal abundances and 2) the variability of the averaged mineral compositions used in the calculation. For 1), we have adopted a universal relative uncertainty of 5%, noting that this may be lower for major phases and higher for accessory phases. For 2), we observe that relative standard deviations of multiple EPMA analyses of a given component (in a given phase and in a given inclusion) are up to 10%. This uncertainty may be lower for major components (such as MgO, FeO and SiO_2) and higher for minor components (such as Na_2O and SrO). Thus, we report a propagated overall uncertainty of ~11% for each component of the reconstructed bulk compositions (Appendix A2.14.).

Oxide totals range from ~63 wt.% in 'carbonate-rich' inclusions to ~86 wt.% in 'silicate-rich' inclusions (Appendix A2.14.). Low totals are attributed to major components that were not analyzed, such as CO_2 in carbonates and H_2O in phlogopite and serpentine. P_2O_5 and S hosted in accessory apatite and sulfides presumably have a minor effect on the bulk composition, as well.

Notably, reconstructed bulk compositions of the inclusions plot along nearly continuous trends rather than forming discrete clusters of 'carbonate-rich' and 'silicate-rich' end-members (Figure 2-11). The calculated bulk compositions of 'carbonate-rich' inclusions (>50% modal calcite) in Cr-diopside consistently lie below the threshold of 20 wt.% SiO_2 required for the designation of "carbonatite" (Le Maitre et al. 2002), whereas 'silicate-rich' inclusions extend to SiO_2 contents of up to ~40 wt.%. CaO steeply decreases with increasing SiO_2 content (Figure 2-11a) whereas MgO and FeO increase (Figure 2-11b, c). Polymineralic inclusions in the two hosts display similar general trends, but inclusions in Cr-pyrope are significantly more enriched in the components FeO, Cr_2O_3, and Al_2O_3 (Figure 2-11d), as expected from the mineral chemistry described in the previous sections.

The Mg#s of the reconstructed bulk compositions have a large range from 0.76 to 0.98 (Appendix A2.14.). Inclusions hosted in cpx have a mean Mg# of 0.93, whereas inclusions in grt have lower Mg# averaging around 0.81. It should be noted that Mg# is highest in inclusions

where a great proportion of high-Mg serpentine and phlogopite is exposed. Mg# thus appears to be easily skewed by a sampling or cross-section effect (see Discussion).

2.8. Discussion

2.8.1. Polymineralic Inclusions as Snapshots of Melt-Rock Reaction

Each polymineralic inclusion within Cr-diopside is surrounded by a halo of micro-inclusions of phlogopite and calcite within a matrix of recrystallized cpx depleted in the jadeite component (Figure 2-4). We interpret this halo as a reaction rim between incoming melt and the original host phase. The textural and chemical character of these reaction rims is independent of whether the inclusion is of the 'carbonate-rich' or 'silicate-rich' type and is similar to the spongy rims commonly observed around the outside of cpx grains in mantle-derived xenoliths (Taylor and Neal 1989; Ionov 1998; Carpenter et al. 2002; Su et al. 2012; Lu et al. 2015). Similarly, Cr-pyropes display a kelyphitic reaction zone around polymineralic inclusions of both types. Kelyphite – typically as a fine-grained intergrowth of opx, spinel, olivine, phlogopite and glass – is a commonly observed product of reaction between kimberlite melt and grt xenocrysts (e.g., Canil and Fedortchouk 1999; Spetsius and Taylor 2002).

We interpret spongy textures in Cr-diopsides and kelyphite zones in Cr-pyrope as different textural representations of the same process, namely the reaction of a melt with mantle minerals during ascent. Thus, it seems likely that the original melt in the two different host minerals was the same, as previously suggested for polymineralic inclusions in cpx and grt megacrysts from Kentucky kimberlites (Schulze 1985).

New and published Sr isotopic data on the host megacrysts and inclusions support the reaction relationship deduced from textures (Figure 2-10). The host megacrysts are less radiogenic than the carbonate within the polymineralic inclusions, but the range in Sr isotopic compositions of the inclusions trends towards their hosts. This trend is more evident for carbonate included within Cr-diopside, for which there are two possible explanations: 1) The reaction between melt and host scavenges more Sr from the Cr-diopside (usually containing ~200 ppm Sr) than from the Cr-pyrope (< 2 ppm Sr); 2) The reaction between melt and host Cr-diopside is stronger, as indicated by the presence of spongy rims around polymineralic inclusions that can be > 100 μm wide (Figure 2-2d, 2-3, 2-4) and possibly by reaction rims around the outside of single Cr-diopside megacrysts (Figure 2-2a). Polymineralic inclusions in Cr-pyrope tend to be smaller and

their kelyphite zones narrower, so that the volume of interaction is smaller. But both hosts record clear evidence of reaction with the invading melt.

2.8.2. Evidence for Decarbonation Reactions

Both textural and isotopic data indicate that the melt parental to the polymineralic inclusions has reacted with their mantle-derived hosts, with a potentially stronger reaction observed for Cr-diopsides. The possible driving factors behind these processes might lie in a suite of decarbonation reactions – reactions that release CO_2 – long suspected to occur during the ascent of kimberlites (e.g., Wyllie and Huang 1975; Eggler 1986). In addition to the commonly invoked reaction of melt with opx (enstatite + dolomite melt → forsterite + diopside + CO_2; "opx dissolution"), the decarbonation reaction involving diopside has the form:

$$\text{diopside} + \text{dolomite (melt)} \rightarrow \text{forsterite} + \text{calcite} + CO_2,$$
$$\text{(more general: diopside} + L \rightarrow \text{forsterite} + \text{calcite} + V)$$

This reaction is expected to occur at pressures < 2.5 GPa (Stone 2016; Stone and Luth 2016). Polymineralic inclusions in Cr-diopside appear to preserve direct evidence of this reaction, as their mineralogy is dominated by the presence of pure calcite and forsteritic olivine, while the abundant fluid inclusion trails extending outward from the polymineralic inclusions could be the result of the accompanying exsolution of CO_2. General exsolution of a vapor phase (if H_2O is included in the system) may further be responsible for the crystallization of phlogopite and serpentine inside polymineralic inclusions, and/or in the surrounding micro-inclusions (e.g., Figure 2-4).

Polymineralic inclusions in Cr-pyrope also show evidence for extensive chemical interaction with the host (as evident from kelyphite zones), but commonly contain dolomite. As there is no experimental evidence for an analogous reaction between dolomite melt and grt to produce calcite, it seems logical that the dolomite preserved in polymineralic inclusions in Cr-pyrope could be pristine in nature.

2.8.3. Process and Timing of Melt Entrapment

A likely process for entrapment of a melt in mantle minerals is described as "necking down" by Roedder (1984) and has been proposed in previous studies on polymineralic inclusions in megacrysts (Schulze 1985; van Achterbergh et al. 2002; van Achterbergh et al. 2004; Araújo et

al. 2009). In this process, a melt enters the host crystal along fractures and cleavage planes by dissolution and recrystallization. Surface reduction then results in the entrapment of discrete inclusions that may coalesce to form larger, rounded inclusions. Hence, reaction and the production of new minerals are an integral part of the necking down process. This process of melt infiltration may be further aided by crack formation due to rapid decompression, as described for the formation of fractures in kimberlitic olivine lined with carbonate (Brett et al. 2015).

Thermobarometry of the host Cr-diopsides indicates that they equilibrated at pressures of 4 - 5 GPa (~130 - 160 km), deep in the lithospheric mantle (Appendix A2.6.). The preservation of polymineralic inclusions and the striking compositional zoning around them, such as spongy rims in Cr-diopside, suggest that the melt infiltration occurred shortly prior to or during kimberlite ascent. Otherwise the compositional zoning would have equilibrated quickly at their original deep lithospheric mantle temperature conditions (e.g., Schulze 1985). Similarly, the fine-grained texture of the kelyphite zones around inclusions within Cr-pyrope documents a rapid process during kimberlite ascent. In fact, dissolution experiments of grt xenocrysts in kimberlite melt suggest that this process occurs on a time scale of minutes (Canil and Fedortchouk 1999). Moreover, the decarbonation reaction proposed to account for the calcite-olivine(-phlogopite) assemblage of the inclusions within Cr-diopsides should take place at pressures < 2.5 GPa, consistent with reaction during kimberlite ascent.

2.8.4. Compositional Link to the Transporting Kimberlite Magma

Detailed investigation of individual mineral phases within polymineralic inclusions has shown that their compositions are similar to those crystallizing from kimberlite magma. Moreover, the phase compositions lie at the beginning of kimberlite mineral differentiation trends, suggesting that an early stage of kimberlite melt was trapped at mantle pressures. Particularly the evolution of spinels along magmatic trend 2 of the kimberlite compositional array (Figure 2-8), and olivines falling along the megacryst trend (Figure 2-5), suggests that polymineralic inclusions in both Cr-diopsides and Cr-pyropes from LDG kimberlites represent snapshots of kimberlite melt reacting with the lithospheric mantle during ascent. This model is further supported by the clear difference in the trace element compositions of phlogopite within the polymineralic inclusions versus groundmass phlogopite typically found in kimberlite (Figure 2-6d-f). The phlogopite

within the inclusions shows a striking similarity to high Ti-Cr phlogopite zones interpreted to have crystallized at depth (Giuliani et al. 2016).

No significant differences in mineral compositions exist between 'carbonate-rich' and 'silicate-rich' inclusion types, or between samples from different kimberlite pipes. Instead, mineral compositions appear to be controlled mainly by reaction and equilibration with the host megacrysts. Extensive chemical exchange between the invading melt and the host megacrysts is evident from the enrichment of individual inclusion phases in components such as Cr_2O_3, Al_2O_3, FeO, and MnO, in relation to the chemical character of their hosts; i.e. greater enrichment of these elements in Cr-pyropes compared to Cr-diopsides. In Cr-pyropes, elemental exchange may even lead to the stabilization of additional phases that are not typical of kimberlite, such as Al-rich cpx and Al-spinel by Al exchange.

The continuous range of bulk compositions from 'carbonate-rich' to 'silicate-rich' inclusions (Figure 2-11) led van Achterbergh et al. (2002) to propose separate origins for the two inclusion types. However, we posit that the range in inclusion mineralogy and hence bulk compositions can be explained by a combination of: 1) The way in which the inclusions are exposed during sectioning will lead to random sampling of an assemblage dominated by carbonate and silicates (olivine, phlogopite, etc.), yielding the nearly continuous range in bulk compositions illustrated well by CaO-SiO_2 and MgO-SiO_2 relations (Figure 2-11a, b). 2) Small-scale fractional crystallization of the melt in a small fixed volume will produce different compositions that are then exposed in two-dimensional sections. This can explain observations such as the two generations of calcite in the inclusions, with the later generation being more enriched in incompatible elements such as Sr (evident as bright zones in BSE images). 3) The polymineralic inclusions represent trapped melts at various stages of reaction and differentiation prior to entrapment. Evidence for differentiation of the melt prior to entrapment comes from the range of olivine compositions seen in different inclusions that define a typical igneous fractionation trend (Figure 2-5), as documented originally in olivine megacrysts by Boyd (1974). Fractionation is also clearly evident in the range of spinel compositions (Figure 2-8). Differentiation is likely to be associated with the progressive assimilation of mantle material, such as opx (Kamenetsky et al. 2008; Russell et al. 2012; Pilbeam et al. 2013; Brett et al. 2015) and cpx – as observed here.

Because bulk compositions are easily skewed by a combination of the above processes (in addition to reaction with the host), the Mg# of the reconstructed bulk compositions cannot be reliably compared to the expected range of Mg# for LDG kimberlite liquids (Canil and Bellis 2008). Instead, we think it is more instructive to examine the calculated melts in equilibrium with olivine inside the polymineralic inclusions. Using the equation by Canil and Bellis (2008) along with their lower and upper estimates for Kd_{FeMg} ol/liq (0.12 and 0.27) we arrive at average Mg# for all polymineralic inclusions of 0.50 and 0.69, respectively. Olivines within inclusions in cpx yield higher liquid Mg# (0.52 and 0.71, respectively) than those in inclusions in grt (0.47 and 0.66, respectively), as expected from the higher Mg# of the host cpx relative to grt. These estimates of liquid Mg# overlap those by Canil and Bellis (2008) for LDG kimberlites (mostly < 0.60) which we interpret as further evidence that the polymineralic inclusions in cpx and grt megacrysts are linked to the early evolutionary stage of the transporting kimberlite magma.

2.8.5. A Glimpse at Primary Kimberlite Melt?

The reconstructed bulk compositions of polymineralic inclusions in Cr-diopside fall along a distinct trend in CaO-SiO_2 and MgO-SiO_2 space, produced by a combination of the three mechanisms described above (cross-section effect, internal fractional crystallization, and melt differentiation prior to entrapment), which essentially describes a mixing line between the end-member inclusion phases calcite and olivine (Figure 2-12). The compositions of polymineralic inclusions in Cr-pyrope generally also fall along this trend, although they are more enriched in SiO_2, FeO, Cr_2O_3, and Al_2O_3 due to equilibration with the host (Figure 2-11c, d).

The clear evidence of reactions between melt and host crystals makes an *original melt* composition difficult to obtain. The only possible result, using the inclusions themselves, is to arrive at an estimate for the composition of the melt after it has experienced reaction with the host. This composition will, necessarily, be subject to large uncertainties. Based on the observation that inclusions within Cr-pyrope have been more influenced by later equilibration with the host and noting that the reconstructed bulk compositions represent random samples of melt compositions, we use the average of the range of bulk compositions of inclusions in Cr-diopsides to obtain an average bulk composition. The resulting composition, which represents a melt *after* reaction with the host, has ~22 wt.% SiO_2, ~24 wt.% CaO and ~15 wt% MgO (star

symbol in Figure 2-11, 2-12). This composition is compared to experimental melts and primary kimberlite magma estimates in order to explore possible precursor melts (Figure 2-12).

Partial melts of carbonated peridotite produced in different experimental studies (at T ≤1500°C) generally lie at lower SiO_2 contents. However, a correlation of SiO_2 with T is observed in these experiments, so that the high T (1500°C) runs, e.g., by Gudfinnsson and Presnall (2005), approach our estimate of the average melt composition. These experiments are ~500°C above the equilibration temperature of the Cr-diopside megacrysts (Appendix A2.6.), which seems excessively high. Alternatively, the experimental melts can be shifted onto the polymineralic inclusion array by reaction with the host crystals. In Figure 2-12, this is demonstrated with reaction vectors towards cpx and grt compositions extending from one possible primary composition characterized by maximum overlap of the experimental fields at melting conditions of roughly 6 GPa and 1400°C (question mark in Figure 2-12). The digestion of other mantle silicates, especially opx, causes a similar displacement and may have started before the melt became trapped in the Cr-diopside and Cr-pyrope hosts (Kamenetsky et al. 2008; Russell et al. 2012; Pilbeam et al. 2013; Brett et al. 2015). Recent experimental studies, using carbonatite compositions obtained from previous low-degree partial melting experiments on mantle peridotite, suggest that opx dissolution does not occur until the kimberlite magma reaches pressures < 3.5 GPa (Stone and Luth 2016; and references therein). An indication that opx dissolution may be an important process during final (< 100 km) ascent and phenocryst crystallization of kimberlite magma – as opposed to the melt trapped as inclusions in cpx and grt megacrysts – lies in the mineral chemistry of olivine: Whereas olivines within the polymineralic inclusions define a fractionation trend (Figure 2-5a), phenocrystic rims on olivines in kimberlite show a characteristic trend of decreasing Ni at buffered Mg# (arrow in Figure 2-5a) which has previously been attributed to the effect of opx dissolution (e.g., Pilbeam et al. 2013; Bussweiler et al. 2015).

Previous estimates of primary or parent kimberlite magma obtained through whole rock considerations (Le Roex et al. 2003; Kjarsgaard et al. 2009) also plot along the trend of reconstructed bulk compositions of polymineralic inclusions (Figure 2-12). Compared to our average bulk composition, they are characterized by lower CaO and higher MgO and SiO_2 contents, which may suggest that these magma compositions, as well, have experienced some degree of mantle assimilation.

While the polymineralic inclusions constitute snapshots of kimberlite melt reacting with mantle minerals during ascent, it is important to note that they do not represent the primary or protokimberlite melt. Evidence for such precursor melts to LDG kimberlites may be preserved as melt inclusions in phenocryst phases (Kamenetsky et al. 2013), or as fluid inclusions in fibrous diamonds (Klein-BenDavid et al. 2007; Weiss et al. 2015), or can be gleaned from isotopic studies (Tappe et al. 2013). Together with the occurrence of sublithospheric diamonds at LDG (e.g., Tappert et al. 2005) these studies point towards an asthenospheric origin of the protokimberlite. The generally SiO_2-poor and CaO-rich compositions of the already reacted kimberlite melt, as represented by the now crystallized polymineralic inclusions, is consistent with suggestions of the carbonatite-like nature of the protokimberlite melt (e.g., Dawson 1971; Dawson and Hawthorne 1973; Russell et al. 2012; Kamenetsky and Yaxley 2015; Kamenetsky 2016).

2.8.6. General Role of Decarbonation Reactions in Producing Calcite-Bearing Kimberlites

Oxybarometry studies applied to cratonic grt peridotites have shown that the lithospheric mantle below the LDG kimberlite field of the central Slave Craton tends to be more oxidized than the mantle below other cratons (Creighton et al. 2010; Luth and Stachel 2014), especially in the pressure-range of 4.5 to 6 GPa (~140 – 180 km), corresponding roughly to the depth of formation of the host megacrysts (Appendix A2.6.; Supplementary Figure 3, here Figure 2-16). This has been attributed to the oxidizing effects of carbonate-rich fluids/melts (e.g., Creighton et al. 2008). The result of this metasomatism is the oxidation of local zones in the mid- to lowermost lithosphere beneath the LDG kimberlite field to levels conducive to the stabilization of carbonate. The expected stable carbonate phase is Mg-rich in any four-phase peridotite assemblage, i.e. dolomite (e.g., Wyllie and Huang 1975; Dalton and Presnall 1998a) or magnesite at higher pressure (Brey et al. 1983), and the melt produced from such carbonated peridotites is always dolomitic in composition (e.g., Irving and Wyllie 1975; Brey et al. 2008). However, LDG kimberlites, and kimberlites globally, are mostly dominated by calcite (e.g., Skinner and Clement 1979; Armstrong et al. 2004), as are the early kimberlite melts trapped as polymineralic inclusions in LDG megacrysts.

The reactions illustrated by the polymineralic inclusions provide an explanation for this discrepancy between expected high pressure melt compositions produced from carbonated peridotite and the calcite-rich nature of kimberlites in general, via the decarbonation reaction:

$$\text{diopside} + \text{dolomite (melt)} \rightarrow \text{forsterite} + \text{calcite} + CO_2,$$

This reaction is expected to begin during kimberlite ascent at depths around 70 km based on experimental and theoretical constraints (Wyllie and Huang 1975; Stone 2016; Stone and Luth 2016). The reaction may continue up to kimberlite emplacement in the crust, as indicated by the presence of reaction rinds (often containing calcite segregations) around single Cr-diopside megacrysts in their host kimberlite (Figure 2-2a, b). The latter observation also indicates that the dolomite-diopside decarbonation reaction is not just relevant for melt differentiation within the limited volume of polymineralic inclusions, but affects the entire rising batch of kimberlite magma. The similarity of the phase composition variations present in the kimberlite melt inclusions with those observed in kimberlites emplaced in the crust, indicates that this process of melt-rock reaction is critical in producing the observed compositions and mineralogy of kimberlites worldwide. In this scheme, the resulting exsolution of a vapor phase during the proposed reaction may be responsible for the crystallization of phlogopite and serpentine in the inclusions (and in the host kimberlite), as water may be present in the original melt and will accumulate during reaction and crystallization. In addition to driving the evolution of a dolomitic to a calcitic kimberlite melt at pressures in the shallower portion of the lithospheric mantle, the reaction provides a means of further CO_2 exsolution, which is seen as an important process in driving kimberlite emplacement (e.g., Eggler 1986; Brey et al. 1991; Russell et al. 2012). The reaction could proceed as long as the kimberlite magma contains a dolomitic melt component that can react with disaggregated diopside (either as Cr-diopside megacrysts or from peridotite xenoliths). While the abundance of diopside in lithospheric peridotites is relatively low (~10%), the presence of lherzolites and discrete Cr-diopside megacrysts in kimberlites is ubiquitous, indicating the likelihood of this reaction occurring in any section of cratonic lithosphere.

A schematic illustration of the formation of polymineralic inclusions and the concomitant evolution of the host kimberlite is summarized in Figure 2-13. In sequence, the process is envisioned as (1) the formation of a dolomitic silico-carbonatite melt via partial melting of carbonated peridotite, (2) initial reaction with lithospheric mantle and early high pressure CO_2

exsolution, (3) lower pressure reactions with lithospheric wall rocks that change the bulk composition and release more CO_2, producing calcite, (4) the emplacement in the crust of the evolved kimberlite with the calcite-bearing mineral assemblage. The widespread occurrence of polymineralic inclusions in kimberlite megacrysts from numerous cratons (Haggerty and Boyd 1975; Schulze 1985; van Achterbergh et al. 2002; Pivin et al. 2009; Araújo et al. 2009) is evidence of the general applicability of this process to the evolution of kimberlites.

2.9. Conclusions

1. Lac de Gras Cr-diopside and Cr-pyrope megacrysts contain abundant, large (up to 2 mm) polymineralic inclusions formed by necking down of melts starting at lithospheric mantle depths. The megacrysts genetically are mantle xenocrysts with peridotitic chemical signatures. Geothermobarometry suggests that they originate from within the lithospheric mantle (~4.6 GPa, 1015°C).
2. There is clear textural and isotopic evidence for disequilibrium between the host crystals and their polymineralic inclusions, the preservation of which establishes a temporal link to the kimberlite eruption.
3. The inclusion phases are broadly characteristic of kimberlite, with their compositions being overall consistent with the early stages of kimberlite differentiation trends. Enrichment of inclusion phases in components more abundant in the host crystals, such as Cr_2O_3 and Al_2O_3, points towards extensive reaction between inclusions and hosts. Trace element signatures of phlogopites within the inclusions constrain their crystallization from the melt inclusions at lithospheric mantle depths.
4. Although scattered by sectioning effects and reaction with the host phases, reconstructed bulk compositions of the inclusions bear a general resemblance to the experimentally derived partial melts of carbonated peridotites, if allowance is made for the assimilation of mantle minerals (including the host minerals cpx and grt). Thus, the polymineralic inclusions represent snapshots of kimberlite melt reacting with the lithospheric mantle during ascent.
5. Inclusions in Cr-diopside record direct evidence for a decarbonation reaction of the form: dolomitic melt + diopside → forsterite + calcite + CO_2, expected to begin at pressures < 2.5 GPa. This reaction may play an important role in the en-route transformation of an upward moving dolomitic silico-carbonatite melt into the calcite-bearing kimberlite

observed at the surface. As such, it is one of many reactions likely to occur between carbonatitic melt and lithospheric mantle that drive the chemical and volatile evolution in kimberlite.

2.10. Figures

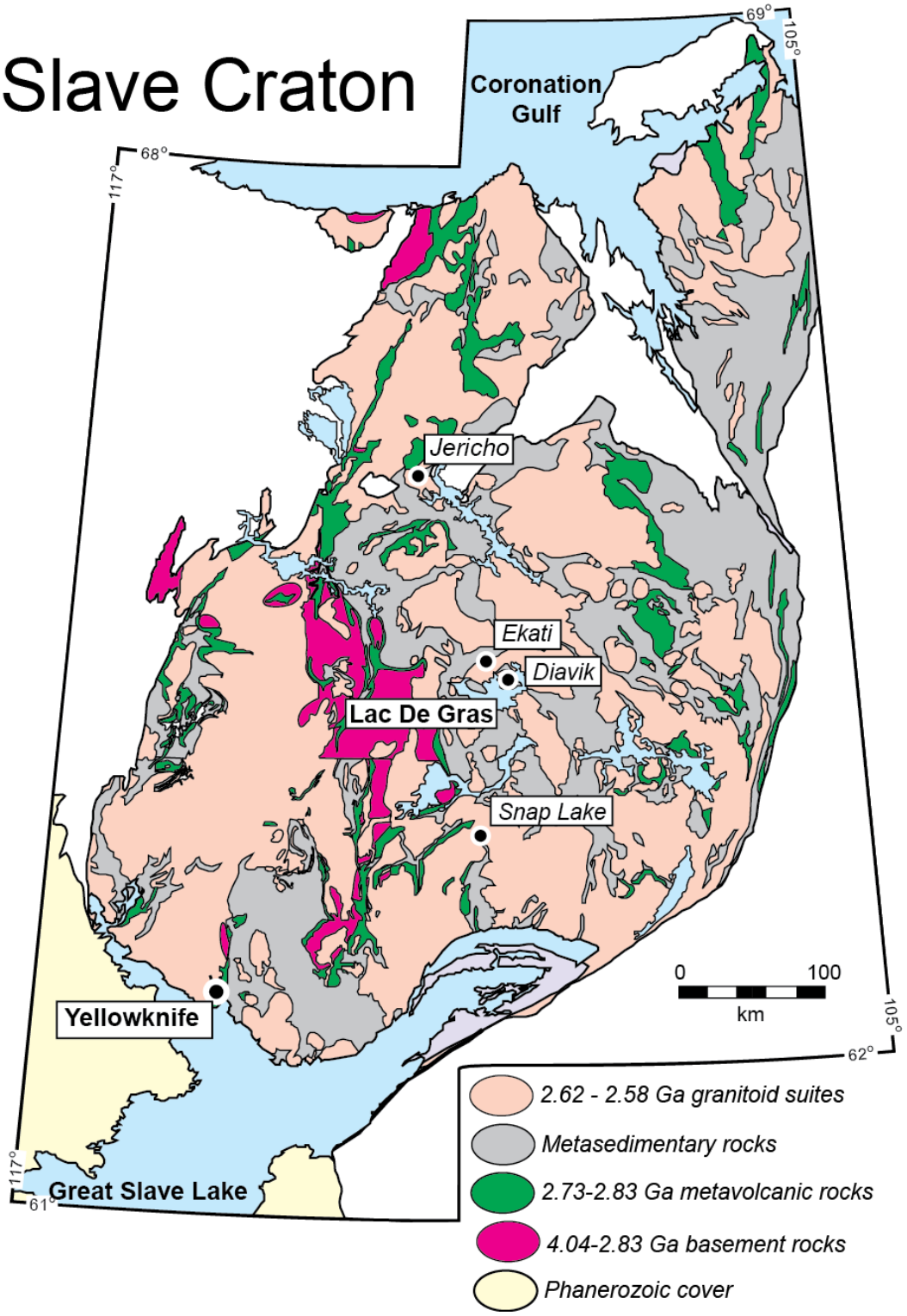

Figure 2-1: Geological overview map of the Slave Craton. Modified from Bleeker et al. (2004). The locations of major diamond mines are indicated. Samples for this study are from the Lac de Gras area (Diavik and Ekati).

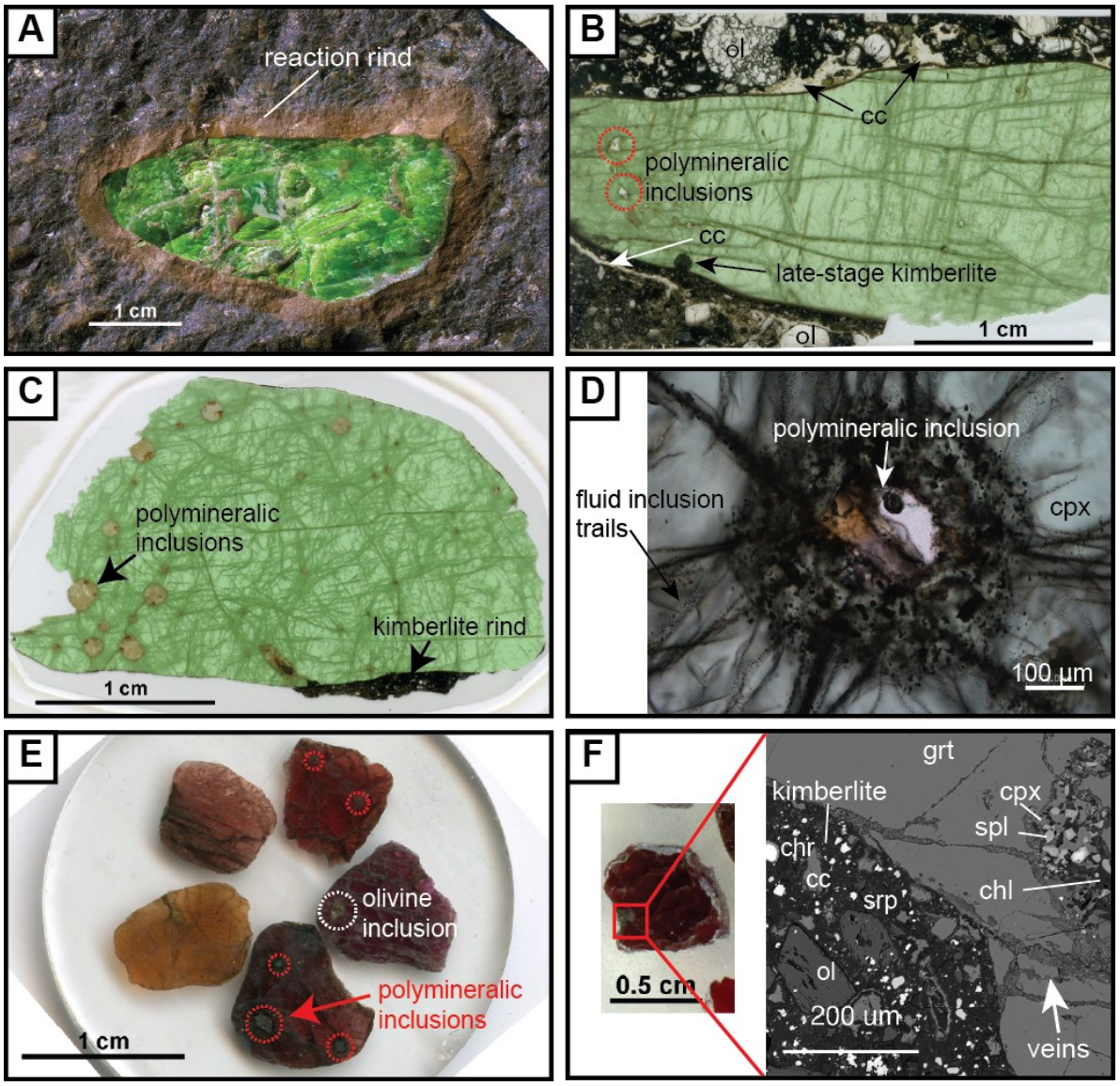

Figure 2-2: Photomicrographs of megacryst samples containing polymineralic inclusions. A) Section through kimberlite drill core exposing cpx megacryst with brownish reaction rind. B) Thin section of cpx megacryst in direct contact with calcite segregations in coherent (hypabyssal) kimberlite from the A154N pipe, Diavik. C) Thin section of cpx megacryst with abundant polymineralic inclusions and remnant host kimberlite ('kimberlite rind'). D) Photomicrograph of a polymineralic inclusion in cpx megacryst (courtesy of V.S. Kamenetsky). Polymineralic inclusions are typically located where fractures/veins with fluid inclusions converge and are typically surrounded by a thick reaction rim (spongy rim). E) Sample mount section of grt megacrysts from < 1 cm concentrates from Diavik. Color range indicates different origins. Polymineralic inclusions are most common in red grt grains (lherzolitic or megacrystic). F) Back-scattered electron (BSE) image of a polymineralic inclusion in a grt megacryst. Veins connect polymineralic inclusion to the host kimberlite, but mineralogy of inclusion and host kimberlite is markedly different.

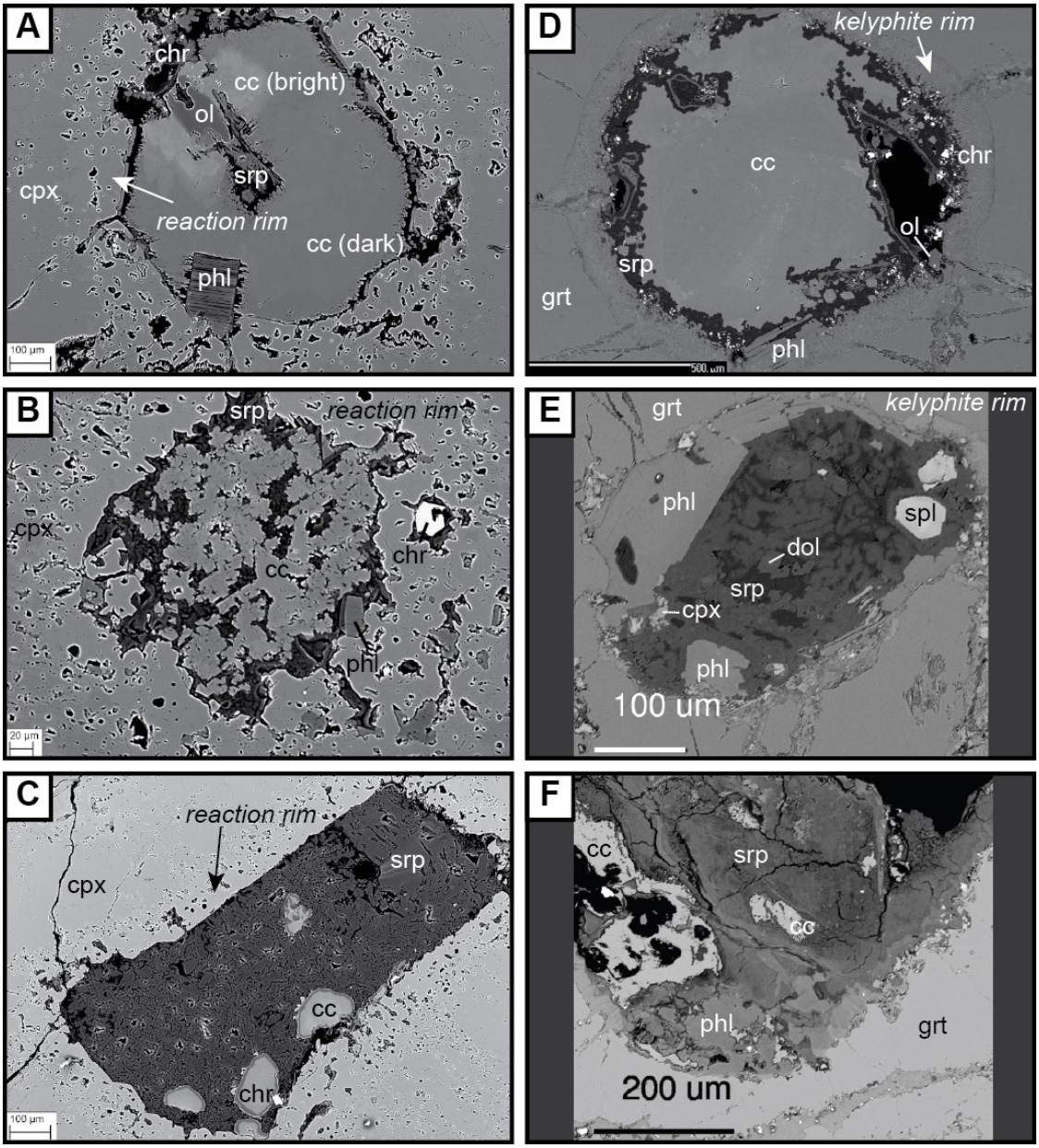

Figure 2-3: BSE images for polymineralic inclusions in Cr-diopside (cpx) megacrysts (A-C) and in Cr-pyrope (grt) megacrysts (D-F). All inclusions in cpx are surrounded by spongy 'reaction rims', whereas inclusions in grt are surrounded by 'kelyphite zones'. A) 'Carbonate-rich' end-member inclusion with calcite (cc) groundmass composed of bright and dark zones, containing phlogopite (phl), olivine (ol), serpentine (srp), and chromite (chr). B) Intermediate inclusion with 'colloform' cc in Mg-Fe silicate groundmass, containing phl and chr. C) 'Silicate-rich' end-member inclusion with Mg-Fe-silicate groundmass composed of srp/chlorite (with distinctive vermicular texture), containing cc blebs and chr. D) 'Carbonate-rich' end-member inclusion with cc groundmass, containing phl, ol, srp, and chr. E) Intermediate inclusion with Mg-Fe silicate groundmass (vermicular texture) containing dolomite (dol), spinel (spl), and cpx in addition to phl and chr. F) 'Silicate-rich' end-member inclusion with Mg-Fe-silicate groundmass containing cc as irregular blebs, phl, and chr.

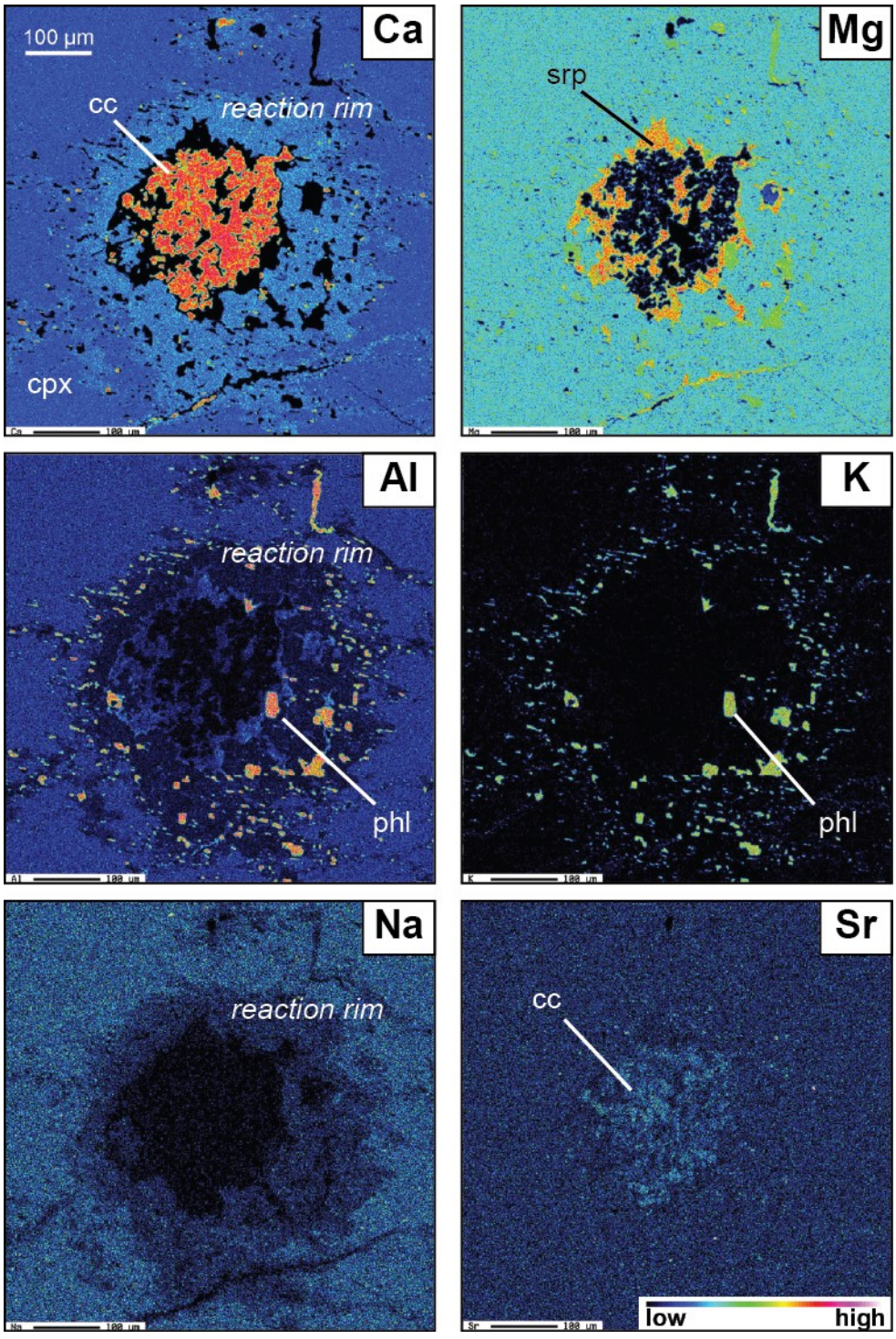

Figure 2-4: EPMA element distribution maps for Ca, Al, Na, Mg, K, and Sr of a polymineralic inclusion (intermediate type) in a cpx megacryst. Warmer colors indicate higher element concentrations. Reaction rims are enriched in Ca, and depleted in Al and Na. The maps highlight the presence of phlogopite (phl), calcite (cc), and serpentine (srp) in micro-inclusions around the main inclusion.

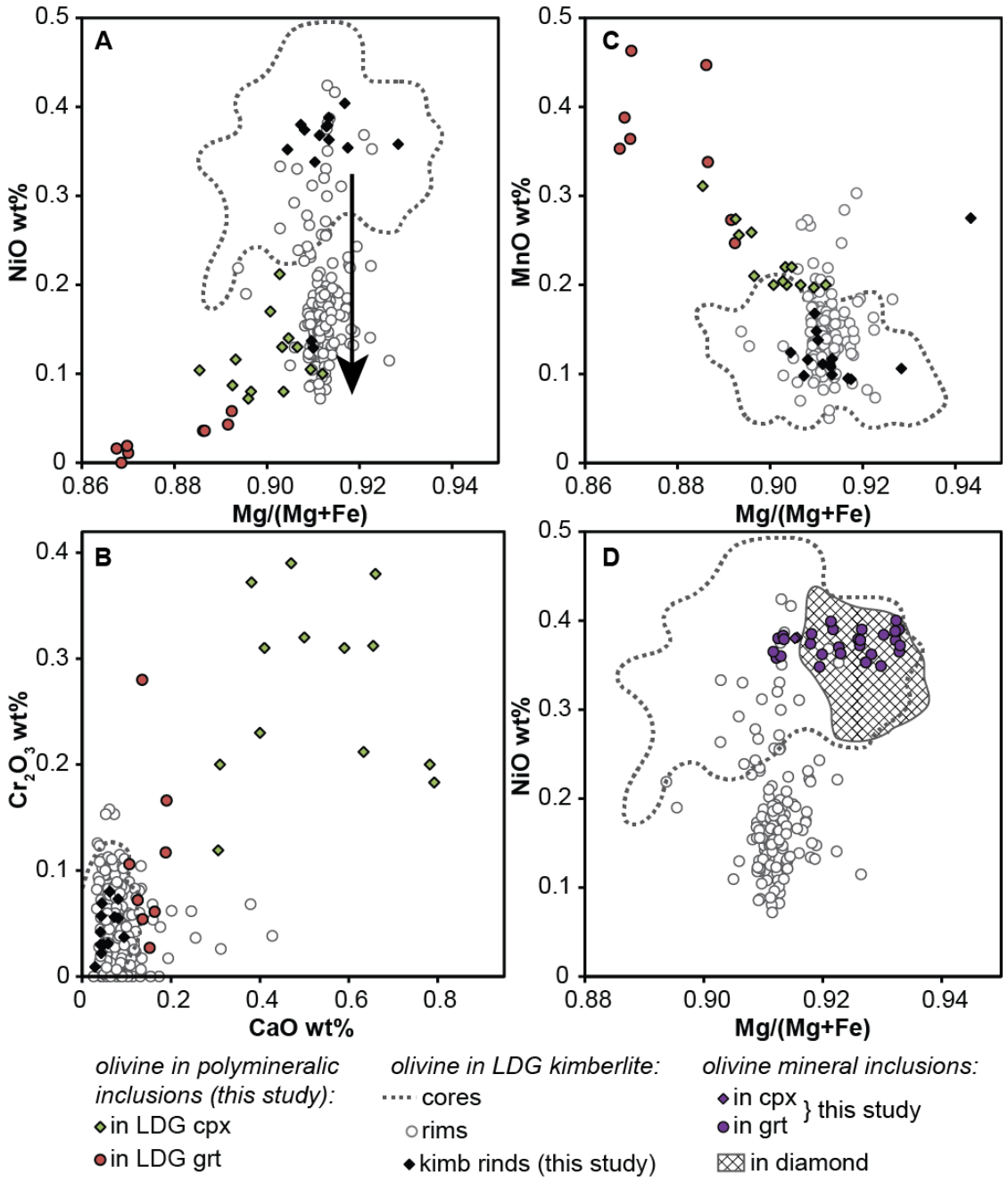

Figure 2-5: Bivariate plots for olivine in polymineralic inclusions resolved by megacryst host (Cr-diopside and Cr-pyrope), and olivine in kimberlite rinds (A-C) and as mineral inclusions and intergrowths (D). Olivine was analyzed in eight polymineralic inclusions in Cr-diopside from Diavik and Point lake (seven 'carbonate-rich', one 'silicate-rich'), and in four polymineralic inclusions in Cr-pyrope from Diavik (two 'carbonate-rich', two 'silicate-rich'). 12 olivine mineral inclusions were measured in Cr-pyropes from Diavik, one in Cr-pyrope from Point lake, and one in Cr-diopside from Diavik. Reference data for LDG kimberlite olivines divided into cores and rims are from Brett et al. (2009) and Bussweiler et al. (2015). The arrow in (a) highlights the differentiation trend of phenocrystic rims (see text). Data of olivine inclusions in diamond from Lac de Gras, Slave Craton, Canada, are from Donnelly et al. (2007) and Stachel et al. (2003).

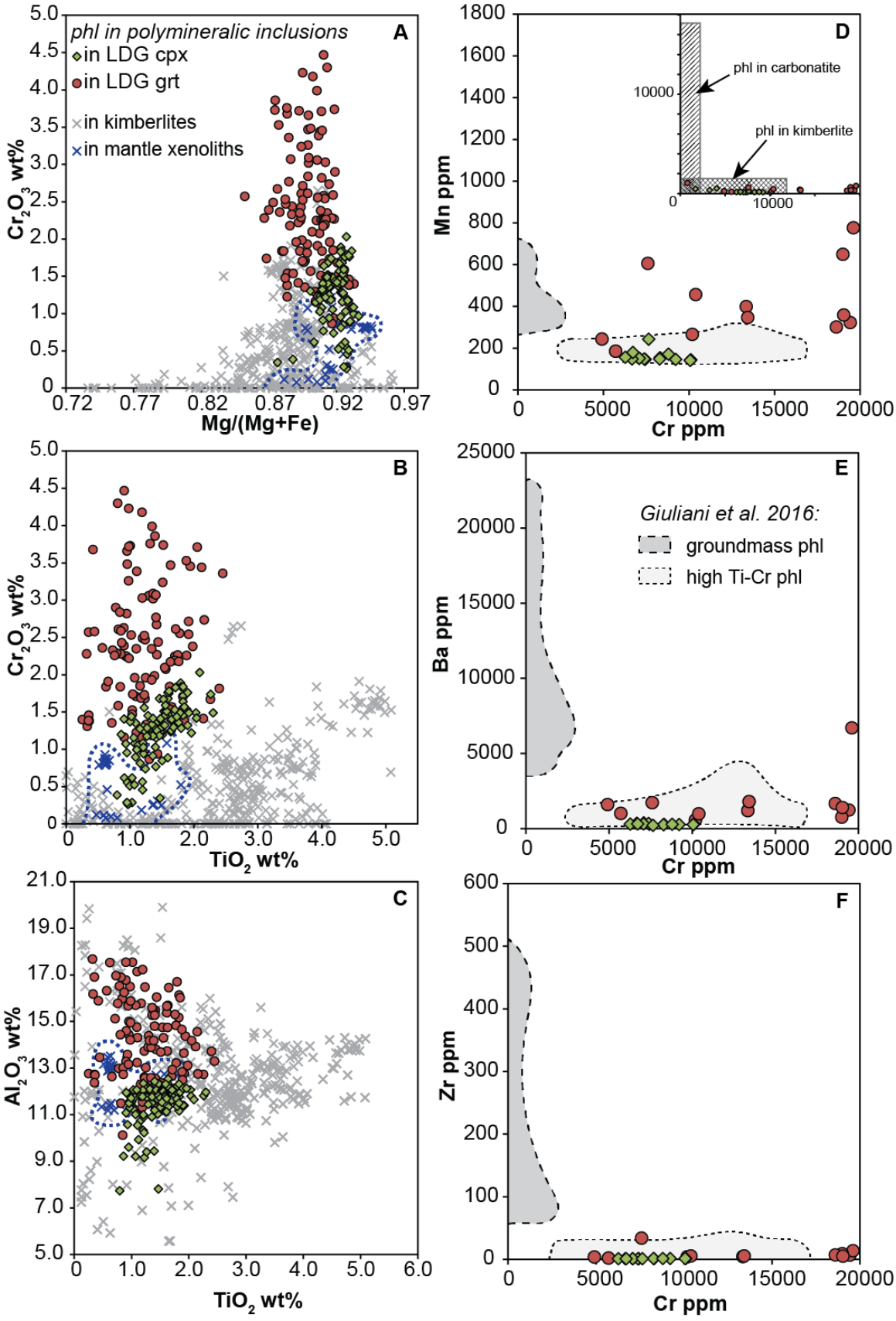
A
phl in polymineralic inclusions
in LDG cpx
in LDG grt
in kimberlites
in mantle xenoliths
Cr2O3 wt%
Mg/(Mg+Fe)
B
Cr2O3 wt%
TiO2 wt%
C
Al2O3 wt%
TiO2 wt%
D
Mn ppm
Cr ppm
phl in carbonatite
phl in kimberlite
E
Giuliani et al. 2016:
groundmass phl
high Ti-Cr phl
Ba ppm
Cr ppm
F
Zr ppm
Cr ppm

Figure 2-6 (previous page): A-C: Major element (EPMA data) bivariate plots for phlogopite in polymineralic inclusions resolved by megacryst host (Cr-diopside and Cr-pyrope). Phlogopite was analyzed in polymineralic inclusions in Cr-diopside from Diavik and Point lake (five 'carbonate-rich', 19 'silicate-rich'), and in polymineralic inclusions in Cr-pyrope from Diavik, Point lake, and Wolverine (four 'carbonate-rich', 29 'silicate-rich'). Reference data for phlogopite in kimberlites are from Eccles et al. (2004), Armstrong et al. (2004), and Kopylova et al. (2010). Mantle phlogopite data are from Menzies et al. (2004) and Giuliani et al. (2014). D-F: Trace element (LA-ICP-MS data) bivariate plots for phlogopite in polymineralic inclusions. The inset in D shows compositional fields for global carbonatite- and kimberlite-derived phlogopite (Reguir et al. 2009). Phlogopite in polymineralic inclusions clearly falls into the kimberlite field. Compositional fields for groundmass phlogopite and high Ti-Cr phlogopite cores are based on data from Giuliani et al. (2016). Phlogopite in polymineralic inclusions is similar to the high Ti-Cr group (crystallized at depth) in many trace elements.

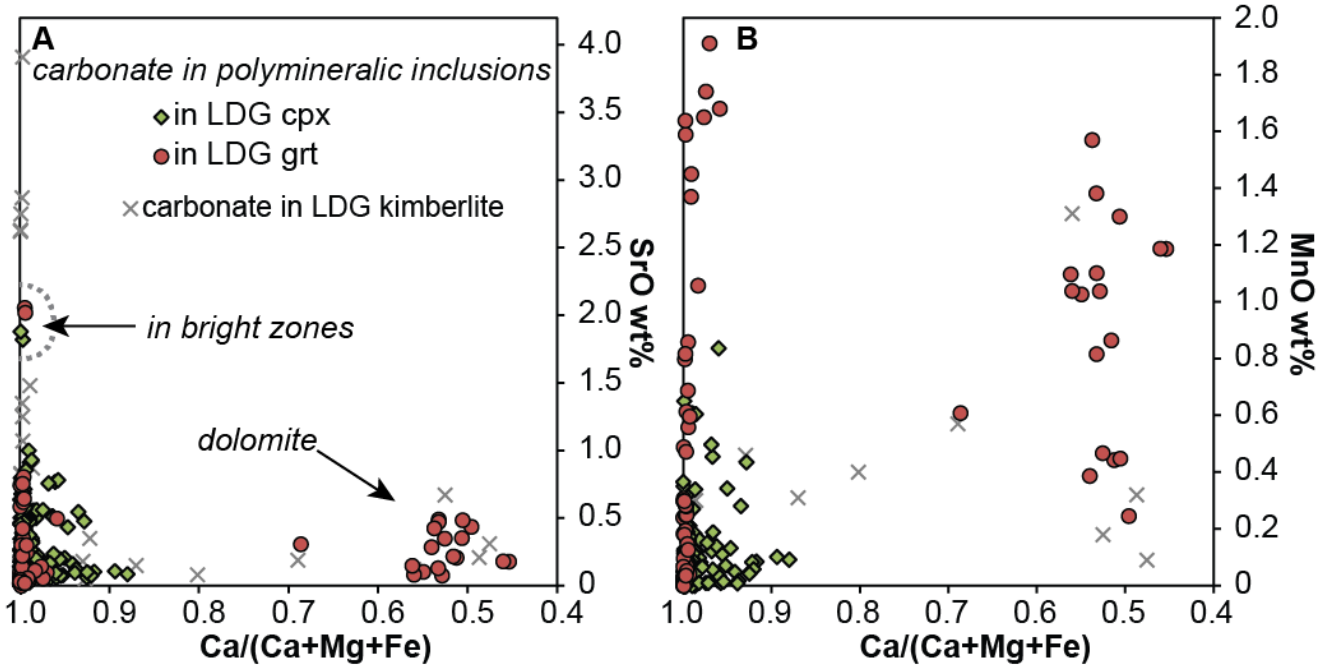

Figure 2-7: Bivariate plots for carbonates resolved by megacryst host (Cr-diopside and Cr-pyrope). Carbonate was analyzed in polymineralic inclusions in Cr-diopside from Diavik (10 'carbonate-rich', 26 'silicate-rich'), Point lake (four 'carbonate-rich', five 'silicate-rich'), and in polymineralic inclusions in Cr-pyrope from Diavik (two'carbonate-rich', nine 'silicate-rich') and Point lake (three 'carbonate-rich', 11 'silicate-rich'). Carbonate was further analyzed in veins, kimberlite rinds, and altered olivine inclusions (in Cr-pyrope). Reference data for kimberlitic carbonate are from Armstrong et al. (2004).

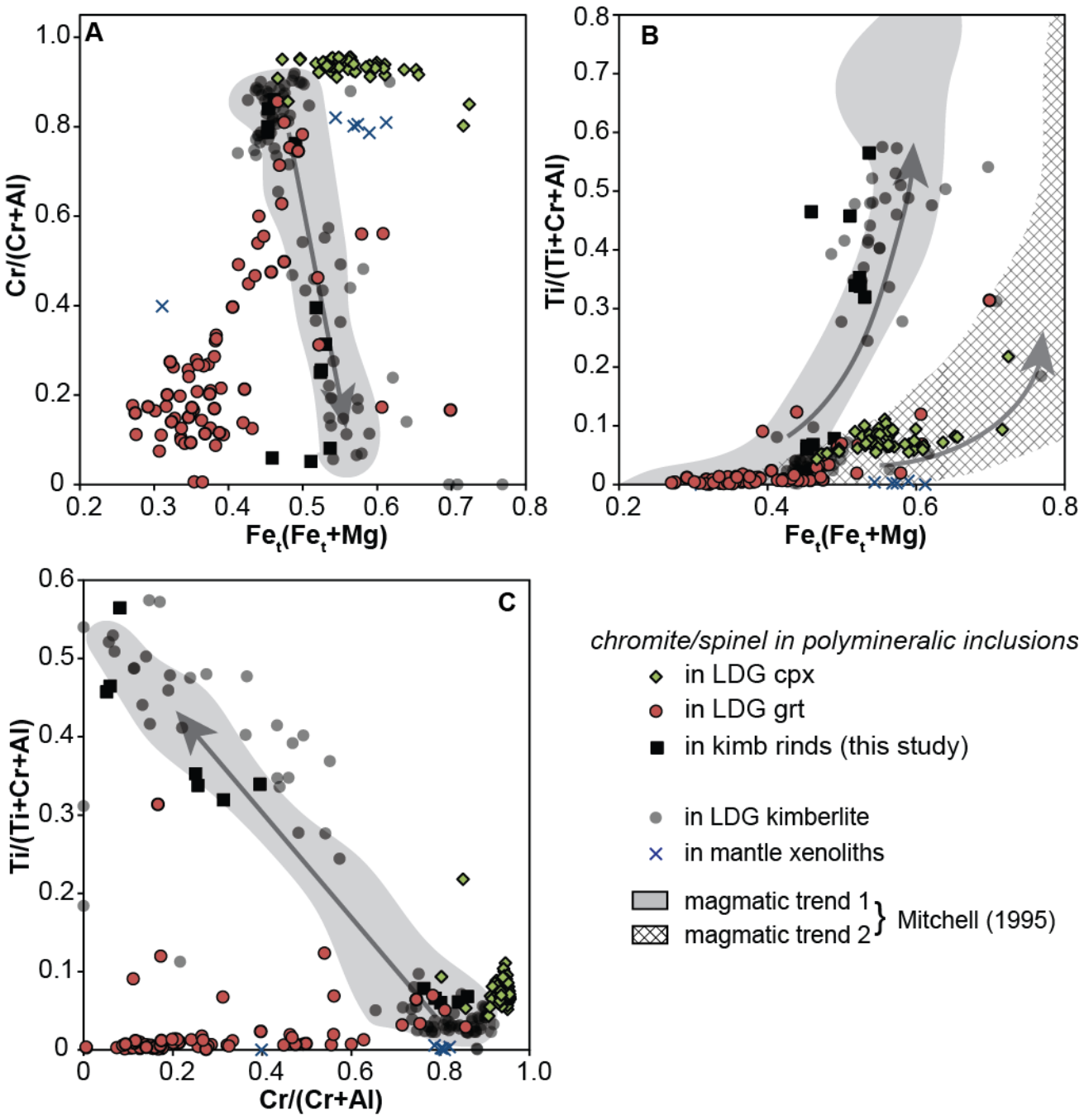

Figure 2-8: Bivariate plots for chromite/spinel in polymineralic inclusions resolved by megacryst host (Cr-diopside and Cr-pyrope) and in kimberlite rinds. Chromite/spinel was analyzed in inclusions in Cr-diopside from Diavik (six 'carbonate-rich', 21 'silicate-rich') and Point lake (one 'silicate-rich'), and in inclusions in Cr-pyrope from Diavik (one 'carbonate-rich', 13 'silicate-rich'), Point lake (one 'carbonate-rich', 19 'silicate-rich') and Wolverine (four 'silicate-rich'). In addition, chromite was analyzed in veins, kimberlite rinds, and around altered mineral inclusions. Reference data for spinel in LDG kimberlites are from Armstrong et al. (2004) and Roeder and Schulze (2008), for spinel in Jericho mantle xenoliths (peridotite/pyroxenite) from Kopylova et al. (1999). Shaded field represents magmatic spinel trend in kimberlitic chromites from Mitchell (1986).

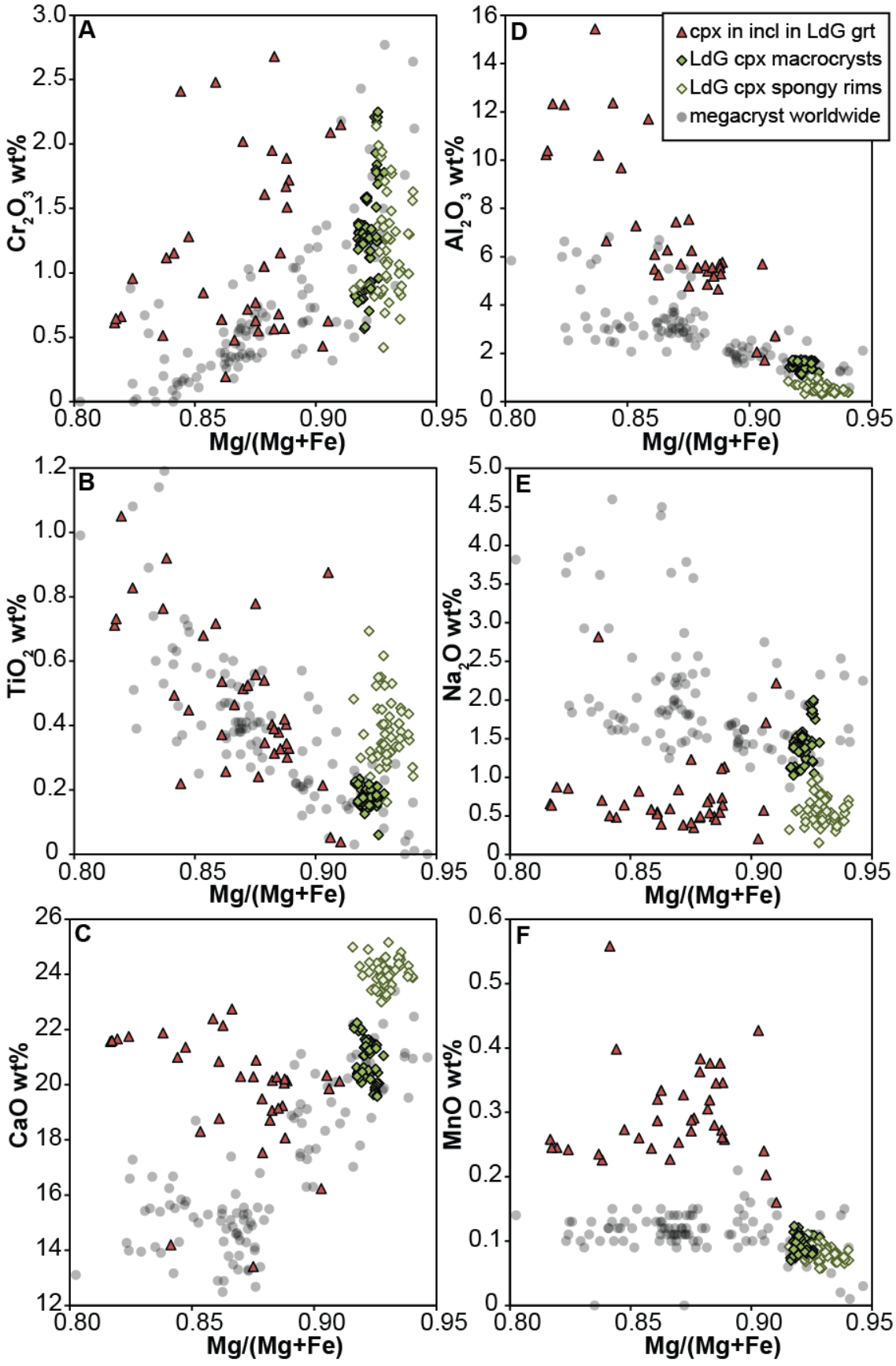
A
B
C
D
E
F
cpx in incl in LdG grt
LdG cpx macrocrysts
LdG cpx spongy rims
megacryst worldwide
Cr2O3 wt%
TiO2 wt%
CaO wt%
Al2O3 wt%
Na2O wt%
MnO wt%
Mg/(Mg+Fe)

Figure 2-9 (previous page): Bivariate plots for major and minor elements of cpx in polymineralic inclusions in Cr-pyrope. Data are compared against Cr-diopside hosts and spongy reaction rims (around polymineralic inclusions) from this study, and against megacrysts worldwide (Eggler et al. 1979; Hunter and Taylor 1984; de Bruin 2005; Pivin et al. 2009).

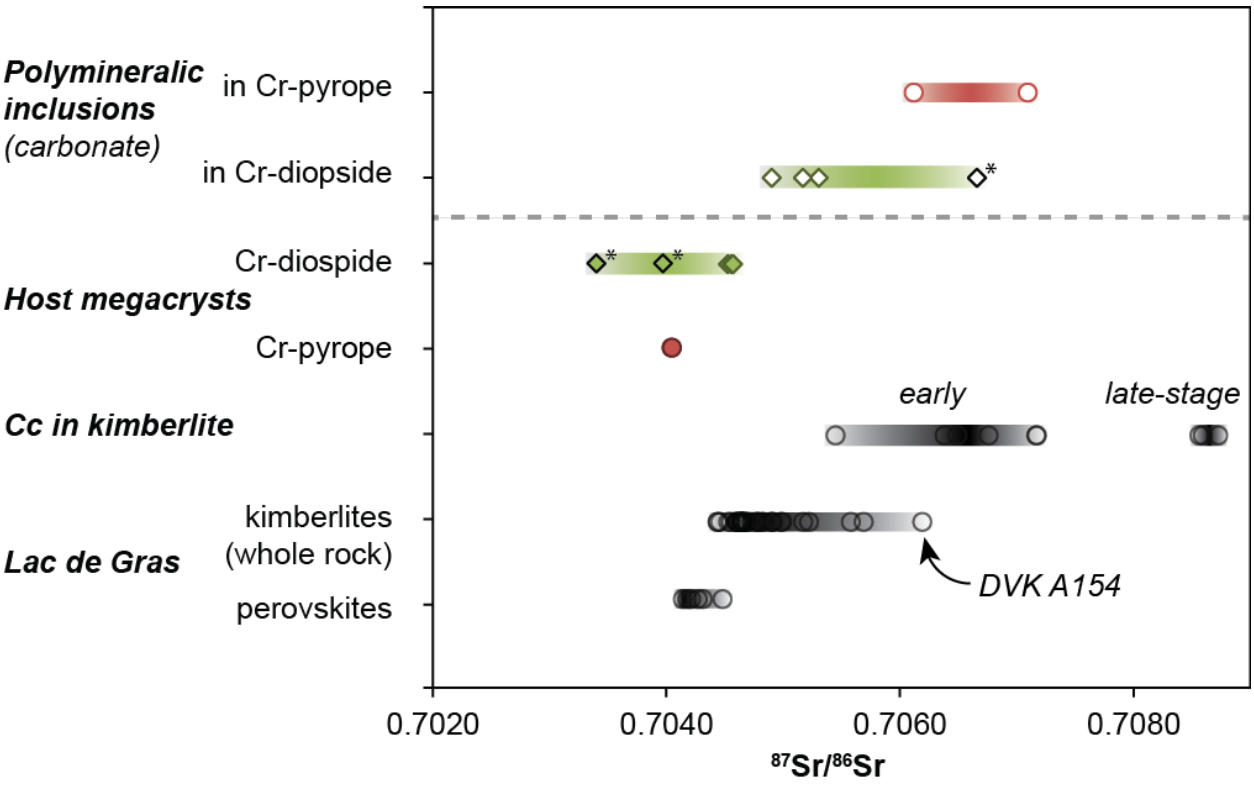

Figure 2-10: $^{87}Sr/^{86}Sr$ ratios for 'carbonate-rich' inclusions and their Cr-diopside and Cr-pyrope hosts. Data points marked with * are previous analyses from van Achterbergh et al. (2002). Reference data for calcite in the Jos kimberlite, Somerset Island, Nunavut, Canada are from Malarkey et al. (2010). LDG kimberlite whole rock data are from Tappe et al. (2013). LDG perovskite data are from Sarkar et al. (2015).

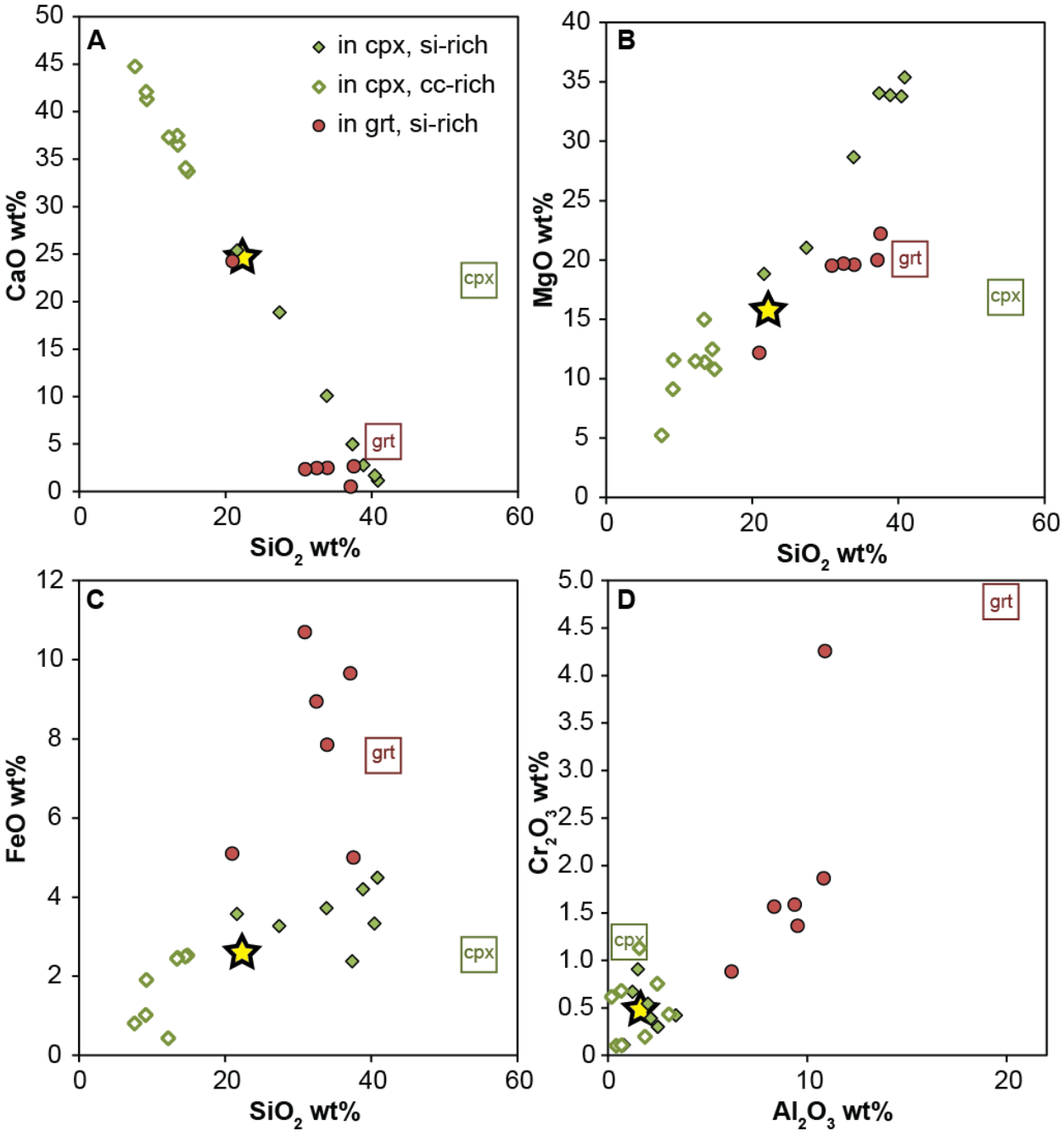

Figure 2-11: Reconstructed bulk compositions of polymineralic inclusions resolved by megacryst host (Cr-diopside and Cr-pyrope). Inclusions in Cr-diopside are further resolved by end-member type based on carbonate-rich or silicate-rich groundmass. The star symbol represents an estimate of the average bulk composition as an average of all inclusions hosted in Cr-diopside (see Discussion).

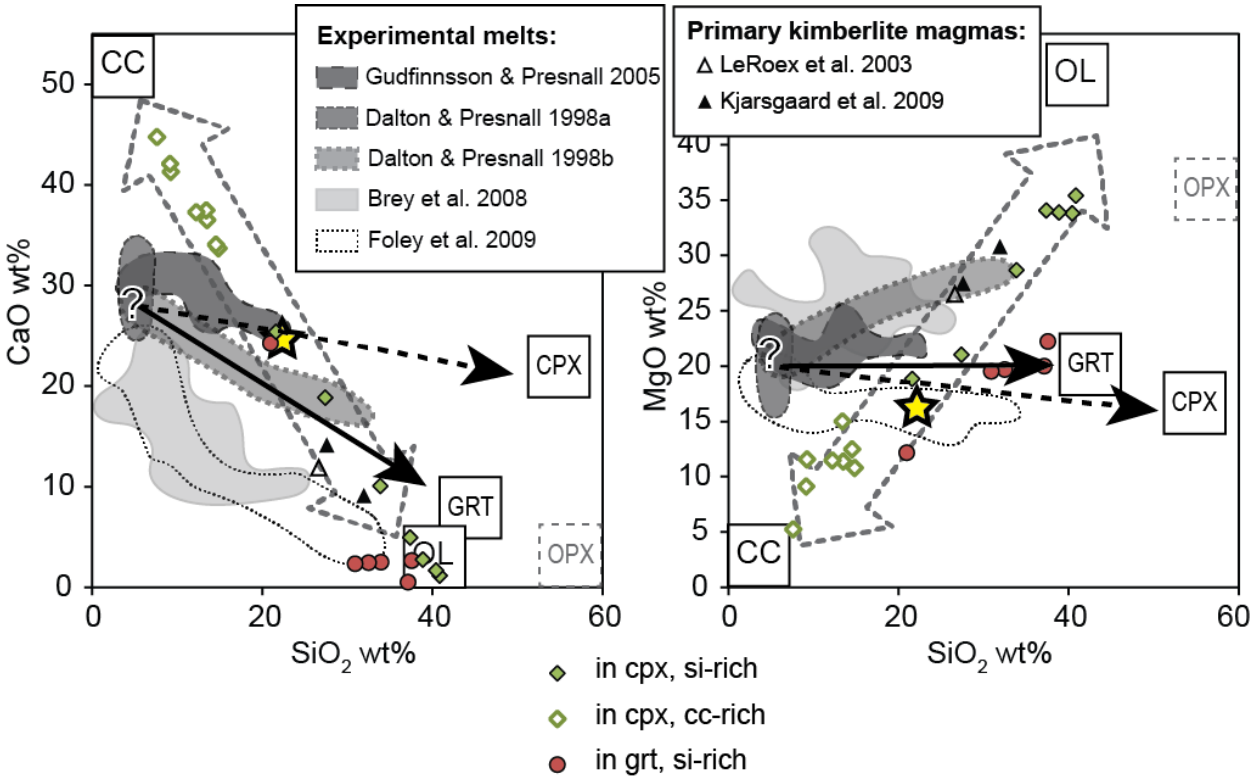

Figure 2-12: Schematic diagram relating the observed range of reconstructed bulk compositions of polymineralic inclusions (dashed, grey, double-arrow field) to partial melts of carbonated peridotite produced in high-P-T experiments, by reaction with the host phases Cr-diopside (cpx) and Cr-pyrope (grt), and to previous estimates of primary kimberlite magma based on whole rock geochemistry of hypabyssal kimberlites from Kimberley, South Africa (Le Roex et al. 2003) and from Lac de Gras (Kjarsgaard et al. 2009). Only experimental melts produced at T ≤1500°C are included in the fields, so that experimental conditions for the different melts are as follows, Gudfinnsson and Presnall (2005): 3.2-5.9 GPa, 1340-1500°C; Dalton and Presnall (1998a): 3-7 GPa, 1245-1430°C; Dalton and Presnall (1998b): 6 GPa, 1380-1480°; Brey et al. (2008): 6-10 GPa, 1300-1500°C; Foley et al. (2009): 4-6 GPa, 1090-1290°C.

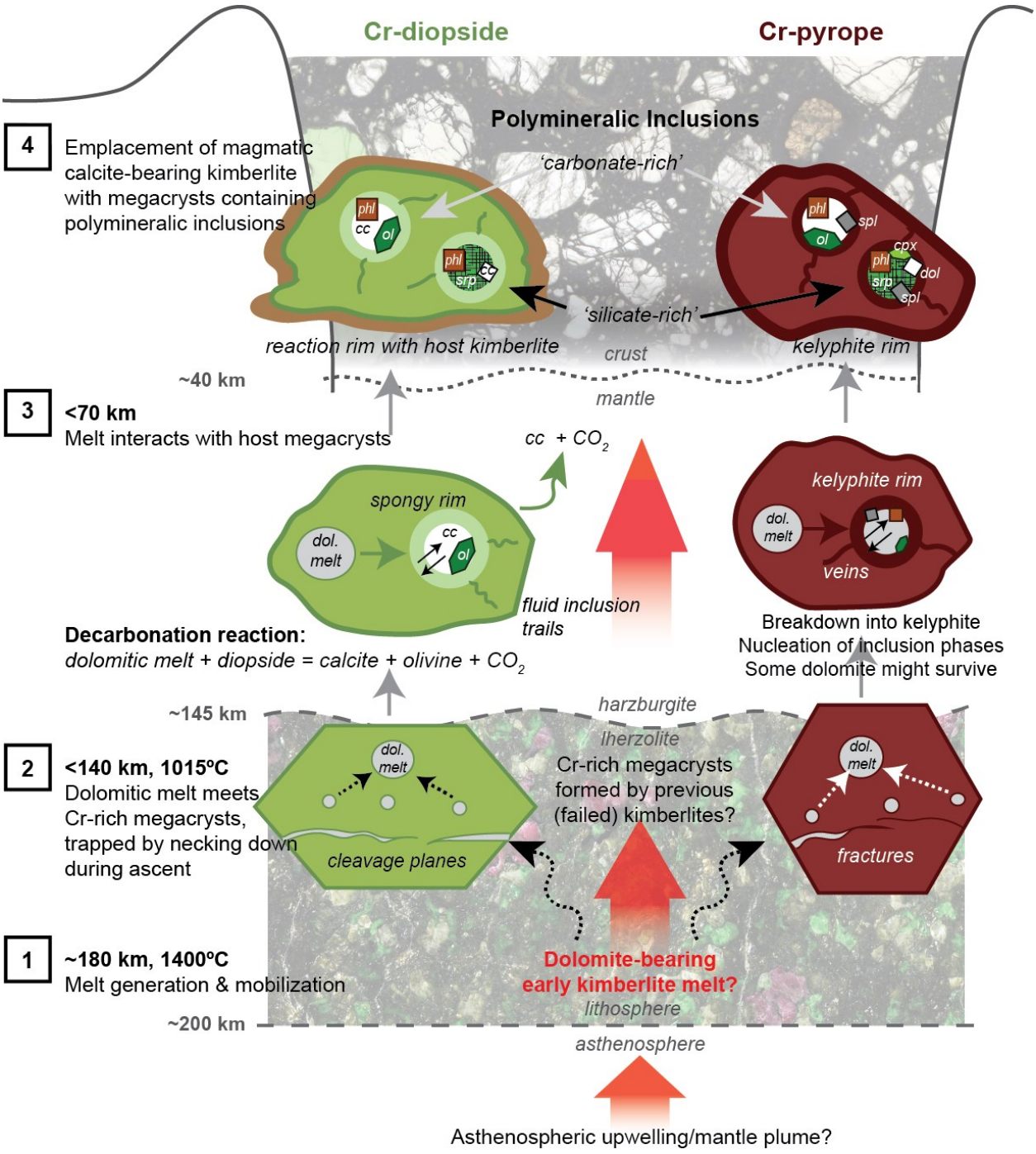

Figure 2-13: Schematic model of formation for polymineralic inclusions in Cr-diopside and Cr-pyrope megacrysts and the concomitant evolution of the host kimberlite. 1) Formation of a dolomitic silico-carbonatite melt via partial melting of carbonated peridotite close to the base of the lithosphere. 2) Ascending kimberlite melt infiltrates megacrysts after interaction with other mantle minerals (above 150 km) and is trapped by process of necking down (Roedder 1984) and/or decompression cracking (Brett et al. 2015). 3) Decarbonation reactions cause chemical exchange between inclusions and hosts during kimberlite ascent, forming spongy rims around inclusions in Cr-diopside, whereas kelyphite zones around inclusions in Cr-pyrope form by decompression reactions. In Cr-diopside, all Mg-carbonate is transformed to calcite, whereas primary dolomite may be preserved in inclusions in Cr-pyrope.

Some trails of fluid inclusions and veins form outwards due to the release of CO_2. Importantly, the reaction also occurs around the outside of the megacryst hosts, thereby releasing calcite and CO_2 into the transporting kimberlite. 4) Upon kimberlite emplacement globules have fully crystallized to polymineralic inclusions. 'Carbonate-rich' and 'silicate-rich' zones, formed by internal fractional crystallization within the inclusions, are exposed in two-dimensional sections and create the impression of compositional bimodality. Reaction rims and calcite segregations around Cr-diopsides and kelyphite rims around Cr-pyropes may suggest that they react with the host kimberlite until emplacement.

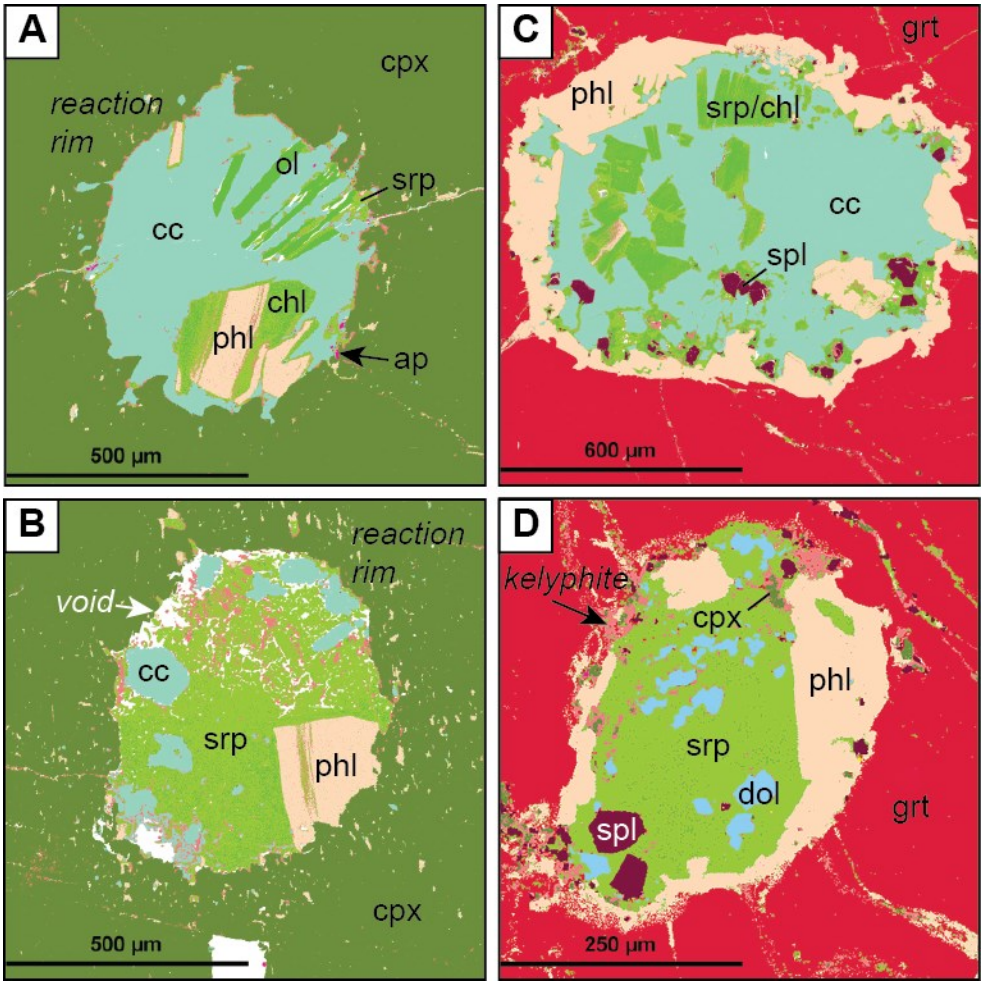

Figure 2-14: QEMSCAN® maps of polymineralic inclusions in Cr-diopside (A-B) and Cr-pyrope (C-D). Inclusions A) and C) are of the 'carbonate-rich', and B) and D) of the 'silicate-rich' end-member type. Modal proportions of the inclusions as obtained with QEMSCAN® are as follows: A) 10.3% ol; 11.4% srp; 11.2% phl; 65.8% cc; 0.1% ap. B) 4.0% ol; 60.4% srp; 16.5% phl; 15.2% cc; 0.1% ap. C) 8.2% ol; 0.2% cpx; 15.0% srp; 30.2% phl; 3.7% spl; 40.7% cc; 0.9% dol; 0.1% py. D) 0.8% ol; 2.0% cpx; 45.7% srp; 31.1% phl; 6.2% spl; 0.1% cc; 6.0% dol; 0.1% ap; 0.1% py. Mineral abbreviations are as follows: ol = olivine; cpx = clinopyroxene; srp = serpentine; phl = phlogopite; spl = spinel; cc = calcite; dol = dolomite; ap = apatite; py = pyrite.

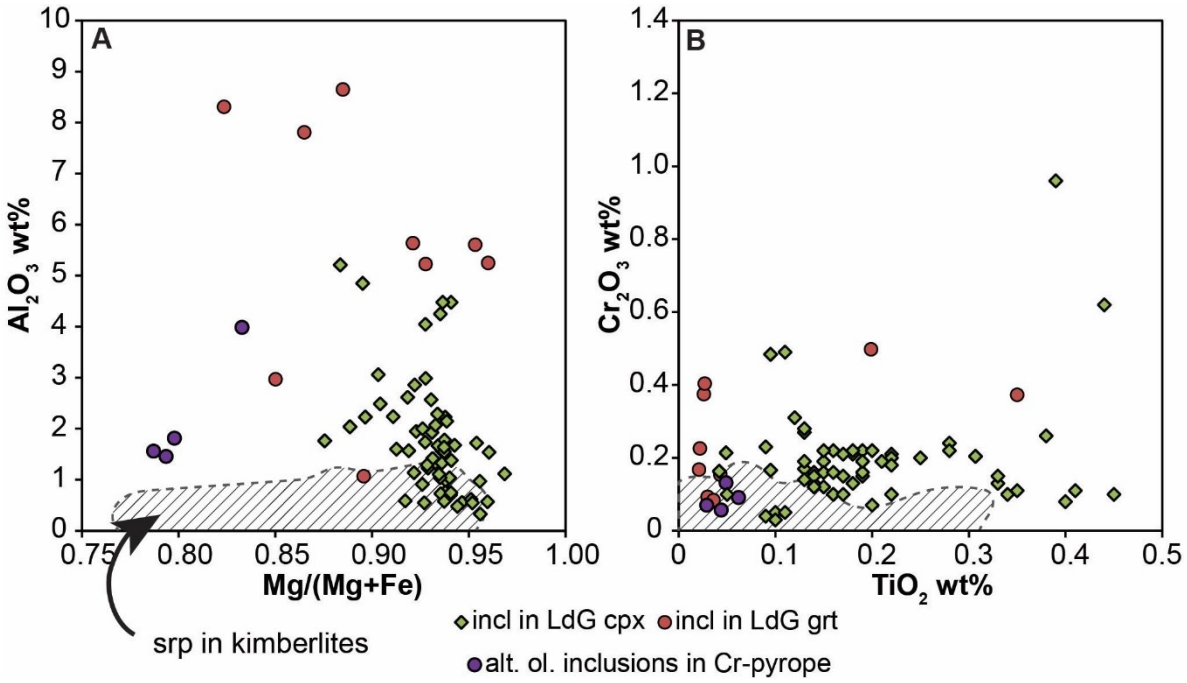

Figure 2-15: Bivariate plots for major and minor elements in serpentine/chlorite in polymineralic inclusions resolved by megacryst host (Cr-diopside and Cr-pyrope) and in altered olivine mineral inclusions in Cr-pyrope. Reference data for kimberlitic serpentine are from Hayman et al. (2009) and Mitchell (1986).

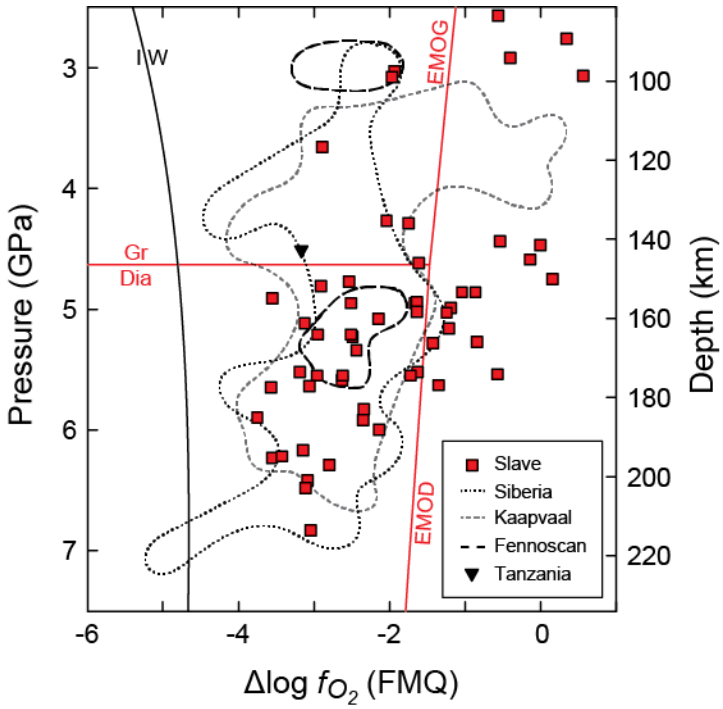

Figure 2-16: ΔlogfO2 (FMQ) values for grt peridotites from different cratons (modified from Luth and Stachel 2014). Samples from the central Slave Craton (Creighton et al. 2010) are notably more oxidized than those from other cratons.

3. Cr-rich Megacrysts of Clinopyroxene and Garnet from Lac de Gras Kimberlites, Slave Craton, Canada, and Potential Implications for the Origin of Clinopyroxene and Garnet in Cratonic Peridotites

Y. Bussweiler*[a], D.G. Pearson[a], T. Stachel[a], B.A. Kjarsgaard[b]

[a)] Department of Earth and Atmospheric Sciences, University of Alberta, 126 ESB, Edmonton, AB T6G 2E3, Canada

[b)] Geological Survey of Canada, 601 Booth Street, Ottawa, ON, Canada K1A 0E8

3.1. Abstract

We present a geochemical investigation of large (> 1 cm) clinopyroxene (Cr-diopside) and garnet (Cr-pyrope) crystals found in kimberlites from the Diavik and Ekati diamond mines in the Lac de Gras kimberlite field, Slave Craton, Canada. Using comparisons to local peridotite phases and megacrysts worldwide, we conclude that these Cr-diopside and Cr-pyrope megacrysts belong to the Cr-rich megacryst suite. Evidence for textural, compositional, and isotopic disequilibrium implies that they constitute xenocrysts in their host kimberlite. Yet, their formation may be linked to extensive kimberlite magmatism and accompanying mantle metasomatism preceding the eruption of their host kimberlites. We propose a model in which the formation of megacrysts may be linked to failed kimberlites, as has been previously invoked for the formation of polymict mantle breccias. The Cr-rich megacrysts are formed by progressing interaction of percolating melts with the surrounding depleted mantle (originally harzburgite). The melts may percolate further outwards and contribute to the introduction of clinopyroxene and garnet into the depleted mantle, thereby forming lherzolite. This model hinges on the observation that lherzolitic clinopyroxenes and garnets at Lac de Gras are compositionally strikingly similar to the Cr-rich megacrysts, in terms of major and trace elements, as well as Sr isotopes. As such, the Cr-rich megacrysts may have implications for the origin of clinopyroxene and garnet in cratonic peridotites worldwide.

3.2. Introduction

Megacrysts, or discrete nodules, are large crystals (> 1 cm, some > 20 cm) typically found in kimberlites and commonly comprise the phases garnet, clinopyroxene, orthopyroxene, ilmenite, phlogopite, olivine and zircon (Nixon and Boyd 1973; Mitchell 1986; Mitchell 1995). Megacrysts can be subdivided into a Cr-poor and a Cr-rich suite, but compositional thresholds vary between different localities in the spectrum of published studies, so that in worldwide megacryst compositional space there is large overlap between the two suites (Moore and Belousova 2005; Kopylova et al. 2009). In general, the more common Cr-poor suite is characterized by lower Cr contents and higher Fe and Ti contents compared to equivalent peridotite phases (Harte 1983). Megacrysts of the Cr-rich suite are enriched in Cr and depleted in Fe and Ti and thus chemically indistinguishable from their peridotite equivalents. The Cr-rich suite was first documented in kimberlites from the Colorado-Wyoming province (Eggler et al. 1979). Another type of Cr-rich megacrysts are so-called Granny Smith diopsides from South Africa (Boyd et al. 1984).

Traditionally, megacrysts are assumed to crystallize from a fractionating magma at depths of 150-200 km, i.e. near the base of the lithosphere (Harte 1983). In this model the Cr-poor suite is thought to crystallize first, within the magma chamber, whereas Cr-rich megacrysts are the product of progressing chemical interaction with the surrounding peridotite. The exact nature of the proposed megacryst magma and its relationship to the kimberlite melt are an ongoing matter of debate (Mitchell 1995; Bell and Moore 2004; Moore and Belousova 2005). A direct phenocrystic or cognate relationship between megacrysts and kimberlites has been questioned by isotopic studies that show disequilibrium (e.g., Hops et al. 1992; Davies et al. 2001), although other studies find greater similarity (Nowell et al. 2004; Malarkey et al. 2010). More recently, especially the Cr-rich suite has been interpreted to originate from multi-stage metasomatic processes, based on studies on Cr-rich megacrysts from the Jericho kimberlite, Slave Craton (Kopylova et al. 2009) and from kimberlites in the Democratic Republic of Congo (Pivin et al. 2009). Metasomatism is commonly attributed to proto-kimberlitic fluids/melts and appears to occur shortly prior to kimberlite eruption.

3.3. Geological Setting

The Archean Slave Craton forms the north-western part of the Canadian Shield and is exposed in the Northwest Territories and Nunavut (e.g., Kusky, 1989; Padgham, 1992). The Slave Craton formed by tectonic accretion of a western pre-3 Ga nucleus to a Neoarchean juvenile arc in the east, creating a north-south trending suture (e.g., Davis et al., 1996). Collisional events in the Paleoproterozoic led to the formation of the Thelon-Taltson and Wopmay orogens that now partially surround the craton (e.g., Isachsen and Bowring, 1994). The Slave Craton hosts multiple kimberlite fields with various emplacement ages ranging from Cambrian to Eocene (Heaman et al. 2003; Creaser et al. 2004). The Lac de Gras (LDG) kimberlite field, which includes the Diavik and Ekati diamond mines (Figure 3-1), constitutes the central Tertiary/Cretaceous volcanic domain within the Slave Province (Nowicki et al. 2004). Importantly, kimberlite magmatism at LDG occurred over a large time interval (potentially up to 250 myr) with significant volcanism from 75 to 45 Ma (Sarkar et al. 2015).

The LDG field is located east of the inferred craton suture, e.g., based on Pb isotopic studies (Davis et al. 1996), and its kimberlite pipes define a 100 km by 200 km northwest-trending zone (Lockhart et al. 2004). The generally small pipes (2-12 ha surface area) intrude into metamorphosed Archean basement rock and are overlain by Quaternary glacial deposits (Fedortchouk and Canil 2004; Nowicki et al. 2004). For a detailed description of Diavik and Ekati kimberlites, the reader is referred to Moss et al. (2008) and Nowicki et al. (2004), respectively.

Various xenolith studies have revealed a layered lithospheric mantle below the central Slave Craton (Griffin et al. 1999; Gaul et al. 2000; Menzies et al. 2004; Helmstaedt 2009). A shallow (< 145 km) ultra-depleted layer, consisting mainly of harzburgite, is interpreted as an ancient oceanic/sub-arc mantle formed during terrane accretion, whereas a deeper (145-200 km) more enriched layer, dominated by lherzolite, was suggested to result from underplating of a plume head near 2.6 Ga (Griffin et al. 1999).

3.4. Analytical Methods

Polished thin sections of single megacrysts or of kimberlite containing megacrysts were prepared in the Department of Earth and Atmospheric Sciences (EAS) thin section laboratory. Major and minor element analyses of megacrysts were collected in multiple sessions by wavelength dispersive X-ray spectroscopy (WDS) using a JEOL 8900 electron probe micro-analyzer (EPMA). Natural secondary standards for the respective minerals were analyzed in each session (Appendix A2.2.). Trace element analyses were obtained by laser ablation inductively coupled plasma mass spectrometry (LA-ICP-MS) at the EAS Arctic Resources Laboratory using a RESOlution LR 193 nm ArF Excimer Laser Ablation System coupled to a Thermo Scientific ELEMENT II XR mass spectrometer. Analytical conditions and calibration materials for the different sessions are summarized in Appendix A3.1. LA-ICP-MS data reduction was performed using the Iolite software (Paton et al. 2011). Results for secondary standards are given in Appendix A2.4. Strontium isotopes were measured by thermal ionization mass spectrometry (TIMS) at the EAS Arctic Resources Laboratory using a Thermo Scientific TRITON mass spectrometer. Megacrysts were crushed and clear fragments were picked. The fragments underwent two cleaning cycles (leached in 6N HCl at 120°C overnight, and rinsed in ultrapure water). The crystal fragments were dissolved in a mixture of HF and HNO_3. Column chemistry procedures to separate Sr from other potentially interfering elements were performed as described by Sarkar et al. (2015). A drop of H_3PO_4 was added to the sample solution before drying down at 90 °C. $TaCl_5$ was added as an activator to the sample solution, which was then loaded to Re filaments. All isotopes were measured with a detector resistance of 10^{11} Ω. Two analyses of the NBS987 standard yielded a $^{87}Sr/^{86}Sr$ ratio of 0.71027 with a standard error of 0.00001. No corrections were applied to the data.

3.5. Petrography

The majority of the clinopyroxene and garnet crystals from Lac de Gras examined here exceed 1 cm in size and thus classify as megacrysts in the non-genetic sense (Mitchell, 1986). The sample suite of this study is biased towards megacrysts that contain polymineralic inclusions – melt inclusions of early kimberlite (Figure 3-2c, d). These inclusions have been described in detail in a previous study (Bussweiler et al. 2016; Chapter 2).

Clinopyroxene megacrysts were collected directly from drill core at the Diavik Diamond Mine (Figure 3-2a). The host kimberlite is coherent (hypabyssal) kimberlite from the A154-North pipe that also contains abundant macrocrysts of olivine, ilmenite, and garnet (with prominent kelyphite rims), and calcite veins (Figure 3-2b). The clinopyroxene megacrysts are remarkably fresh, but are commonly surrounded by a reaction rim, evidenced by a brownish discoloration of the surrounding kimberlite. Signs of infiltration of groundmass kimberlite along cracks and veins into the megacrysts are rare. Clinopyroxene crystals from the Point lake and Wolverine kimberlite pipes, located on the Ekati claim block were obtained from mineral concentrates (> 6 mm) and are likely to represent fragments of larger crystals (Figure 3-2c). Clinopyroxene megacrysts can contain rounded inclusions of fresh olivine (Figure 3-2e).

Garnet crystals in this study have different genetic origins, as suggested by a color range from orange (eclogitic or megacrystic) to purple (harzburgitic) (McLean et al. 2007) (Figure 3-2d). They are hence collectively referred to as ‘macrocrysts’ until they are further distinguished based on mineral chemistry.

Diavik garnet samples were obtained from ~ 1 cm mineral concentrates (courtesy of Rio Tinto) (Figure 3-2d). Garnet from the Point lake and Wolverine kimberlite pipes (Ekati), were also taken from coarse heavy mineral concentrates (> 6 mm). In garnet crystals (especially purple garnets) mineral inclusions of olivine are common, but often are pervasively altered (Figure 3-2e). Garnet macrocrysts may also contain inclusions of diopside and orthopyroxene (opx). The mineral inclusions are often rounded and lie in a network of veins that may contain minerals also present in the polymineralic inclusions, i.e. phlogopite, serpentine, chromite and spinel. One garnet grain is pervasively veined, contains polymineralic inclusions, and is intergrown with phlogopite, diopside and olivine (Figure 3-2f).

3.6. Results

3.6.1. Mineral Chemistry

Compositions of clinopyroxene megacrysts from LDG kimberlites are predominantly diopside extending into the augite field, i.e. towards lower Ca and higher Mg contents (representative EPMA data in Appendix A2.5.). All analyzed samples contain ≥ 1.0 wt.% Cr_2O_3 (Diavik samples can contain up to 2.2 wt.%). The samples are hence best described as chrome diopsides (Cr-diopsides). Such compositions, as applied to the megacryst suite in kimberlites, are sometimes referred to as Granny Smith diopsides (Boyd et al. 1984).

Compared to compositions of megacrysts from Cr-rich and Cr-poor suites from other kimberlite fields, Granny Smith diopsides from South Africa, and peridotitic clinopyroxene from the LDG area, the LDG Cr-diopsides bear great resemblance to Cr-diopside megacrysts from kimberlites in the Democratic Republic of Congo (Pivin et al. 2009) and to one of two Granny Smith diopsides in our database (Figure 3-3). The LDG Cr-diopside megacrysts plot at the high-Mg# (Mg/(Mg+Fe)) end of the global kimberlite megacryst trend, having higher Cr_2O_3 and CaO and lower TiO_2 and Al_2O_3 contents than most megacrysts. The LDG clinopyroxene megacrysts are compositionally also similar to Cr-diopsides in garnet peridotite xenoliths from LDG kimberlites (Figure 3-3).

The majority of garnet macrocrysts with polymineralic inclusions are Cr-pyropes (representative EPMA data in Appendix A2.5.) and classify as lherzolitic (G9) garnets according to the classification by Grütter et al. (2004) (Figure 3-4d). The next most abundant group containing polymineralic inclusions are high-TiO_2 peridotitic (G11) garnets. Garnets with compositions in the Cr-poor megacryst field (G1) contain polymineralic inclusions and can exhibit macroscopic intergrowths with other megacryst-suite minerals, such as diopside, olivine, and phlogopite (Figure 3-2f). Harzburgitic (G10) garnets mainly contain olivine mineral inclusions that may be pervasively altered. In summary, polymineralic inclusions are most common and best preserved in G9 garnets and occur to a lesser extent in G11 and G1 garnets.

The inclusion-bearing LDG garnet macrocrysts can be clearly distinguished from compositions typical of the Cr-poor megacryst suite (e.g., Nixon and Boyd 1973; Bell et al. 2004) by generally higher Cr#, lower Ti, and higher Mn contents (Figure 3-4). Like the LDG Cr-diopside megacrysts, the garnet macrocrysts have very similar compositions to those of Cr-pyrope

megacrysts from kimberlites of the Democratic Republic of Congo (Pivin et al. 2009) (Figure 3-4). Furthermore, they overlap with garnet compositions of the Cr-rich megacryst suite from kimberlites of Pennsylvania (Hunter and Taylor 1984) and the Colorado-Wyoming craton (Eggler et al. 1979), although the latter are characterized by even higher Cr# (Cr/(Cr+Al)). Cr-pyrope macrocrysts from LDG that contain polymineralic inclusions plot at the high-Mg# end of the global kimberlite garnet megacryst trend. As with the LDG Cr-diopside megacrysts, the Cr-pyrope macrocrysts show strong overlap with garnets from LDG peridotites (mostly low-T garnet lherzolites).

3.6.2. Geothermobarometry

In order to obtain pressure and temperature (P-T) estimates of formation for Cr-diopside megacrysts, the single-clinopyroxene thermobarometer of Nimis and Taylor (2000) was used in combination with the compositional filters suggested by Grütter (2009). It should be noted that this thermobarometer requires the coexistence of clinopyroxene with orthopyroxene and garnet. However, no orthopyroxene inclusions were found in Cr-diopside megacrysts in this study. In the absence of orthopyroxene, the single-clinopyroxene thermobarometer yields minimum estimates. Cr-diopside megacrysts from Diavik yield average P-T conditions of 4.8 GPa (~ 150 km) and ~1020 °C. Samples from Point lake yield very similar average results of 4.6 GPa and ~1030 °C. The majority of the LDG Cr-diopside megacryst data yield P-T conditions of 4.0-5.0 GPa and 900-1100 °C. Thus, single grain Cr-diopside megacrysts with polymineralic inclusions from this study all plot at intermediate mantle levels along the geotherm of the central Slave Craton (Figure 3-5). The estimated P-T conditions are markedly lower than those previously obtained for Diavik samples by van Achterbergh et al. (2002, 2004) (6.2 GPa and 1240 °C) that were reportedly obtained for a garnet lherzolite xenolith. The only data point with such a high P-T in this study corresponds to a diopside inclusion within olivine from a peridotite micro-xenolith (Figure 3-5).

For Cr-pyrope macrocrysts, the most robust P-T estimates were calculated for garnet with coexisting clinopyroxene (as inclusions). The clinopyroxene thermometer of Nimis and Taylor (2000) and the garnet-clinopyroxene thermometer of Krogh (1988) yield average T of ~1050 °C for samples from Diavik and Wolverine. The observed agreement between these two thermometers suggests good equilibrium, which warrants the use of the single-clinopyroxene

barometer. Pressures calculated with the barometer of Nimis and Taylor (2000) for clinopyroxene inclusions in garnet range from 4.9-5.3 GPa. The conditions calculated with these thermobarometers overlap at the high-P end with those of the Cr-diopsides (Figure 3-5).

For pyrope with only olivine inclusions, the Al-in-olivine thermometer of De Hoog et al. (2010) and the Ni-in-garnet thermometer (Canil, 1999) were utilized, and the resulting temperatures were projected onto the Slave Craton geotherm. Al thermometry yields T ≤ 1150 °C; whereas Ni temperatures (calculated assuming that coexisting olivine contains 3000 ppm Ni) extend up to 1250 °C (Figure 3-5). Such high-T (1050-1150 °C) conditions are far displaced from those of the Cr-diopside megacrysts, and might indicate that a population of high-T garnet peridotites is present among the garnet macrocrysts. For Ekati samples, such high temperatures are mainly associated with G11 garnets.

3.6.3. Trace Elements

Cr-diopsides: Trace element compositions were analyzed with LA-ICP-MS in Cr-diopside megacrysts from Diavik (Appendix A3.2.). The rare earth element (REE) patterns of the different Cr-diopside samples from Diavik are relatively uniform and characterized by light REE enrichment with $(La/Yb)_N$ of ~37 to 100 (Figure 3-6a). Compared to megacrysts from the Jericho kimberlite (Kopylova et al. 2009) and kimberlites in the Democratic Republic of Congo (Pivin et al. 2009), the REE patterns and concentration levels are similar. There also is strong overlap with REE patterns of peridotitic clinopyroxene (mostly grt lherzolite) from Diavik (Aulbach et al. 2007). Peridotitic clinopyroxene from the Kimberley area in the Kaapvaal craton (Simon et al. 2003) have similar REE patterns, in terms of their inter-element fractionations, compared to Diavik megacrysts, but plot at higher concentration levels (Figure 3-6a).

For one sample from Diavik, the trace element composition of the pristine Cr-diopside host and that of the modified clinopyroxene in the alteration rim (spongy rim) around polymineralic inclusions (Bussweiler et al. 2016) are directly compared (Figure 3-6b). The trace element patterns of the rims range from similar concentrations to those of the host to significantly enriched in Rb, Ba, light REE, Nb, Ta, Th and U. From time-resolved LA-ICP-MS signals it is evident that sampling of micro-inclusions (e.g., phlogopite and calcite) results in high concentrations of the respective elements. Such inclusions are difficult to avoid during analysis due to the integration of a relatively large sample volume (laser spot size ≥ 33 µm). As such, the

alteration rim patterns represent mixed signatures of different micro-inclusions and the Cr-diopside host, and cannot be used to calculate the melt in equilibrium with such patterns (Araújo et al. 2009).

Cr-pyropes: Chondrite normalized REE patterns in garnet xenocrysts from kimberlites can have two end-member shapes that are termed 1) "normal" or "L-shaped" (typically assumed to be equilibrated with a silicate melt) and 2) "sinusoidal" or "S-shaped" (assumed to be of fluid-metasomatic origin, in extreme cases U-shaped) and correspond broadly to lherzolitic and harzburgitic garnets, respectively (e.g., Stachel et al., 1998) (Figure 3-7a).

The LDG Cr-pyrope macrocryst patterns from this study dominantly fall into the "normal" light REE-depleted range (Figure 3-7a; Appendix A3.3.), typical of worldwide garnet megacrysts from kimberlites (e.g., Bell and Moore, 2004). End-member sinusoidal patterns are absent, but G11 garnets from Ekati show slightly sinusoidal patterns. As with their major and minor element compositions, there is overlap with Cr-pyrope megacrysts from kimberlites in the Democratic Republic of Congo (Pivin et al. 2009), and also with Diavik peridotite garnets (Creighton et al. 2010; Mather 2012).

While reaction rims similar to those in Cr-diopsides are absent in Cr-pyrope macrocrysts, zones around inclusions can contain abundant micro-inclusions and the resulting patterns are significantly enriched in the light REE (Figure 3-7a, b).

3.6.4. Strontium Isotopes

Sr isotopes were measured by TIMS for Cr-diopside from Ekati and Diavik and Cr-pyrope from Ekati. Because Rb concentrations were generally very low (commonly below detection limits) the measured ratios were not corrected for radiogenic ingrowth of Sr since kimberlite eruption.

The Cr-diopside megacryst from Diavik has a $^{87}Sr/^{86}Sr$ ratio of 0.7045. Ekati samples are less radiogenic, with Cr-diopside from the Jay kimberlite yielding 0.7041, and Cr-pyrope from the Wolverine kimberlite yielding 0.7040. Yet, if previous analyses of Diavik Cr-diopside megacrysts from van Achterbergh et al. (2002) are included, there is overlap between the LDG occurrences (Figure 3-8). Compared to Cr-rich megacryst phases (clinopyroxene and garnet) from the Jericho kimberlite (Kopylova et al. 2009), the LDG phases overlap, although Cr-diopside measured in this study extends to slightly more radiogenic signatures. There also is

overlap with isotopic compositions of clinopyroxene from peridotite from Diavik (Aulbach et al. 2013). The latter however, can extend to significantly lower $^{87}Sr/^{86}Sr$ ratios. The Sr signature of Diavik Cr-diopside overlaps with the least radiogenic signatures of LDG kimberlites (Tappe et al. 2013). However, the host kimberlite for the samples of this study (Diavik A154) has the most radiogenic signature of all LDG kimberlites (~0.7062) (Figure 3-8). The relatively radiogenic character has been previously attributed to derivation by low degree partial melting of a more fertile peridotite domain within otherwise highly depleted convecting upper mantle (Tappe et al. 2013). However, since kimberlite isotope ratios are obtained from bulk samples, this may also be associated to sampling of more radiogenic, late-stage phases (e.g., calcite) or crustal components (e.g., granite). The latter scenario seems plausible, because Sr isotope signatures measured in LDG perovskites, an early crystallizing phase in kimberlites, are lower and have a narrower range (Sarkar et al. 2015). Interestingly, Cr-diopside and Cr-pyrope measured in this study bracket the range of signatures of perovskite in LDG kimberlites (Figure 3-8).

3.7. Discussion

3.7.1. Disaggregated Megacrystalline Lherzolites or Cr-rich Megacrysts?

No significant compositional differences between megacryst samples from the Diavik and Ekati occurrences were detected in terms of major elements (Figures 3-3, 3-4), trace elements (Figure 3-7), and, including previous analyses of van Achterbergh et al. (2002), Sr isotopes (Figure 3-8). The samples are thus collectively referred to as Lac de Gras (LDG) samples.

The LDG samples plot at the Cr-rich and high-Mg# end of the global megacryst trend (Figure 3-3, 3-4). There is consistent overlap with LDG lherzolitic phases, but also with Cr-rich megacrysts from other locations, e.g., the Jericho kimberlite, northern Slave Craton (Kopylova et al. 2009) or kimberlites in the Democratic Republic of Congo (Pivin et al. 2009). In terms of trace element signatures, there is no distinction between the LDG samples, the world-wide Cr-rich megacryst suite, and clinopyroxene and garnet from LDG lherzolites (Figure 3-6a, 3-7a). Their Sr isotope signatures overlap with those of typical mantle phases and are less radiogenic than the host kimberlite, but also overlap with Sr isotope data of primitive perovskites (Figure 3-8) – a typical magmatic phase in kimberlites (Sarkar et al. 2015). Thus, we suggest that the LDG samples described here are associated with the Cr-rich megacryst suite, first documented by

Eggler et al. (1979), and may have grown from sources that are isotopically similar to LDG kimberlites.

Most of the analyzed samples from LDG host crystallized melt inclusions that are described in detail in Bussweiler et al. (2016) (Chapter 2). Previous studies on melt inclusion-bearing Cr-diopsides from Diavik described them as belonging to "megacrystalline lherzolites" (van Achterbergh et al. 2002; van Achterbergh et al. 2004; Araújo et al. 2009). This description accounts for their large crystal size (> 1 cm) and chemical similarity to lherzolitic clinopyroxene. However, geologic evidence of such megacrystalline lherzolites in the form of xenoliths is extremely rare to absent. Brett et al. (2015) ascribe the absence of coarse-grained xenoliths in kimberlites to preferential disaggregation of coarse xenoliths during ascent due to their weaker rock strength.

While disaggregation of extremely coarse peridotites is perhaps the simplest explanation for the presence of large Cr-diopside and Cr-pyrope crystals in LDG kimberlites, their abundant occurrence together with ilmenite megacrysts (> 1 cm) (Figure 3-2b) seems suspicious. Ilmenite is rare to absent in lherzolite xenoliths but commonly forms macro- (> 2 mm) or megacrysts (> 1 cm) in kimberlites, that are considered to have a magmatic origin linked to the Cr-poor megacryst suite (Schulze 1987; Schulze et al. 1995; Kopylova et al. 2009). Moreover, abundant olivine "megacrysts" were observed in the host kimberlite (Figure 3-2b). The different origins of olivine in kimberlite are still a matter of debate (Fedortchouk and Canil 2004; Kamenetsky et al. 2008; Brett et al. 2009; Arndt et al. 2010; Bussweiler et al. 2015; Howarth and Taylor 2016; Moore and Costin 2016). Various different populations appear to be present, the exact proportions of which still remain to be established based on reliable geochemical discriminators (e.g., trace element systematics). So far, olivine megacrysts (in the genetic sense) could not be reliably excluded from these populations, and some workers argue for a widespread occurrence of megacrystic olivine (Moore and Costin 2016). The detection of megacrystic olivine is hindered by its preferential disaggregation during ascent and/or during crushing (mineral concentrates), and their chemical overlap, in terms of major elements, with peridotite populations.

The presence of other megacryst minerals, such as ilmenite and potentially olivine, corroborates our interpretation that the large Cr-diopside and Cr-pyrope crystals found in LDG kimberlites likely are part of the Cr-rich megacryst suite.

3.7.2. Equilibrium Melts

In order to constrain a melt composition from which the megacrysts may have crystallized, equilibrium melts were calculated from their trace element signatures (Figure 3-9). Experimentally determined partition coefficients between carbonate-silicate melts and Cr-diopsides (Keshav et al. 2005) and Cr-pyropes (Brey et al. 2008) were used. This was done for the Diavik sample suite because the equilibrium melts can be directly compared to the trace element budget of the host kimberlite (Tappe et al. 2013). Bearing in mind the uncertainties associated with the partition coefficients and the bulk rock composition, some qualitative comparisons can be made.

The equilibrium melt REE patterns for garnets are generally close to the kimberlite pattern. In particular, the slope of the medium to heavy REE (Nd to Lu), as well as the "kink" in Y, Zr, and Hf mimic the kimberlite pattern very closely (Figure 3-9). However, the calculated garnet equilibrium melts have significantly lower LREE and incompatible elements (e.g., Sr, Ba, La, Ce, and Pr). The latter feature could simply reflect inaccuracies in the overall magnitude of partition coeffcients. Kopylova et al. (2009) reported patterns for Jericho garnet megacrysts with even greater resemblance to the host kimberlite, based on corresponding garnet trace element patterns that showed enrichment in these elements. Here, we have found such LREE enriched patterns only close to the polymineralic inclusions where micro-inclusions are abundant, whereas the rest of the grain has normal patterns (Figures 3-7).

The equilibrium melt patterns calculated for Cr-diopsides also show similarity to the host kimberlite for the medium to heavy REE, although less data are available due to lack of partition coefficients (Figure 3-9). The Cr-diopside equilibrium melts, are significantly more enriched in Sr, the LREE (La to Eu), as well as Zr and Hf.

The calculated equilibrium melt patterns are somewhat ambiguous. We conclude that the megacrysts may have crystallized from kimberlite-like melts, but are not in equilibrium with the host kimberlite, i.e. the magma that transported them to the Earth's surface. In a more general

sense, the discrepancies may also be due to the fact that kimberlites observed at the surface are vastly different from their primary melts at depth (e.g., Eggler 1986).

3.7.3. Depth of Formation

Earlier studies on large Cr-diopsides from Diavik have advocated for a deep origin of the megacrysts at the base of the lithosphere (van Achterbergh et al. 2002; 2004; Araújo et al. 2009). This is in accordance with traditional models of megacryst formation that envisage that megacrysts crystallize from a magma which pools at the lithosphere-asthenosphere boundary (e.g., Nixon and Boyd 1973). However, the P-T estimates by van Achterbergh et al. (2002) were based on geothermobarometry using compositions of a peridotitic assemblage and applied across the suite they studied. Our results yield significantly lower P-T conditions placing them well within the lithospheric mantle (4.0-5.0 GPa and 900-1100 °C) (Figure 3-5). Conditions of formation are in the lherzolite-dominated lower layer, located below the ultra-depleted upper layer of the mantle underneath the central Slave Craton (Griffin et al. 1999). We note, however, that the application of single-grain thermobarometers to megacrysts is not ideal because coexistence with other phases, such as opx, is required, for which there is no direct evidence. In any case, a larger range of conditions of formation is perhaps likely as it is known from xenolith studies that LDG kimberlites sample the entire cross-section through the lithospheric mantle (Griffin et al. 1999; Gaul et al. 2000; Menzies et al. 2004; Helmstaedt 2009). However, the observed range of conditions of formation/equilibration for the Cr-rich megacrysts would be in conflict with traditional models where the megacryst magma pools at lithosphere-asthenosphere boundary.

3.7.4. Evidence from Polymineralic Inclusions

The Cr-diopside and Cr-pyrope megacrysts examined in this study often contain fully crystallized melt inclusions, that are described in detail in Bussweiler et al. (2016) (Chapter 2). Such polymineralic inclusions have previously been interpreted as remnants of the enigmatic megacryst magma, i.e. the magma from which the host megacrysts had crystallized (e.g., Schulze 1985). For example, Mitchell (1995) cites the presence of such inclusions as primary evidence for a phenocrystic origin of Cr-poor megacrysts.

Polymineralic inclusions with strikingly similar mineralogy have since been reported in different mineral phases from both the Cr-poor and Cr-rich megacryst suite (Bussweiler et al. 2016; and

references therein). This seems to indicate that the inclusions cannot constitute the megacryst magma; if the trapped melt had been responsible for crystallizing the hosts a large degree of differentiation by fractional crystallization would be expected, which is not substantiated by the strikingly similar mineralogical character of inclusions in different host minerals. Moreover, there is ample evidence for elemental and isotopic disequilibrium between the inclusions and the host megacrysts, suggesting that the melt that formed the inclusions is not the megacryst magma. It thus seems more likely that the polymineralic inclusions represent samples of the ascending kimberlite melt in the process of reacting with the lithospheric mantle (Bussweiler et al. 2016). This in turn, would underline the xenocrystic nature of the megacrysts in their host kimberlite.

3.7.5. Cr-rich Megacrysts as Crystallization Products of Failed Kimberlites?

The evidence for disequilibrium provided by the polymineralic inclusions, trace element systematics, and Sr isotope signatures argues against a strictly cognate relationship of the Cr-rich megacrysts with their host kimberlite. However, the megacrysts could have crystallized from previous kimberlitic melts at mantle depths. Experimental studies have shown that clinopyroxene and olivine (Edgar et al. 1988), as well as garnet (Sokol and Kruk 2015), can be liquidus phases of kimberlitic melts at mantle conditions.

A possible scenario is the formation of megacrysts in any failed kimberlite that did not reach crustal levels. Similarly, “polymict mantle breccias” are interpreted to constitute failed kimberlites that entrained xenocrysts from different sources, ranging from depleted to fertile peridotites and eclogites (Lawless et al. 1979; Höfer et al. 2009; Giuliani et al. 2013; Giuliani et al. 2014). Polymict mantle breccias crystallize typical kimberlite groundmass phases, such as olivine and phlogopite, at lithospheric mantle depths prior to their subsequent re-sampling by later kimberlite melts that successfully ascend to the surface. Interestingly, the groundmass phases in polymict mantle breccias can be enriched in Cr which is interpreted to result from progressive interaction with the surrounding depleted lithospheric mantle (Giuliani et al. 2016). This progressive interaction with surrounding mantle may also be recorded in the observed range of Sr isotopes of the Cr-rich megacrysts in this study; the signatures of the megacrysts overlap those of primitive kimberlitic perovskites at LDG and trend towards lower values, similar to those of peridotitic phases (Figure 3-8). In previous studies on Cr-poor megacrysts, a range of Sr,

Nd, and Hf isotopic compositions has been attributed to variable interaction of a melt with surrounding mantle (Hops et al. 1992; Nowell et al. 2004).

Thus, we tentatively conclude that the LDG Cr-rich megacrysts are the products of extensive reaction of stalled kimberlitic melts with the surrounding mantle rocks. The long time span of kimberlite magmatism observed at LDG (Sarkar et al. 2015) may have contributed to widespread megacryst crystallization. Such a model would also account for the observed range of P-T conditions (Figure 3-5), as previous kimberlite pulses could have stalled at different depths.

3.7.6. Implications for the Origin of Clinopyroxene and Garnet in Cratonic Peridotites

For the Kaapvaal craton, there is now substantial evidence, from trace elements and radiogenic isotopes, for the recent metasomatic addition of much of the Cr-diopside and some of the garnet in cratonic lherzolites (Günther and Jagoutz 1994; Shimizu et al. 1997; Pearson et al. 2002; Simon et al. 2003). The over-abundance of diopside in highly depleted peridotites with high Mg# olivines is strong petrological evidence of this process (Pearson et al. 2002). Based on trace element and isotopic evidence for peridotite xenoliths from Lesotho kimberlites, Simon et al. (2003) concluded that the clinopyroxene in cratonic lherzolites from the Kaapvaal craton may have crystallized from melts precursory to the host kimberlite. This similarity in formation processes might explain the observed compositional overlap of Cr-megacrysts with corresponding lherzolite phases, observed in this study.

A physically plausible model combining the crystallization of the Cr-rich megacryst suite and the introduction of lherzolitic clinopyroxene and garnet into the surrounding mantle could involve the process of percolative fractional crystallization, first proposed by Harte et al. (1993). A main difference to the original model is that, here, kimberlite-like melts are envisaged as the agents of metasomatism, rather than the products thereof. Reaction between previous kimberlite-like melts, associated with a failed kimberlite, and a lithospheric mantle column is illustrated schematically in Figure 3-10. The crystallization of Cr-rich megacrysts (predominantly Cr-diopside and Cr-pyrope) could occur along channel walls, where they could grow to large sizes. Further away from the channel, where the flow is more percolative, the diopsides (and pyropes) distributed throughout cratonic lherzolites may form.

3.8. Conclusions

We document clinopyroxene and garnet megacrysts in LDG kimberlites that can be classified as belonging to the Cr-rich megacryst suite due to their large crystal size and chemical characteristics, such as high Cr and low Fe and Ti contents. Based on the extensive evidence for disequilibrium with the transporting kimberlite, a strictly cognate relationship is ruled out. Instead, an older metasomatic origin is proposed for their formation. Cr-rich megacrysts may have formed metasomatically by percolating fluids either replacing or enlarging pre-existing mantle minerals (Pivin et al. 2009; Kopylova et al. 2009). Alternatively, the large size of the megacrysts may be explained by crystallization from failed kimberlite-related melts in zones of focussed/channelized flow. In accordance to older models (Harte 1983), the Cr-rich megacrysts are envisaged to have formed from melts that have experienced more interaction with the surrounding peridotite than the Cr-poor megacrysts. The formation of megacrysts from precursor kimberlite magmas stalled at depth is in accordance with the large time span and multiple episodes of kimberlite magmatism at LDG (e.g., Sarkar et al. 2015). As found for Cr-diopside megacrysts from Diavik (van Achterbergh et al. 2002), we show that Cr-rich megacrysts from both Diavik and Ekati have striking compositional overlap with clinopyroxene and garnet found in lherzolitic xenoliths that underpin the central Slave Craton. This compositional similarity, in major and trace elements as well as Sr isotopes, can be explained by the metasomatic reaction of failed kimberlite-related melts in a percolative flow regime, in which the melts re-fertilize depleted harzburgite by introducing clinopyroxene and garnet. A similar process has been proposed for Kaapvaal cratonic lherzolites (Simon et al. 2003), but our study is the first to demonstrate this relationship of the lithospheric mantle underneath the central Slave Craton.

3.9. Figures

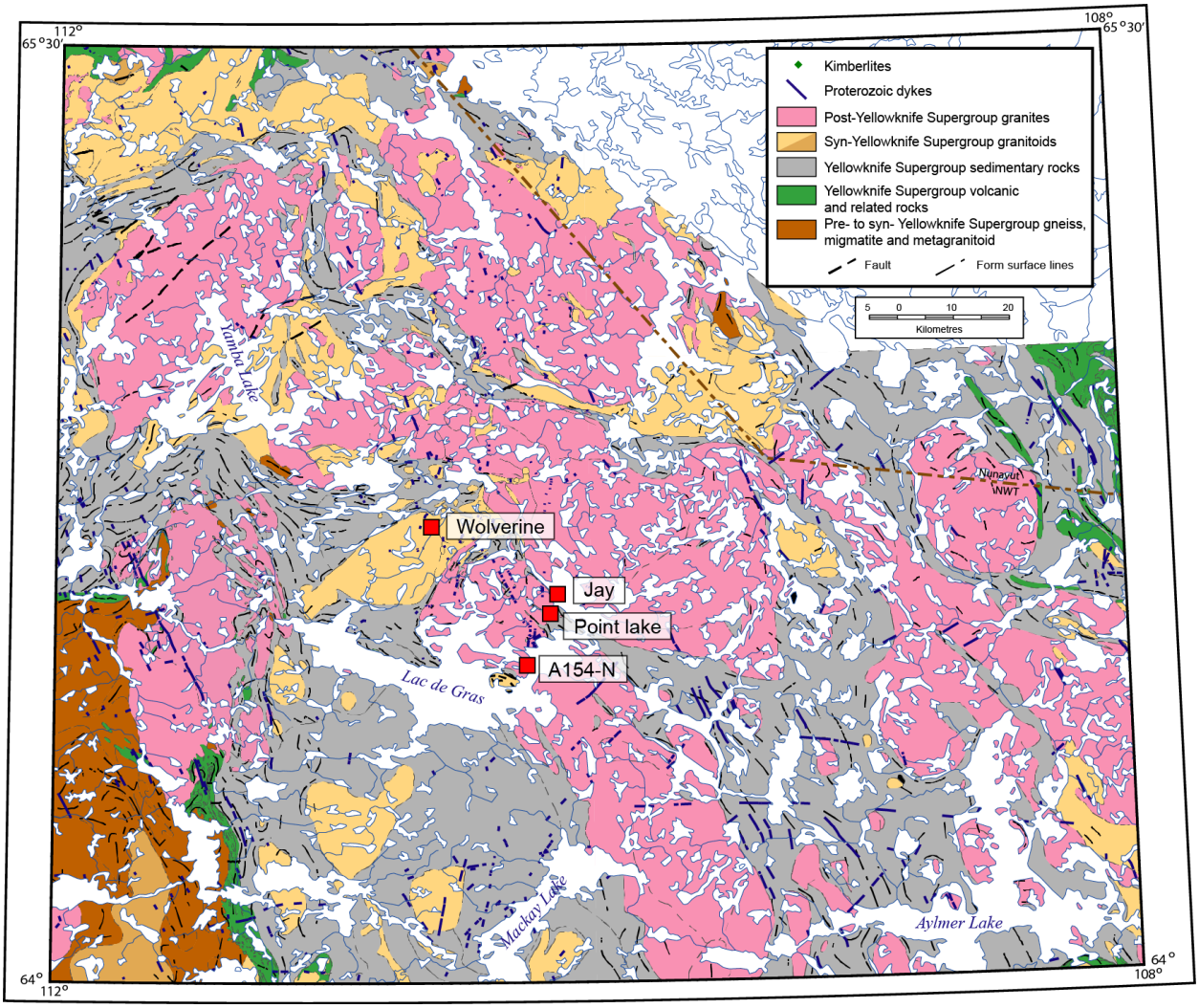

Figure 3-1: Geological overview map of the Lac de Gras area (Kjarsgaard et al. 2002). The location of the Wolverine, Jay, and Point lake kimberlite pipes (Ekati) and the A154-North kimberlite pipe (Diavik) are shown. Clinopyroxene and garnet megacryst samples from these pipes are the focus of this study.

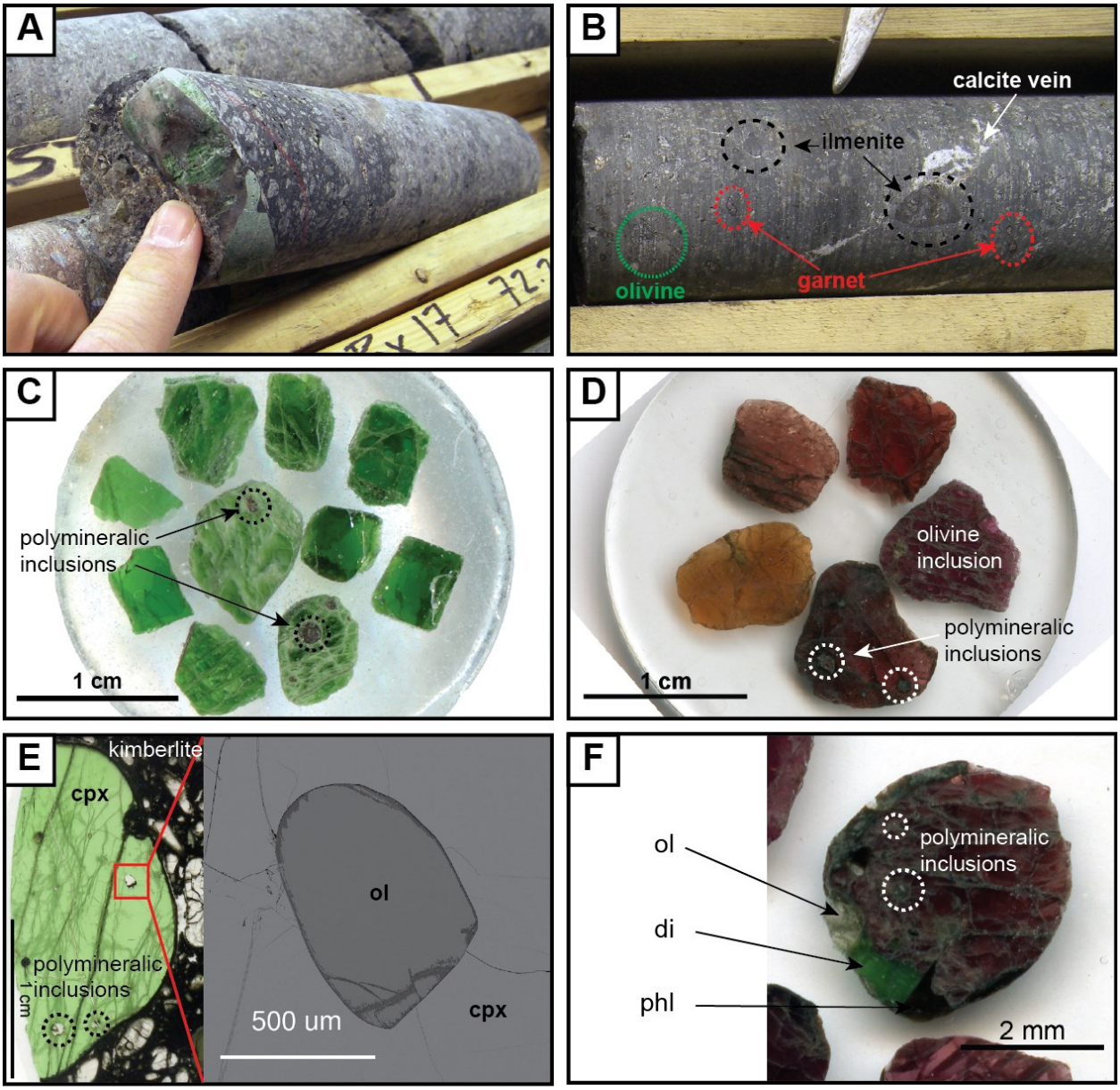

Figure 3-2: Photographs and photomicrographs of megacryst samples. A) Clinopyroxene(cpx) megacryst (~ 10 cm) within drill core of coherent (hypabyssal) kimberlite from the A154N pipe (Diavik). B) Coherent (hypabyssal) kimberlite from the A154N pipe (Diavik) with abundant macrocrysts of olivine, ilmenite, and garnet (with kelyphite rims), plus calcite veins. C) Clinopyroxene fragments from mineral concentrate from the Point lake kimberlite (Ekati). D) Garnet fragments from mineral concentrate from Diavik. Different colors indicate different origins (see text). E) Rounded olivine inclusion in clinopyroxene megacryst. F) Garnet grain intergrown with olivine, diopside (di), and phlogopite.

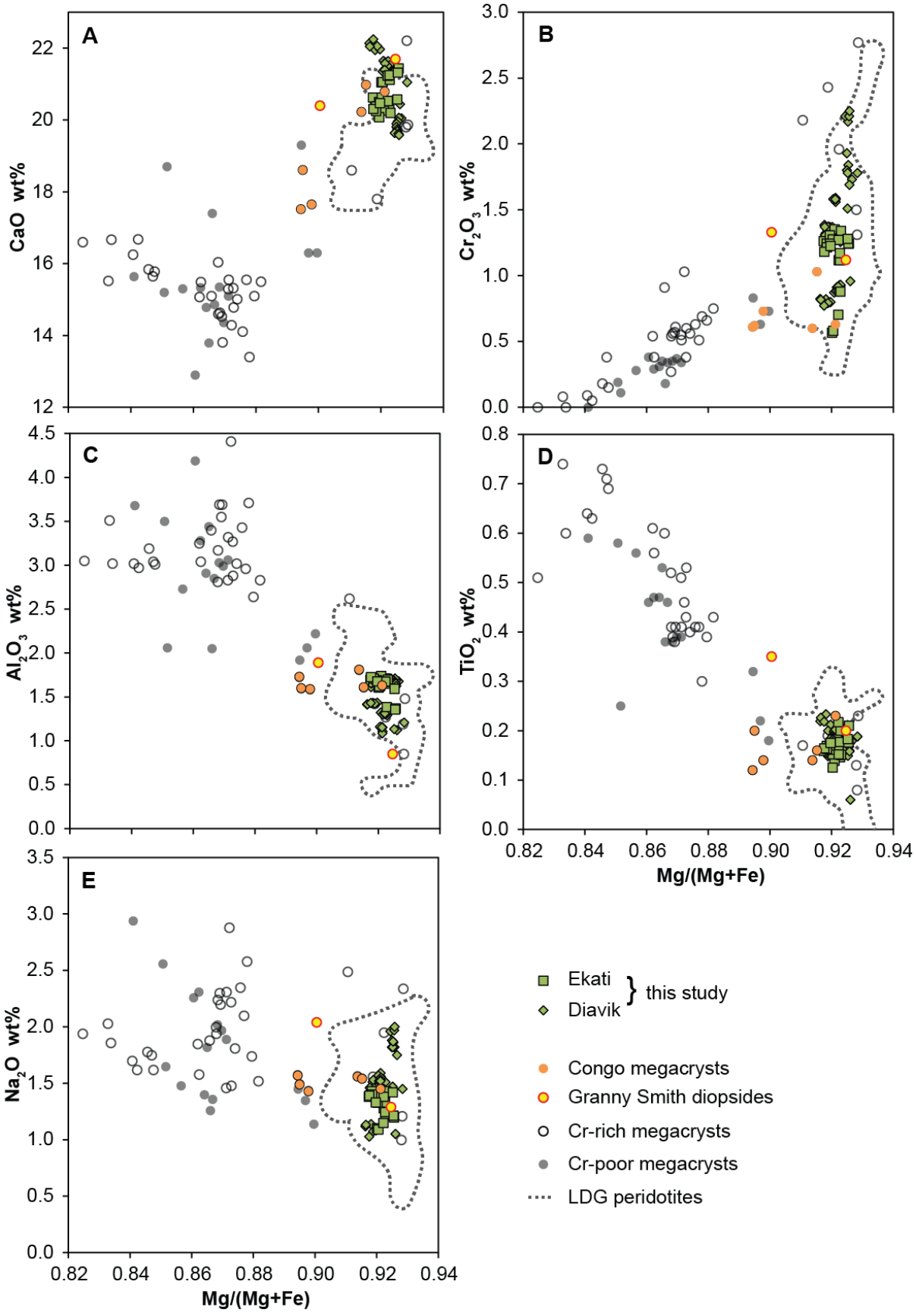
A
B
C
D
E
CaO wt%
Cr_2O_3 wt%
Al_2O_3 wt%
TiO_2 wt%
Na_2O wt%
Mg/(Mg+Fe)
Ekati
Diavik
this study
Congo megacrysts
Granny Smith diopsides
Cr-rich megacrysts
Cr-poor megacrysts
LDG peridotites

Figure 3-3 (previous page): Major and minor elements in LDG Cr-diopside megacrysts. The samples plot at the Cr-rich, high-Mg# (Mg/(Mg+Fe)) end of the megacryst trend, and overlap compositions of clinopyroxene in LDG peridotites. Reference data for megacrysts are from de Bruin (2005), Eggler et al. (1979), Hunter and Taylor (1984). Data for Congo megacrysts are from Pivin et al. (2009). Data for Granny Smith diopsides are from Boyd et al. (1984). Contours for LDG peridotites are based on data from Aulbach et al. (2007) and Mather (2012).

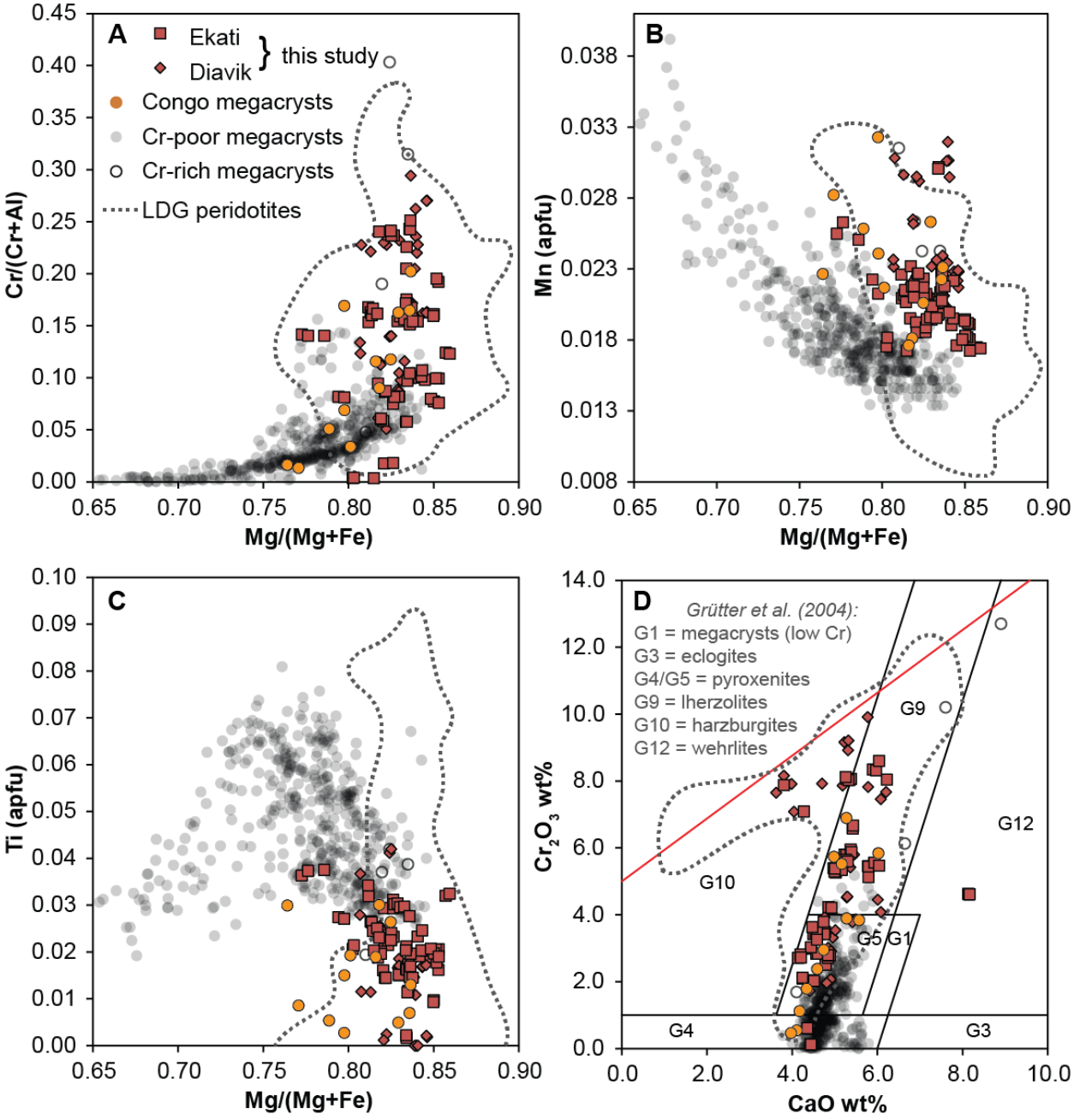

Figure 3-4: Major and minor elements in LDG Cr-pyrope megacrysts. A-C) Bivariate plots of major and minor elements versus Mg# (Mg/(Mg+Fe)). D) Cr_2O_3 vs. CaO (wt%) plot for classification of mantle-derived garnets with

fields by Grütter et al. (2004). The samples plot at the Cr-rich, high-Mg# end of the megacryst trend, and overlap compositions of garnet in LDG peridotites. Reference data for megacrysts are from Schulze (1997), Bell and Rossman (1992), Eggler et al. (1979), and Hunter and Taylor (1984). Data for Congo megacrysts are from Pivin et al. (2009). Fields for LDG peridotites are based on data from Aulbach et al. (2007) and Mather (2012).

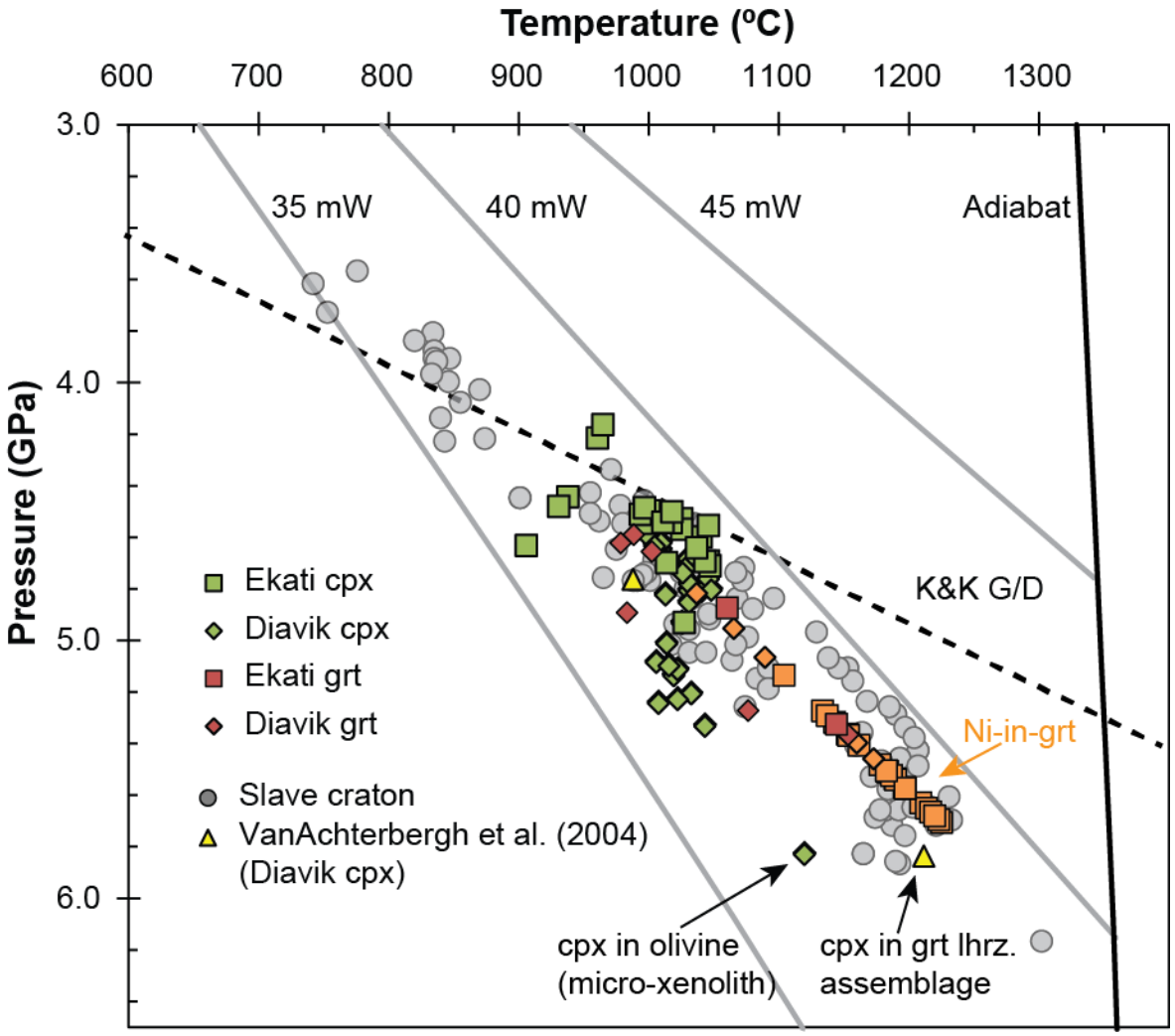

Figure 3-5: Geotherm plot with P-T results for LDG Cr-diopside (green) and Cr-pyrope (red and orange) megacrysts using different geothermobarometers (see text). Temperatures were projected onto the geotherm if no barometers could be applied due to lack of coexisting phases (e.g., mineral inclusions).

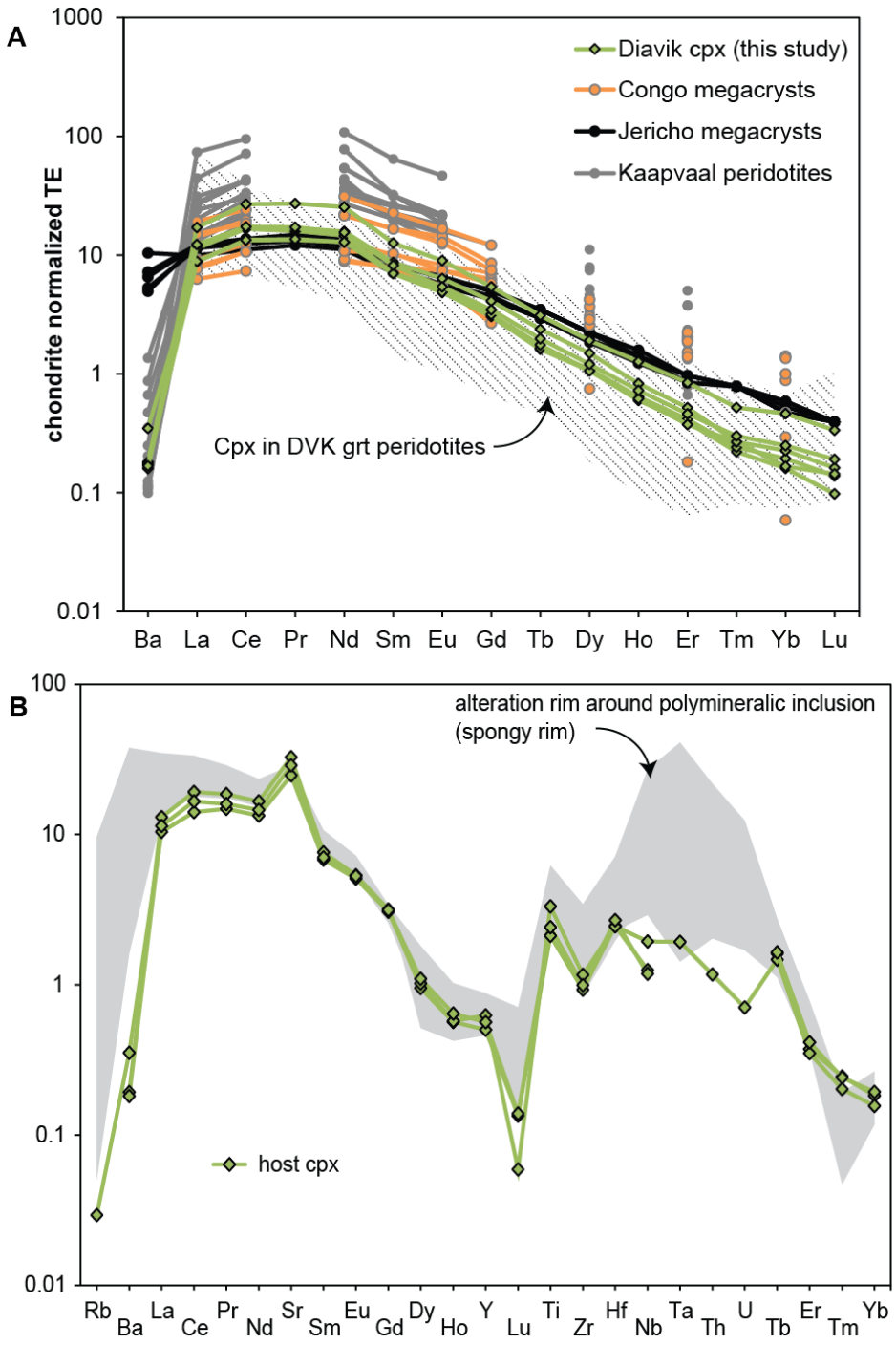

Figure 3-6: Trace element systematics of Diavik Cr-diopside megacrysts. A) Chondrite normalized REE patterns for Diavik Cr-diopside megacrysts. Chondrite values are from McDonough and Sun (1995). There is overlap with patterns of megacrysts from Congo kimberlites (Pivin et al. 2009) and with megacrysts from the Jericho kimberlite (Kopylova et al. 2009). Patterns of clinopyroxene in peridotites from the Kaapvaal craton are more enriched (Simon et al. 2003). There is also overlap with patterns with clinopyroxene in peridotites from LDG (Aulbach et al. 2007). B) Chondrite normalized trace element patterns of clinopyroxene in reaction rims around polymineralic inclusions

compared to patterns of the pristine host. The rims can show significant enrichment due to the sampling of micro-inclusions of phlogopite and calcite.

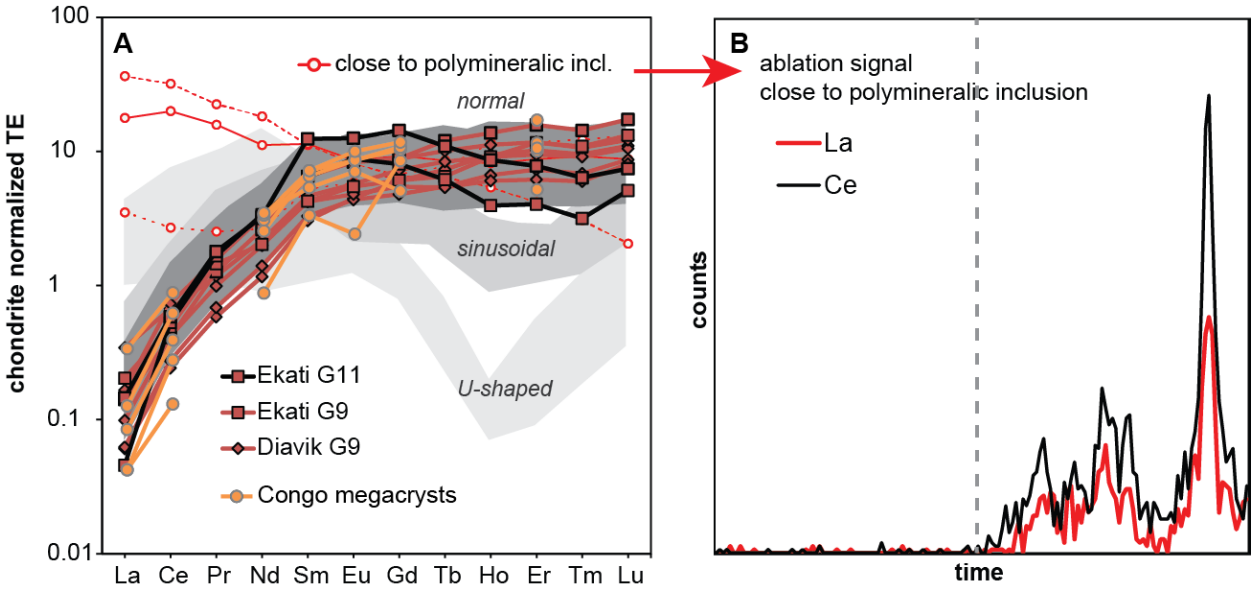

Figure 3-7: Trace element systematics of LDG Cr-pyrope megacrysts. A) Chondrite normalized REE patterns for Cr-pyrope hosts. Chondrite values are from McDonough and Sun (1995). Congo megacryst data is from Pivin et al. (2009). Shaded areas are based on Diavik garnet data (Creighton et al. 2010; Mather 2012). Dark gray = normal pattern (L-shaped), medium gray = sinusoidal pattern (S-shaped), light gray = U-shaped. The samples of this study have exclusively normal patterns where clear zones were analyzed. Sampling of micro-inclusions close to polymineralic inclusions can lead to patterns enriched in light REE. B) Ablation signal of garnet close to a polymineralic inclusion shows spikes in light REE (e.g., La, Ce) due to sampling of micro-inclusions. Dashed line indicates beginning of ablation.

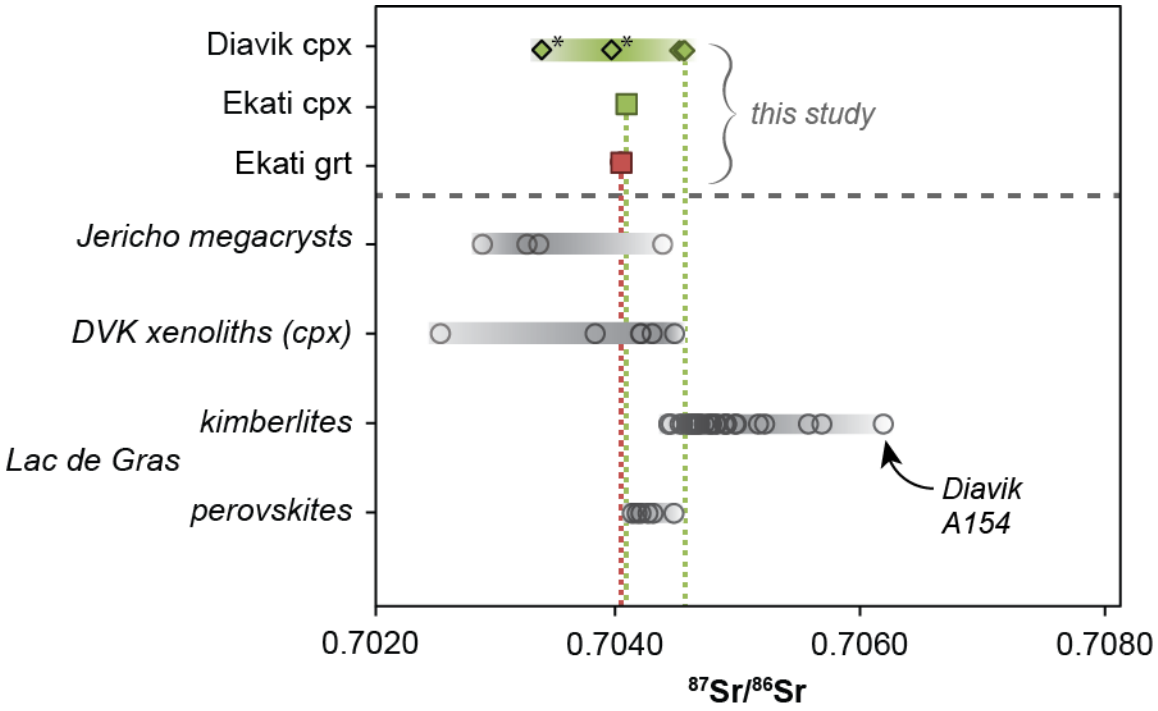

Figure 3-8: Sr isotope systematics of Cr-diopside and Cr-pyrope megacrysts. $^{87}Sr/^{86}Sr$ ratios of Cr-diopside from Diavik (A154N) (* are previous analyses from van Achterbergh et al. (2002)) and Ekati (Jay), and Cr-pyrope from Ekati (Wolverine), compared against garnet and clinopyroxene megacrysts from the Jericho kimberlite (Kopylova et al. 2009), clinopyroxene in Diavik mantle xenoliths (Aulbach et al. 2013), LDG whole rock kimberlites (Tappe et al. 2013), and LDG perovskites (Sarkar et al. 2015). Vertical dashed lines are drawn downwards from the ratios measured in this study to facilitate comparison with other isotopic signatures.

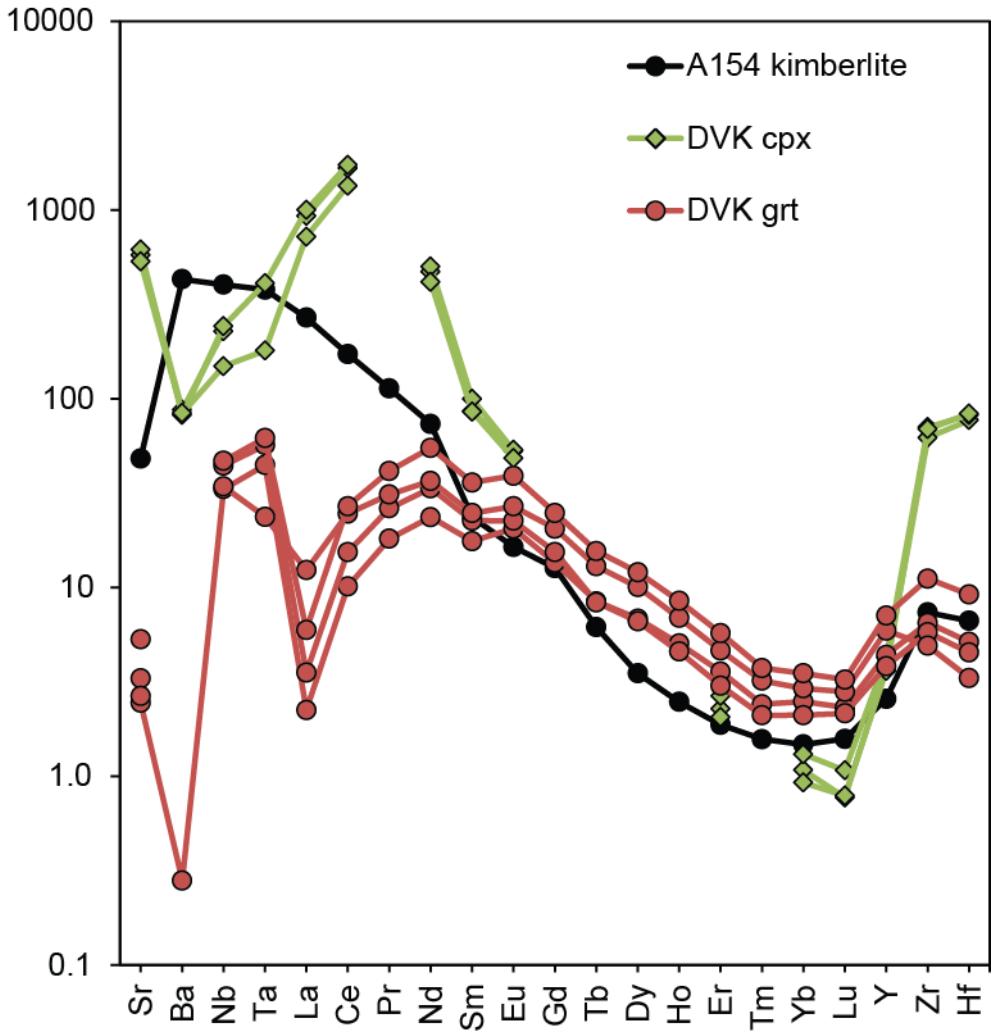

Figure 3-9: Equilibrium melts for Diavik Cr-diopside (cpx) and Cr-pyrope (grt) megacrysts. Melt patterns were calculated from the trace element signatures of Diavik Cr-diopside and Cr-pyrope megacrysts using partition coefficients for carbonate-silicate melts (see text). The trace element signature of the host kimberlite (Diavik A154) is from Tappe et al. (2013).

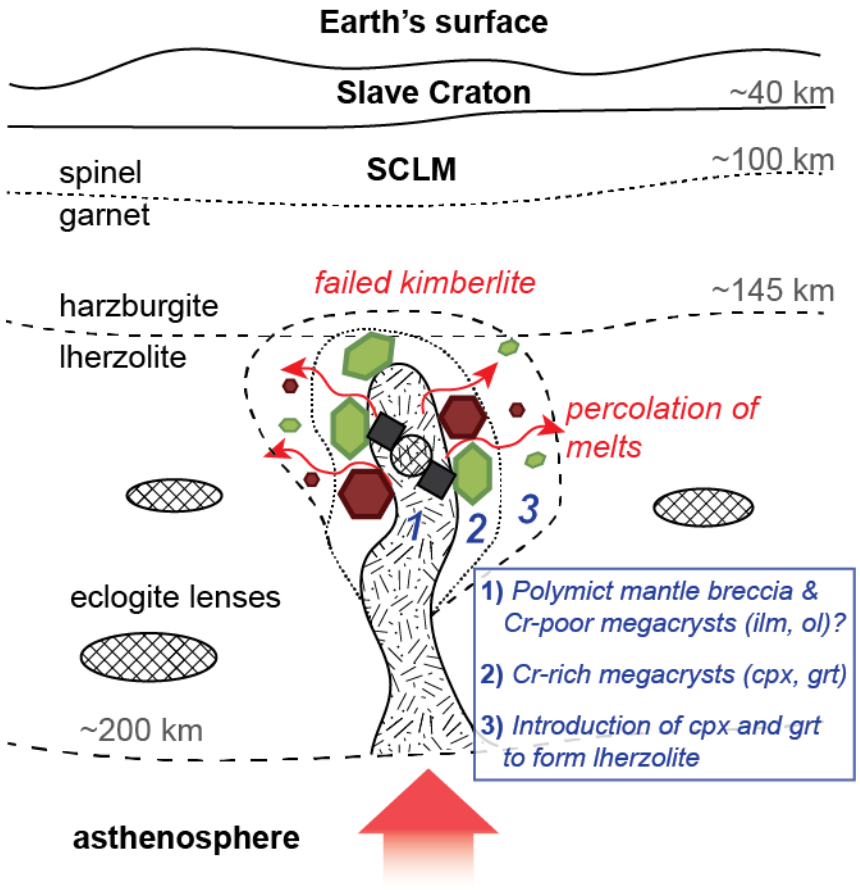

Figure 3-10: Schematic cartoon for the formation of Cr-rich megacrysts at Lac de Gras. In this cartoon, a kimberlite magma originating from the asthenosphere underneath Lac de Gras (Tappe et al. 2013) is envisaged to stall within the lower lithospheric mantle below the upper depleted (harzburgite) layer. 1) This failed kimberlite is responsible for the formation of polymict mantle breccias (Giuliani et al. 2013), possibly accompanied by crystallization of Cr-poor megacrysts (ilmenite, garnet, olivine). 2) By progressing interaction of percolating melts with the surrounding depleted mantle (originally harzburgite) the Cr-rich megacrysts (Cr-diopside and Cr-pyrope) are formed. 3) The melts may percolate further outwards and lead to the introduction of clinopyroxene and garnet (compositionally similar to Cr-rich megacrysts) into the depleted mantle, thereby forming lherzolite. The megacrysts may be re-sampled by a later kimberlite that successfully ascends to the surface. The polymineralic inclusions commonly observed in the megacryst samples are formed after this later entrainment (Bussweiler et al. 2016).

4. The Aluminum-in-Olivine Thermometer for Mantle Peridotites – Experimental versus Empirical Calibration and Potential Applications

Y. Bussweiler*[a], G. P. Brey[b], D. G. Pearson[a], T. Stachel[a], R. A. Stern[a], M. F. Hardman[a], B. A. Kjarsgaard[c], S. E. Jackson[c]

[a)] Department of Earth and Atmospheric Sciences, University of Alberta, 126 ESB, Edmonton, AB T6G 2E3, Canada

[b)] Institut für Geowissenschaften, FE Mineralogie, Johann Wolfgang Goethe-Universität Frankfurt, Altenhöferallee 1, 60438 Frankfurt, Germany

[c)] Geological Survey of Canada, 601 Booth Street, Ottawa, ON, Canada K1A 0E8

*Corresponding author at: Department of Earth and Atmospheric Sciences, University of Alberta, 126 ESB, Edmonton, AB T6G 2E3, Canada. Tel.: +1 780 492 3265; Fax: +1 780 492 2030. E-mail address: bussweil@ualberta.ca (Y. Bussweiler)

4.1. Acknowledgements

This study forms part of Y.B.'s Ph.D. research, funded through the Canada Excellence Research Chair awarded to D.G.P. Analytical work for this project was funded through an NSERC Discovery Grant to T.S., and a Society of Economic Geologists Canada Foundation (SEGCF) grant awarded to Y.B. The author is further grateful for a University of Alberta Doctoral Recruitment Scholarship. Kate Hogberg is thanked for help with sample preparation for SIMS. Pedro Waterton is thanked for assistance with solution ICP-MS. Natasha Barrett is thanked for providing olivines from spinel lherzolites (Fiji). The manuscript has benefitted greatly from two very constructive reviews from Paolo Nimis and Cees-Jan De Hoog. We thank Marco Scambelluri for the efficient editorial handling.

4.2. Abstract

This study provides an experimental calibration of the empirical Al-in-olivine thermometer for mantle peridotites proposed by De Hoog et al. (2010). We report Al concentrations measured by secondary ion mass spectrometry (SIMS) in olivines produced in the original high-pressure, high-temperature, four-phase lherzolite experiments by Brey et al. (1990). These reversed

experiments were used for the calibration of the two-pyroxene thermometer and Al-in-orthopyroxene barometer by Brey and Köhler (1990). The experimental conditions of the runs investigated here range from 28 to 60 kbar and 1000 to 1300 °C. Olivine compositions from this range of experiments have Al concentrations that are consistent, within analytical uncertainties, with those predicted by the empirical calibration of the Al-in-olivine thermometer for mantle peridotites. Fitting the experimental data to a thermometer equation, using the least squares method, results in the expression:

$$T\,[°C] = (11245 + 46.0 * P\,[kbar]) / (13.68 - \ln(Al\,[ppm]) - 273$$

This version of the Al-in-olivine thermometer appears to be applicable to garnet peridotites (lherzolites and harzburgites) well outside the experimental range investigated here. However, the thermometer is not applicable to spinel-bearing peridotites. We provide new trace element criteria to distinguish between olivine from garnet-, garnet-spinel-, and spinel-facies peridotites. The estimated accuracy of the thermometer is ±20 °C. Thus, the thermometer could serve as a useful tool in settings where two-pyroxene thermometry cannot be applied, such as garnet harzburgites and single inclusions in diamond.

4.3. Keywords

Aluminum; Olivine; Thermometry; Experimental Calibration; Garnet Peridotite; Kimberlite

4.4. Introduction

Olivine and its high-pressure polymorphs dominate the mineralogy of Earth's upper mantle and transition zone (e.g., Ringwood, 1966; Stachel et al., 2005). Despite its overwhelming presence in the mantle cargo of kimberlites, thus far, olivine has played only a minor role in diamond exploration efforts. Meanwhile, other, much less abundant minerals, occurring in till samples and concentrate from kimberlite, such as garnet and clinopyroxene, are routinely used in diamond exploration as indicator minerals. These minerals have proved to be crucial in finding kimberlite occurrences and, more importantly, in helping to assess the diamond potential of a kimberlite pipe (e.g., Gurney 1984; Schulze 1997; Grütter et al. 2004). Recent studies have shown that the majority of olivine in kimberlite may originate from disaggregated mantle xenoliths (e.g., Kamenetsky et al. 2008; Brett et al. 2009; Arndt et al. 2010; Bussweiler et al. 2015). Moreover, in Arctic regions, such as the Slave Craton, olivine is well preserved, even in till samples. Thus,

in these settings olivine has great potential in exploration as an indicator mineral, with an especially promising application being the Al-in-olivine geothermometer.

While the incorporation of Al in olivine appears to be dominantly controlled by T, a variety of substitution and exchange mechanisms are operative in different settings (De Hoog et al. 2010, and references therein). Thus, different expressions of the thermometer are required, for example, for magmatic and mantle olivines. Among mantle olivines, the different facies (garnet-, spinel-, or garnet-spinel) may further play an important role in element partitioning. As the olivine paragenesis cannot always be determined from the sample context, i.e. for single grains from till or concentrate, developing reliable olivine trace element screens is of great importance.

The empirical calibration of the Al-in-olivine thermometer for mantle peridotites by De Hoog et al. (2010) is based on Al concentrations measured by laser ablation inductively coupled mass spectrometry (LA-ICP-MS) in olivines from natural mantle xenoliths derived from different volcanic rock types, including kimberlites and alkali basalts, from a variety of locations and tectonic settings. In combination with P and T estimates from other geothermobarometers, namely the two-pyroxene thermometer and Al-in-orthopyroxene barometer (Brey and Köhler 1990), an expression of T as a function of P and a compositional term, Cr/(Cr+Al) (Cr#), was obtained:

$T_{Al\text{-}Ol}$ [°C] = (9423 + 51.4*P [kbar] + 1860*Cr#) / (13.409 – ln Al [ppm]) – 273

Eqn. 1 (De Hoog et al. 2010)

Although only olivines from garnet lherzolites were used in deriving this calibration, the thermometer was found to be applicable to garnet harzburgites and garnet-spinel lherzolites as well (De Hoog et al. 2010). A strength of this calibration is that samples with natural Al abundances were used, and that the T calibration range is large, ~800 to 1400 °C, effectively spanning much of the mantle sampling window of kimberlites. A disadvantage of any empirical thermometer is, however, that it critically depends on the accuracy of the geothermobarometers used for the independent P and T estimates (Canil 1999). Thus far, no independent experimental calibration of this thermometer exists, in contrast to its lower-P, magmatic analog, based on the exchange of Al between olivine and Cr-spinel (Wan et al. 2008; Coogan et al. 2014).

A simplified equation, based on an earlier version of the empirical calibration (De Hoog and Gall 2005), has been proposed by Korolyuk and Pokhilenko (2014), albeit without an estimate of the applicable range of conditions or the resulting uncertainties in the estimated T. Such a simplified equation would have great potential as a single-crystal thermometer in settings where other indicator minerals, such as pyroxenes and garnet, are rare to absent. Another important example of application is single olivine inclusions in diamond.

In this study, we focus on the accuracy of the empirical calibration of the Al-in-olivine thermometer from an experimental perspective. We revisit the original experiments used for the calibration of the two-pyroxene thermometer and Al-in-orthopyroxene barometer (Brey and Köhler 1990) and measure Al directly in the experimentally-equilibrated olivines by SIMS. We then present a calibration of the Al-in-olivine thermometer based on the precisely known experimental P and T conditions, and compare the results with the empirical version of the thermometer. We test the applicability of our experimental calibration to natural samples by comparison to the two pyroxene thermometer and the Ca-in-orthopyroxene thermometer by Brey and Köhler (1990), and the single-clinopyroxene thermometer by Nimis and Taylor (2000).

The use of SIMS in this study is necessary due to the need for high spatial resolution and high analytical sensitivity, given that olivines in the experimental runs are usually < 30 μm in size, with Al concentrations of usually < 200 ppm. Moreover, a minimally-destructive approach was preferred in order to preserve the experimental charges for future work.

4.5. Samples

The experiments used here were performed by Brey et al. (1990) on fertile natural lherzolite compositions over a P range of 10 to 60 kbar and a T range of 900 to 1400 °C. The reversed experiments were performed in a piston cylinder apparatus (for P ≤ 28 kbar) and in a belt apparatus (for P > 28 kbar). Importantly, the experimental conditions are very precisely known, T to ±7 °C and P to ±1% (relative) (Brey et al. 1990). Different starting materials were used in the experiments, with their bulk compositions approximating primitive upper mantle. The mineral compositions of each starting material differed, so that equilibrium mineral compositions could be inferred from overlap of microprobe analyses. Starting materials considered in the present study are 1) mineral mix ‘SC-1’, which constitutes handpicked mineral separates (olivine, orthopyroxene, clinopyroxene, and spinel) of spinel lherzolite SC-1 (Jagoutz et al.

1979), 2) mineral mix 'J4', which constitutes magnetic separates of orthopyroxene-, clinopyroxene-, and garnet-porphyroclasts from the sheared garnet lherzolite nodule J4 from Jagersfontein, South Africa, combined with olivine from either J4 or from spinel lherzolite Mog 32, and 3) oxide mix 'SCS', which constitutes a synthetic mix of sintered pure oxides (SiO_2, TiO_2, Al_2O_3, Cr_2O_3, MnO, NiO, and MgO) and carbonates ($CaCO_3$ and Na_2CO_3) together with synthetic fayalite to match the SC-1 composition. In two out of 14 cases, the starting composition could not be reliably identified in this study, due to loss of sample material and/or documentation to the original dataset.

4.6. Methods

Restoration and preparation of the experimental samples and secondary ion mass spectrometry (SIMS) were carried out at the Canadian Centre for Isotopic Microanalysis (CCIM), University of Alberta. All original experimental run products were extracted from their existing epoxy mounts and re-assembled into four new 25 mm diameter epoxy discs (mount numbers M1348, M1349, M1350, M1351). In-house olivine reference materials were also included in the new assemblies. The surfaces were polished lightly with diamond compounds on rotary equipment to create a uniformly flat surface, cleaned with a lab soap solution and de-ionized H_2O, and then coated with 7 nm of high-purity Au prior to scanning electron microscopy (SEM). Detailed SEM imaging using a backscattered electron detector was carried out utilizing a Zeiss EVO MA15 instrument with beam conditions of 20 kV and 3 – 4 nA. A further 23 nm of Au was subsequently deposited on the mounts prior to SIMS analysis.

Al concentrations were determined from $^{27}Al^-/^{29}Si^-$ ratios in olivine using the IMS-1280 multi-collector ion microprobe at the CCIM. Primary beam conditions utilized 20 keV $^{133}Cs^+$ ions focused to a diameter of 8 µm and a beam current of 0.5 nA. The normal incidence electron gun was utilized for charge compensation. No analytical advantage was found in measuring $^{27}Al^+/^{29}Si^+$ utilizing an O^- primary beam, and the Cs probe was preferred due to the comparative ease of working at small beam diameters with high beam density. Scanning ion imaging of $^{27}Al^-$ preceded many analyses to aid the placement of analytical spots and to avoid overlap with adjacent high-Al minerals such as garnet (see 4.11. Extended Analytical Methods for images). The primary beam was rastered across a 15 x 15 µm area for 30 s prior to analysis, to clean the surface of Au and contaminants, and to implant Cs. Negative secondary ions were extracted

through a 10 kV potential into the secondary column (Transfer section). Conditions for the Transfer section included an entrance slit width of 100 µm, field aperture of 3 x 3 mm, and a field aperture-to-sample magnification of 200 x. Automated tuning of the secondary ions in the Transfer section preceded each analysis. The energy slit was fully open. Both $^{27}Al^-$ and $^{29}Si^-$ were analyzed simultaneously, utilizing a large-format electron multiplier and a Faraday cup, respectively (EM and H'2 using 10^{11} Ω amplifier). The only significant isobar for $^{27}Al^-$ in olivine is $^{26}MgH^-$ and requires a nominal mass resolution of ~3000 to resolve. Although olivine is nominally anhydrous, adsorbed hydrogen is ubiquitous on the mounts and becomes ionized when electron charge compensation is employed. The $^{26}MgH^-$ count rate is generally similar to or lower than that of $^{27}Al^-$, and therefore well-resolved using the working mass resolution > 3500 while maintaining a flat-topped peak scan. Mass scans comparing $^{26}MgH^-$ in Mg-rich and Fe-rich olivine are consistent with its identity. Similarly, for $^{29}Si^-$ the only interference is a weak $^{28}SiH^-$ signal, requiring a mass resolution of ~3400. Separation of $^{29}Si^-$ from the hydride was achieved by using a combination of a larger exit slit (500 µm) and offsetting the peak center to lower mass to allow a wider flat top than possible with the available fixed exit slits. Examples of mass scans are shown in 4.11. Extended Analytical Methods. The secondary ion count rates for $^{27}Al^-$ and $^{29}Si^-$ in an Fe-rich olivine reference material (Fo12) were both found to be significantly lower (~1/3) than those of Mg-rich olivine (Fo90) with the same Al (and Si) content, indicating a matrix effect. Nevertheless, the Al/Si ratio remained constant, showing that this ratio is a robust proxy for Al concentration in olivine over a wide range of olivine Fo composition.

Mean count rates for $^{27}Al^-$ were in the range 10^2 to 10^4 c/s, and for $^{29}Si^-$ were > 10^6 c/s, determined over a 75 s total counting interval for each analysis. The analytical protocol interspersed analyses of unknowns with regular analyses of an olivine xenocryst SC-GB from San Carlos (CCIM primary reference material S0355) with an average Al concentration of 86 ±3 ppm (based on EPMA, LA-ICP-MS and solution-ICP-MS, 4.11. Extended Analytical Methods). A mean $^{27}Al^-/^{29}Si^-$ was determined for each analytical session (one for each mount), and used along with the Al concentration of SC-GB to determine the session sensitivity factor to calculate Al concentrations in unknowns. Only insignificant systematic changes in $^{27}Al^-/^{29}Si^-$ in the primary reference material were observed during a session. Uncertainties in Al concentration propagate within-spot counting errors, the uncertainty in the mean $^{27}Al^-/^{29}Si^-$ for the session, and a blanket spot-to-spot uncertainty of 1.0 ‰ in the $^{27}Al^-/^{29}Si^-$. The total uncertainties (95%

confidence) in [Al] per spot, excluding those associated with the absolute abundance of Al in the primary reference material, are generally in the range ±3% to ±10%.

4.7. Results

A total of 14 experimental charges produced in seven runs (Appendix A4.1.) were chosen for SIMS analysis. The selected samples show textural evidence for equilibrium, such as equigranular crystals with common 120° grain boundary intersections (Figure 4-1). Grain sizes for olivine and other phases range from 5 to 30 μm. Brey et al. (1990) describe a dependency of grain size on the type of starting material (smaller for synthetic mixtures) and temperature (larger for higher T). Based on only small variations in Mg# (±0.3, 1σ) in all experiments, Brey et al. (1990) concluded that olivines are generally well-equilibrated in the experiments.

Al concentrations were measured by SIMS for up to 10 different olivine grains per experiment. The data were carefully screened for analytical overlap with surrounding high-Al minerals. This could be done based on the analytical uncertainties associated with the measured Al concentrations, given that "contaminated" concentrations are usually associated with higher uncertainties (> 10%). Additionally, post-SIMS BSE images recorded for each analytical spot were checked visually to exclude the possibility that neighboring phases were sampled during analysis. The complete dataset of screened analyses is shown in Appendix A4.2.

The observed ranges of Al concentrations in olivines within individual experiments can be relatively large (up to 50 ppm, Appendix A4.2., Figure 4-2), whereas the Mg# of the olivines was found to be more narrowly defined (Brey et al. 1990). This observation can be attributed to the slower diffusion of Al^{3+} compared to divalent atoms, Mg and Fe, in olivine (e.g., Spandler and O'Neill 2010).

In order to obtain an equilibrium value from the observed ranges in Al for a particular set of P and T conditions, the overlap in Al concentration for runs using different starting materials was used, following the procedure outlined by Brey et al. (1990). The high analytical precision of SIMS allows us to constrain the overlap range and the associated midpoint reliably (Figure 4-2). The midpoint of the overlap range was taken as the equilibrium value, and the maximum analytical uncertainty of the two data points constraining the overlap range was adopted as the uncertainty of the equilibrium value (2σ).

For cases where only one starting material was available, i.e. where no midpoints could be determined from compositional overlap (see 50 kbar data plotted in Figure 4-2), the mean of the measured range (weighted by the uncertainties of the individual data points) was used as the equilibrium value. The greater analytical uncertainty of the group of data points was assigned as the uncertainty of the equilibrium value (2σ).

The resulting equilibrium Al concentrations and their uncertainties for the different runs (i.e. fixed P-T condition) are shown in Figure 4-2 and listed in Appendix A4.3.

Cr was not measured in the experimental olivines during this study. However, Brey (1989) reported Cr_2O_3 average concentrations for the different experimental runs (equilibrium values) from electron probe microanalysis (EPMA). Using these published values and the measured Al equilibrium values from this study, the Cr# for all experiments could be calculated (Appendix A4.3.).

4.8. Discussion

The calculated equilibrium Al concentrations from the experiments were compared against the Al concentrations expected from the empirical calibration by De Hoog et al. (2010) in ln (Al) versus 1000/T space (Figure 4-3). De Hoog et al. (2010) suggested that the empirical calibration is most reliable for olivines with Cr# between 0.35 and 0.75. The equilibrium Al values from the experiments fall consistently within this empirical range for all experimental P and T (Figure 4-3a). Moreover, inserting the respective Cr# for each run (Appendix A4.3.) along with experimental P and T into the empirical expression by De Hoog et al. (2010) (Equation 1), yields Al values that are within uncertainty of the measured Al concentrations (Figure 4-3b). However, we note that the latter is not a completely independent test, as Cr# was calculated with the equilibrium Al concentrations from our measurements.

4.8.1. Experimental Calibrations versus Empirical Calibration

The experimental dataset (n = 7, Table 3) was fitted to the expected thermometer equation (e.g., Equation 1) following the least squares method (using the Solver function in Excel). By describing the experimental T with the three variables experimental P, ln(Al), and Cr#, the following relationship was obtained:

$$T\,[°C] = (14750 + 45.1 * P\,[kbar] - 2831 * Cr\#) / (14.97 - \ln(Al\,[ppm]) - 273 \qquad \text{Eqn. 2}$$

Cr#, however, is not a strictly independent variable in this dataset, as it is directly related to Al concentration, and there is a strong negative correlation of Cr# with T ($R^2 = 0.89$). Moreover, the incorporation of Cr itself into olivine has been found to be related to P and T under common mantle redox conditions (De Hoog et al. 2010). To avoid any detrimental effect of these correlations on statistical regression, we now describe T in terms of only P and Al concentration only, which yields the expression:

$$T\,[°C] = (11245 + 46.0 * P\,[kbar]) / (13.68 - \ln(Al\,[ppm]) - 273 \qquad \text{Eqn. 3}$$

The uncertainties on any calculated temperatures using these equations are dominated by the uncertainties in the equilibrium Al concentrations from the experiments, i.e. the 2σ errors in Appendix A4.3. Thus, the extremes of the measured Al concentrations in the experimental olivines were inserted into Equations 2 and 3, and also into Equation 1, the empirical calibration by De Hoog et al. (2010) to obtain uncertainty estimates at the 95% confidence level. It should be noted that Equations 1 and 2 are affected by an additional uncertainty associated with the calculation of the Cr# value, which also may be on the order of ±10 °C (assuming an average absolute uncertainty of Cr# of 0.03, based on analytical uncertainties). The uncertainties for Equations 1 and 2 were thus doubled to take into account propagation of uncertainties on the Cr# measurement. The resulting maximum uncertainties for Equations 1, 2, and 3 are observed for Run 320b, and amount to ±19, ±17, and ±9 °C, respectively (error bars in Figure 4-4). Uncertainties in the experimental conditions were not propagated, but the uncertainty for experimental T of ±7 °C (Brey et al. 1990) becomes relevant when evaluating the accuracy of the thermometers (Figure 4-4b).

Both expressions derived from the experimental calibration (Equations 2 and 3) as well as the empirical calibration by De Hoog et al. (2010) (Equation 1) reproduce the experimental T closely (Figure 4-4a). This underlines the good agreement between empirical and experimental calibration of the Al-in-olivine thermometer. The empirical calibration is consistently within error of at least one of the experimental calibrations. However, the empirical calibration (De Hoog et al. 2010; Equation 1) yields, on average, slightly lower temperatures than the experimental calibrations with a somewhat larger spread (Figure 4-4b).

In terms of accuracy of the different equations, the average absolute deviations from the experimental T of the mean values of the experimental calibrations are 7 °C for Equation 2, 8 °C

for Equation 3, and slightly higher for the empirical calibration (17 °C for Equation 1). Yet, given the uncertainty of ±7 °C for the experimental T, these deviations are small.

4.8.2. Critical Evaluation of Cr# in Experimental Olivines

In mantle peridotites, Cr substitutes for Al extensively and if only olivine is analyzed, Cr# in olivine is the best proxy for this substitution (De Hoog et al. 2010). Because the Al-in-olivine thermometer for mantle peridotites presented here constitutes a single-mineral thermometer which ignores any Al variation in the other phases that olivine equilibrates with (i.e., garnet, ±clinopyroxene, ±spinel), the Cr# of olivine is, in principle, a crucial parameter in the Al-in-olivine thermometer equation.

Here, Cr# values of the experimental olivines were calculated using the original Cr contents reported by Brey (1989) and the new Al values measured by SIMS (Appendix A4.3.). When comparing the calculated Cr# values to those of natural samples, some potential limitations become evident (Figure 4-5a). Firstly, the range of Cr# in the experimental olivines (~0.50 to 0.63) is relatively restricted compared to that of olivines from typical cratonic garnet peridotites (~0.35 to >0.75; e.g., De Hoog et al. (2010)). Moreover, when comparing the Cr# of olivine to that of coexisting clinopyroxene, it appears that the experiments by Brey et al. (1990) behave differently than natural garnet peridotites in that the experimental olivines are displaced towards higher Cr# (Figure 4-5a).

The observed displacement of the experimental olivines away from the natural xenolith trend can have various underlying reasons. Firstly, the equilibrium of Cr may not have been fully attained in the experimental olivines, due to the slow diffusion of Cr in olivine (Milman-Barris et al. 2008). Secondly, Na loss (due to the presence of a fluid or melt phase) was reported in the original experiments (Brey et al. 1990). Not only does Na have an effect on the substitution of Al into olivine (by charge balancing the substitution for Mg^{2+}), but it also influences the incorporation of Al and Cr into clinopyroxene. In fact, Brey et al. (1990) attributed variable Cr/Al ratios in clinopyroxene to Na loss. Thus, we cannot confidently establish whether the observed mismatch in Cr# between experiments and natural samples (Figure 4-5a) is due to disequilibrium in olivine or clinopyroxene, or both.

In order to test qualitatively whether Cr# of olivine has an effect on the accuracy of our experimental calibration, we have plotted deviations in temperatures (ΔT) calculated with our

Al-in-olivine thermometer (Equation 3) from temperatures calculated with the single-clinopyroxene thermometer of Nimis and Taylor (2000), against the range in Cr# of natural olivines (Figure 4-5b). No clear correlation of ΔT with Cr# of natural olivines is evident, but Al-in-olivine temperatures appear to be shifted consistently to higher values. The same holds true when comparing against the orthopyroxene-garnet thermometer of Harley (1984) (Figure 4-5c). It should be noted that using the thermometer equation which includes the Cr# term (Equation 2) does not change the observed deviations significantly. The systematically slightly higher temperatures obtained with our Al-in-olivine thermometer equation(s) may thus be a function of Na loss in the original experiments, which could have slightly suppressed the incorporation of Al into olivine.

Finally, it should be noted that the coefficient for Cr# in the experimental thermometer formulation (Equation 2) is negative, whereas the corresponding coefficient in the empirical calibration of De Hoog et al. (2010) (Equation 1) is positive. This highlights that the effect of Cr# in Al-in-olivine thermometry still remains somewhat uncertain. For this reason, and due to the equilibrium issues described above, we advise against the use of Equation 2. Instead, we recommend, for the present time, a formulation without the Cr# term (Equation 3) which also shows a generally better fit when applied to natural samples (see below).

4.8.3. Applicability of Experimental Calibrations to Natural Samples

In order to test whether the new experimental calibrations (Equations 2 and 3) are also valid for natural samples that have equilibrated at conditions outside of the experimental range, the formulations were applied to the dataset of mantle xenoliths from kimberlites published by De Hoog et al. (2010), and additional data for garnet peridotites derived from kimberlites at Diavik (Mather 2012) and Somerset Island (Kjarsgaard and Peterson 1992) (Appendix A4.4.). The calculated temperatures were compared to values obtained with the two-pyroxene thermometer of Brey and Köhler (1990), the single-clinopyroxene thermometer of Nimis and Taylor (2000), and the orthopyroxene-garnet thermometer of Harley (1984). For consistency, all temperatures were calculated iteratively in combination with the Al-in-orthopyroxene barometer of Brey and Köhler (1990) and the respective P estimates were inserted into the experimental calibrations of the Al-in-olivine thermometer (Appendix A4.4.).

Both experimental calibrations of the Al-in-olivine thermometer result in good agreement with the two-pyroxene thermometer, outside the range of experimental conditions used in this study (1000 to 1300 °C; Figure 4-6a, b). This is true for the garnet lherzolite samples from the dataset of De Hoog et al. (2010) and our new data for garnet peridotites from Diavik and Somerset Island. Equation 2, the formulation including the Cr# term, however, results in more scatter and overall offset from the 1:1 line towards lower temperatures (Figure 4-6a). We thus prefer the formulation without Cr# (Equation 3). Another advantage of this equation is that the uncertainties are potentially reduced as it removes the need for precise and accurate Cr determination in addition to Al.

Our preferred formulation (Equation 3) yields results for olivines derived from garnet lherzolites that show excellent fit with the two-pyroxene thermometer (T_{BKN}) over a temperature range from 850 to 1450 °C (Figure 4-6b). For garnet lherzolites, the median absolute deviations of our preferred Equation 3 and T_{BKN} indicate agreement within ~ ±20 °C, i.e. agreement within the respective uncertainties of the thermometers. There is also reasonable agreement with the single-clinopyroxene thermometer (T_{NT}), although Al-in-olivine temperatures lie increasingly above T_{NT} towards lower T (Figure 4-6c), which could be a function of Na loss in the experiments (see above). The difference in slope between the two thermometers could also be a function of the barometer used in the iterative calculations; T_{NT} gives best results with the corresponding single-clinopyroxene barometer (Nimis and Taylor 2000).

De Hoog et al. (2010) suggested that the Al-in-olivine thermometer is also applicable to garnet harzburgites. At present there is no reliable thermometer available for garnet harzburgite assemblages that could be used for comparison. The garnet-orthopyroxene Mg-Fe exchange thermometer of Harley (1984) systematically overestimates temperatures at low T (< 1000 °C) and underestimates at high T (> 1100 °C; for full discussion see Brey and Köhler (1990) and Nimis and Grütter (2010)). On that basis, the key observation in Figure 4-6d is that the harzburgitic and lherzolitic samples fall on the same linear array, suggesting that the Al-in-olivine thermometer indeed yields reliable T estimates for garnet harzburgites. A possible Al-exchange reaction in clinopyroxene-free harzburgites is:

$MgAl[AlO_4] + 2\ Mg_2Si_2O_6 \leftrightarrow Mg_3Al_2Si_3O_{12} + Mg_2[SiO_4]$

olivine + orthopyroxene ↔ garnet + olivine

Below 850 °C, the excellent correlation between Al-in-olivine and pyroxene based thermometry breaks down (Figure 4-6). All these low-T samples correspond to xenolith samples that also contain spinel (i.e. spinel and spinel-garnet peridotites). This may suggest that the Al-in-olivine thermometer is not applicable to spinel-bearing samples, including garnet-spinel peridotites. Alternatively, it may relate to a decoupling of Al- and Ca-based thermometers at temperatures where Al diffusion becomes exceedingly slow (e.g., Spandler and O'Neill, 2010). In the latter case, a simple cut-off at a minimum T of 850 °C for the applicability of the Al-in-olivine thermometer would be sufficient. In the former case, however, the well-established existence of depleted spinel-garnet peridotites (e.g., 5-phase lherzolites) at higher temperatures (and pressures) needs to be considered (Klemme 2004; Grütter et al. 2006; Ziberna et al. 2013).

In order to distinguish between olivine derived from garnet peridotites, garnet-spinel peridotites, and spinel peridotites, other trace element systematics in olivine can be used. De Hoog et al. (2010) proposed that the different lithologies can be most successfully separated by plotting Zr vs. Sc, and to a lesser extent Al vs. Mn (their Figure 7), with olivine in garnet peridotites being characterized by higher Zr and lower Sc and Mn.

Here, we recommend Al vs. V as a more robust discriminating plot. V is another T-sensitive element in mantle olivine and thus shows a positive relationship with Al (De Hoog et al. 2010). Moreover, V is strongly compatible with spinel and thus displays lower concentrations in olivine from spinel-bearing lithologies. This leads to distinct trends for the different peridotite facies (Figure 4-7). Olivines from garnet-facies peridotites trend towards the highest Al and V concentrations with increasing T (Figure 4-7). Olivines from garnet-spinel peridotites have consistently low Al concentrations, often < 10 ppm (Figure 4-7). This can be expected to be primarily a function of their lower equilibration temperatures. The modal proportion of spinel in garnet-spinel peridotites is typically very low, usually < 1 vol% (Ziberna et al. 2013), so that the effect on Al partitioning into olivine is likely to be small. Olivines from true spinel peridotites (garnet absent) have higher Al concentrations, as the exchange dominantly occurs between olivine and spinel. The latter exchange mechanism has been exploited for the calibration of the Al-in-olivine thermometer for spinel peridotites and for magmatic systems (e.g., Wan et al. 2008; Coogan et al. 2014). An exception to these trace element systematics are olivines that have experienced substantial metasomatism in the mantle, such as those recently reported from the Benfontein sill, South Africa (Howarth and Taylor 2016). Such olivines have elevated Al, Ca,

and Na contents, and thus overlap with olivines from spinel-peridotites in Figure 4-7, whereas other discriminating plots place them within the garnet peridotite field (Howarth and Taylor, 2016; their Fig. 8a). Al-in-olivine temperatures calculated for such metasomatized grains are likely to be overestimated. A combination of discriminating plots can be applied in order to increase the reliability of the Al-in-olivine thermometer.

4.8.4. The Al-in-Olivine Thermometer as an Exploration Tool?

As for almost all geothermometers, a P estimate is required in order to calculate T with Equation 3, which is problematic when dealing with single olivine grains (e.g, recovered during indicator mineral sampling). We thus suggest a simplified approach in which the Al-in-olivine thermometer may be used without a corresponding P estimate, in order to evaluate the depth of mantle sampling, which is similar to the application of the Ni-in-garnet thermometer (Griffin et al. 1989; Canil 1999). A realistic example for this simplified approach would be a kimberlite occurrence that is under-explored, for example due to the paucity of other indicator minerals such as garnet, but which is located in a reasonably well-understood setting where the geotherm at the time of kimberlite eruption (paleogeotherm) is known. In such a case, T can be extrapolated to the geotherm to yield P, which can be converted to mantle sampling depth. It should be noted, however, that this method does not take into account possible thermal perturbations, which occur in deep lithospheric mantle sections, associated in particular with hot sheared peridotites.

In practice, a large, random sample of olivine grains should be analyzed for their major element composition (e.g., Mg and Fe), minor elements (e.g., Ni, Mn, and Ca), as well as trace elements (e.g., Al and V). Except for V, all of these components are accessible by EPMA, if proper background limits, high probe currents, and long count times are used (e.g., Korolyuk and Pokhilenko, 2014; Sobolev et al., 2007). However, in order to obtain precise Al and V concentrations (down to < 10 ppm) LA-ICP-MS is required. Alternatively, SIMS may be used to maximize spatial resolution and precision. We suggest EPMA followed by LA-ICP-MS, however, if the goal is to limit the analysis to one method, we recommend that LA-ICP-MS is used (if Si is used as the internal standard, a constant content of ~19.1 wt% can be assumed for olivine). When dealing with mineral mounts that have been polished, it can be assumed that the vast majority of the exposed cores represent mantle xenocrysts, because magmatic overgrowths

are usually thin and easily removed. Olivine from mantle peridotites should fulfill the following compositional criteria (e.g., Arndt et al., 2010; Brett et al., 2009; Bussweiler et al., 2015; Foley et al., 2013; Kamenetsky et al., 2008):

1. Mg# ≥ 0.90
2. NiO ≥ 0.3 wt% (~2350 ppm)
3. MnO ≤ 0.15 wt% (~1160 ppm)
4. CaO ≤ 0.1 wt% (~715 ppm)

These screens should exclude magmatic olivine, e.g. in the form of magmatic overgrowths/phenocrysts (Fedortchouk and Canil 2004; Kamenetsky et al. 2008; Brett et al. 2009; Arndt et al. 2010; Bussweiler et al. 2015; Howarth and Taylor 2016) and also olivines belonging to the Cr-poor megacryst suite (Moore 2012; Moore and Costin 2016). Olivines of the Cr-rich suite, however, have similar composition to lherzolitic olivines (Moore and Costin 2016) and may, by extension, also yield robust Al-in-olivine temperatures. Moreover, we emphasize that our thermometer equation is most applicable to olivine from cratonic garnet peridotites and their corresponding olivines should have Cr# >0.45 (Figure 4-5).

All olivine analyses from our example dataset from Somerset Island (n = 69; see Extended Data) pass the above screens. In order to test whether the olivines come from spinel-, garnet-, or garnet-spinel peridotites, they can be plotted in the Al vs V diagram (Figure 4-7). This test is important because the Al-in-olivine thermometer presented in this study (Equation 3) is applicable only to garnet-facies olivines. The Somerset Island data mostly overlap with the garnet-facies field (Supplementary Fig. 1, here Figure 4-9). They are thus suitable for the Al-in-olivine thermometer presented in this study (Equation 3). However, at Al concentrations below ~10 ppm, it becomes difficult to distinguish between olivines from garnet-facies and garnet-spinel-facies peridotites. Thus, to minimize incorrect facies classification, we recommend excluding all data points with < ~10 ppm Al. In our example dataset from Somerset Island, this results in the screening of 14 from 69 analyses (hollow symbols in Figure 4-8).

Al-in-olivine temperatures can then be projected onto the geotherm by expressing the latter as a linear equation (solved for P), combining it with Equation 3, and calculating P and T iteratively. For the geotherm projections, simplified equations of the geotherms of Hasterok and Chapman

(2011) may be used, or the software package FITPLOT may be applied for more sophisticated fitting equations (Mather et al., 2011; and references therein). Here, the first approach was followed, yielding somewhat lower values than published in Mather et al. (2011), e.g., 42 vs. 44 mW/m^2 for Somerset Island.

In Figure 4-8a, the projected example olivine dataset from Somerset Island (n = 69) and a smaller (non-statistical) dataset from Diavik (n = 7) are shown. The mantle beneath Diavik is characterized by a cold geotherm (~38 mW/m^2) which usually implies high diamond potential (Grütter 2009). Here, all of the analyzed olivines fall within the "diamond window", i.e. below the graphite/diamond boundary (Kennedy and Kennedy 1976; Day 2012) before intersecting the mantle adiabat. At Somerset Island, the geotherm is significantly hotter (~42 mW/m^2) so that only a small number of olivines fall within the diamond window. This is in agreement with Somerset Island kimberlites having an extremely low diamond grade of < 1 ct per 100 t (Kjarsgaard and Levinson 2002; Irvine et al. 2003).

The P-T points, obtained from projecting Al-in-olivine temperatures onto a geotherm, can further be plotted as a histogram. For clarity, P can be converted into depth in km, for example by using a simplified conversion factor of 3.15 (Figure 4-8b). The bin size should be chosen to be larger than the uncertainty of the thermometer (~20 °C, which in this example relates to ~3 km). Such a probability density plot will provide an estimate of the "mantle sampling behavior" of the transporting magma, i.e. kimberlite. In the example of Somerset Island, the majority of olivines were derived from ~140 km depth. Moreover, the histogram plot allows an estimation of the proportion of olivines that have equilibrated with spinel. In Figure 4-8b, the more erratically distributed depths below ~100 km (i.e., Al-in-olivine temperatures < 850 °C), correspond to spinel-bearing samples and are probably not reliable (see above).

Importantly, olivine sampling depth profiles, such as the one obtained for Somerset Island (Figure 4-8b), can further be coupled to other compositional parameters, such as Mg# (Figure 4-8b), minor and trace elements. Olivine, being the most abundant mineral in the mantle, should yield more reliable results for overall mantle sampling than garnet, which usually constitutes < 10 modal % of mantle peridotite xenoliths. As such, depth profiles obtained from Al-in-olivine thermometry, as presented in this study, provide a powerful tool aiding in the mapping of lithospheric mantle (e.g., Gaul et al., 2000).

4.9. Conclusions

Al concentrations measured by SIMS in olivines from the original high-P, high-T experiments by Brey et al. (1990) are in agreement with the empirical calibration of the Al-in-olivine thermometer by De Hoog et al. (2010). Our experimental dataset allows for an independent calibration of the thermometer as a function of Al concentration and pressure. The expression appears to be applicable to olivines from garnet peridotites that have equilibrated over a large P-T range, with an estimated accuracy of ~ ±20 °C. The applicability of the thermometer to garnet harzburgites, in addition to garnet lherzolites, makes the Al-in-olivine thermometer an important tool in mantle studies. Moreover, the Al-in-olivine geothermometer could serve as a useful diamond exploration tool in settings where other indicator minerals are rare. Olivine sampling depth profiles, obtained from projecting Al-in-olivine temperatures onto geotherms, can provide an important reference frame for future lithospheric mantle mapping studies.

4.10. Figures

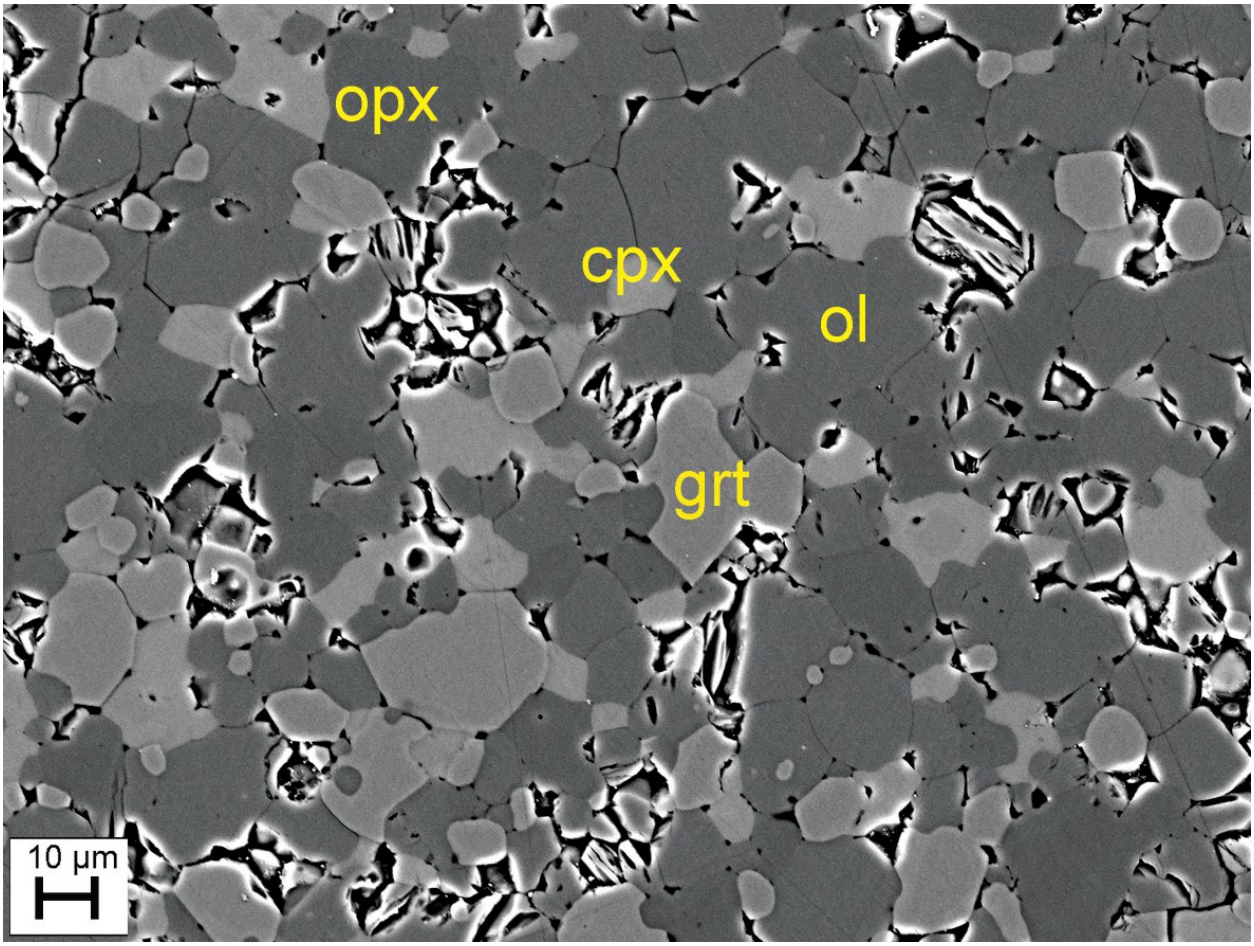

Figure 4-1: Backscattered electron (BSE) image of a high-pressure, high-temperature experimental charge. The sample is S3321A, run P3, at 28 kbar and 1150 °C with starting material J4 (Brey et al. 1990). The sample contains orthopyroxene (opx, dark grey), olivine (ol, grey), garnet (grt, light grey), and clinopyroxene (cpx, light grey with low relief).

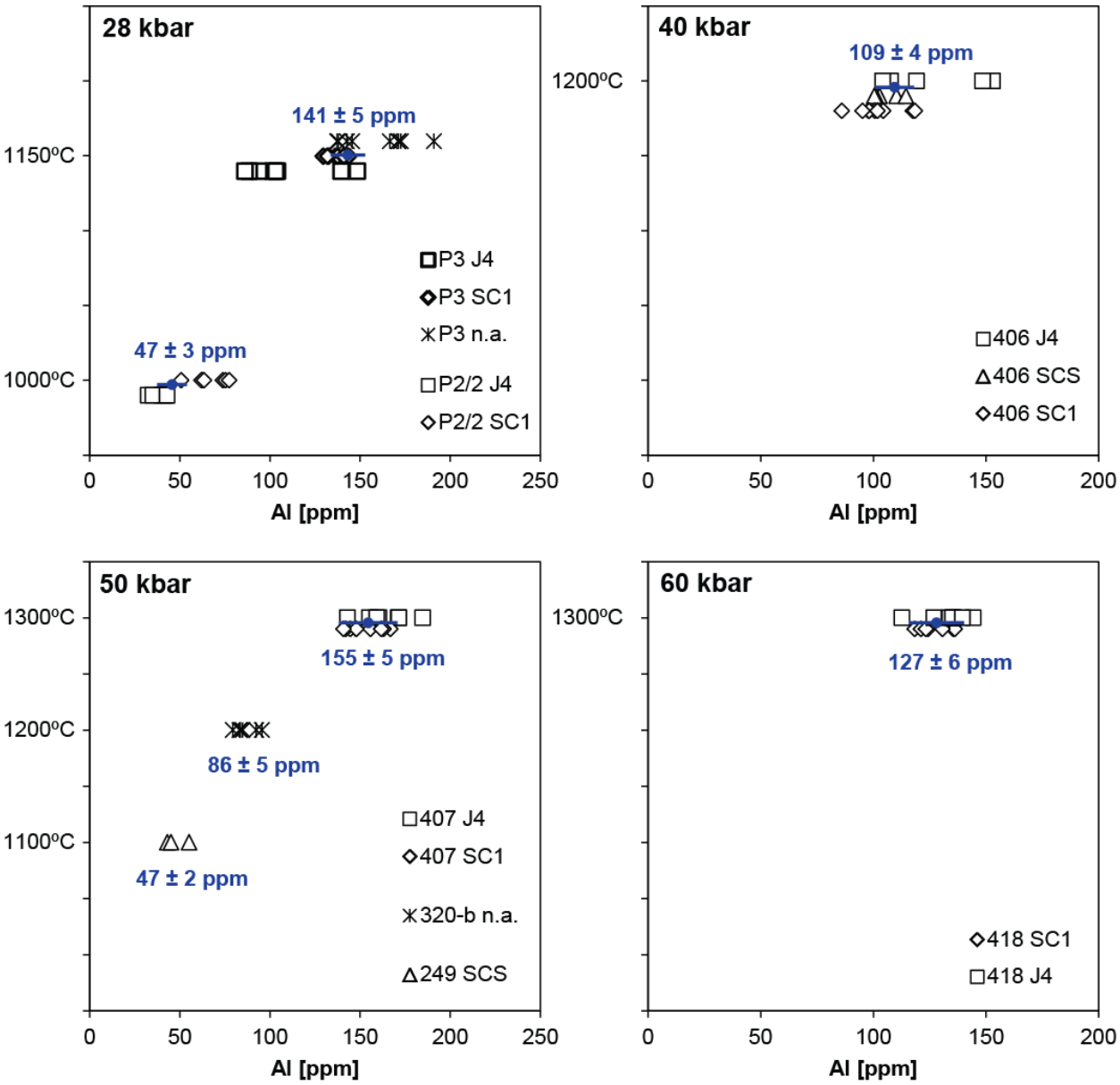

Figure 4-2: Measured Al concentrations by SIMS versus experimental temperatures, for four different experimental pressures (28, 40, 50, and 60 kbar). Where possible, equilibrium Al values (in blue) for the different runs were constrained from the midpoints of compositional overlap (filled blue circles) of different starting materials. In cases where only one starting material was available (e.g., the lower T runs at 50 kbar), the weighted mean of the measured range was used as the equilibrium value (see text).

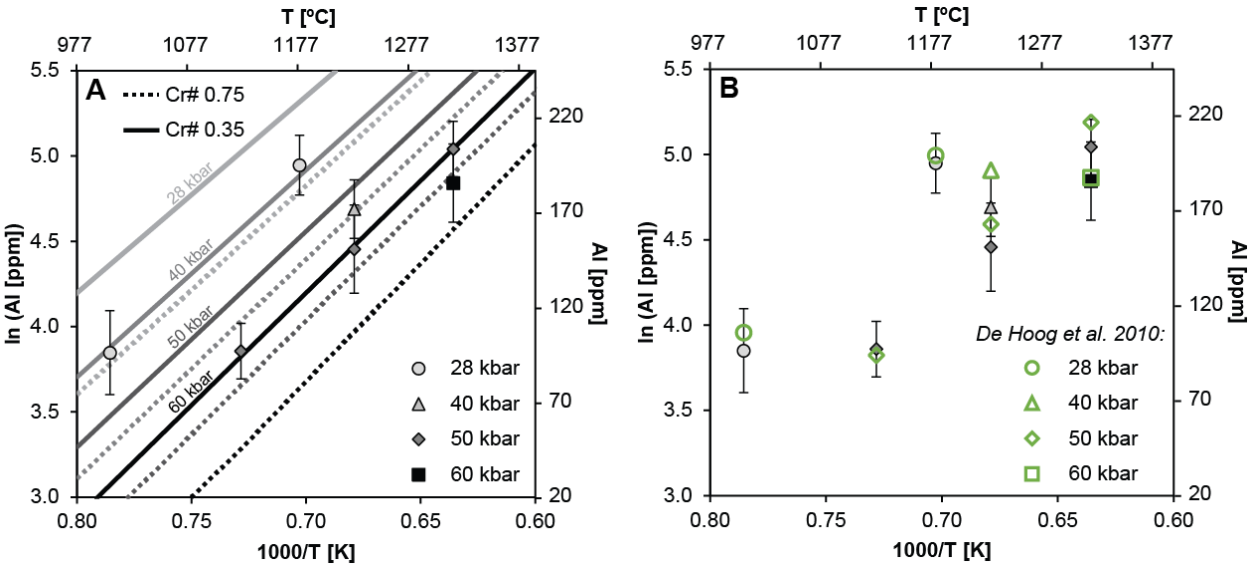

Figure 4-3: Ln(Al) versus 1000/T plots. A) Ln(Al) versus 1000/T plot, relating equilibrium Al concentrations in olivines from experiments used in this study to the empirical calibration by De Hoog et al. (2010). Contours were calculated with Equation 1, solved for Al and inserting the respective Cr# threshold values (0.35 and 0.75) and pressures. Symbols correspond to Al values measured by SIMS (this study) coded by their respective experimental P and plotted at their respective experimental T. Error bars correspond to 2σ uncertainty in the equilibrium values (see text). B) Same plot without Cr# and P contours, including expected Al concentrations (green symbols) calculated by inserting experimental P, T, and Cr# into the empirical equation by De Hoog et al. (2010).

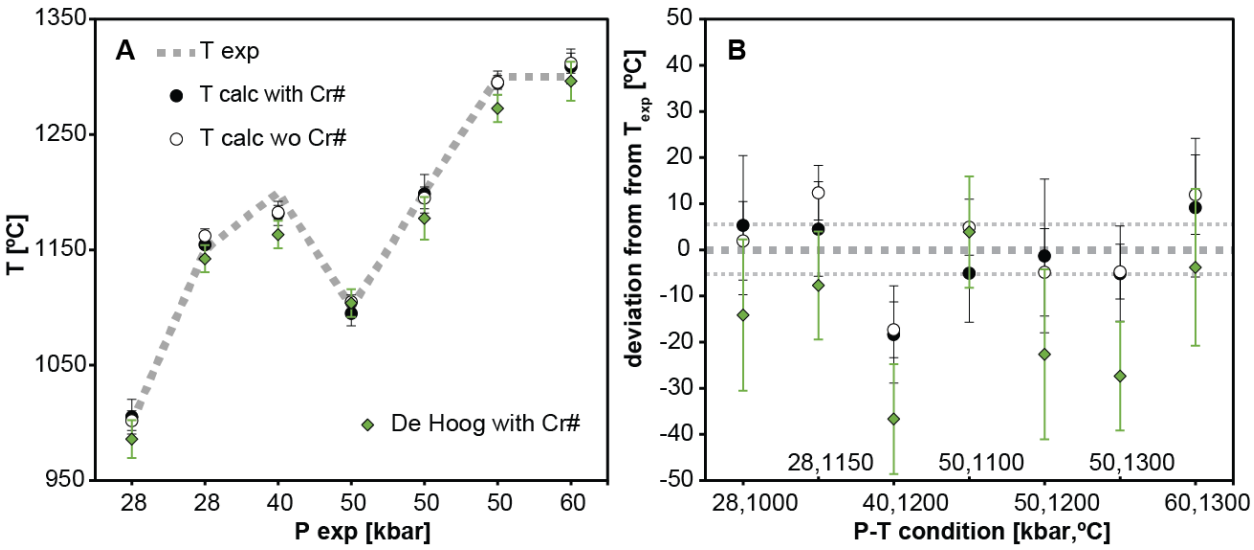

Figure 4-4: Calculated Al-in-olivine temperatures versus experimental temperature. A) Temperature versus experimental pressure (not continuous). Dashed grey line represents experimental temperatures (Brey et al. 1990). The experimental calibrations in this study, with Cr# (Equation 2, solid black circles) and without Cr# (Equation 3, open circles), and the empirical calibration by De Hoog et al. (2010) with Cr# of the experimental olivines (Equation 1, green diamonds), all reproduce the experimental T closely. B) Deviation from experimental T in °C at the different experimental P-T conditions. Average absolute deviations are 7 °C for the experimental calibration with Cr# (Equation 2), 8 °C for the experimental calibration without Cr# (Equation 3), and 17 °C for the empirical calibration by De Hoog et al. (2010) (Equation 1).

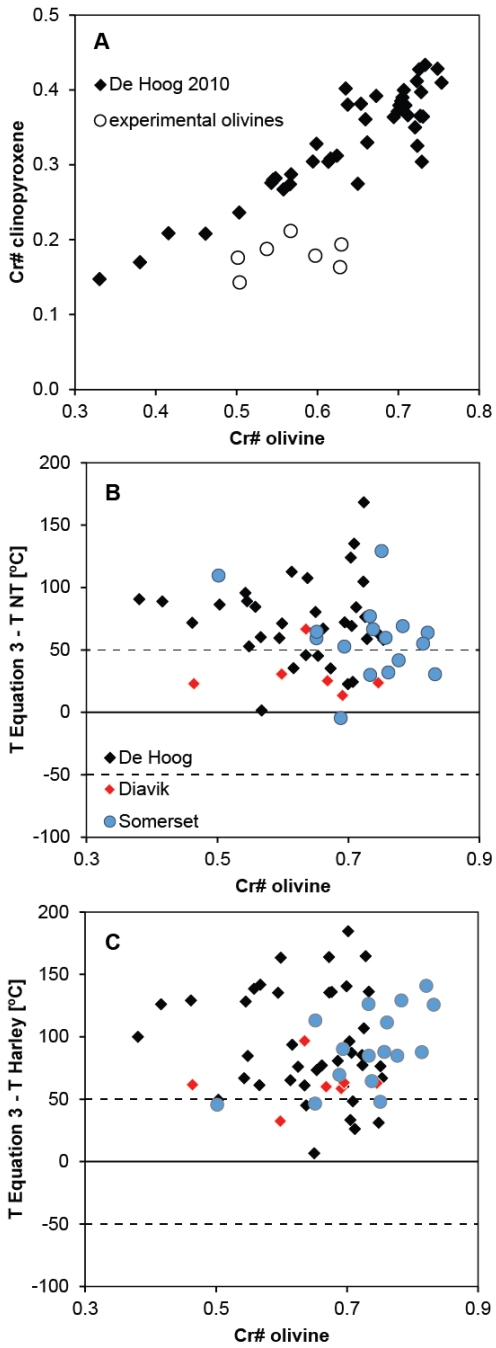

Figure 4-5: A) Cr# (Cr/[Cr+Al]) of olivine versus Cr# of coexisting clinopyroxene in the experiments of Brey et al. (1990) (open circles) and in natural olivines from garnet peridotite xenoliths from kimberlites (solid diamonds) (De Hoog et al. 2010). The experimental olivines are displaced towards higher Cr#, which may indicate imperfect equilibrium in the experiments (see text). B) Deviations in temperatures (ΔT) calculated with our Al-in-olivine thermometer (Equation 3) from temperatures calculated with the single-clinopyroxene thermometer of Nimis and Taylor (2000) plotted against Cr# of natural olivines from cratonic garnet peridotites. C) Deviations in temperatures (ΔT) calculated with our Al-in-olivine thermometer (Equation 3) from temperatures calculated with the orthopyroxene-garnet thermometer of Harley (1984). Olivine data are from De Hoog et al. (2010) (solid diamonds)

and new data from Diavik, Slave Craton (red diamonds) and from Somerset Island, Northern Canada (blue circles) (see Appendix A4.4).

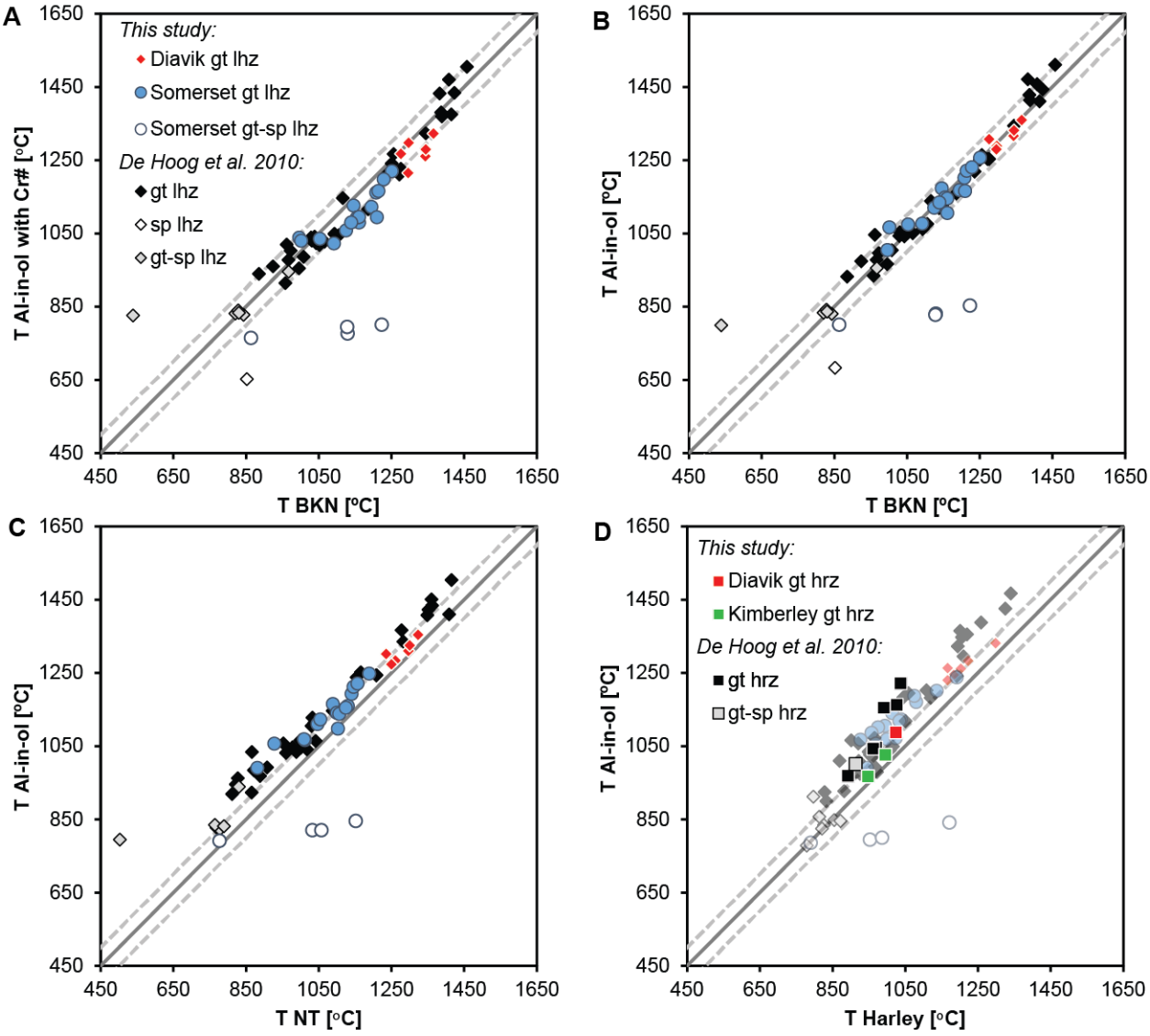

Figure 4-6: Al-in-olivine temperatures calculated for olivine from different mantle xenoliths from kimberlites (De Hoog et al. 2010) including new data (this study) for garnet peridotites from Diavik (red diamonds) and Somerset Island (blue circles). A) Temperatures calculated with Equation 2 (experimental calibration with Cr#) compared to the two-pyroxene thermometer (Brey and Köhler 1990), B) Temperatures calculated with Equation 3 (experimental calibration without Cr#) compared to the two pyroxene-thermometer (Brey and Köhler 1990), C) Temperatures calculated with Equation 3 (experimental calibration without Cr#) compared to the single-clinopyroxene thermometer (Nimis and Taylor 2000), D) Temperatures calculated with Equation 3 (experimental calibration without Cr#) compared to the orthopyroxene-garnet thermometer (Harley 1984), including harzburgitic samples from the dataset of De Hoog et al. (2010), from Diavik (Mather 2012), and from Kimberley (Creighton et al. 2009). The dashed lines represent the ±50 °C interval.

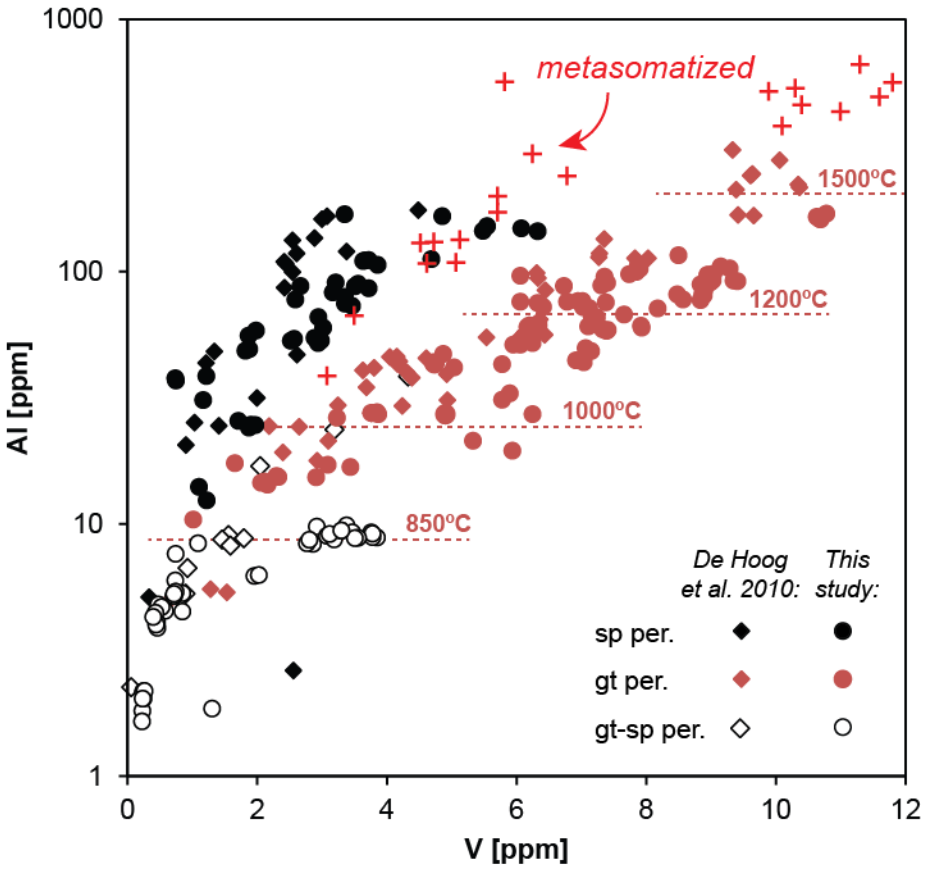

Figure 4-7: Al versus V concentration in olivines from different xenolith facies based on data from De Hoog et al. (2010) (diamond-shaped symbols) and from our own database (circle-shaped symbols), including the data from Diavik and Somerset Island (see Appendix A4.4.). The garnet-(spinel-) facies field is dominated by cratonic peridotite xenoliths derived from kimberlites from different locations (e.g., Kaapvaal Craton, Slave Craton, Siberian Craton) and contains more lherzolites than harzburgites. The spinel-facies field is dominated by non-cratonic settings (e.g., Ray Pic, Massif Central, France; San Carlos, Arizona; Fiji). Olivine from garnet-facies peridotites (gt) has high Al and high V. Olivine from garnet-spinel facies peridotites (gt-sp) has consistently low Al (< 10 ppm). Olivine in spinel-peridotites (sp) again has relatively high Al but low V (< 6 ppm). The red crosses represent core analyses of olivines from the Benfontein kimberlite sill, South Africa, that are interpreted to be derived dominantly from garnet peridotites. A sub-group of these cores have experienced Al-enrichment due to mantle metasomatism (Howarth and Taylor 2016). T contours for the garnet-facies field were calculated by projecting Al-in-olivine temperatures (using Equation 3) onto a cold cratonic geotherm of 38 mW/m^2 (see text).

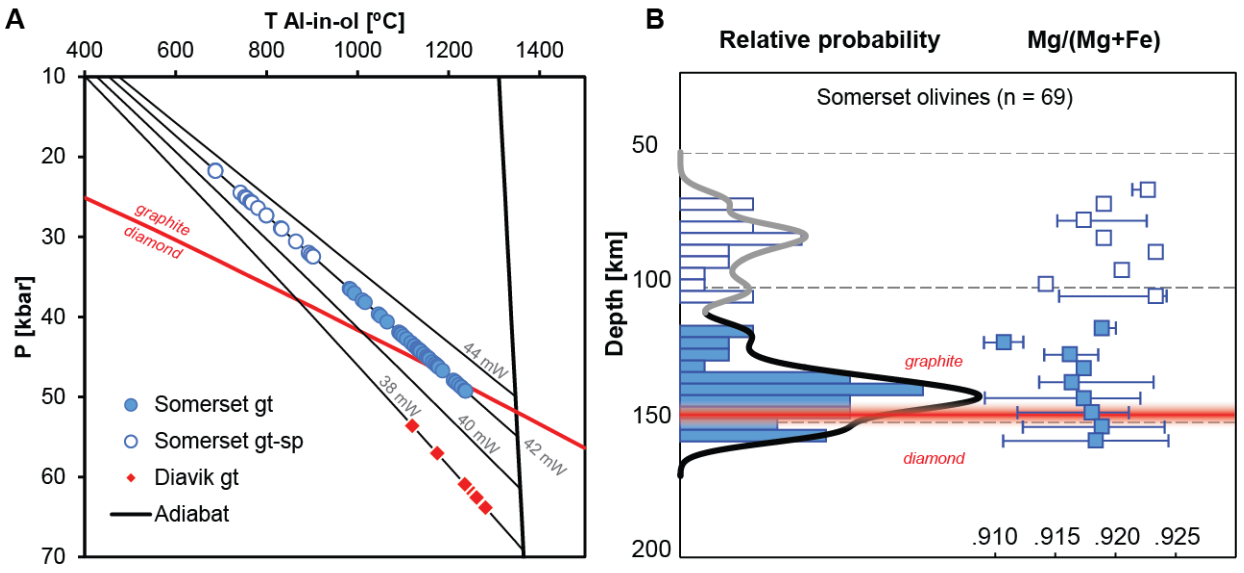

Figure 4-8: Geotherm plot and depth sampling plot obtained from Al-in-olivine temperatures. A) Al-in-olivine temperatures projected onto geotherms (Hasterok and Chapman 2011) by iterative calculation (see text). Two example data sets are shown: Diavik olivines fall along a cold geotherm (38 mW/m^2), Somerset Island olivines fall along a hot geotherm (42 mW/m^2). Based on the graphite/diamond transition (Day 2012), all of the Diavik olivines, but only few Somerset Islands olivines fall within the "diamond window". B) Probability density plot for Somerset Island olivines (n = 69) showing the frequency of olivines derived from a certain depth (or pressure) obtained from projecting Al-in-olivine temperatures onto the geotherm (see text). Such depth profiles applied to a large, random sample (e.g., from heavy mineral concentrates) provide an estimate of the sampling behavior of the transporting magma, i.e. kimberlite. The depth profiles can be coupled to compositional parameters, such as Mg# of olivine, here shown as median value and range (if available). Temperatures < 850 °C (or depths < 100 km) are probably not reliable, but have geological meaning as they can indicate the presence of spinel (see Figures 4-6 and 4-7).

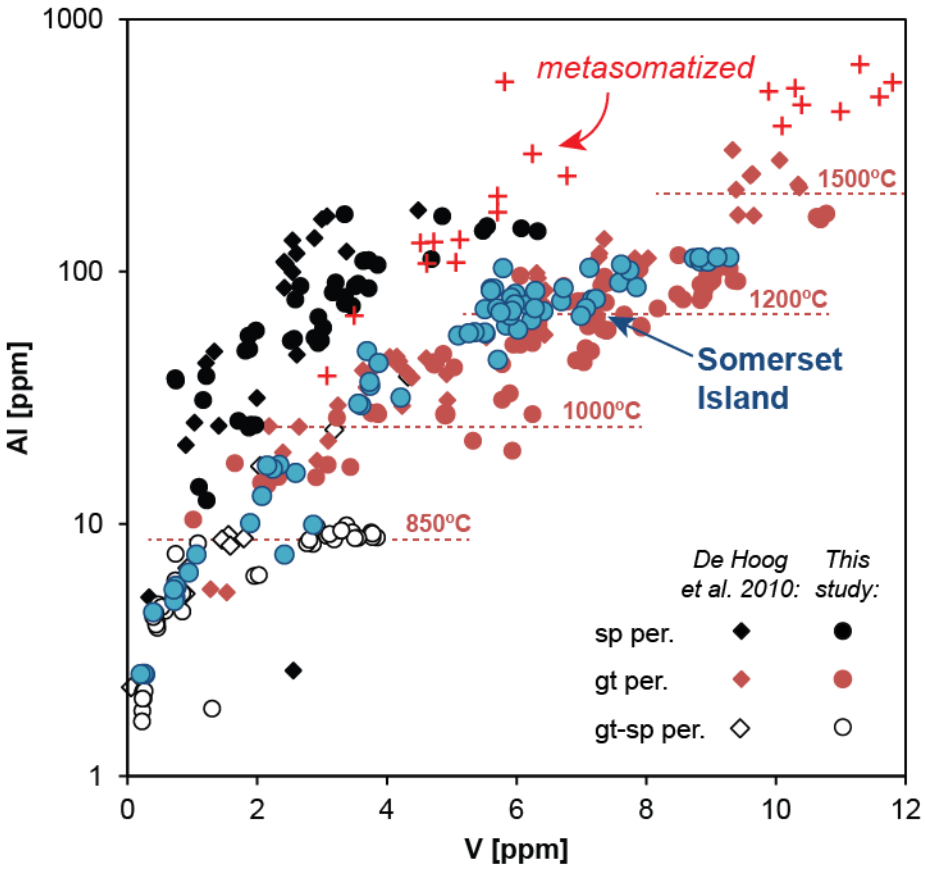

Figure 4-9: Extended Somerset Island olivine dataset (blue circles) plotted onto Figure 4-7 of this study. Most of the data overlap with the garnet-facies trend (dark red symbols) and are thus suitable for the Al-in-thermometer (Equation 3). We recommend excluding data points with < 10 ppm Al, as they cannot be reliably distinguished from olivines from garnet-spinel facies peridotites.

4.11. Extended Analytical Methods

4.11.1. Olivine Standard

The primary reference material, S0355 (alias SC-GB), used for the calibration of Al in experimental olivines by SIMS is a fragment of San Carlos olivine, which serves as a well-characterized in-house secondary standard for microanalysis at the University of Alberta. The original megacryst grain (> 1 cm) originates from a spinel lherzolite from San Carlos, Arizona, USA (e.g., Jagoutz et al. 1979). The olivine standard has been characterized by the following methods at the University of Alberta.

4.11.1.1. Electron Probe Micro Analysis (EPMA)

The standard olivine was analyzed in multiple sessions by Wavelength Dispersive X-Ray Spectroscopy (WDS) using a JEOL 8900 Electron Probe Microanalyzer (EPMA) at the University of Alberta. An accelerating voltage of 20 kV was used in all experiments. For the analysis of Al, a beam current of 50 nA was used on the standard (Frank Smith garnet) and a beam current of 100 nA was used on the olivine. The beam size was 2 μm. The TAPJ detector was used to measure Al. Special attention was given to background limits to avoid peak overlaps. The lower background was 2.6 mm and the upper background 2 mm. Count times on both element peak and backgrounds were 180 s. The ZAF matrix correction was used. In addition to Al_2O_3 to the major oxide components SiO_2, MgO and FeO, the minor components NiO, MnO, CaO, Cr_2O_3, CoO were analyzed. Results (± 2 SD) for the major components of SC-GB are 49.4 ±0.4 wt% MgO, 40.6 ±0.6 wt% SiO_2, and 9.4 ±0.2 wt% FeO. The Al content could be constrained to 0.016 ±0.004 wt% Al_2O_3, or 83 ± 20 ppm Al.

4.11.1.2. Laser Ablation Inductively Coupled Plasma Mass Spectrometry (LA-ICP-MS)

LA-ICP-MS was carried out using a RESOlution M50 ArF 193 nm excimer laser ablation system coupled to a Thermo ELEMENT 2 XR magnetic sector mass spectrometer at the Arctic Resources Laboratory, University of Alberta. The laser ablation system is equipped with a dual volume cell. Helium with a flow rate of 600 mL/min was used as the carrier gas. A 'squid' device was used to smoothen the ablation signal. The laser was operated at a repetition rate of 10 Hz at an output energy of 120 mJ and 26% transmission, resulting in a fluence of ~4.5 J/cm^2 on the target surface. Circular laser spots with a diameter of 130 μm were used for analysis. The ICP-MS was run in 'speed' mode with the AutoLockMass function activated (in low resolution).

Prior to analysis, the Ar plasma was left to stabilize for ~1 hour and then tuned while ablating a 33 μm line on NIST SRM 612 to maximize sensitivity while minimizing oxide production. Optimizing the torch position and gas flows usually resulted in > 250,000 cps on ^{139}La and an oxide production rate (ThO/Th ratio) of < 0.2%. ^{27}Al and ^{51}V (and other elements) were measured on the Secondary Electron Multiplier (SEM). NIST SRM 612 was used as the calibration material. ^{29}Si was used as the internal standard. In medium resolution, NIST SRM 610 (higher element concentrations) was used as the calibration material due to the associated decrease in sensitivity. LA-ICP-MS data reduction was performed using the Iolite software (Paton et al. 2011).

4.11.1.3. Solution Inductively Coupled Plasma Mass Spectrometry (Solution ICP-MS)

An aliquot of the standard olivine SC-GB was crushed with agate pestle and mortar and fresh shards (i.e. free of inclusions) were picked and cleaned in 15% H_2O_2. Three sub-samples of ~100 mg each were dissolved in a 3:1 mixture of HF and HNO_3 at 120°C for ~48 h. After sample dry down in clean lab atmosphere, 1 mL of concentrated HCl was added to break down newly formed fluorides. The samples were dried down again before adding 5 mL of 3% HNO_3 containing 1 ppb In (as the internal standard). This resulted in dilution factors of ~50,000. The samples were analyzed on a Nu Instruments Attom magnetic sector mass spectrometer in the Arctic Resources Laboratory, University of Alberta. ^{27}Al (and other elements) was measured in medium resolution to account for the higher oxide production rate of wet plasma mass spectrometry (ThO/Th ~ 3%) compared to LA-ICP-MS (ThO/Th <0.2%). A multi-element standard solution was used for calibration. Dissolved natural rock standards (OKUM, BIR-1, BHVO-2, BCR-2) were used as secondary standards (see table below). The Al results were generally within 10% of the reported values. The data were processed using an in-house spreadsheet produced by P. Waterton at the University of Alberta.

Measured Al concentrations [ppm] in secondary standards

standard	**OKUM**	**BIR-1**	**BHVO-2**	**BCR-2**
average	38,322	74,827	69,353	67,004
1 σ	2,376	3,562	2,462	2,297
ref. value*	42,181	81,505	71,449	71,449
1 σ	n.a.	1,059	1,059	1,059
accuracy	-9%	-8%	-3%	-6%

**OKUM = IAG; BIR-1, BHVO-2, BCR-2 = GeoReM*

4.11.1.4. Measured Al concentration of S0355 (alias SC-GB)

EPMA	LA-ICP-MS LR	LA-ICP-MS MR	solution ICP-MS	weighted mean
83 ± 20 ppm	85 ± 4 ppm	89 ± 6 ppm	86 ± 7 ppm	**86 ± 3 ppm**

All uncertainties are 2σ.

4.11.2. Secondary Ion Mass Spectrometry (SIMS)

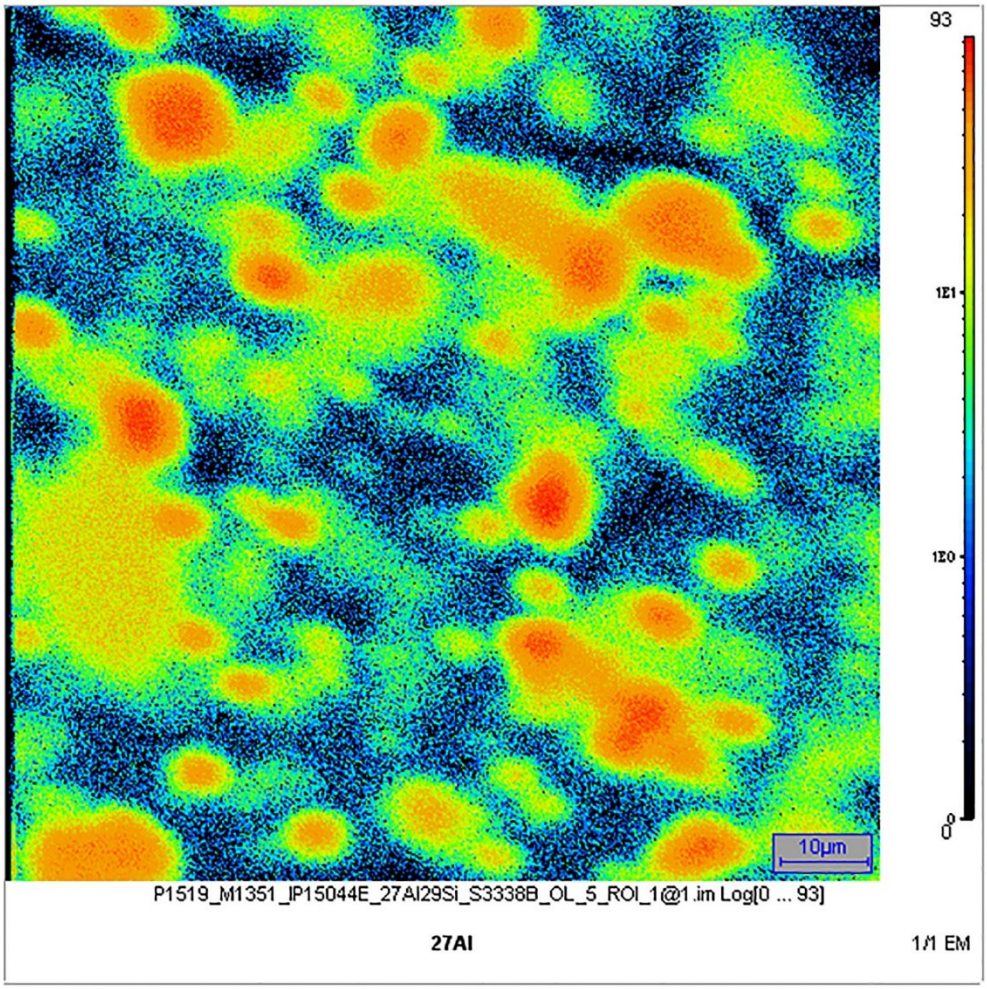

Figure 4-10: Al map obtained by scanning ion imaging of ^{27}Al to help locating olivine (dark blue) in the experimental samples, while avoiding adjacent high-Al minerals such as garnet (bright red). Other phases are clinopyroxene (orange to yellow) and orthopyroxene (green to light blue).

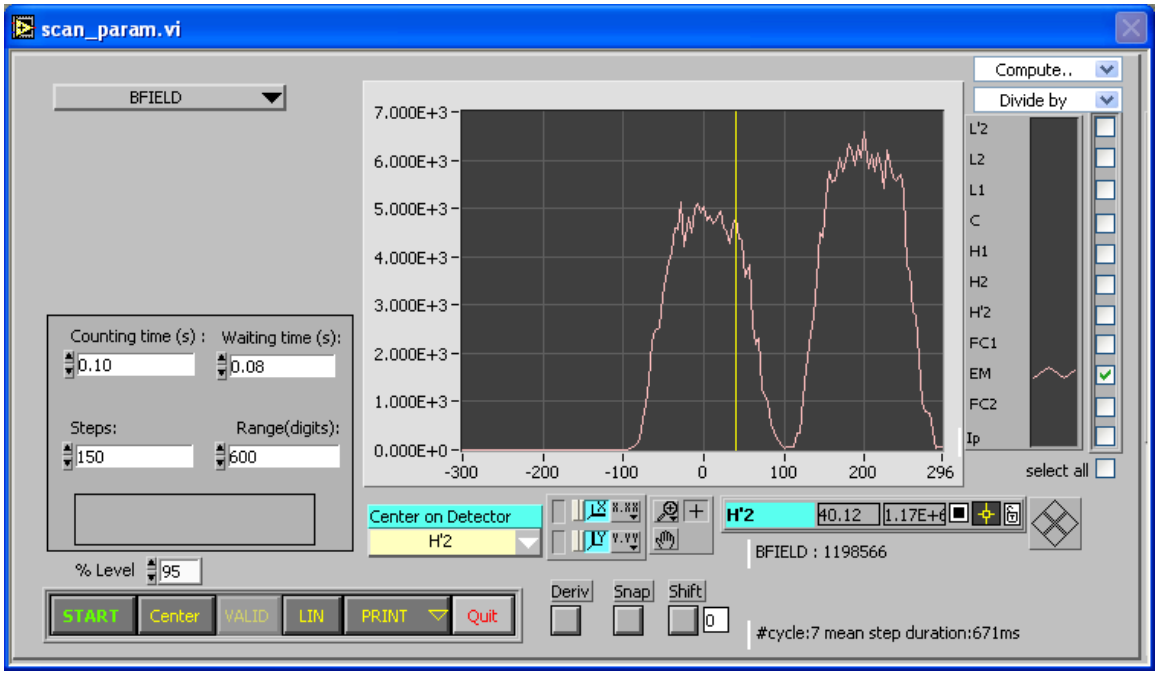

Figure 4-11: Mass scan of $^{27}Al^-$ (left) separated from $^{26}MgH^-$ in olivine S0371 (San Carlos, Fo89.6).

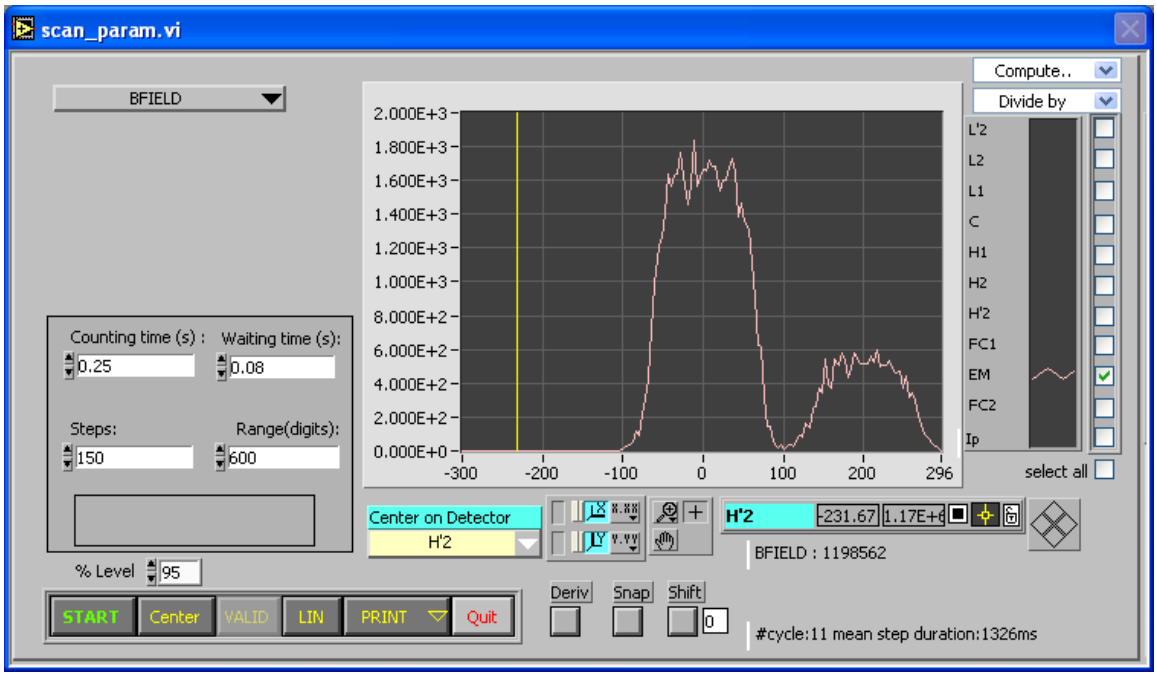

Figure 4-12: Mass scan of $^{27}Al^-$ (left) separated from $^{26}MgH^-$ in olivine S0370 (Fo12.4); note the lower count rate of $^{26}MgH^-$.

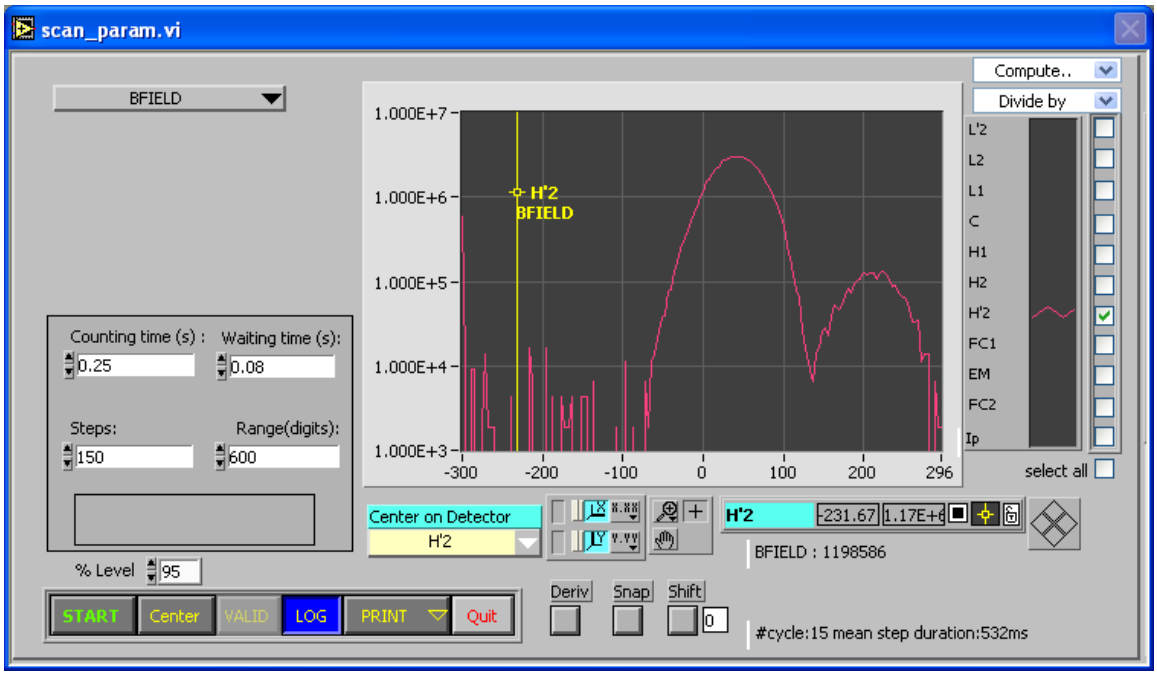

Figure 4-13: Mass scan of $^{29}Si^-$ (left) in S0371 olivine at high mass resolution, showing adjacent $^{28}SiH^-$.

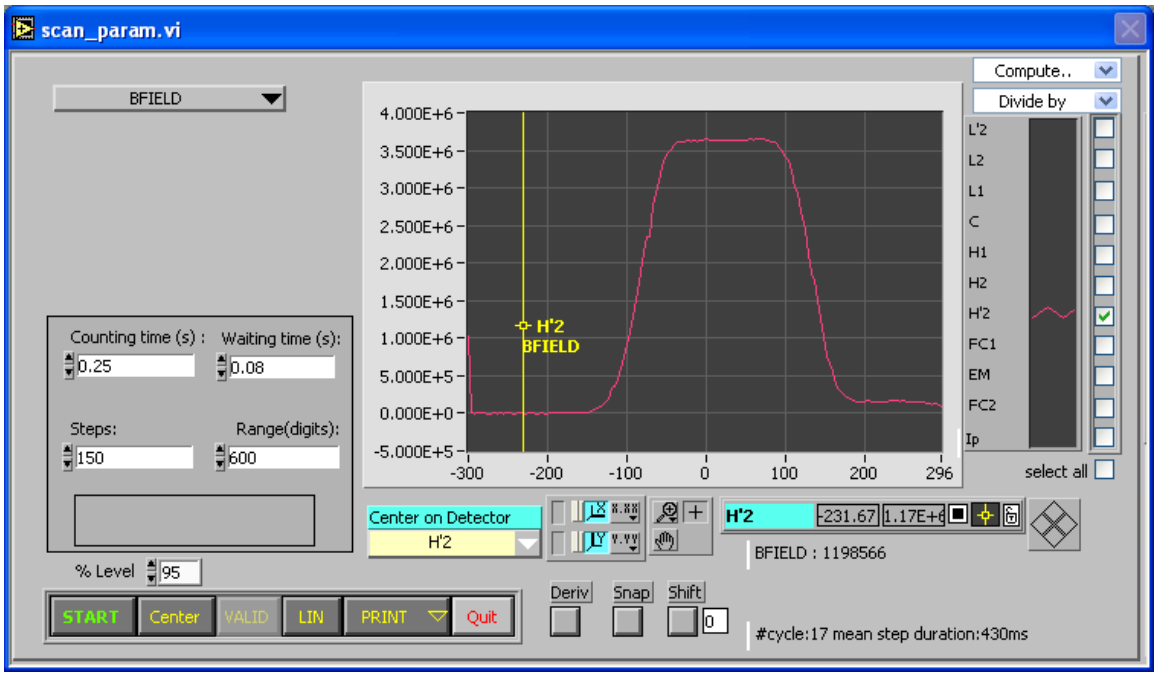

Figure 4-14: Mass scan of $^{29}Si^-$ (left) in S0371 olivine at operational conditions, lower overall resolution, but peak offset (zero point in x-axis) to achieve separation.

4.11.3. LA-ICP-MS on Natural Olivines

The olivines from peridotite xenoliths derived from kimberlites from Diavik, Jericho, and Somerset Island (Appendix A4.4.), were mounted in epoxy and polished. Trace elements (here, Al and V) were measured by LA-ICP-MS at the Geological Survey of Canada. An Analyte 193 laser ablation sampler (Photon Machines Inc.), based on an ArF excimer laser (193 nm), coupled to an Agilent 7700x quadrupole ICP-MS was used. The ICP-MS was run in its standard configuration with addition of a second interface rotary pump, which approximately doubles instrument sensitivity. Helium was used as the carrier gas to transport ablated material from the laser cell to the ICP-MS. A laser spot size of 86 µm was used. The energy density (fluence) was ~5 J/cm^2. GSE-1G was used as the calibration material. GSD-1G, BCR-2G, and two in-house olivine standards were analyzed as unknowns (secondary standards). The data were processed using the GLITTER software (Griffin et al. 2008). Al and V results for the secondary standards were consistently within < 10% of the recommended values. Reproducibility on the natural olivines for both Al and V was usually better than 10%, based on repeated analyses on different grains from the same sample.

Additional LA-ICP-MS on natural olivines (e.g., from Fiji and Kimberley, see Extended Data) was performed at the University of Alberta following the analytical protocol for the olivine standard described above. It should be noted that at sufficiently large spot sizes (86 to 130 µm) fractionation effects between the different calibration materials (GSE-1G and NIST SRM 612) and olivine are small (manuscript in preparation, see Chapter 5). The results for Al and V from the different analytical sessions in different labs should thus be comparable.

5. Strategies for Trace Element Analysis of High-Mg Olivine by LA-ICP-MS – Characterization of Olivine Standards for Matrix-Matched Calibration

Y. Bussweiler*[a], A. Giuliani[b], A. Greig[b], B. A. Kjarsgaard[c], S. E. Jackson[c], D. G. Pearson[a], T. Stachel[a], Y. Luo[a]

[a)] Department of Earth and Atmospheric Sciences, University of Alberta, 126 ESB, Edmonton, AB T6G 2E3, Canada

[b)] The University of Melbourne, School of Earth Sciences, Parkville 3010 VIC Australia

[c)] Geological Survey of Canada, 601 Booth Street, Ottawa, ON, Canada K1A 0E8

5.1. Abstract

The trace element composition of olivine is becoming increasingly important in petrological studies due to its ubiquity in the Earth's upper mantle and primitive magmatic rocks. The LA-ICP-MS method allows for the routine analysis of trace elements in olivine to sub-ppm levels but comes with a number of analytical challenges. A major drawback is the lack of a matrix-matched standard for olivine. Matrix-matched calibration is necessary due to significant differences in laser-induced inter-element fractionation between olivine and calibration materials. This can result in inaccuracies when using common calibration materials, such as NIST SRM 612. Other calibration materials, such as the USGS basalt glasses GSD-1G and GSE-1G, can introduce high backgrounds for certain elements of interest in olivine, especially Al which is an important element in olivine for thermometry applications. Here, we document these analytical challenges and present LA-ICP-MS results for two Mg-rich olivine standards (SC-GB and 355OL) from three different laboratories, each using slightly different instruments and analytical protocols. These natural olivine samples can be used 1) as secondary standards to assess the accuracy of results, and 2) as primary standards for the matrix-matched calibration of olivine analysis. We show that matrix-matched calibration is essential when using small laser spot sizes (< 100 µm). If matrix-matched calibration is not feasible, large laser spot sizes (≥ 100 µm) are recommended in order to minimize fractionation effects between olivine and silicate glass reference materials.

5.2. Introduction

Olivine is the dominant mineral of the upper mantle (e.g., Ringwood, 1966), the most common mineral inclusion in lithospheric diamonds (Meyer and Boyd 1972; Stachel et al. 2005), and the major constituent of deep-seated primitive volcanic rocks (Sobolev et al. 2005; De Hoog et al. 2010; Foley et al. 2013). Because of the petrological importance of olivine it is critical to find additional ways of probing its petrological history via trace elements. The concentration of Al in olivine, for example, has recently received considerable interest, as it can be used to estimate equilibration temperatures for different settings (Wan et al. 2008; De Hoog et al. 2010; Coogan et al. 2014). Recent studies have applied Al-in-olivine thermometry to komatiites (Waterton et al. 2016), as well as to the mantle cargo of kimberlites (Bussweiler et al. 2017, Chapter 4). Moreover, the minor and trace element composition of magmatic olivine can be used as an indicator for different petrogenetic processes (e.g., Sobolev et al. 2005; Ammannati et al. 2016; Weiss et al. 2016; Zhang et al. 2016).

Much of the groundwork to the understanding of minor and trace element chemistry of olivine has been compiled by De Hoog et al. (2010) and Foley et al. (2013). The incorporation of trace elements into olivine is limited by its simple crystal structure and major element composition, with most olivines consisting to > 99 wt% of MgO, SiO_2 and FeO. For olivine from mantle peridotites, the few additional elements that are incorporated into olivine can be divided into three groups (De Hoog et al. 2010): Group I elements (e.g., Ni, Mn, and Co) are the most compatible in olivine being mostly divalent with ionic radii close to that of Mg; Group II elements (e.g., Cr, Al, V, Ca, and Na) are mainly controlled by equilibration temperature and pressure, as well as oxygen fugacity; Group III elements (e.g., Ti, Y, and Zr) show the largest concentration ranges in olivine and are strongly dependent on bulk rock contents and metasomatic overprinting.

Laser ablation inductively coupled plasma mass spectrometry (LA-ICP-MS) allows to routinely quantify a large range of elements in silicate minerals (Heinrich et al. 2003; Günther and Hattendorf 2005). However, while some problems associated with LA-ICP-MS analysis of olivine, such as major isobaric interferences, have been addressed in the literature (e.g., Foley et al., 2011), a more detailed discussion of the analytical challenges and the effects on accuracy is still missing. A major problem with trace element measurements of olivine by LA-ICP-MS is the

lack of a matrix-matched olivine standard (Figure 5-1). Matrix-matching is not always necessary when applying LA-ICP-MS to geological samples (Jackson 2008). This is due to the use of an internal standard (e.g., ^{29}Si) and similar fractionation behavior of the elements of interest (relative to the internal standard) in both the geological sample and the calibration material, especially when deep UV (i.e., 193 nm) lasers are used (Günther et al. 1997). However, for olivine, this similarity has not yet been tested.

Calibration materials routinely employed for LA-ICP-MS analyses of silicate minerals are silicate glasses, such as the NIST SRM 61X series (e.g., Kane 1998). These glasses have significantly higher SiO_2, Na_2O and CaO, but lower MgO contents than olivine (Figure 5-1). Alternatively, USGS glasses with basaltic compositions, such as GSD-1G, can be used (e.g., Guillong et al. 2005). However, these glasses have significantly higher Al_2O_3 contents which can produce background problems when measuring Al concentrations in olivine. The same holds true for the basaltic reference glasses BCR-2G and BHVO-2G (Figure 5-1). A particular problem with analyzing minor elements in olivine, such as Ni and Mn, by LA-ICP-MS, is that these elements are present only at trace amounts in the commonly used reference materials. This can lead to large calibration errors. Recent studies investigating inter-elemental fractionation effects during LA-ICP-MS analysis have found that in addition to chemical matrix matching, choosing calibration materials with similar transparency as the sample is equally important (e.g., Gaboardi and Humayun 2009; Czas et al. 2012).

The aim of this study is to optimize analytical protocols for the quantification of trace element concentrations in olivine by LA-ICP-MS, with a particular focus on calibration strategies. We take a comparative approach by using different analytical methods, including electron probe micro analysis (EPMA), LA-ICP-MS and solution ICP-MS, carried out in three different laboratories at the University of Alberta, the University of Melbourne, and the Geological Survey of Canada. Two natural olivine grains (SC-GB and 355OL) are characterized with the aim of being employed as in-house standards. These olivine standards are applicable as secondary standards and can also be used as primary calibration materials for the matrix-matched LA-ICP-MS analysis of olivine. Although the new standards cannot be distributed on a large scale (due to limited material), they can be used for reliable characterization of new natural olivine standards.

5.3. Samples and Characterization by EPMA and Solution ICP-MS

The two fragments of San Carlos olivine (SC-GB and SC-BK) used in this study originate from a single megacrystic grain (> 1 cm) extracted from a spinel lherzolite from San Carlos, Arizona, USA (e.g., Jagoutz et al. 1979). The two fragments were characterized by different methods at the University of Alberta, University of Melbourne, and Geological Survey of Canada.

SC-GB and SC-BK were analyzed in multiple sessions by wavelength dispersive X-ray spectroscopy (WDS) using a JEOL 8900 electron probe microanalyzer (EPMA) at the University of Alberta. An accelerating voltage of 20 kV was used in all analytical sessions. Depending on element concentration, a beam current of 20, 50, 70 or 100 nA was applied to the reference materials, whereas a constant beam current of 100 nA was used on the olivine samples. The beam size was 2 μm with the exception of the Na standard (albite), for which a defocused (10 μm) beam was used to minimize Na mobilization. Special attention was given to background limits to avoid peak overlaps. Count times on both element peak and backgrounds were increased for the minor elements. The ZAF matrix correction was used. In addition to the major oxide components SiO_2, MgO and FeO, the minor components NiO, MnO, CaO, Cr_2O_3, Al_2O_3, CoO were analyzed. Preliminary measurements of Na_2O, P_2O_5, and TiO_2 yielded concentrations consistently below the detection limits and, therefore, these elements were excluded from the measuring method. Measuring conditions and standards for the different sessions were varied slightly. The optimized conditions are given in Appendix A5.1. Other studies have reported methods that can measure components beyond CoO (e.g., TiO_2, ZnO, P_2O_5, and Na_2O). For example, Batanova et al. (2015) suggested using high accelerating voltages (25 kV or higher) along with high beam currents (900 nA) on the olivine samples. However, these extreme analytical conditions can damage the beam alignment of the instrument, or cause damage to the sample because of excessive heating (A. Locock, pers. comm). Korolyuk and Pokhilenko (2014) described a method in which the major components are measured separately in order to attribute more time to the subsequent analysis of minor and trace components. Here, we followed a method that allows for the analysis of a range of components with a single measurement.

The various analytical sessions were screened separately for outliers (using a Median Absolute Deviates (MAD) filter) and then treated as a single session to calculate a mean value with uncertainties (2 SD). Thus, the uncertainties represent the repeatability of the measurements

within our laboratory. No significant differences were found between the two separate fragments (SC-GB and SC-BK). For simplicity, we therefore treat the two fragments as one grain labeled SC-GB. The major element composition of SC-GB (with 2 SD) is as follows: 49.4 ±0.4 wt% MgO, 40.6 ±0.6 wt% SiO_2, and 9.4 ±0.2 wt% FeO. The corresponding Mg# (Mg/(Mg+Fe)) is 90.3 ±0.3. The minor to trace element composition of SC-GB (with 2 SD) is: 0.39 ±0.02 wt% NiO, 0.137 ±0.005 wt% MnO, 0.077 ±0.003 wt% CaO, 0.022 ±0.005 wt% Cr_2O_3, 0.016 ±0.004 wt% Al_2O_3 (or 83 ± 20 ppm Al), and 0.015 ±0.003 wt% CoO.

An aliquot of the standard olivine SC-GB was crushed with agate pestle and mortar, and fresh shards (i.e. optically free of mineral and fluid inclusions) were picked and cleaned in 15% H_2O_2. Although the standard olivine appeared macroscopically clear, fluid and mineral inclusions were detected during crushing and these smaller fragments were excluded. This highlights the necessity for careful screening of the ablation signal for inclusion peaks when using LA-ICP-MS. Three sub-samples of the crushed material weighing ~100 mg each were dissolved in a 3:1 mixture of HF and HNO_3 at 120°C for ~ 48 h. After sample dry down in a Class 10 laminar flow hood, 1 mL of concentrated HCl was added to break down newly formed fluorides. The samples were dried down again before adding 5 mL of 3% HNO_3 containing 1 ppb In (as the internal standard). This resulted in dilution factors of ~50. The samples were analyzed on a Nu Instruments Attom magnetic sector ICP mass spectrometer in the Arctic Resources Laboratory, University of Alberta. The isotopes ^{7}Li, ^{23}Na, ^{27}Al, ^{43}Ca, ^{45}Sc, ^{49}Ti, ^{51}V, ^{53}Cr, ^{55}Mn, ^{59}Co, ^{60}Ni, ^{63}Cu, and ^{71}Ga, were all measured in medium resolution ($m/\Delta m \sim 3000$) to account for the higher oxide production rate of wet plasma mass spectrometry (ThO/Th ~ 3%) compared to LA-ICP-MS (ThO/Th <0.2%). Importantly, measuring in medium mass resolution should screen out an interference of $^{29}Si^{16}O$ on ^{45}Sc which requires $m/\Delta m$ of ~ 2900 to be resolved. A multi-element standard solution was prepared for calibration. Dissolved natural rock standards (OKUM, BIR-1, BHVO-2, BCR-2) were used as secondary standards. The results were generally within 10% of the reported values.

At the University of Melbourne, two in-house olivine standards are used. ALM-2 is a gem-quality olivine from the Almklovdalen Mine, Norway (courtesy of W.L. Griffin). Several grains of olivine (355OL) were extracted from the garnet harzburgite xenolith XM1/355, which was entrained by the Bultfontein kimberlite, South Africa. Detailed SEM imaging reveals that ALM-2 olivine contains sub-micron sized exsolutions of chromite. In addition, ALM-2 olivine hosts

very small concentrations (usually <10 ppm) of key trace elements (e.g., Na, Al, P). The 355OL grain was therefore found to be better suited as a primary standard due to higher concentrations and more homogeneous distribution of trace elements.

5.4. Laser Ablation Inductively Coupled Plasma Mass Spectrometry

Analytical conditions – University of Alberta: LA-ICP-MS measurements were carried out using a RESOlution M50 ArF 193 nm excimer laser ablation system (24 ns pulse width) coupled to a Thermo Scientific ELEMENT XR II magnetic sector mass spectrometer in the Arctic Resources Laboratory. The laser ablation system is equipped with a dual volume cell. Helium with a flow rate of 600 mL/min was used as the carrier gas. A SQUID device was used to smooth the ablation signal (Müller et al. 2009). The laser was operated at a repetition rate of 10 Hz at an output energy of 120 mJ and 26% transmission, resulting in a fluence of ~4.5 J/cm^2 on the target surface. Different spot sizes were tested, using circular spots with diameters of 33, 75, 130, and 193 μm. The ICP-MS was run in low resolution, m/Δm = 300 (in 'speed' mode with the AutoLockMass function activated). Prior to analysis, the Argon plasma was left to stabilize for ~1 hour and then tuned while ablating a 33 μm line on NIST SRM 612 to maximize sensitivity while minimizing oxide production. Optimizing the torch position and gas flows usually resulted in > 300,000 cps on ^{139}La and an oxide production rate (ThO/Th ratio) of < 0.2%. The following isotopes were measured: ^{7}Li, ^{23}Na, ^{25}Mg, ^{27}Al, ^{28}Si, ^{29}Si, ^{31}P, ^{43}Ca, ^{44}Ca, ^{45}Sc, ^{47}Ti, ^{51}V, ^{53}Cr, ^{55}Mn, ^{57}Fe, ^{59}Co, ^{60}Ni, ^{63}Cu, ^{66}Zn, ^{71}Ga, ^{88}Sr, ^{89}Y, ^{90}Zr, ^{93}Nb, ^{140}Ce, and ^{145}Nd. All isotopes were measured in 'triple' detector mode, so that the signal would be diverted from the Secondary Electron Multiplier (SEM) to the Faraday Cup once a threshold of 10^9 counts is passed. The following isotopes were measured, in separate runs, in medium resolution (m/Δm = 4000): ^{27}Al, ^{29}Si, ^{45}Sc, ^{59}Co, ^{60}Ni, ^{63}Cu, ^{66}Zn, and ^{69}Ga. Measuring in medium resolution mode incurs a sensitivity loss, relative to low resolution, of a factor of ~10.

Different calibration materials were tested, including the NIST SRM 610 and SRM 612 silicate glasses, and the USGS basalt glasses GSD-1G, and GSE-1G. ^{29}Si was used as the internal standard when calibrating with NIST glasses, and ^{25}Mg was used when calibrating with GS glasses. In medium resolution sessions, NIST SRM 610 (higher element concentrations) was used as the calibration material due to the associated decrease in sensitivity. Various secondary standards were employed, including NIST SRM 614, BCR-2G, and BIR-1G. Eventually, the

latter two were omitted because they were found to produce high Al backgrounds. LA-ICP-MS data reduction was performed using the Iolite software (Paton et al. 2011).

Analytical conditions – Geological Survey of Canada: The standard olivines SC-GB and 355OL were also analyzed by LA-ICP-MS at the Geological Survey of Canada. An Analyte (Photon Machines Inc.) ArF 193 nm excimer laser ablation sampler (4 ns pulse width) coupled to an Agilent 7700x quadrupole ICP-MS was used. The ICP-MS was run in its standard configuration with addition of a second interface rotary pump, which approximately doubles instrument sensitivity. All tubing was replaced before analysis to eliminate memory effects. Helium was used as the carrier gas to transport ablated material from the laser cell to the ICP-MS. A SQUID device was utilized. Laser spot sizes of 30, 65, 86 and 135 μm were used. The energy density (fluence) was ~4.5 J/cm^2. The laser repetition rate was 10 Hz. Both GSD-1G (with ^{25}Mg as internal standard), and NIST SRM 612 (with ^{29}Si as internal standard) were used for calibration. GSD-1G, BCR-2G, and two in-house olivine standards were analyzed as unknowns (secondary standards). The data were processed using the GLITTER software (Griffin et al. 2008). Results for the secondary standards were consistently within 10% of the recommended values.

Analytical conditions – University of Melbourne: At the University of Melbourne a 193 nm ArF Excimer laser (24 ns pulse width) coupled to an Agilent 7700x quadrupole was used. The laser was operated at 5 Hz with a fluence of ~4 J/cm^2. Different spot sizes, 26, 50, 104 μm, were tested. Backgrounds (gas blanks) were measured before each analysis for 50 s, followed by 50 s ablation time, and 15 s washout time. Oxide and doubly-charged ion production was usually ~0.2 %. BHVO-2G and NIST SRM 612 were used as the routine calibration materials with ^{29}Si as the internal standard. The in-house standard olivine 355OL was used for calibration as well.

5.5. Results and Discussion

The results from the three laboratories, using different methods, for the olivines SC-GB and 355OL are summarized in Appendix A5.2. and A5.3., respectively. In general, the minor and trace element concentrations of SC-GB olivine obtained using the different measurement methods at the University of Alberta are in good agreement (Figure 5-2). For LA-ICP-MS analyses, however, large downhole fractionation effects between the calibration material and olivine were observed. These fractionation effects are dependent on laser spot size and become increasingly severe at small spot sizes (< 100 μm). This effect appears to be more severe in

olivine than in NIST glass or other silicate minerals, such as garnet or pyroxene (e.g., Norman et al. 1996). The observed fractionation effects are also a function of laser energy on target (fluence), repetition rate, and ablation time. Calibration issues can arise when using conventional LA-ICP-MS calibration materials (e.g., NIST glasses), especially for the minor elements in olivine. Moreover, certain calibration materials can create high backgrounds in elements of interest that are present only at trace amounts in olivine (e.g., Al). Finally, the olivine reference materials themselves (e.g., SC-GB) can display small-scale heterogeneity in trace elements, i.e. natural zoning, which requires caution when using olivine as the primary calibration material. Each of these issues will be addressed in detail in the following sections.

5.5.1. Limits of Detection and Palette of Accessible Elements

Figure 5-3 shows a plot of all elements analyzed in SC-GB, sorted by concentration, along with their limits of detection (LOD), as measured by LA-ICP-MS at the University of Alberta (130 μm laser spots, calibrated with NIST SRM 612). Element concentrations down to ~0.004 ppm (e.g., Sr) can be detected and quantified with the instrumental setup at the University of Alberta. Rb and Ba are problematic because measured concentrations are often below LOD, even at large laser spot sizes. These elements were eventually excluded from the measuring method. However, including them in the method may be useful, for example, to indicate alteration in mantle olivines. Nb, La, and Ce appear to be accessible by LA-ICP-MS, being present above their LODs. However, within a given session, their concentrations were found to be quite variable (relative standard deviations > 100%), often being present just above their LODs (i.e. not above limits of quantitation). Moreover, when using laser spot sizes smaller than 130 μm, these elements also fall below their LODs. Thus, we conclude that measuring rare earth elements (REE) in mantle olivines at spot sizes of ≤ 130 μm is not feasible by current LA-ICP-MS instruments. It should be noted that using even larger spot sizes than 130 μm, in an attempt to improve LODs, does not minimize fractionation effects (see below), and may further lead to "mass load" issues (Kroslakova and Guenther 2007); It has been shown that larger quantities of ablated material can lead to higher backgrounds and memory effects, and affect plasma conditions (e.g., temperature) which may lead to reduced count rates (Jenner and O'Neill 2012; and references therein). Moreover, using such large spot sizes on natural olivines is often not possible due to their limited grain size or the presence of inclusions.

5.5.2. Downhole Fractionation Effects

Inter-elemental downhole fractionation describes the variable behavior of different isotopes (and therefore elements) during deepening of the laser ablation pit (e.g., Fryer et al. 1995). Downhole fractionation becomes especially problematic when the behavior of the calibration material is different from that of the sample (e.g., Jackson 2008). Ideally, downhole fractionation is minimized by employing matrix-matched calibration materials.

In order to determine which calibration material is most appropriate for the analysis of olivine, we calculated fraction factors for NIST SRM 612, GSD-1G, and the standard olivine SC-GB at different spot sizes. Fractionation factors are a measure of the fractionation of a given isotope during ablation relative to an internal standard, such as ^{29}Si (Fryer et al. 1995). They are calculated by dividing the average of the second half of the ablation signal by the average of the first half of the ablation signal. For NIST SRM 612 the internal standard used is ^{29}Si, for GSD-1G ^{25}Mg is used. For olivine, no major differences were found between the two internal standards (here, results using ^{29}Si are presented). If the fractionation factor is equal to 1, the isotope of interest behaves exactly like the internal standard during ablation. If the fractionation factor differs significantly from 1, downhole fractionation is likely to occur. Clearly, for obtaining the most accurate data, the factors of a given element should have similar magnitude for olivine and the calibration material.

5.5.2.1. Fractionation Factors

For a laser spot size of 130 µm, using the RESOlution M50 laser ablation system at the University of Alberta (~4.5 J/cm^2, 10 Hz, 45 s ablation time) the observed fractionation factors for elements from Li to Ga are close to 1, for both calibration materials (NIST SRM 612 and GSD-1G) and olivine (Figure 5-4). For Al, however, the fractionation factor for GSD-1G is lower (~1.0) than the fractionation factors for NIST SRM 612 and olivine (the latter two being ~1.1). Similar trends are observed for the elements Ti and Zn. When decreasing the spot size to 75 µm, the fractionation factors for olivine increase drastically for Li to Ti, and for Cu, Zn, and Ga (Figure 5-4). The reference material NIST SRM 612 appears to follow this behavior more so than GSD-1G. This may be due to the fact that NIST SRM 612 has a similar transparency to that of the high-Mg olivine (SC-GB) and thus behaves similarly during ablation. For even smaller spot sizes (33 µm) the fractionation factors for most elements in olivine become extremely high,

e.g., up to ~1.8 for Na (Figure 5-4). For the University of Alberta laser ablation system, the difference in fractionation factors between olivine and the calibration materials is highest for the elements Na, Ti, Cu, and Zn (Figure 5-6). Only the elements V, Cr, and Mn retain a broadly similar behavior in olivine as in the calibration materials NIST SRM 612 and GSD-1G at such small spot sizes.

5.5.2.2. Ablation Pit Geometries

The observed elemental fractionation effects are reflected in the geometry of the ablation pits in the in-house olivine standard SC-GB compared to the reference glass NIST SRM 612 (Figure 5-5). The pits were imaged in BSE 'topo' mode using the electron microprobe. The depth could be measured using the optical focus of the probe (with standard deviations from measurements on three different pits). The crater depth could not be reliably obtained for the smallest spot sizes (33 µm) due to insufficient light in the optical view of the EPMA.

A first order observation is that pits in NIST SRM 612 maintain flat-bottom craters down to small spot sizes (although they become more oval in shape) (Figure 5-5). In contrast, the pits in SC-GB olivine appear to show more fragmentation along crater walls for large spot sizes (193 µm), and increased melting at small spot sizes, leading to the formation of a plate-shaped "melt disk" at 33 µm (Figure 5-5). Moreover, a considerable degree of deformation of the olivine crystal around the ablation spot is observed at 33 µm. For the 193 µm ablation pits, the depth was measured to be 44 ±2 µm for SC-GB olivine and 53 ±3 µm for NIST SRM 612. For 130 µm ablation pits, the depths are 51 ±2 µm and 50 ±2 µm, respectively. This implies a larger increase in the depth/diameter ratio for olivine with decreasing spot size.

A similar trend of deteriorating geometries with decreasing spot size has been described for zircon (Pearson et al. 2013). These authors described the build-up of prominent crater walls around the ablation pit, on the surface of the grain, due to the addition of melt extruded from the pit. This melting effect was more pronounced for small spot sizes, and thus replicates the effects observed here. Importantly, the deterioration of pit geometry and increased melt build-up was associated with a decay of signal intensity with time, ultimately leading to greater fractionation effects for smaller spot sizes.

5.5.2.3. Underlying Reasons for Spot Size-Dependent Fractionation

We have observed differences in the ablation behavior of high-Mg olivine and silicate glasses (e.g., NIST SRM 612, GSD-1G) that are negligible at large spot sizes (e.g., 130 μm), but become severe at small spot sizes (< 100 μm) (Figure 5-4). In general, the difference in ablation behavior of different materials (e.g., olivine vs. silicate glasses) is governed by their different chemical, physical and optical properties (Jackson 2008). Even if the same laser conditions (e.g., fluence, repetition rate, spot size, laser focus) are employed to measure calibration material and unknown, this will result in differences in the amount and physical form (e.g., particle size in the aerosol) of the ablation product, ultimately resulting in inaccurate estimates of element concentrations. Previous studies have found that elemental fractionation is a function of ablation pit geometries and increases with increasing depth/diameter ratios (e.g., Mank and Mason 1999). Olivine shows a larger increase in the depth/diameter ratio from 193 to 130 μm, compared to NIST SRM 612 (Figure 5-5), and this trend probably holds true at even smaller spot sizes. Moreover, an increasing degree of fractionation, evident from calculated fractionation factors (Figure 5-4), appears to be directly related to an increase in melting of olivine at decreasing laser spot sizes (Figure 5-5). The elemental fractionation effects caused by increased melting of olivine at small laser spot sizes can be expected to be amplified for elements with volatilities vastly different from that of the internal standard (here, Si) (Jackson 2008; their Figure 11-4). While this is true for elements such as Zn, Na, and Cu (all having higher condensation temperatures than Si), it does not explain the fractionation observed for the elements Co, Ti, and Mn (having similar condensation temperatures to Si). Regardless of the ultimate mechanism of downhole fractionation, the spot size-dependent fractionation can have a significant effect on the measured concentrations of these elements (see below).

5.5.2.4. Effect of Spot Size-Dependent Fractionation on Element Concentrations

In order to evaluate the effect of spot size-dependent fractionation on element concentrations measured in olivine, the standard olivine SC-GB was analyzed at three different laboratories using different laser spot sizes and calibration materials (Figures 5-6 and 5-7). 193 nm excimer lasers were used in all experiments. The available spot sizes varied slightly because they are defined by the specific instrumental setup of the respective laboratories.

At the University of Melbourne (UofM) the silicate glasses NIST SRM 612 and BHVO-2G as well as the standard olivine 355OL were used for calibration, with ^{29}Si as the internal standard. A 24 ns pulse width laser was used, fired at 5 Hz. At the Geological Survey of Canada (GSC) NIST SRM 612 and GSD-1G were used for calibration, with ^{29}Si and ^{25}Mg as the internal standard, respectively. Here, the laser pulse width was shorter (~4 ns) but the repetition rate was higher (10 Hz). At the University of Alberta (UofA) NIST SRM 612 (with ^{29}Si as internal standard) and GSD-1G (with ^{25}Mg as internal standard) were used for calibration, using a 24 ns laser pulse width laser, fired at 10 Hz.

As a first order observation, fractionation effects are evident for many elements in the data from all three laboratories, regardless of whether NIST SRM 612, GSD-1G, or BHVO-2G are used for calibration (Figure 5-6, Figure 5-7). The fractionation effects are most pronounced in the UofA dataset. This can be attributed to the laser parameters used; the combination of long pulse width (24 ns) and high repetition rate (10 Hz) can be expected to lead to larger degrees of "misbehavior" of the olivine with respect to the silicate glasses used for calibration. In addition, higher repetition rates can lead to increased elemental fractionation inside the plasma due to mass loading effects (e.g., Guillong et al. 2003; Fietzke and Frische 2016).

The general trend of spot sizes versus elemental concentration is in agreement with the fractionation factors calculated using the University of Alberta data (Figure 5-4). Results from all three laboratories show an increase in Ni and Co (i.e., too high concentrations) with decreasing spot sizes, which relates to fractionation factors that are larger in olivine than in the respective calibration material. Only the elements Mn, Cr, and V show a reversed trend, when calibrated with NIST SRM 612 or GSD-1G (Figure 5-6, Figure 5-7), which is in accordance to smaller fractionation factors in olivine than in the calibration materials for these elements (Figure 5-4). At the University of Alberta, fractionation effects on elemental concentrations are largest for the elements Zn and Na, resulting in deviations of up to ~40% from the preferred values. This is likely due to the volatile nature of these two elements. For Al, it should be noted that the concentrations obtained at large spot sizes (> 100 µm) using NIST SRM 612 show good agreement among the different laboratories. The results also overlap the preferred value obtained by solution ICP-MS (~86 ppm; see Appendix A5.2.).

An important observation is that fractionation effects are minimized for virtually all elements when olivine is used for calibration (see 355OL in the UofM dataset; Figure 5-6, Figure 5-7). Therefore, matrix-matched calibration has the potential to be a successful approach for obtaining more reliable trace element data at small laser spot sizes in olivine. However, careful characterization of the natural olivines, preferably using different independent methods, is an important prerequisite for employing them as primary calibration materials for LA-ICP-MS.

5.5.3. Calibration Effects

In addition to laser spot size-dependent fractionation effects, the trace element composition of the chosen calibration materials can lead to inaccuracies, if the composition is vastly different from that of olivine. In order to determine which calibration material is most suitable for the analysis of olivine, the silicate glasses NIST SRM 612, GSD-1G, as well as the standard olivines SC-GB and 355OL (at the University of Melbourne), were used for standard bracketing. The results were compared to those from other methods, where available (Figure 5-8).

Minor elements in olivine, such as Ni and Mn, have concentrations > 1000 ppm, but are present only at trace amounts in the commonly used reference materials (e.g., 38.8 ppm Ni and 38.7 ppm Mn in NIST SRM 612; 58 ppm Ni and 220 ppm Mn in GSD-1G; GeoRem database (Jochum et al. 2005; Jochum et al. 2011)). Because the measured values lie far outside of the calibration range, this can lead to large calibration errors. For Ni, this is especially evident for LA-ICP-MS using NIST SRM 612 as the calibration material; the resulting concentration is significantly higher than for all other methods (Figure 5-8). For Mn, LA-ICP-MS values calibrated both with NIST SRM 612 and GSD-1G are significantly higher than the solution value, most likely because of calibration errors (Figure 5-8). In the case of Ca, concentrations are significantly higher in the calibration materials (e.g., 11.9 wt% CaO in NIST SRM 612, and 7.2 wt% in GSD-1G; GeoRem database (Jochum et al. 2005; Jochum et al. 2011)) than in olivine (<500 ppm). This difference may also lead to large calibration errors, especially when Ca backgrounds are variable during analysis. This may explain why Ca results for olivine obtained with LA-ICP-MS in this study are lower than those obtained with solution ICP-MS and EPMA measurements (Figure 5-8). When the concentrations of an element in olivine and the calibration material converge (e.g., Cr and Co) the calibration effects are minimized and the LA-ICP-MS results become more accurate and precise than the EPMA results (Figure 5-8). The fact that Cr

concentrations are higher when measured by solution ICP-MS (Figure 5-8) could indicate the presence of submicroscopic inclusions of chromite in SC-GB that are more likely to be avoided when using microanalytical methods (i.e. LA-ICP-MS and EPMA). For Al, the low resolution LA-ICP-MS values calibrated with NIST SRM 612 are consistent with results from medium resolution LA-ICP-MS, solution ICP-MS, and EPMA results, whereas calibration with the GSD-1G reference material yields significantly lower concentrations (Figure 5-8). This can be attributed either to the different transparency of GSD-1G and high-Mg olivine, or to the fact that the Al content of GSD-1G is ~4 orders of magnitude higher than that of olivine (13.4 wt% Al_2O_3 in GSD-1G, 2.03 wt% Al_2O_3 in NIST SRM 612; GeoRem database (Jochum et al. 2011)). The resulting vast difference in signal size between that of the sample and the calibration material make Al determination using the GSD-1G reference material prone to large calibration errors.

5.5.4. Natural Zoning within Olivine Standards

When evaluating the accuracy and precision of element concentrations in the olivine standards, and their possible use as primary standards, the potential presence of natural elemental variation, i.e. zoning, needs to be taken into account. The presence of zoning was tested by ablating LA-ICP-MS transects across the olivine grains in one direction (A to B in Figure 5-9), and confirming with transects in the opposite direction (B to A). The highest degree of zoning (up to ~100% of element concentration) in SC-GB was observed for Ti (Figure 5-9). Other trace elements, such as Y and to a lesser extent Zr, mimic this zoning at lower levels of variability. Thus, for these elements SC-GB is not well-suited as a primary calibration material (unless the exact measuring location is recorded). The variability in the elements Ti, Y, and Zr is consistent with the argument of De Hoog et al. (2010) that these Group III elements are most affected by mantle metasomatic processes in peridotites.

5.5.5. LA-ICP-MS Memory Effects and Background Issues

The analytical challenges with LA-ICP-MS outlined above are mainly of a systematic nature, implying that they are constantly present during the analysis of olivine. These challenges need to be resolved by choosing appropriate analytical parameters such as laser settings, choice of calibration material, and specific sampling location on the standard olivine. An additional set of less systematic analytical artefacts include memory effects, either from previous analytical sessions or from preceding measurements in the same session. One example is measuring Zr, a

trace element with concentrations < 1 ppm in olivine, after the mineral zircon was measured on the same instrument in previous sessions. Ablation residue can build up anywhere between the ablation chamber and the introduction system of the ICP-MS, most commonly in the carrier tubes or on the sample cones, and can then become remobilized during ablation of olivine. This may lead to "spiky" ablation patterns and calculated element concentrations that are too high. This effect can clearly be mitigated by regular replacement of the carrier tubing or even, as we have now adopted, specific tubing dedicated exclusively for olivine analysis.

A related issue, which contributes to non-systematic background issues, is the long washout time (observed with the instrument setup at the University of Alberta) for certain elements, such as Al. This becomes especially problematic when calibration materials high in Al are used, either as the calibration material or as secondary standards, such as BCR-2G, BIR-1G, and BHVO-2G (see Figure 5-1). The effect of ablation of BCR-2G on background Al counts is illustrated in Figure 5-10. The background increases by a factor of ~2 and takes several minutes to decay to decay to the level prior to the ablation of the high-Al material. It is possible that the washout time may be related to the gas flow settings of the laser ablation system, and also to the length of carrier tubing, which is greatly increased with the use of the SQUID device. For this reason, calibration materials high in Al are avoided in the analytical protocol at the University of Alberta.

5.6. Conclusions

The undertaking to improve LA-ICP-MS methods for the analysis of trace elements in olivine has shown that matrix-matched calibration is preferable in order to avoid inaccuracies caused by calibration and fractionation effects. The fractionation effects are spot size-dependent and become especially problematic at small spot sizes. They are caused by different ablation characteristics of olivine compared to the reference silicate glasses (e.g., NIST SRM 612). Specifically, olivine exhibits a faster increase in the depth/beam diameter ratio, and increased melting at small spot sizes (e.g., 33 μm). Thus, an important pillar of this study is the characterization of two natural in-house olivine reference materials (SC-GB and 355OL) by different methods and laboratories. These olivine standards can be used 1) as secondary standards to test the accuracy of results for olivine samples, and 2) as primary standards for the matrix-matched calibration of olivine samples. Because of the analytical challenges that we

highlight when analyzing olivine via LA-ICP-MS, it is essential to have at least one olivine reference material available to verify the accuracy of trace element analyses. We recommend an analytical protocol in which olivine is preferentially measured using large laser spots (> 100 μm) with NIST SRM 612 as the calibration material and ^{29}Si as the internal standard. For the quantification of minor elements (e.g., Ni, Mn, Ca) an olivine standard (e.g., SC-GB or 355OL) needs to be used as the calibration material. Alternatively, EPMA can be used for quantification of the minor elements. For small laser spot sizes (< 100 μm), matrix-matched calibration becomes essential and olivine should be used as the calibration material. Although the new standards cannot be distributed on a large scale (due to limited material), they can be used for reliable characterization of new natural olivine standards in other laboratories.

5.7. Figures

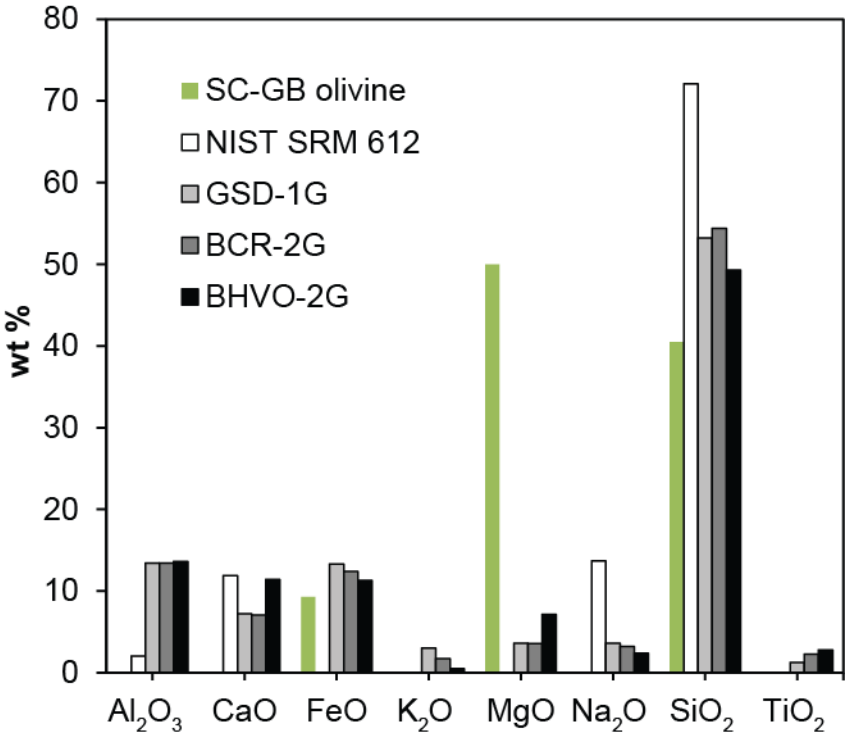

Figure 5-1: Major and minor element compositions of commonly used calibration materials (NIST SRM 612, GSD-1G, BCR-2G, BHVO-2G) and of olivine (SC-GB). Preferred values for the calibration materials are from the GeoRem database. None of the commonly used calibration materials have a matrix, i.e. major element composition, similar to that of olivine.

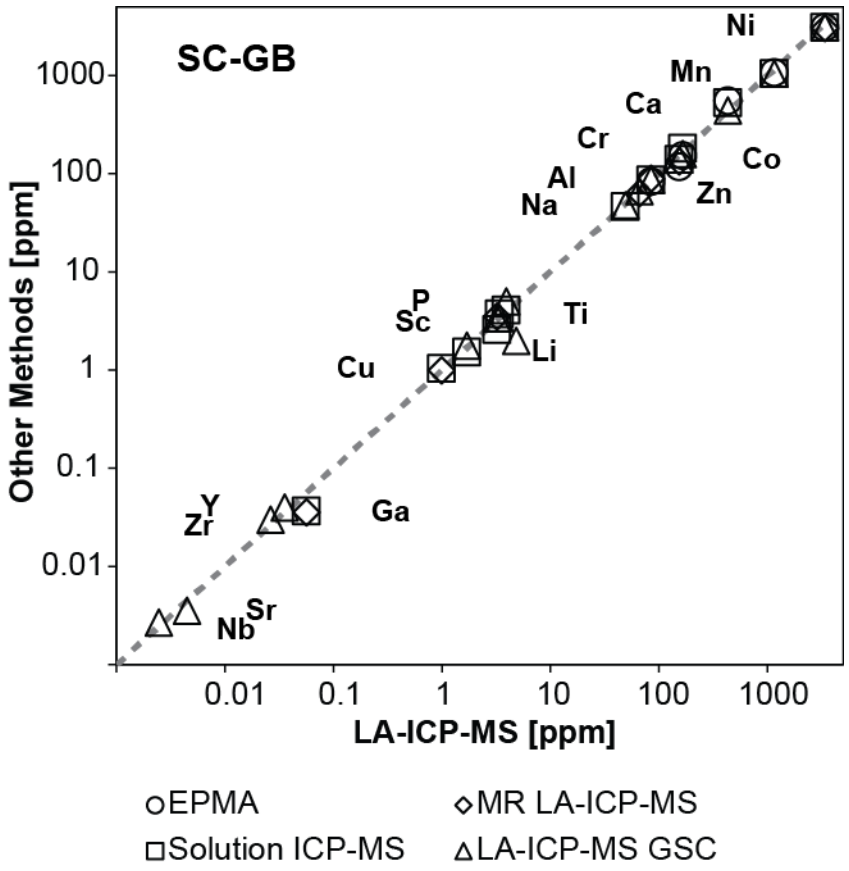

Figure 5-2: Comparison of results for olivine standard SC-GB using different methods. University of Alberta LA-ICP-MS results (at 130 µm laser spot size) are compared against results from other methods, including EPMA, solution ICP-MS, medium resolution LA-ICP-MS, and LA-ICP-MS at the Geological Survey of Canada (GSC). There is general agreement between the different methods and LA-ICP-MS as long as large laser spot sizes are used; the challenge lies in analyzing trace elements at small spot sizes.

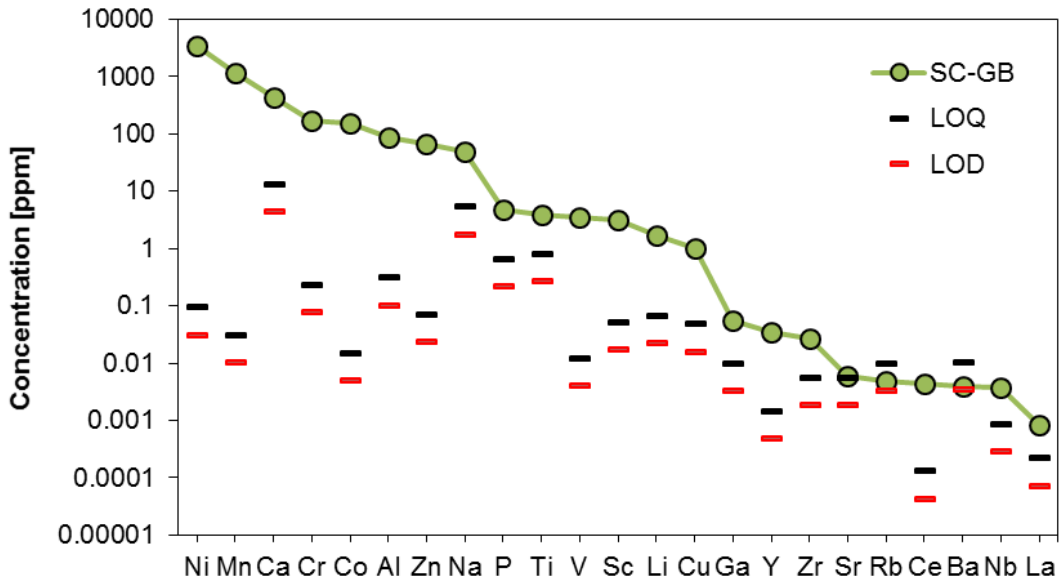

Figure 5-3: All elements analyzed in SC-GB and their limits of detection (LOD) and limits of quantitation (LOQ). The data were obtained following the University of Alberta LA-ICP-MS protocol using NIST SRM 612 as the calibration material, ^{29}Si as the internal standard, 10 Hz repetition rate, and a laser spot size of 130 μm.

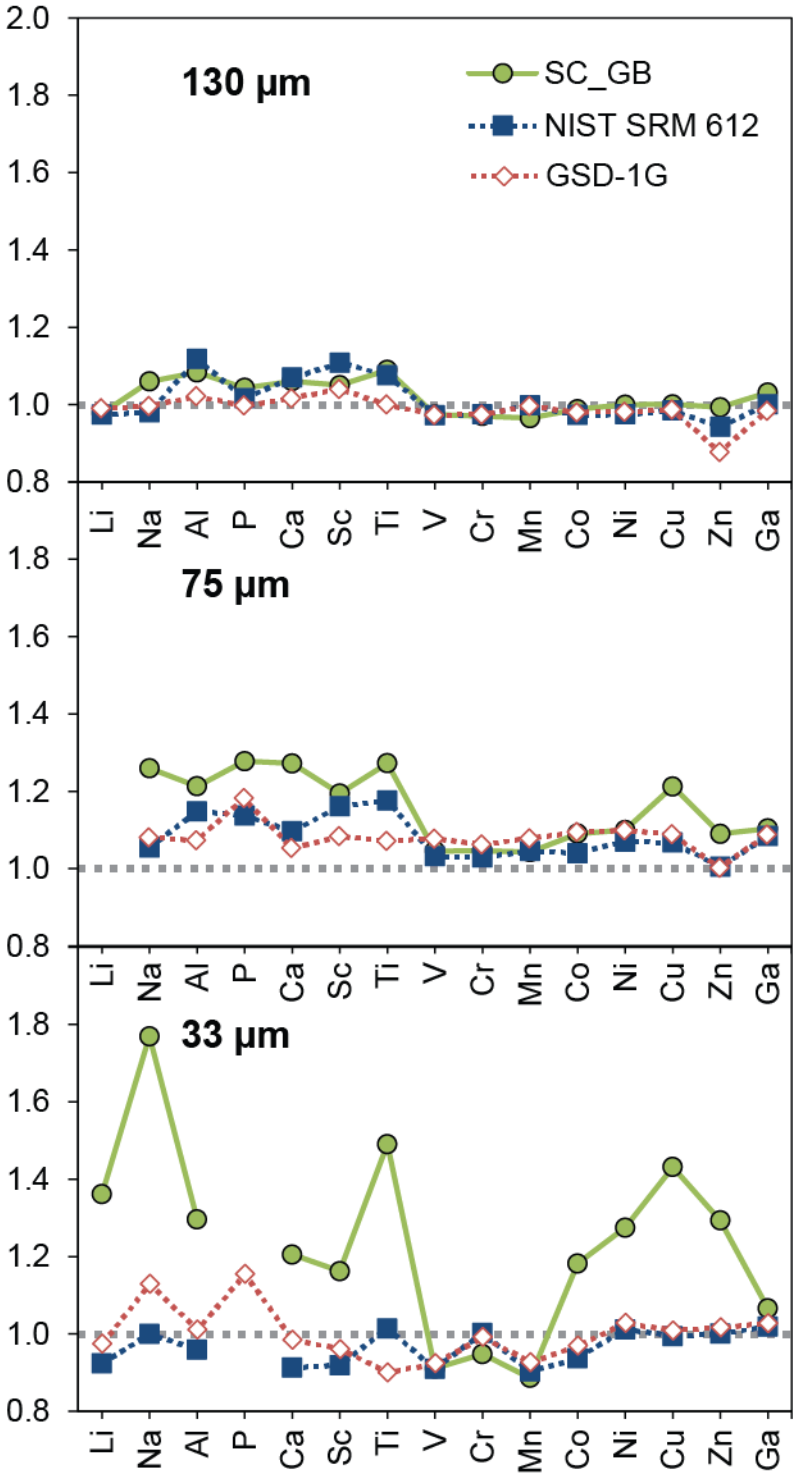

Figure 5-4: Fractionation factors calculated for standard olivine SC-GB and the calibration materials NIST SRM 612 and GSD-1G at laser spot sizes of 130, 75, and 33 µm. Laser settings for all spots were 10 Hz repetition rate, ~4.5 J/cm^2 fluence, 45 s ablation time.

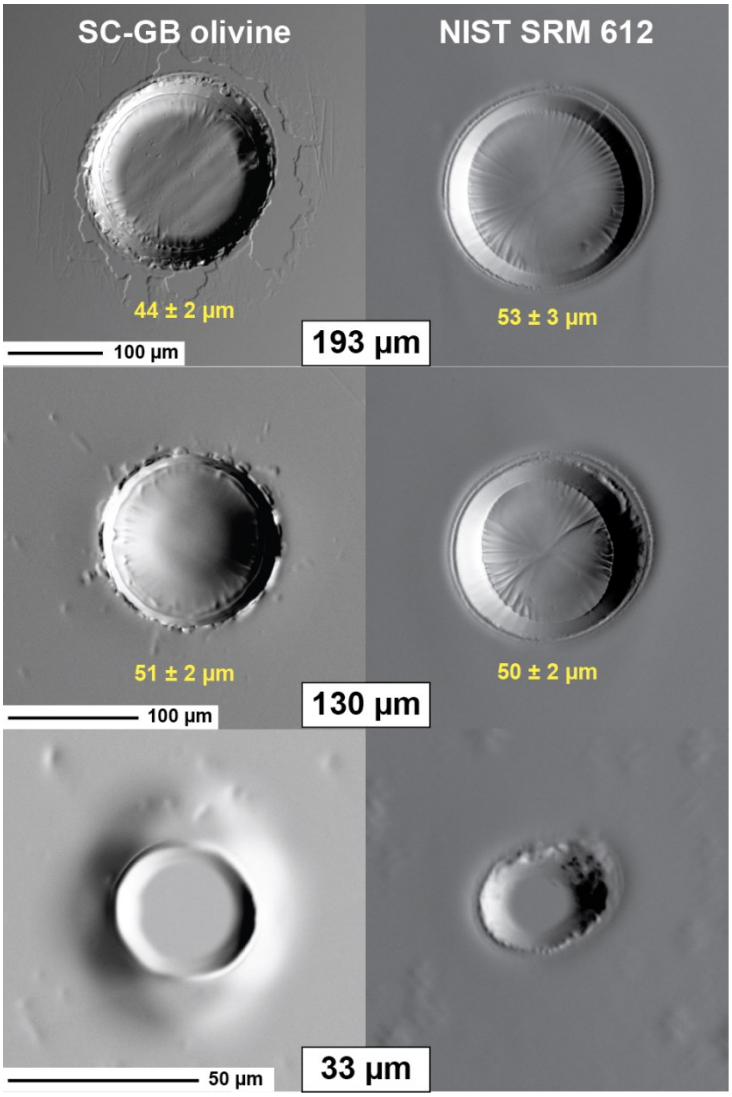

Figure 5-5: Secondary electron images obtained with EPMA showing the geometry of laser ablation pits at different spot sizes in standard olivine SC-GB (left) and in the reference glass NIST SRM 612 (right). For 193 and 130 µm pits, the crater depth is indicated in yellow (measured with the optical system of the EPMA). Laser settings for all spots were 10 Hz, fluence of ~4.5 J/cm^2, ablation time 45 s. For SC-GB, increasing degrees of melting are observed with decreasing spot size, leading to the formation of a protruding "melt disk" at 33 µm. In contrast, NIST SRM 612 shows flat-bottomed craters throughout (although the pits become more oval with decreasing spot size).

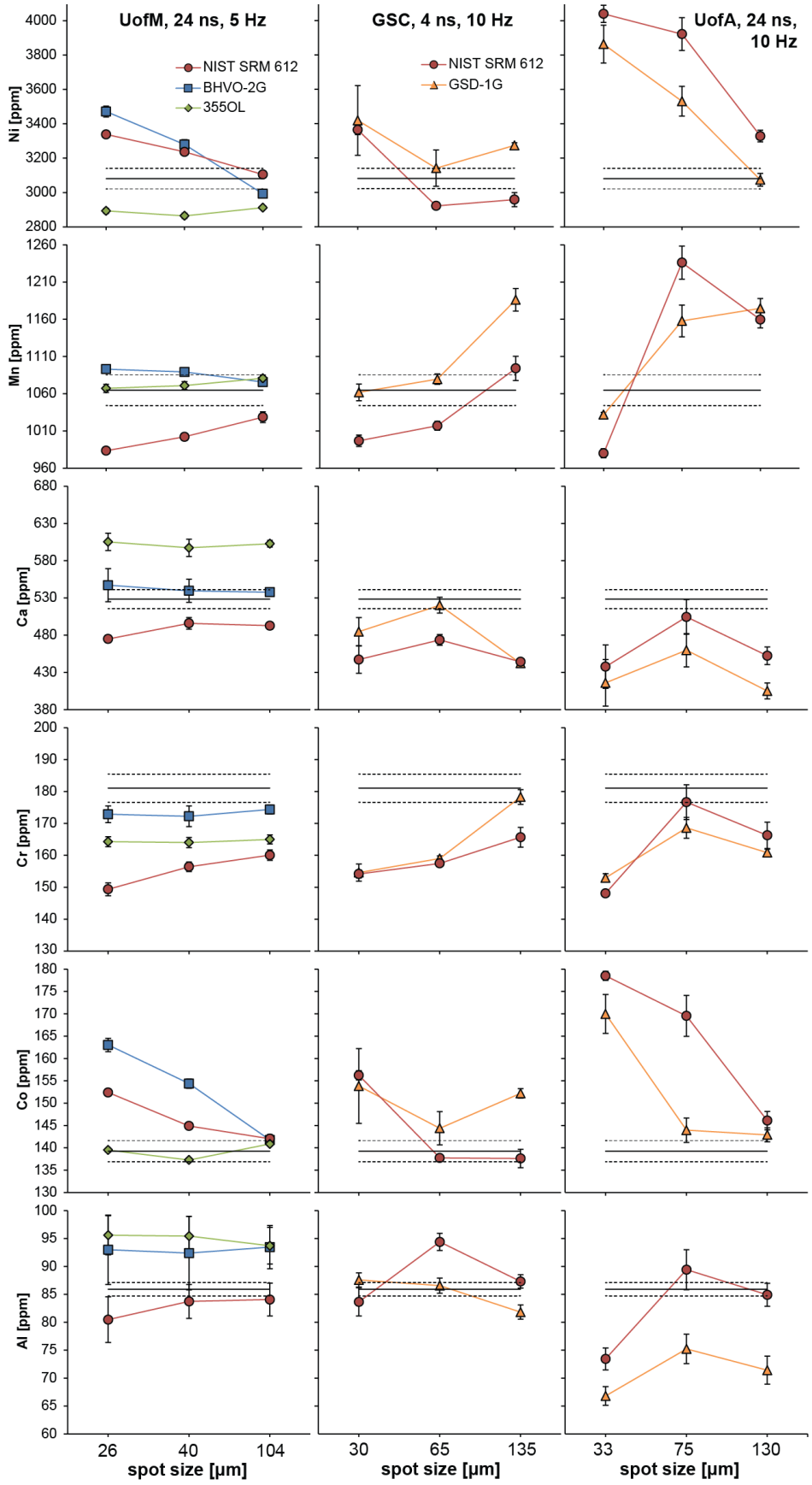
UofM, 24 ns, 5 Hz
GSC, 4 ns, 10 Hz
UofA, 24 ns, 10 Hz
NIST SRM 612
BHVO-2G
355OL
NIST SRM 612
GSD-1G
Ni [ppm]
Mn [ppm]
Ca [ppm]
Cr [ppm]
Co [ppm]
Al [ppm]
spot size [µm]
spot size [µm]
spot size [µm]

Figure 5-6 (previous page): Spot size-dependent fractionation effects on element concentration (Ni, Mn, Ca, Cr, Co, Al) in standard olivine SC-GB observed at the University of Melbourne (UofM; left-hand panel), the Geological Survey of Canada (GSC; middle panel), and the University of Alberta (UofA; right-hand panel). At the UofM, the calibration materials NIST SRM 612, BHVO-2G, and 355OL (olivine) were used (with ^{29}Si as the internal standard), using a 24 ns pulse width laser at a repetition rate of 5 Hz, with spot sizes of 26, 40, and 104 μm. At the GSC, the calibration materials NIST SRM 612 (with ^{29}Si) and GSD-1G (with ^{25}Mg) and a 4 ns pulse width laser at a repetition rate of 10 Hz were used, with spot sizes of 30, 65, and 135 μm. At the UofA, the calibration materials NIST SRM 612 (with ^{29}Si) and GSD-1G (with ^{25}Mg) and a 24 ns pulse width laser at a repetition rate of 10 Hz were used, with spot sizes of 33, 75, and 130 μm. Reference values (solid black lines, with ± 1 SD as dashed lines) are EPMA data for Ni and Mn, solution ICP-MS values for Ca, Cr, Co, and Al measured in SC-GB at the UofA (see Appendix A5.2.1). The fractionation effects at small spot sizes between calibration material and olivine are most pronounced in the UofA data due to longer laser pulse width and higher repetition rate. Matrix-matched calibration, i.e., using 355OL, minimizes spot size-dependent fractionation (see UofM data in Appendix A5.2.2).

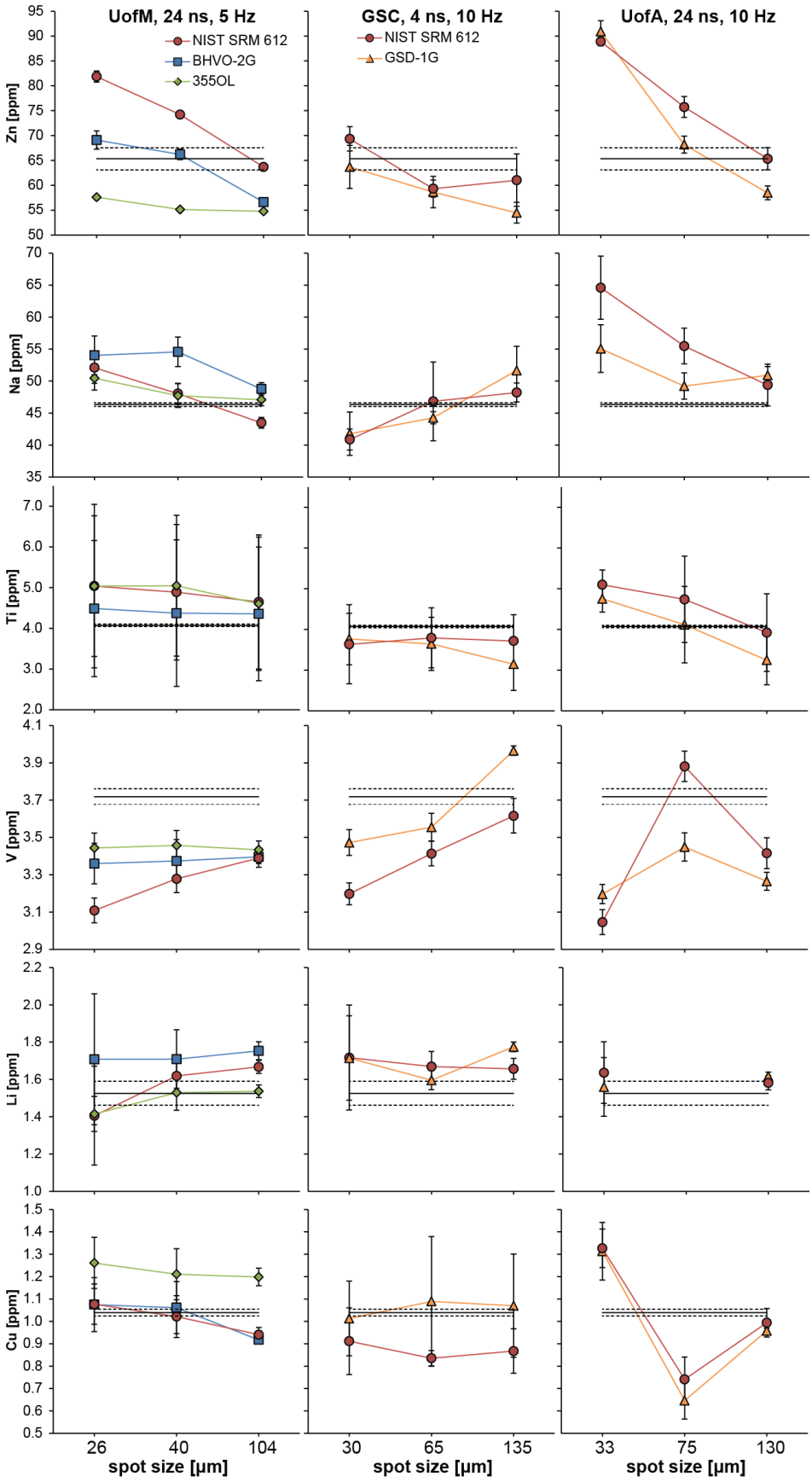
UofM, 24 ns, 5 Hz
GSC, 4 ns, 10 Hz
UofA, 24 ns, 10 Hz
NIST SRM 612
BHVO-2G
355OL
NIST SRM 612
GSD-1G
Zn [ppm]
Na [ppm]
Ti [ppm]
V [ppm]
Li [ppm]
Cu [ppm]
26
40
104
30
65
135
33
75
130
spot size [µm]
spot size [µm]
spot size [µm]

Figure 5-7 (previous page): Spot size-dependent fractionation effects on element concentration (Zn, Na, Ti, V, Li, Cu) in standard olivine SC-GB observed at the University of Melbourne (UofM; left-hand panel), the Geological Survey of Canada (GSC; middle panel), and the University of Alberta (UofA; right-hand panel). At the UofM, the calibration materials NIST SRM 612, BHVO-2G, and 355OL (olivine) were used (with ^{29}Si as the internal standard), using a 24 ns pulse width laser at a repetition rate of 5 Hz, with spot sizes of 26, 40, and 104 μm. At the GSC, the calibration materials NIST SRM 612 (with ^{29}Si) and GSD-1G (with ^{25}Mg) and a 4 ns pulse width laser at a repetition rate of 10 Hz were used, with spot sizes of 30, 65, and 135 μm. At the UofA, the calibration materials NIST SRM 612 (with ^{29}Si) and GSD-1G (with ^{25}Mg) and a 24 ns pulse width laser at a repetition rate of 10 Hz were used, with spot sizes of 33, 75, and 130 μm. Reference values (solid black lines, with ± 1 SD as dashed lines) are solution ICP-MS values for Na, Ti, V, Li, and Cu, and LA-ICP-MS (NIST SRM 612, ^{29}Si, 130 μm) for Zn, measured in SC-GB at the UofA (see Appendix A5.2.1). The fractionation effects at small spot sizes between calibration material and olivine are most pronounced in the UofA data due to longer laser pulse width and higher repetition rate. Matrix-matched calibration, i.e., using 355OL, minimizes spot size-dependent fractionation (see UofM data in Appendix A5.2.2).

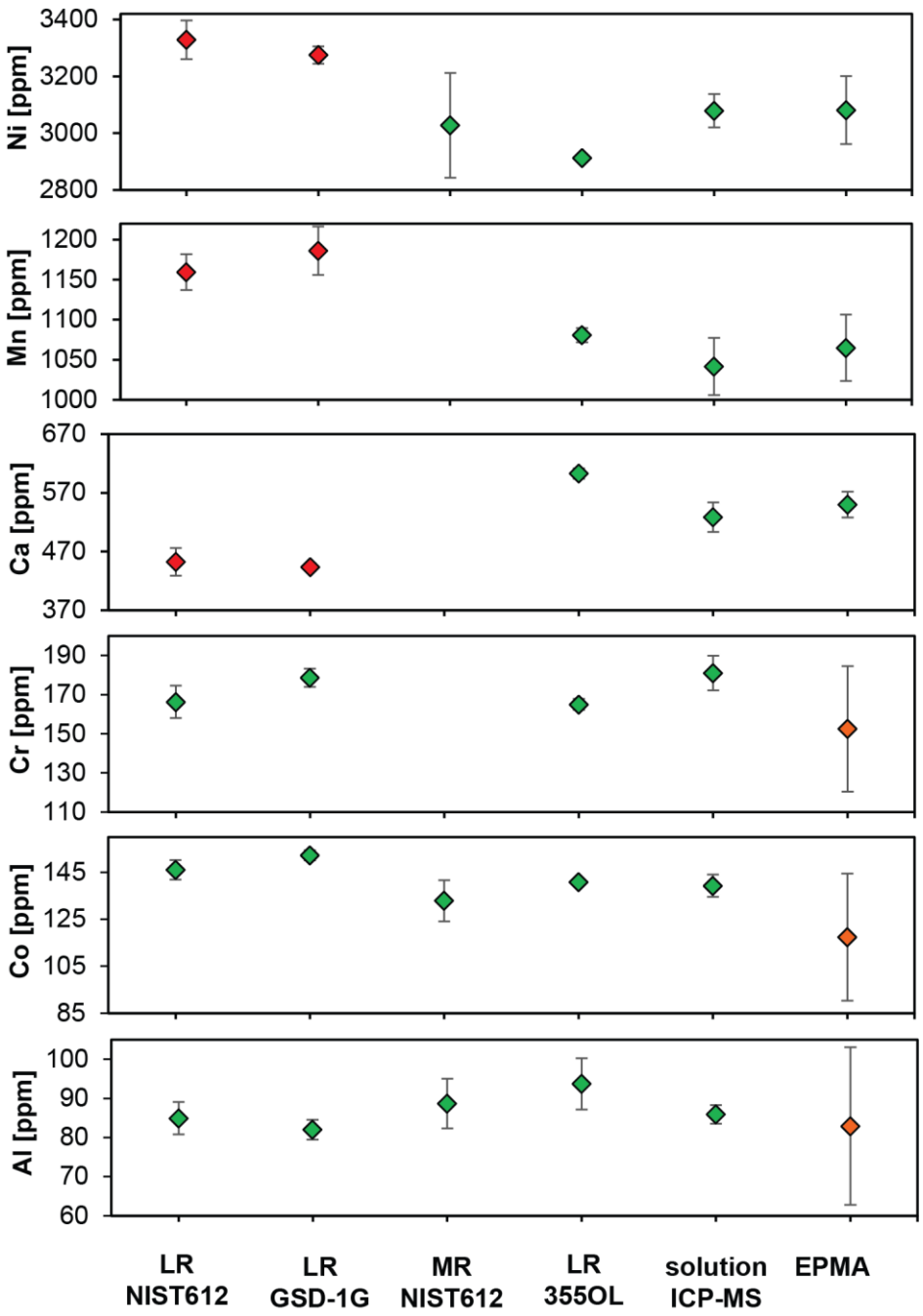

Figure 5-8: Comparison of results obtained with different methods for SC-GB olivine. LR = low resolution LA-ICP-MS, MR = medium resolution LA-ICP-MS. The values calibrated with NIST SRM 612 were measured at the University of Alberta (spot size 130 µm). The value calibrated with GSD-1G was measured at the Geological Survey of Canada (spot size 135 µm). The value calibrated with 355OL olivine was measured at the University of Melbourne (spot size 104 µm). Error bars represent 2 SD of the measured values. Red symbols indicate problematic elements for a given method (see text). Orange symbols indicate EPMA data with relatively poor precision.

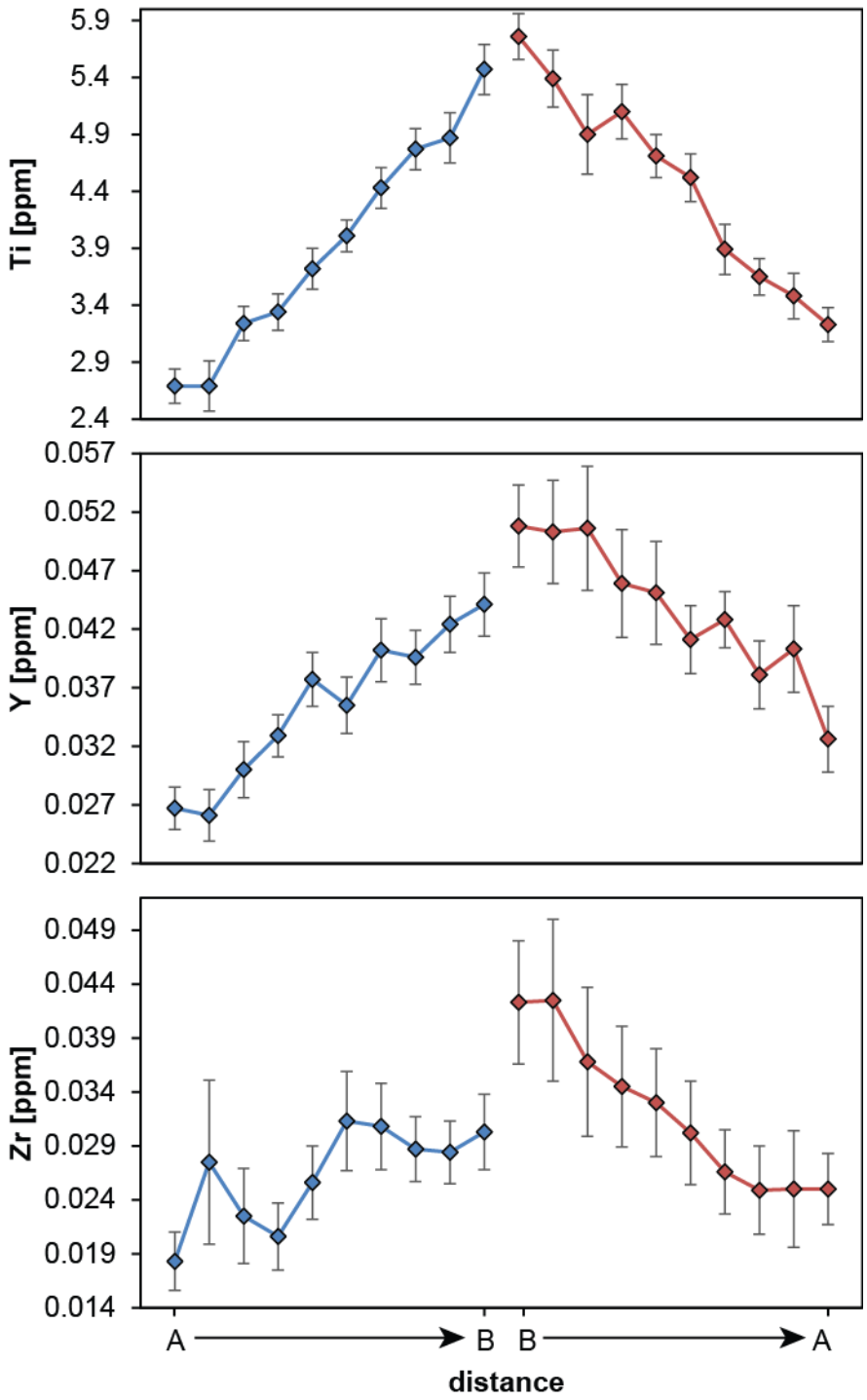

Figure 5-9: Trace element zoning in olivine standard SC-GB. Transects were measured from one side of the grain (A) to another (B), and in the opposite direction in a separate session in order to exclude instrumental drift as the cause for zoning. Error bars are 2 internal standard errors as calculated by Iolite.

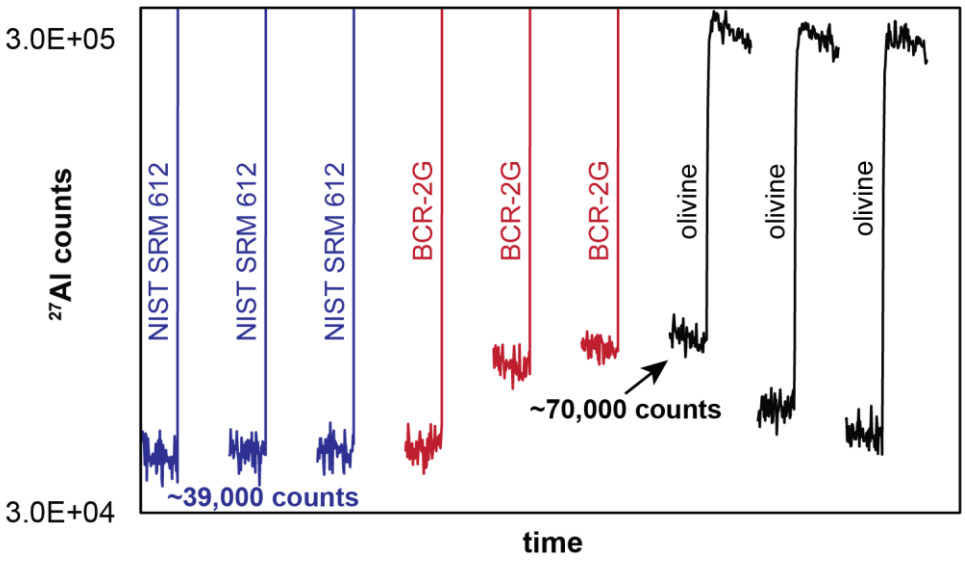

Figure 5-10: Time resolved background signal for ^{27}Al. The ablation of NIST SRM 612 (blue signals) has no significant effect on Al background, whereas the ablation of BCR-2G increases the background by a factor of ~2. The decay of the Al background takes several minutes and, in this instance, is carried into the sample ablations (olivine). Laser settings were 75 µm spot size, ~5 J/cm^2 fluence, 10 Hz repetition rate, 30 s background, 45 s ablation time.

6. Conclusions

This thesis has contributed to the scientific knowledge on kimberlites and their mantle cargo.

The study of clinopyroxene and garnet megacrysts and their polymineralic inclusions produced new insights on the reactive nature of early kimberlite melt. The inclusions document decarbonation reactions that may play an important role in the formation of calcite-bearing kimberlites. As such, polymineralic inclusions are important petrogenetic tools that can help to unravel the origin and evolution of kimberlites.

The study of the host megacrysts constitutes the first report of the presence of Cr-rich megacrysts in Lac de Gras kimberlites. A detailed geochemical investigation suggests that the megacrysts may have crystallized from previous, failed kimberlite pulses that reacted extensively with the surrounding mantle. The striking chemical similarity between the Cr-rich megacrysts and lherzolitic phases from Lac de Gras suggests that the percolation of stalled kimberlite melts may contribute to the introduction of clinopyroxene and garnet into the depleted cratonic mantle. The megacrysts were later entrained by and reacted with the host kimberlite (e.g., to form polymineralic inclusions).

The study of olivines produced in the high-pressure, high-temperature experiments by Brey et al. (1990) allowed for verification and refinement of the empirical calibration of the Al-in-olivine thermometer by De Hoog et al. (2010). It was shown that this thermometer is applicable to olivine from garnet peridotites, but not to spinel-bearing peridotites. New trace element screens to single out olivines from garnet peridotite are presented (e.g., Al vs. V). Moreover, potential applications of the Al-in-olivine thermometer as an exploration tool are described. Importantly, the Al-in-olivine thermometer may be the most reliable geothermometer applicable to garnet harzburgites.

The concerted efforts of the University of Alberta, the University of Melbourne, and the Geological Survey of Canada to improve analytical methods for LA-ICP-MS on olivine can be expected to be of great value for the scientific community. The findings are not limited to the analysis of olivine from kimberlites. Common analytical challenges, such as calibration effects and fractionation effects, were highlighted and natural olivines were characterized as standards. The matrix-matched calibration is important to minimize inaccuracies arising from calibration and fractionation effects.

Bibliography

Ammannati E, Jacob DE, Avanzinelli R, et al (2016) Low Ni olivine in silica-undersaturated ultrapotassic igneous rocks as evidence for carbonate metasomatism in the mantle. Earth Planet Sci Lett 444:64–74. doi: 10.1016/j.epsl.2016.03.039

Araújo DP, Griffin WL, O'Reilly SY (2009) Mantle melts, metasomatism and diamond formation: Insights from melt inclusions in xenoliths from Diavik, Slave Craton. Lithos 112:675–682. doi: 10.1016/j.lithos.2009.06.005

Armstrong JP, Wilson M, Barnett RL, et al (2004) Mineralogy of primary carbonate-bearing hypabyssal kimberlite, Lac de Gras, Slave Province, Northwest Territories, Canada. Lithos 76:415–433. doi: 10.1016/j.lithos.2004.03.025

Arndt NT, Guitreau M, Boullier AM, et al (2010) Olivine, and the origin of kimberlite. J Petrol 51:573–602. doi: 10.1093/petrology/egp080

Aulbach S, Griffin WL, Pearson NJ, et al (2007) Lithosphere formation in the central Slave Craton (Canada): plume subcretion or lithosphere accretion? Contrib to Mineral Petrol 154:409–427. doi: 10.1007/s00410-007-0200-1

Aulbach S, Griffin WL, Pearson NJ, O'Reilly SY (2013) Nature and timing of metasomatism in the stratified mantle lithosphere beneath the central Slave craton (Canada). Chem Geol 352:153–169. doi: 10.1016/j.chemgeo.2013.05.037

Ayling B, Rose P, Petty S (2011) Using QEMSCAN to Characterize Fracture Mineralization at the Newberry Volcano EGS Project, Oregon: A Pilot Study. GRC Trans 35:301–305.

Batanova VG, Sobolev A V., Kuzmin D V. (2015) Trace element analysis of olivine: High precision analytical method for JEOL JXA-8230 electron probe microanalyser. Chem Geol 419:149–157. doi: 10.1016/j.chemgeo.2015.10.042

Bell DR, Moore RO (2004) Deep chemical structure of the southern African mantle from kimberlite megacrysts. South African J Geol 107:59–80.

Bell DR, Rossman GR (1992) The distribution of hydroxyl in garnets from the subcontinental mantle of southern Africa. Contrib to Mineral Petrol 111:161–178. doi:

10.1007/BF00348949

Bell DR, Rossman GR, Moore RO (2004) Abundance and Partitioning of OH in a High-pressure Magmatic System: Megacrysts from the Monastery Kimberlite, South Africa. J Petrol 45:1539–1564. doi: 10.1093/petrology/egh015

Bleeker W, Ketchum J, Davis B, Sircombe K (2004) The Slave Craton From On Top: The Crustal View. courses.eas.ualberta.ca 1–5.

Boyd F, Dawson J, Smith J (1984) Granny Smith diopside megacrysts from the kimberlites of the Kimberley area and Jagersfontein, South Africa. Geochim Cosmochim Acta 48:381–384.

Boyd FR (1974) Olivine megacrysts from the kimberlites of Monastery and Frank Smith Mines, South Africa. Carnegie Inst Washingt Yearb 73 282–285.

Boyd FR, Nixon PH (1973) Origin of the ilmenite-silicate nodules in kimberlites from Lesotho and South Africa. Lesotho kimberlites 254.

Brett RC, Russell JK, Andrews GDM, Jones TJ (2015) The ascent of kimberlite: Insights from olivine. Earth Planet Sci Lett 424:119–131. doi: 10.1016/j.epsl.2015.05.024

Brett RC, Russell JK, Moss S (2009) Origin of olivine in kimberlite: Phenocryst or impostor? Lithos 112:201–212. doi: 10.1016/j.lithos.2009.04.030

Brey G, Brice WR, Ellis DJ, et al (1983) Pyroxene-carbonate reactions in the upper mantle. Earth Planet Sci Lett 62:63–74. doi: 10.1016/0012-821X(83)90071-7

Brey GP (1989) Geothermobarometry for lherzolites: experiments from 10 to 60 kb, new thermobarometers and application to natural rocks. Habilit Thesis, TU, Darmstadt 227.

Brey GP, Bulatov VK, Girnis a. V., Lahaye Y (2008) Experimental Melting of Carbonated Peridotite at 6-10 GPa. J Petrol 49:797–821. doi: 10.1093/petrology/egn002

Brey GP, Kogarko LN, Ryabchikov ID (1991) Carbon Dioxide in kimberlitic melts. Neues Jahrb für Mineral Monatshefte 4:159–168.

Brey GP, Köhler TP (1990) Geothermobarometry in four phase lherzolites II. New thermobarometers and practical assessment of existing thermobarometers. J Petrol 31:1353–1378.

Brey GP, Köhler TP, Nickel KG (1990) Geothermobarometry in Four-phase Lherzolites I. Experimental Results From 10 To 60 kb. J Petrol 31:1313–1352.

Bussweiler Y, Brey GP, Pearson DG, et al (2017) The aluminum-in-olivine thermometer for mantle peridotites — Experimental versus empirical calibration and potential applications. Lithos 272–273:301–314. doi: 10.1016/j.lithos.2016.12.015

Bussweiler Y, Foley SF, Prelević D, Jacob DE (2015) The olivine macrocryst problem: New insights from minor and trace element compositions of olivine from Lac de Gras kimberlites, Canada. Lithos 220–223:238–252. doi: 10.1016/j.lithos.2015.02.016

Bussweiler Y, Stone RS, Pearson DG, et al (2016) The evolution of calcite-bearing kimberlites by melt-rock reaction: evidence from polymineralic inclusions within clinopyroxene and garnet megacrysts from Lac de Gras kimberlites, Canada. Contrib to Mineral Petrol 171:65. doi: 10.1007/s00410-016-1275-3

Canil D (1999) The Ni-in-garnet geothermometer: Calibration at natural abundances. Contrib to Mineral Petrol 136:240–246. doi: 10.1007/s004100050535

Canil D, Bellis AJ (2008) Phase equilibria in a volatile-free kimberlite at 0.1 MPa and the search for primary kimberlite magma. Lithos 105:111–117. doi: 10.1016/j.lithos.2008.02.011

Canil D, Fedortchouk Y (1999) Garnet dissolution and the emplacement of kimberlites. Earth Planet Sci Lett 167:227–237. doi: 10.1016/S0012-821X(99)00019-9

Carlson RW, Pearson DG, James DE (2005) Physical , Chemical , and Chronological Characteristics of Continental Mantle. Rev Geophys 1–24. doi: 10.1029/2004RG000156.1.INTRODUCTION

Carpenter RL, Edgar AD, Thibault Y (2002) Origin of spongy textures in clinopyroxene and spinel from mantle xenoliths, Hessian Depression, Germany. Mineral Petrol 74:149–162. doi: 10.1007/s007100200002

Coogan LA, Saunders AD, Wilson RN (2014) Aluminum-in-olivine thermometry of primitive basalts: Evidence of an anomalously hot mantle source for large igneous provinces. Chem Geol 368:1–10. doi: 10.1016/j.chemgeo.2014.01.004

Creaser RA, Grütter H, Carlson J, Crawford B (2004) Macrocrystal phlogopite Rb–Sr dates for

the Ekati property kimberlites, Slave Province, Canada: evidence for multiple intrusive episodes in the Paleocene and Eocene. Lithos 76:399–414. doi: 10.1016/j.lithos.2004.03.039

Creighton S, Stachel T, Eichenberg D, Luth RW (2010) Oxidation state of the lithospheric mantle beneath Diavik diamond mine, central Slave craton, NWT, Canada. Contrib to Mineral Petrol 159:645–657. doi: 10.1007/s00410-009-0446-x

Creighton S, Stachel T, Matveev S, et al (2009) Oxidation of the Kaapvaal lithospheric mantle driven by metasomatism. Contrib to Mineral Petrol 157:491–504. doi: 10.1007/s00410-008-0348-3

Creighton S, Stachel T, McLean H, et al (2008) Diamondiferous peridotitic microxenoliths from the Diavik Diamond Mine, NT. Contrib to Mineral Petrol 155:541–554. doi: 10.1007/s00410-007-0257-x

Czas J, Jochum KP, Stoll B, et al (2012) Investigation of matrix effects in 193 nm laser ablation-inductively coupled plasma-mass spectrometry analysis using reference glasses of different transparencies. Spectrochim Acta - Part B At Spectrosc 78:20–28. doi: 10.1016/j.sab.2012.09.004

Dalton JA, Presnall DC (1998a) The Continuum of Primary Carbonatitic – Kimberlitic Melt Compositions in Equilibrium with Lherzolite : Data from at 6 GPa. J Petrol 39:1953–1964.

Dalton J, Presnall D (1998b) Carbonatitic melts along the solidus of model lherzolite in the system CaO-MgO-Al2O3-SiO2-CO2 from 3 to 7 GPa. Contrib to Mineral Petrol 131:123–135.

Davies G, Spriggs A, Nixon P (2001) A non-cognate origin for the Gibeon kimberlite megacryst suite, Namibia: implications for the origin of Namibian kimberlites. J Petrol 42:159–172. doi: 10.1093/petrology/42.1.159

Davis W, Gariepy C, Breemen O Van (1996) Pb isotopic composition of late Archaean granites and the extent of recycling early Archaean crust in the Slave Province, northwest Canada. Chem Geol 130:255–269.

Dawson JB (1971) Advances in kimberlite geology. Earth Sci Rev 7:187–214. doi: 10.1016/0012-8252(71)90120-6

Dawson JB, Hawthorne JB (1973) Magmatic sedimentation and carbonatite differentiation in kimberlite sills at Benfontein, South Africa. J Geol Soc London 129:64–85.

Day HW (2012) A revised diamond-graphite transition curve. Am Mineral 97:52–62. doi: 10.2138/am.2011.3763

de Bruin D (2005) Multiple compositional megacryst groups from the Uintjiesberg and Witberg kimberlites, South Africa. South African J Geol 108:233–246. doi: 10.2113/108.2.233

De Hoog JCM, Gall L (2005) TRACE ELEMENT GEOCHEMISTRY OF MANTLE OLIVINE AND ITS APPLICATION TO GEOTHERMOMETRY. Ofioliti 20:289–290.

De Hoog JCM, Gall L, Cornell DH (2010) Trace-element geochemistry of mantle olivine and application to mantle petrogenesis and geothermobarometry. Chem Geol 270:196–215. doi: 10.1016/j.chemgeo.2009.11.017

Donnelly CL, Stachel T, Creighton S, et al (2007) Diamonds and their mineral inclusions from the A154 South pipe, Diavik Diamond Mine, Northwest territories, Canada. Lithos 98:160–176. doi: 10.1016/j.lithos.2007.03.003

Eccles DR, Heaman LM, Luth RW, Creaser R a. (2004) Petrogenesis of the Late Cretaceous northern Alberta kimberlite province. Lithos 76:435–459. doi: 10.1016/j.lithos.2004.03.046

Edgar AD, Arima M, Baldwin DK, et al (1988) High-pressure-high-temperature melting experiments on a SiO2-poor aphanitic kimberlite from the Wesselton mine, Kimberley, South Africa. Am Mineral 73:524–533. doi: 10.1130/0091-7613(1997)025<0903:RCSITL>2.3.CO;2

Eggler DH (1986) Kimberlites: How do they form? In: Kimberlites and Related Rocks. pp 489–504

Eggler DH, McCallum ME, Smith CB (1979) Megacryst assemblages in kimberlite from northern Colorado and southern Wyoming: Petrology, geothermometry-barometry and areal distribution. Boyd Meyer 2:213–226.

Fedortchouk Y, Canil D (2004) Intensive Variables in Kimberlite Magmas, Lac de Gras, Canada and Implications for Diamond Survival. J Petrol 45:1725–1745. doi: 10.1093/petrology/egh031

Fietzke J, Frische M (2016) Experimental evaluation of elemental behavior during LA-ICP-MS: influences of plasma conditions and limits of plasma robustness. J Anal At Spectrom 0:1–11. doi: 10.1039/C5JA00253B

Foley SF, Jacob DE, O'Neill HSC (2011) Trace element variations in olivine phenocrysts from Ugandan potassic rocks as clues to the chemical characteristics of parental magmas. Contrib to Mineral Petrol 162:1–20. doi: 10.1007/s00410-010-0579-y

Foley SF, Prelevic D, Rehfeldt T, Jacob DE (2013) Minor and trace elements in olivines as probes into early igneous and mantle melting processes. Earth Planet Sci Lett 363:181–191. doi: 10.1016/j.epsl.2012.11.025

Foley SF, Yaxley GM, Rosenthal A, et al (2009) The composition of near-solidus melts of peridotite in the presence of CO2 and H2O between 40 and 60 kbar. Lithos 112:274–283. doi: 10.1016/j.lithos.2009.03.020

Fryer BJ, Jackson SE, Longerich HP (1995) Design, Operation and Role of the Laser-Ablation Microprobe Coupled With an Inductively-Coupled Plasma - Mass-Spectrometer (Lam-Icp-Ms) in the Earth-Sciences. Can Mineral 33:303–312.

Gaboardi M, Humayun M (2009) Elemental fractionation during LA-ICP-MS analysis of silicate glasses: implications for matrix-independent standardization. J Anal At Spectrom 24:1188. doi: 10.1039/b900876d

Gaul O, Griffin W, O'Reilly S, Pearson N (2000) Mapping olivine composition in the lithospheric mantle. Earth Planet Sci Lett 182:223–235.

Giuliani A, Kamenetsky VS, Kendrick MA, et al (2013) Oxide, sulphide and carbonate minerals in a mantle polymict breccia: Metasomatism by proto-kimberlite magmas, and relationship to the kimberlite megacrystic suite. Chem Geol 353:4–18. doi: 10.1016/j.chemgeo.2012.09.025

Giuliani A, Phillips D, Kamenetsky VS, et al (2014) Petrogenesis of Mantle Polymict Breccias: Insights into Mantle Processes Coeval with Kimberlite Magmatism. J Petrol 55:831–858. doi: 10.1093/petrology/egu008

Giuliani A, Phillips D, Kamenetsky VS, Goemann K (2016) Constraints on kimberlite ascent mechanisms revealed by phlogopite compositions in kimberlites and mantle xenoliths.

Lithos 240–243:189–201. doi: 10.1016/j.lithos.2015.11.013

Griffin W, Doyle B, Ryan C (1999) Layered mantle lithosphere in the Lac de Gras area, Slave craton: composition, structure and origin. J Petrol 40:705–727.

Griffin WL, Cousens DR, Ryan CG, et al (1989) Ni in chrome pyrope garnets: a new geothermometer. Contrib to Mineral Petrol 103:199–202. doi: 10.1007/BF00378505

Griffin WL, O'Reilly SY, Afonso JC, Begg GC (2009) The composition and evolution of lithospheric mantle: A re-evaluation and its tectonic implications. J Petrol 50:1185–1204. doi: 10.1093/petrology/egn033

Griffin WL, Powell WJ, Pearson NJ, O'Reilly SY (2008) GLITTER: data reduction software for laser ablation ICP-MS. Laser Ablation-ICP-MS earth Sci Mineral Assoc Canada short course Ser 40:204–207.

Grütter H, Latti D, Menzies A (2006) Cr-saturation arrays in concentrate garnet compositions from kimberlite and their use in mantle barometry. J Petrol 47:801–820. doi: 10.1093/petrology/egi096

Grütter HS (2009) Pyroxene xenocryst geotherms: Techniques and application. Lithos 112:1167–1178. doi: 10.1016/j.lithos.2009.03.023

Grütter HS, Gurney JJ, Menzies AH, Winter F (2004) An updated classification scheme for mantle-derived garnet, for use by diamond explorers. Lithos 77:841–857. doi: 10.1016/j.lithos.2004.04.012

Gudfinnsson GH, Presnall DC (2005) Continuous gradations among primary carbonatitic, kimberlitic, melilititic, basaltic, picritic, and komatiitic melts in equilibrium with garnet lherzolite at 3-8 GPa. J Petrol 46:1645–1659. doi: 10.1093/petrology/egi029

Guillong M, Hametner K, Reusser E, et al (2005) Preliminary characterisation of new glass reference materials (GSA-1G, GSC-1G, GSD-1G and GSE-1G) by laser ablation-inductively coupled plasma-mass spectrometry using 193 nm, 213 nm and 266 nm wavelengths. Geostand Geoanalytical Res 29:315–331. doi: 10.1111/j.1751-908X.2005.tb00903.x

Guillong M, Kuhn HR, Günther D (2003) Application of a particle separation device to reduce

inductively coupled plasma-enhanced elemental fractionation in laser ablation-inductively coupled plasma-mass spectrometry. Spectrochim Acta - Part B At Spectrosc 58:211–220. doi: 10.1016/S0584-8547(02)00257-4

Günther D, Frischknecht R, Heinrich C a., Kahlert H-J (1997) Capabilities of an Argon Fluoride 193 nm Excimer Laser for Laser Ablation Inductively Coupled Plasma Mass Spectometry Microanalysis of Geological Materials. J Anal At Spectrom 12:939–944. doi: 10.1039/a701423f

Günther D, Hattendorf B (2005) Solid sample analysis using laser ablation inductively coupled plasma mass spectrometry. TrAC - Trends Anal Chem 24:255–265. doi: 10.1016/j.trac.2004.11.017

Günther M, Jagoutz E (1994) Isotopic disequilibria (Sm/Nd, Rb/Sr) between minerals of coarse grained, low temperature garnet peridotites from Kimberley floors, Southern Africa. In: Meyer HOA, Leonardos OH (eds) Proc. 5 th Int. Kimberlite Conf. I. CPRM Spec. Publ. 1A. Brasilia, pp 354–365

Gurney JJ (1984) A correlation between garnets and diamonds in kimberlites. In: Kimberlite occurrence and origin: a basis for conceptual models in exploration. pp 143–166

Gurney JJ, Jakob WRO, Dawson JB (1979) Megacrysts from the Monastery Kimberlite Pipe, South Africa. The Mantle Sample: Inclusions in Kimberlites and Other Volcanics 16:227–243.

Haggerty SE, Boyd FR (1975) Kimberlite inclusions in an olivine megacryst from Monastery. In: De Beers Kimberlite Symposium I. Cambridge,

Harley SL (1984) An experimental study of the partitioning of Fe and Mg between garnet and orthopyroxene. Contrib to Mineral Petrol 86:359–373. doi: 10.1007/BF01187140

Harte B (1983) Mantle peridotites and processes - the kimberlite sample. In: Hawkesworth CJ, Norry MJ (eds) Continental Basalt and Mantle Xenoliths. Shiva, Nantwich, pp 46–91

Harte B, Hunter RH, Kinny PD (1993) Melt geometry, movement and crystallization, in relation to mantle dykes, veins and metasomatism. Phil Trans R Soc Lond 342:1–21.

Hasterok D, Chapman DS (2011) Heat production and geotherms for the continental lithosphere.

Earth Planet Sci Lett 307:59–70. doi: 10.1016/j.epsl.2011.04.034

Hayman PC, Cas RAF, Johnson M (2009) Characteristics and alteration origins of matrix minerals in volcaniclastic kimberlite of the Muskox pipe (Nunavut, Canada). Lithos 112:473–487. doi: 10.1016/j.lithos.2009.06.025

Heaman LM, Kjarsgaard BA, Creaser RA (2004) The temporal evolution of North American kimberlites. Lithos 76:377–397. doi: 10.1016/j.lithos.2004.03.047

Heinrich CA, Pettke T, Halter WE, et al (2003) Quantitative multi-element analysis of minerals, fluid and melt inclusions by laser-ablation inductively-coupled-plasma mass-spectrometry. Geochim Cosmochim Acta 67:3473–3496. doi: 10.1016/S0016-7037(03)00084-X

Helmstaedt H (2009) Crust–mantle coupling revisited: The Archean Slave craton, NWT, Canada. Lithos 112:1055–1068. doi: 10.1016/j.lithos.2009.04.046

Höfer HE, Lazarov M, Brey GP, Woodland AB (2009) Oxygen fugacity of the metasomatizing melt in a polymict peridotite from Kimberley. Lithos 112:1150–1154. doi: 10.1016/j.lithos.2009.05.037

Hops JJ, Gurney JJ, Harte B (1992) The jagersfontein Cr-poor megacryst suite — towards a model for megacryst petrogenesis. J Volcanol Geotherm Res 50:143–160. doi: 10.1016/0377-0273(92)90042-C

Howarth GH, Taylor LA (2016) Multi-stage kimberlite evolution tracked in zoned olivine from the Benfontein sill, South Africa. Lithos 262:384–397. doi: 10.1016/j.lithos.2016.07.028

Hunter RH, Taylor LA (1984) Magma-mixing in the low velocity zone: kimberlitic megacrysts from Fayette County, Pennsylvania. Am Mineral 69:16–29.

Ionov D (1998) Trace Element Composition of Mantle-derived Carbonates and Coexisting Phasesin Peridotite Xenoliths from Alkali Basalts. J Petrol 39:1931–1941. doi: 10.1093/petroj/39.11-12.1931

Irvine GJ, Graham Pearson D, Kjarsgaard BA, et al (2003) A Re–Os isotope and PGE study of kimberlite-derived peridotite xenoliths from Somerset Island and a comparison to the Slave and Kaapvaal cratons. Lithos 71:461–488. doi: 10.1016/S0024-4937(03)00126-9

Irving AJ, Wyllie PJ (1975) Subsolidus and melting relationships for calcite, magnesite and the

join CaCO3-MgCO3 to 36 kb. Geochim Cosmochim Acta 39:35–53. doi: 10.1016/0016-7037(75)90183-0

Isachsen C, Bowring S (1994) Evolution of the Slave craton. Geology 22:917–920.

Jackson SE (2008) Calibration strategies for elemental analysis by LA-ICP-MS. Mineral Assoc Canada Short Course 40 169–188.

Jacob DE (2004) Nature and origin of eclogite xenoliths from kimberlites. Lithos 77:295–316. doi: 10.1016/j.lithos.2004.03.038

Jagoutz E, Palme H, Baddenhausen H, et al (1979) The abundances of major, minor and trace elements in the earth's mantle as derived from primitive ultramafic nodules. In: Proc. Lunar Planet. Sci. Conf. 10th. pp 2031–2050

Jenner FE, O'Neill HSC (2012) Major and trace analysis of basaltic glasses by laser-ablation ICP-MS. Geochemistry, Geophys Geosystems 13:1–17. doi: 10.1029/2011GC003890

Jochum KP, Nohl U, Herwig K, et al (2005) GeoReM: a new geochemical database for reference materials and isotopic standards. Geostand Geoanalytical Res 29:333–338. doi: 10.1111/j.1751-908X.2005.tb00904.x

Jochum KP, Weis U, Stoll B, et al (2011) Determination of reference values for NIST SRM 610-617 glasses following ISO guidelines. Geostand Geoanalytical Res 35:397–429. doi: 10.1111/j.1751-908X.2011.00120.x

Kamenetsky VS (2016) Comment on: The ascent of kimberlite: Insights from olivine" authored by Brett R.C. et al. [Earth Planet. Sci. Lett. 424 (2015) 119–131]. Earth Planet Sci Lett 440:187–189. doi: 10.1016/j.epsl.2016.02.016

Kamenetsky VS, Grütter H, Kamenetsky MB, Gömann K (2013) Parental carbonatitic melt of the Koala kimberlite (Canada): Constraints from melt inclusions in olivine and Cr-spinel, and groundmass carbonate. Chem Geol 353:96–111. doi: 10.1016/j.chemgeo.2012.09.022

Kamenetsky VS, Kamenetsky MB, Golovin A V., et al (2012) Ultrafresh salty kimberlite of the Udachnaya–East pipe (Yakutia, Russia): A petrological oddity or fortuitous discovery? Lithos 152:173–186. doi: 10.1016/j.lithos.2012.04.032

Kamenetsky VS, Kamenetsky MB, Sobolev a. V., et al (2008) Olivine in the Udachnaya-East

Kimberlite (Yakutia, Russia): Types, Compositions and Origins. J Petrol 49:823–839. doi: 10.1093/petrology/egm033

Kamenetsky VS, Yaxley GM (2015) Carbonate-silicate liquid immiscibility in the mantle propels kimberlite magma ascent. Geochim Cosmochim Acta 158:48–56. doi: 10.1016/j.gca.2015.03.004

Kane JS (1998) A history of the development and certification of NIST glass SRMs 610-617. Geostand Newsl 22:7–13. doi: 10.1111/j.1751-908X.1998.tb00541.x

Kennedy CS, Kennedy GC (1976) The Equilibrium Boundary Between Graphite and Diamond. J Geophys Res 81:2467–2470.

Keshav S, Corgne A, Gudfinnsson GH, et al (2005) Kimberlite petrogenesis: Insights from clinopyroxene-melt partitioning experiments at 6 GPa in the CaO-MgO-Al2O3 -SiO2-CO2 system. Geochim Cosmochim Acta 69:2829–2845. doi: 10.1016/j.gca.2005.01.012

Kjarsgaard BA, Levinson AA (2002) Diamonds in Canada. Gems Gemol 38:208–238.

Kjarsgaard BA, Pearson DG, Tappe S, et al (2009) Geochemistry of hypabyssal kimberlites from Lac de Gras, Canada: Comparisons to a global database and applications to the parent magma problem. Lithos 112:236–248. doi: 10.1016/j.lithos.2009.06.001

Kjarsgaard BA, Peterson TD (1992) Kimberlite-derived ultramafic xenoliths from the diamond stability field : a new Cretaceous geotherm for Somerset Island , Northwest Territories. Curr Res Part B Pap Geol Surv Can 92–1B:1–6.

Kjarsgaard B, Wilkinson L, Armstrong J (2002) Geology, Lac de Gras kimberlite Field, Central Slave Province, Northwest Territories - Nunavut, (NTS 76C, D, E, F), 1:250,000 scale color map with descriptive notes. Geological Survey of Canada, Open File 3228.

Klein-BenDavid O, Izraeli ES, Hauri E, Navon O (2007) Fluid inclusions in diamonds from the Diavik mine, Canada and the evolution of diamond-forming fluids. Geochim Cosmochim Acta 71:723–744. doi: 10.1016/j.gca.2006.10.008

Klemme S (2004) The influence of Cr on the garnet-spinel transition in the Earth's mantle: Experiments in the system MgO-Cr2O3-SiO2 and thermodynamic modelling. Lithos 77:639–646. doi: 10.1016/j.lithos.2004.03.017

Kopylova MG, Matveev S, Raudsepp M (2007) Searching for parental kimberlite melt. Geochim Cosmochim Acta 71:3616–3629. doi: 10.1016/j.gca.2007.05.009

Kopylova MG, Mogg T, Smith BS (2010) Mineralogy of the Snap Lake kimberlite, Northwest Territories, Canada, and compositions of phlogopite as records of its crystallization. Can Mineral 48:549–570. doi: 10.3749/canmin.48.3.549

Kopylova MG, Nowell GM, Pearson DG, Markovic G (2009) Crystallization of megacrysts from protokimberlitic fluids: Geochemical evidence from high-Cr megacrysts in the Jericho kimberlite. Lithos 112:284–295. doi: 10.1016/j.lithos.2009.06.008

Kopylova MG, Russell JK, Cookenboo H (1999) Petrology of Peridotite and Pyroxenite Xenoliths from the Jericho Kimberlite: Implications for the Thermal State of the Mantle beneath the Slave Craton, Northern Canada. J Petrol 40:79–104. doi: 10.1093/petroj/40.1.79

Korolyuk VN, Pokhilenko LN (2014) Electron probe determination of trace elements in olivine. X-Ray Spectrom 43:353–358. doi: 10.1002/xrs.2562

Krogh EJ (1988) The garnet-clinopyroxene Fe-Mg geothermometer - a reinterpretation of existing experimental data. Contrib to Mineral Petrol 99:44–48. doi: 10.1007/BF00399364

Kroslakova I, Guenther D (2007) Elemental fractionation in laser ablation-inductively coupled plasma-mass spectrometry: evidence for mass load induced matrix effects in the ICP during ablation of a silicate glass. J Anal At Spectrom 22:51–62. doi: 10.1039/B606522H

Kusky T (1989) Accretion of the Archean Slave province. Geology 17:63–67.

Lawless PJ, Gurney JJ, Dawson JB (1979) Polymict Peridotites from the Bultfontein and de Beers Mines, Kimberly, South Africa. The Mantle Sample: Inclusions in Kimberlites and Other Volcanics 144–155.

Le Maitre RW, Streckeisen A, Zanettin B, et al (eds) (2002) Igneous Rocks: A Classification and Glossary of Terms. Cambridge University Press

Le Roex AP, Bell DR, Davis P (2003) Petrogenesis of Group I Kimberlites from Kimberley, South Africa: Evidence from Bulk-rock Geochemistry. J Petrol 44:2261–2286. doi: 10.1093/petrology/egg077

Lockhart G, Grütter H, Carlson J (2004) Temporal, geomagnetic and related attributes of

kimberlite magmatism at Ekati, Northwest Territories, Canada. Lithos 77:665–682. doi: 10.1016/j.lithos.2004.03.029

Lu J, Zheng JP, Griffin WL, O'Reilly SY (2015) Microscale effects of melt infiltration into the lithospheric mantle : Peridotite xenoliths from Xilong , South China. Lithos 232:111–123. doi: 10.1016/j.lithos.2015.06.013

Luth RW, Stachel T (2014) The buffering capacity of lithospheric mantle: implications for diamond formation. Contrib to Mineral Petrol 168:1083. doi: 10.1007/s00410-014-1083-6

Malarkey J, Pearson DG, Kjarsgaard BA, et al (2010) From source to crust: Tracing magmatic evolution in a kimberlite and a melilitite using microsample geochemistry. Earth Planet Sci Lett 299:80–90. doi: 10.1016/j.epsl.2010.08.020

Mank AJG, Mason PRD (1999) A critical assessment of laser ablation ICP-MS as an analytical tool for depth analysis in silica-based glass samples. J Anal At Spectrom 14:1143–1153. doi: 10.1039/A903304A

Mather K (2012) A Xenolith-Based Lithospheric Transect of the Slave Craton, NWT, Canada. Durham University

Mather KA, Pearson DG, McKenzie D, et al (2011) Constraints on the depth and thermal history of cratonic lithosphere from peridotite xenoliths, xenocrysts and seismology. Lithos 125:729–742. doi: 10.1016/j.lithos.2011.04.003

McDonough WF, Sun S -s. (1995) The composition of the Earth. Chem Geol 120:223–253. doi: 10.1016/0009-2541(94)00140-4

McLean H, Banas A, Creighton S, et al (2007) Garnet xenocrysts from the Diavik mine, NWT, Canada: Composition, color, and paragenesis. Can Mineral 45:1131–1145. doi: 10.2113/gscanmin.45.5.1131

Menzies A, Alvarez E, Belmar M, et al (2015) Quantification of trace REE-minerals using automated mineralogy. In: Chilean Geological Congress, La Serena, Chile.

Menzies A, Westerlund K, Grütter H, et al (2004) Peridotitic mantle xenoliths from kimberlites on the Ekati Diamond Mine property, N.W.T., Canada: major element compositions and implications for the lithosphere beneath the central Slave craton☆. Lithos 77:395–412. doi:

10.1016/j.lithos.2004.04.013

Meyer HOA, Boyd FR (1972) Composition and origin of crystalline inclusions in natural diamonds. Geochim Cosmochim Acta 36:1255–1273. doi: 10.1016/0016-7037(72)90048-8

Milman-Barris MS, Beckett JR, Baker MB, et al (2008) Zoning of phosphorus in igneous olivine. Contrib to Mineral Petrol 155:739–765. doi: 10.1007/s00410-007-0268-7

Mitchell RH (1995) Kimberlites, Orangeites, and Related Rocks. Plenum Press, New York

Mitchell RH (1986) Kimberlites: Mineralogy, Geochemistry and Petrology. Plenum Press, New York

Moore A, Belousova E (2005) Crystallization of Cr-poor and Cr-rich megacryst suites from the host kimberlite magma: implications for mantle structure and the generation of kimberlite magmas. Contrib to Mineral Petrol 149:462–481. doi: 10.1007/s00410-005-0663-x

Moore A, Costin G (2016) Kimberlitic olivines derived from the Cr-poor and Cr-rich megacryst suites. Lithos 258–259:215–227. doi: 10.1016/j.lithos.2016.04.022

Moore AE (2012) The case for a cognate, polybaric origin for kimberlitic olivines. Lithos 128–131:1–10. doi: 10.1016/j.lithos.2011.11.002

Moss S, Russell JK, Andrews GDM (2008) Progressive infilling of a kimberlite pipe at Diavik, Northwest Territories, Canada: Insights from volcanic facies architecture, textures, and granulometry. J Volcanol Geotherm Res 174:103–116. doi: 10.1016/j.jvolgeores.2007.12.020

Müller W, Shelley M, Miller P, Broude S (2009) Initial performance metrics of a new custom-designed ArF excimer LA-ICPMS system coupled to a two-volume laser-ablation cell. J Anal At Spectrom 24:209–214. doi: 10.1039/b805995k

Nielsen T, Sand K (2008) The Majuagaa kimberlite dike, Maniitsoq region, West Greenland: constraints on an Mg-rich silicocarbonatitic melt composition from groundmass mineralogy and bulk. Can Mineral 46:1043–1061.

Nimis P, Grütter H (2010) Internally consistent geothermometers for garnet peridotites and pyroxenites. Contrib to Mineral Petrol 159:411–427. doi: 10.1007/s00410-009-0455-9

Nimis P, Taylor WR (2000) Single clinopyroxene thermobarometry for garnet peridotites. Part I.

Calibration and testing of a Cr-in-Cpx barometer and an enstatite-in-Cpx thermometer. Contrib to Mineral Petrol 139:541–554. doi: 10.1007/s004100000156

Nixon PH, Boyd FR (1973) The discrete nodule association in kimberlites from northern Lesotho. Lesotho kimberlites Maseru, Lesotho Natl Dev Corp 97–75.

Norman MD, Pearson NJ, Sharma a., Griffin WL (1996) Quantitative Analysis of Trace Elements in Geological Materials by Laser Ablation ICPMS: Instrumental Operating Conditions and Calibration of NIST Glasses. Geostand Newsl 20:247–261. doi: 10.1111/j.1751-908X.1996.tb00186.x

Nowell GM, Pearson DG, Bell DR, et al (2004) Hf isotope systematics of kimberlites and their megacrysts: New constraints on their source regions. J Petrol 45:1583–1612. doi: 10.1093/petrology/egh024

Nowicki T, Crawford B, Dyck D, et al (2004) The geology of kimberlite pipes of the Ekati property, Northwest Territories, Canada. Lithos 76:1–27. doi: 10.1016/j.lithos.2004.03.020

Padgham WA (1992) Mineral deposits in the Archean Slave Structural Province; lithological and tectonic setting. Precambrian Res 58:1–24.

Paton C, Hellstrom J, Paul B, et al (2011) Iolite: Freeware for the visualisation and processing of mass spectrometric data. J Anal At Spectrom 26:2508–2518. doi: 10.1039/c1ja10172b

Pearson DG, Canil D, Shirey SB (2003) Mantle Samples Included in Volcanic Rocks : Xenoliths and Diamonds. Treatise on Geochemistry 2:171–275.

Pearson DG, Irivine GJ, Carlson RW, et al (2002) The development of lithospheric keels beneath the earliest continents: time constraints using PGE and Re-Os isotope systematics. Geol Soc London, Spec Publ 199:65–90.

Pearson NJ, Powell WJ, Grant KJ, et al (2013) The hole story about laser ablation ICP-MS. In: Goldschmidt2013 Conference Abstracts.

Pilbeam LH, Nielsen TFD, Waight TE (2013) Digestion Fractional Crystallization (DFC): an Important Process in the Genesis of Kimberlites. Evidence from Olivine in the Majuagaa Kimberlite, Southern West Greenland. J Petrol. doi: 10.1093/petrology/egt016

Pivin M, Féménias O, Demaiffe D (2009) Metasomatic mantle origin for Mbuji-Mayi and

Kundelungu garnet and clinopyroxene megacrysts (Democratic Republic of Congo). Lithos 112:951–960. doi: 10.1016/j.lithos.2009.03.050

Price SE, Russell JK, Kopylova MG (2000) Primitive magma from the Jericho Pipe, NWT, Canada: constraints on primary kimberlite melt chemistry. J Petrol 41:789–808.

Reguir EP, Chakhmouradian AR, Halden NM, et al (2009) Major- and trace-element compositional variation of phlogopite from kimberlites and carbonatites as a petrogenetic indicator. Lithos 112:372–384. doi: 10.1016/j.lithos.2009.05.023

Ringwood AE (1966) Mineralogy of the mantle. In: Advances in earth science. p 357

Roedder E (1984) Fluid Inclusions, Volume 12. Mineralogical Society of America

Roeder PL, Schulze DJ (2008) Crystallization of groundmass spinel in kimberlite. J Petrol 49:1473–1495. doi: 10.1093/petrology/egn034

Russell JK, Porritt LA, Lavallée Y, Dingwell DB (2012) Kimberlite ascent by assimilation-fuelled buoyancy. Nature 481:352–6. doi: 10.1038/nature10740

Sarkar C, Heaman LM, Pearson DG (2015) Duration and periodicity of kimberlite volcanic activity in the Lac de Gras kimberlite field, Canada and some recommendations for kimberlite geochronology. Lithos 218–219:155–166. doi: 10.1016/j.lithos.2015.01.017

Schulze D (1985) Evidence for primary kimberlitic liquids in megacrysts from kimberlites in Kentucky, USA. J Geol 93:75–79.

Schulze D (1987) Megacrysts from alkalic volcanic rocks. In: Mantle xenoliths. Wiley, Chichester, pp 433–451

Schulze DJ (1997) The significance of eclogite and Cr-poor megacryst Garnets in diamond exploration. Explor Min Geol 6:349–366.

Schulze DJ, Anderson PFN, Hearn BC, Hetman CM (1995) Origin and Significance of Ilmenite Megacrysts and Macrocrysts from Kimberlite. Int Geol Rev 37:780–812. doi: 10.1080/00206819509465427

Shimizu N, Pokhilenko NP, Boyd FR, Pearson DG (1997) Geochemical characteristics of mantle xenoliths from Udachnaya kimberlite pipe. Geol i Geofiz 194–205.

Simon NSC, Irvine GJ, Davies GR, et al (2003) The origin of garnet and clinopyroxene in "depleted" Kaapvaal peridotites. Lithos 71:289–322. doi: 10.1016/S0024-4937(03)00118-X

Skinner E, Clement C (1979) Mineralogical classification of southern African kimberlites. In: Kimberlites, Diatremes, and Diamonds: Their Geology, Petrology, and Geochemistry. pp 129–139

Sobolev A V., Hofmann AW, Sobolev S V., Nikogosian IK (2005) An olivine-free mantle source of Hawaiian shield basalts. Nature 434:590–597. doi: 10.1038/nature03411

Sobolev A V, Hofmann AW, Kuzmin D V, et al (2007) The amount of recycled crust in sources of mantle-derived melts. Science (80-) 316:412–417. doi: 10.1126/science.1138113

Sokol AG, Kruk AN (2015) Conditions of kimberlite magma generation: experimental constraints. Russ Geol Geophys 56:245–259. doi: 10.1016/j.rgg.2015.01.018

Sokol AG, Kruk AN, Chebotarev DA, Palyanov YN (2016) Carbonatite melt–peridotite interaction at 5.5–7.0 GPa: Implications for metasomatism in lithospheric mantle. Lithos 248–251:66–79. doi: 10.1016/j.lithos.2016.01.013

Spandler C, O'Neill HSC (2010) Diffusion and partition coefficients of minor and trace elements in San Carlos olivine at 1,300ºC with some geochemical implications. Contrib to Mineral Petrol 159:1–28. doi: 10.1007/s00410-009-0456-8

Sparks RSJ, Brooker RA, Field M, et al (2009) The nature of erupting kimberlite melts. Lithos 112:429–438. doi: 10.1016/j.lithos.2009.05.032

Spetsius Z V., Taylor LA (2002) Partial Melting in Mantle Eclogite Xenoliths: Connections with Diamond Paragenesis. Int Geol Rev 44:973–987. doi: 10.2747/0020-6814.44.11.973

Stachel T, Brey GP, Harris JW (2005) Inclusions in Sublithospheric Diamonds: Glimpses of Deep Earth. Elements 1:73–78. doi: 10.2113/gselements.1.2.73

Stachel T, Harris JW, Tappert R, Brey GP (2003) Peridotitic diamonds from the Slave and the Kaapvaal cratons—similarities and differences based on a preliminary data set. Lithos 71:489–503. doi: 10.1016/S0024-4937(03)00127-0

Stachel T, Viljoen KS, Brey G, Harris JW (1998) Metasomatic processes in lherzolitic and harzburgitic domains of diamondiferous lithospheric mantle: REE in garnets from xenoliths

and inclusions in diamonds. Earth Planet Sci Lett 159:1–12. doi: 10.1016/S0012-821X(98)00064-8

Stone RS (2016) The behavior of orthopyroxene in carbonatitic melts. In: MSc Thesis. University of Alberta, p 142

Stone RS, Luth RW (2016) Orthopyroxene survival in deep carbonatite melts: implications for kimberlites. Contrib to Mineral Petrol 171:63. doi: 10.1007/s00410-016-1276-2

Su B-X, Zhang H-F, Deloule E, et al (2012) Extremely high Li and low δ7Li signatures in the lithospheric mantle. Chem Geol 292–293:149–157. doi: 10.1016/j.chemgeo.2011.11.023

Tappe S, Graham Pearson D, Kjarsgaard BA, et al (2013) Mantle transition zone input to kimberlite magmatism near a subduction zone: Origin of anomalous Nd-Hf isotope systematics at Lac de Gras, Canada. Earth Planet Sci Lett 371–372:235–251. doi: 10.1016/j.epsl.2013.03.039

Tappert R, Stachel T, Harris JW, et al (2005) Mineral inclusions in diamonds from the Panda kimberlite, Slave Province, Canada. Eur J Mineral 17:423–440. doi: 10.1127/0935-1221/2005/0017-0423

Taylor LA, Neal CR (1989) Eclogites with Oceanic Crustal and Mantle Signatures from the Bellsbank Kimberlite , South Africa , Part I : Mineralogy , Petrography , and Whole Rock Chemistry Author (s): Lawrence A . Taylor and Clive R . Neal Published by : The University of Chicago. Group 97:551–567.

van Achterbergh E, Griffin WL, Ryan CG, et al (2002) Subduction signature for quenched carbonatites from the deep lithosphere. Geology 30:743. doi: 10.1130/0091-7613(2002)030<0743:SSFQCF>2.0.CO;2

van Achterbergh E, Griffin WL, Ryan CG, et al (2004) Melt inclusions from the deep Slave lithosphere: implications for the origin and evolution of mantle-derived carbonatite and kimberlite. Lithos 76:461–474. doi: 10.1016/j.lithos.2004.04.007

Wan Z, Coogan LA, Canil D (2008) Experimental calibration of aluminum partitioning between olivine and spinel as a geothermometer. Am Mineral 93:1142–1147. doi: 10.2138/am.2008.2758

Waterton P, Pearson DG, Kjarsgaard B, et al (2016) Age, Origin, and Thermal Evolution of the ultra-fresh ~1.9 Ga Winnipegosis Komatiites, Manitoba, Canada. Lithos. doi: 10.1016/j.lithos.2016.10.033

Weiss Y, Class C, Goldstein SL, Hanyu T (2016) Key new pieces of the HIMU puzzle from olivines and diamond inclusions. Nature 537:666–670. doi: 10.1038/nature19113

Weiss Y, McNeill J, Pearson DG, et al (2015) Highly saline fluids from a subducting slab as the source for fluid-rich diamonds. Nature 524:339–342. doi: 10.1038/nature14857

Wyllie PJ, Huang WL (1975) Peridotite, kimberlite, and carbonatite explained in the system CaO-MgO-SiO2-CO2. Geology 621–624.

Zhang L-Y, Prelević D, Li N, et al (2016) Variation of olivine composition in the volcanic rocks in the Songliao basin, NE China: lithosphere control on the origin of the K-rich intraplate mafic lavas. Lithos 262:153–168. doi: 10.1016/j.lithos.2016.06.028

Ziberna L, Klemme S, Nimis P (2013) Garnet and spinel in fertile and depleted mantle: Insights from thermodynamic modelling. Contrib to Mineral Petrol 166:411–421. doi: 10.1007/s00410-013-0882-5

Appendix

A2.1. EPMA Analytical Conditions

1. Clinopyroxene

Element	Cr	Mg	Ca	Na	Mn	Ti	Al	K	Si	Fe	Zn	Ni	P
Curr.(A)	2.00E-08	1.98E-08	1.98E-08	2.00E-08	2.01E-08	2.08E-08	2.05E-08	2.00E-08	1.98E-08	2.08E-08	2.00E-08	2.08E-08	2.01E-08
X-ray	Ka	Ka	Ka	Ka	Ka	Ka	Ka	Ka	Ka	Ka	La	Ka	Ka
Crystal	PET	TAP	PETH	TAPJ, TAP	LIFH	PET	TAP, TAPJ	PETH	TAPJ	LIFH	TAPJ	LIFH	PETH
Peak (s)	60, 40	60, 50	60, 40	40, 60	40, 30	60, 50	60	60	40, 60	40, 30	40	40	50
Back (s)	30, 20	30, 25	30, 20	20, 30	20, 15	30, 25	30	30	20, 30	20, 15	20	20	25
Element	Cr_2O_3	MgO	CaO	Na_2O	MnO	TiO_2	Al_2O_3	K_2O	SiO_2	FeO	ZnO	NiO	P_2O_5
Standard	chromite	diopside	diopside	albite	rhodonite	rutile	Gore_CB1	sanidine	diopside	Fayalite_CB1	willemite	Ni_wire_CB1	apatite
Wt.(%)	40.7	18.63	25.74	11.59	36.85	100	22.51	12.11	55.37	66.94	66.87	127.2526	40.87

2. Garnet

Element	Cr	Na	P	Si	Ni	Ti	Mg	K	Al	Fe	Ca	Mn
Curr.(A)	2.00E-08	2.01E-08	2.01E-08	2.01E-08	2.01E-08	2.01E-08	2.01E-08	2.01E-08	2.01E-08	2.01E-08	2.01E-08	2.01E-08
X-ray	Ka	Ka	Ka	Ka	Ka	Ka	Ka	Ka	Ka	Ka	Ka	Ka
Crystal	PET	TAP	PETH	TAPJ	LIFH	PET	TAP	PETH	TAPJ	LIFH	PETH	LIFH
Peak (s)	40	60	50	60	40	50	50	60	60	30	40	30
Back (s)	20	30	25	30	20	25	25	30	30	15	20	15
Element	Cr_2O_3	Na_2O	P_2O_5	SiO_2	NiO	TiO_2	MgO	K_2O	Al_2O_3	FeO	CaO	MnO
Standard	Cr_2O_3_CB1	albite	apatite	FrankSmith_CB1	Ni_wire_CB1	rutile	Fo93	sanidine	FrankSmith_CB1	Fayalite_CB1	diopside	rhodonite
Wt.(%)	100	11.59	40.87	41.52	127.2526	100	51.63	12.11	21.75	66.94	25.74	36.85

3. Carbonate

Element	Ba	Mg	Ca	Sr	Fe	Mn	Na
Curr.(A)	1.00E-08	1.00E-08	1.00E-08	1.00E-08	1.01E-08	1.00E-08	1.01E-08
X-ray	La	Ka	Ka	La	Ka	Ka	Ka
Crystal	PET	TAP	PETH	TAPJ	LIFH	LIFH	TAPJ
Peak (s)	20, 40	20, 40	20, 40	40	20, 40	20, 40	40
Back (s)	10, 20	10, 20	10, 20	20	10, 20	10, 20	20
Element	BaO	MgO	CaO	SrO	FeO	MnO	MnO
Standard	barite	dolomite	calcite	strontianite	siderite	willemite	willemite
Wt.(%)	65.7	22.04	56.1	67.67	59.08	4.82	4.82

4. Olivine

Element	Cr	Mg	Ca	Si	Ni	Ti	Na	K	Al	Fe	Mn	Zn
Curr.(A)	2.00E-08	2.04E-08	2.00E-08	2.04E-08	2.00E-08	2.00E-08	2.00E-08	2.02E-08	2.00E-08	2.00E-08	2.00E-08	2.02E-08
X-ray	Ka	Ka	Ka	Ka	Ka	Ka	Ka	Ka	Ka	Ka	Ka	Ka
Crystal	PET	TAP	PETH	TAPJ	LIFH	PET	TAP	PETH	TAPJ	LIFH	LIFH	LIFH
Peak (s)	40	50	60	40	40	50	60	60	60	30	30	40
Back (s)	20	25	30	20	20	25	30	30	30	15	15	20
Element	Cr_2O_3	MgO	CaO	SiO_2	NiO	TiO_2	Na_2O	K_2O	Al_2O_3	FeO	MnO	ZnO
Standard	chromite	Fo90	diopside	Fo90	Ni_wire_CB1	rutile	albite	orthoclase	Gore_CB1	Fayalite_CB1	willemite	gahnite
Wt.(%)	40.7	49.42	25.74	40.81	127.2526	100	11.59	14.92	22.51	66.94	4.82	42.5

5. Chromite

Element	Cr	Mg	Ca	Al	Mn	Ti	K	Si	Fe	Ni	Zn
Curr.(A)	2.00E-08	2.04E-08	2.00E-08	2.02E-08	2.00E-08	2.00E-08	2.02E-08	2.04E-08	2.00E-08	2.00E-08	2.02E-08
X-ray	Ka	Ka	Ka	Ka	Ka	Ka	Ka	Ka	Ka	Ka	Ka
Crystal	PET	TAP	PETH	TAPJ	LIFH	PET	PETH	TAPJ	LIFH	LIFH	LIFH
Peak (s)	40	50	60	60	30	50	60	40	30	40	40
Back (s)	20	25	30	30	15	25	30	20	15	20	20
Element	Cr_2O_3	MgO	CaO	Al_2O_3	MnO	TiO_2	K_2O	SiO_2	FeO	NiO	ZnO
Standard	chromite	Fo90	diopside	gahnite	willemite	rutile	orthoclase	Fo90	hematite	Ni_wire_CB1	gahnite
Wt.(%)	40.7	49.42	25.74	55.32	4.82	100	14.92	40.81	89.7113	127.2526	42.5

6. Phlogopite

Element	F	Na	K	Cr	Mn	Mg	Cl	Ti	Fe	Al	Ca	Ba	Ni
Curr.(A)	1.52E-08	1.52E-08	1.51E-08	1.52E-08	1.52E-08	1.52E-08	1.50E-08	1.50E-08	1.52E-08	1.53E-08	1.52E-08	1.50E-08	1.53E-08
X-ray	Ka	Ka	Ka	Ka	Ka	Ka	Ka	Ka	Ka	Ka	Ka	La	Ka
Crystal	LDE1	TAP	PETH	PET	LIFH	TAP	PETH	PET	LIFH	TAP	PETH	PET	LIFH
Peak (s)	40, 60	60, 40	60, 50	40, 50	30, 40	50, 40	40, 50	50	30, 50	60, 40	60, 50	40, 50	40
Back (s)	20, 30	30, 20	30, 25	20, 25	15, 20	25, 20	20, 25	25	15, 25	30, 20	30, 25	20, 25	20
Element Standard	F apatite	Na_2O albite	K_2O sanidine	Cr_2O_3 chromite	MnO willemite	MgO diopside	Cl tugtupite	TiO_2 rutile	FeO Fayalite_CB1	Al_2O_3 Gore_CB1	CaO diopside	BaO sanidine	NiO Ni_wire_CB1
Wt.(%)	3.53	11.59	12.11	40.7	4.82	18.63	7.58	100	66.94	22.51	25.74	0.99	127.2526

6. Phlogopite cont.

Element	Si	Zn
Curr.(A)	1.52E-08	1.49E-08
X-ray	Ka	Ka
Crystal	TAP	LIFH
Peak (s)	40	40
Back (s)	20	20
Element	SiO_2	ZnO
Standard	diopside	willemite
Wt.(%)	55.37	66.87

A2.2. EPMA Secondary Standards

Session	Cpx	SiO_2	TiO_2	Al_2O_3	Cr_2O_3	FeO	MnO	MgO	CaO	Na_2O	Total	Comment
2013-06-20	mean	**50.09**	**0.84**	**8.50**	**0.16**	**6.14**	**0.13**	**15.91**	**16.22**	**1.30**	**99.29**	639 augite
	SD	0.11	0.01	0.03	0.01	0.04	0.01	0.07	0.06	0.02	0.16	
Jarosewich 1980	Augite	**50.73**	**0.74**	**8.79**		**6.37**	**0.13**	**16.65**	**15.82**	**1.27**		
	accuracy	-1.3%	13.2%	-3.3%		-3.6%	2.7%	-4.4%	2.5%	2.6%		
2013-06-20	mean	**55.36**	**0.06**	**0.07**	**0.01**	**0.05**	**0.04**	**18.18**	**26.13**	**0.02**	**99.92**	639 diopside
	SD	0.08	0.01	0.00	0.01	0.01	0.01	0.06	0.10	0.01	0.20	
Micronex	diopside	**55.36**	**0.09**	**0.09**	**0.01**	**0.05**	**0.05**	**18.63**	**25.73**	**0.02**		
	accuracy	0.0%	-34.2%	-19.4%	-30.0%	-3.8%	-14.8%	-2.4%	1.6%	-20.6%		
2013-08-26	mean	**50.25**	**0.83**	**8.12**	**0.16**	**6.18**	**0.14**	**16.09**	**16.26**	**1.38**	**99.41**	639 augite
	SD	0.16	0.02	0.12	0.01	0.04	0.01	0.13	0.12	0.03	0.40	
Jarosewich 1980	Augite	**50.73**	**0.74**	**8.79**		**6.37**	**0.13**	**16.65**	**15.82**	**1.27**		
	accuracy	-0.9%	12.6%	-7.6%		-3.1%	10.9%	-3.4%	2.8%	8.3%		
2013-08-26	mean	**55.43**	**0.06**	**0.06**	**0.00**	**0.05**	**0.05**	**18.45**	**26.31**	**0.02**	**100.42**	639 diopside
	SD	0.18	0.01	0.00	0.00	0.00	0.00	0.08	0.09	0.01	0.11	
Micronex	diopside	**55.36**	**0.09**	**0.09**	**0.01**	**0.05**	**0.05**	**18.63**	**25.73**	**0.02**		
	accuracy	0.1%	-35.4%	-32.6%	-83.3%	-9.7%	-0.3%	-1.0%	2.3%	-21.7%		
2013-11-14	mean	**50.21**	**0.79**	**8.42**	**0.15**	**6.34**	**0.14**	**15.67**	**16.10**	**1.26**	**99.08**	639 augite
	SD	0.17	0.02	0.01	0.01	0.03	0.00	0.08	0.07	0.03	0.19	
Jarosewich 1980	Augite	**50.73**	**0.74**	**8.79**		**6.37**	**0.13**	**16.65**	**15.82**	**1.27**		
	accuracy	-1.0%	6.5%	-4.2%		-0.4%	9.8%	-5.9%	1.8%	-0.8%		

Session	Cpx	SiO_2	TiO_2	Al_2O_3	Cr_2O_3	FeO	MnO	MgO	CaO	Na_2O	Total	Comment
2014-02-12	mean	**50.10**	**0.80**	**8.36**	**0.16**	**6.29**	**0.15**	**16.16**	**15.86**	**1.30**	**99.18**	639 augite
	SD	0.09	0.01	0.05	0.01	0.02	0.01	0.09	0.16	0.06	0.26	
Jarosewich 1980	Augite	**50.73**	**0.74**	**8.79**		**6.37**	**0.13**	**16.65**	**15.82**	**1.27**		
	accuracy	-1.2%	8.6%	-4.9%		-1.3%	12.8%	-2.9%	0.3%	2.1%		
2014-02-13	mean	**50.42**	**0.85**	**8.21**	**0.13**	**6.37**	**0.14**	**16.42**	**16.63**	**1.38**	**100.56**	639 augite
	SD	0.26	0.04	0.05	0.03	0.05	0.04	0.11	0.12	0.09	0.16	
Jarosewich 1980	Augite	**50.73**	**0.74**	**8.79**		**6.37**	**0.13**	**16.65**	**15.82**	**1.27**		
	accuracy	-0.6%	14.8%	-6.6%		0.0%	7.7%	-1.4%	5.1%	8.8%		
2014-07-28	mean	**50.44**	**0.83**	**8.43**	**0.15**	**6.24**	**0.15**	**16.80**	**16.23**	**1.36**	**100.64**	639 augite
	SD	0.21	0.01	0.05	0.02	0.03	0.00	0.05	0.05	0.02	0.22	
Jarosewich 1980	Augite	**50.73**	**0.74**	**8.79**		**6.37**	**0.13**	**16.65**	**15.82**	**1.27**		
	accuracy	-0.6%	12.6%	-4.2%		-2.0%	17.1%	0.9%	2.6%	7.3%		

Session	Garnet	SiO_2	TiO_2	Al_2O_3	Cr_2O_3	FeO	MnO	MgO	CaO	Total	Comment
2013-11-14	mean	**41.73**	**0.40**	**23.74**	**0.08**	**10.56**	**0.33**	**18.59**	**5.09**	**100.52**	639 pyrope
	SD	0.10	0.01	0.02	0.01	0.06	0.02	0.15	0.03	0.24	
Jarosewich 1980	pyrope Kakanui	**41.46**	**0.47**	**23.73**		**10.69**	**0.28**	**18.52**	**5.16**		
accuracy		0.6%	-14.6%	0.0%		-1.2%	16.5%	0.4%	-1.3%		
2014-02-12	mean	**41.54**	**0.41**	**23.66**	**0.08**	**10.51**	**0.32**	**19.59**	**4.95**	**101.04**	639 pyrope
	SD	0.09	0.01	0.05	0.01	0.03	0.01	0.06	0.08	0.14	
Jarosewich 1980	pyrope Kakanui	**41.46**	**0.47**	**23.73**		**10.69**	**0.28**	**18.52**	**5.16**		
	accuracy	0.2%	-13.3%	-0.3%		-1.7%	15.8%	5.8%	-4.2%		
2014-07-28	mean	**40.99**	**0.46**	**22.90**	**0.10**	**10.31**	**0.32**	**19.01**	**5.31**	**99.39**	639 pyrope
	SD	0.19	0.01	0.13	0.01	0.05	0.01	0.08	0.01	0.30	
Jarosewich 1980	pyrope Kakanui	**41.46**	**0.47**	**23.73**		**10.69**	**0.28**	**18.52**	**5.16**		
	accuracy	-1.1%	-2.3%	-3.5%		-3.6%	15.5%	2.6%	2.8%		

Session	Carbonate	CaO	MgO	FeO	MnO	SrO	BaO	Total	Comment
2013-06-19	mean	**56.28**	**0.02**	**0.01**	**0.08**	**0.02**	**0.01**	**56.42**	EPS3 calcite std
	SD	1.05	0.01	0.01	0.02	0.01	0.02	1.07	
Jarosewich 1982	calcite USNM 136321	**56.10**							
	accuracy	0.3%							
2013-06-19	mean	**29.84**	**22.25**	**0.06**	**0.03**	**0.04**	**0.02**	**52.23**	EPS3 dolomite std
	SD	0.17	0.12	0.03	0.02	0.01	0.03	0.19	
Jarosewich 1982	dolomite USNM 10057	**30.56**	**22.04**						
	accuracy	-2.4%	0.9%						
2013-06-19	mean	**0.01**	**0.17**	**58.44**	**2.84**	**0.01**	**0.01**	**61.47**	EPS3 siderite std
	SD	0.01	0.07	0.29	0.05	0.01	0.01	0.31	
Jarosewich 1982	siderite USNM R2460			**59.08**	**2.95**				
	accuracy			-1.1%	-3.9%				
2013-08-27	mean	**30.46**	**22.73**	**0.05**	**0.01**	**0.02**	**0.02**	**53.30**	EPS-3 dolomite
	SD	0.21	0.12	0.01	0.01	0.01	0.03	0.25	
Jarosewich 1982	dolomite USNM 10057	**30.56**	**22.04**						
	accuracy	-0.3%	3.1%						
2013-08-27	mean	**56.29**	**0.01**	**0.00**	**0.09**	**0.02**	**0.01**	**56.43**	EPS-3 calcite
Jarosewich 1982	calcite USNM 136321	**56.10**							
	accuracy	0.3%							

Session	Carbonate	CaO	MgO	FeO	MnO	SrO	BaO	F	Total
2013-11-15	mean	**31.24**	**22.27**	**0.08**	**0.03**	**0.03**		**0.20**	**53.84**
	SD	0.42	0.43	0.03	0.01	0.02		0.05	0.50
Jarosewich 1982	dolomite USNM 10057	**30.56**	**22.04**						
	accuracy	2.2%	1.0%						
2014-02-13	mean	**30.67**	**21.50**	**0.09**	**0.03**	**0.02**	**0.05**	**0.10**	**52.45**
	SD	0.18	0.15	0.02	0.02	0.01	0.04	0.04	0.18
Jarosewich 1982	dolomite USNM 10057	**30.56**	**22.04**						
	accuracy	0.4%	-2.5%						

Session	Carbonate	CaO	MgO	FeO	MnO	SrO	BaO	Total	Comment
2014-07-29	mean	**55.15**	**0.00**	**0.00**	**0.12**	**0.04**	**0.18**	**55.49**	EPS3 calcite
	SD	0.28	0.00	0.00	0.02	0.03	0.11	0.22	
Jarosewich 1982	calcite USNM 136321	**56.10**							
	accuracy	-1.7%							

Session	Olivine	SiO_2	Al_2O_3	Cr_2O_3	FeO	MnO	NiO	MgO	CaO	Total	Comment
2013-06-20	mean	**40.47**	**0.04**	**0.01**	**9.62**	**0.13**	**0.30**	**49.50**	**0.10**	**100.17**	EPS1 Fo90 std
	SD	0.05	0.01	0.01	0.03	0.01	0.03	0.24	0.01	0.27	
Jarosewich 1980	Fo90 SC	**40.81**			**9.55**	**0.14**		**49.42**			
	accuracy	-0.8%			0.8%	-5.7%		0.2%			
2013-06-20	mean	**41.03**	**0.01**	**0.00**	**7.29**	**0.11**	**0.32**	**51.11**	**0.01**	**99.88**	EPS1 Fo93 std
	SD	0.11	0.01	0.00	0.05	0.02	0.03	0.17	0.00	0.12	
Hofmeister	Balsam Gap	**40.85**	**0.13**		**7.17**	**0.07**	**0.30**	**51.63**			
	accuracy	0.5%	-90.8%		1.6%	51.4%	6.7%	-1.0%			
2013-06-21	mean	**40.53**	**0.05**	**0.02**	**9.65**	**0.14**	**0.30**	**49.29**	**0.10**	**100.07**	EPS1 Fo90 std
	SD	0.14	0.01	0.01	0.04	0.01	0.03	0.11	0.00	0.10	
Jarosewich 1980	Fo90 SC	**40.81**			**9.55**	**0.14**		**49.42**			
	accuracy	-0.7%			1.0%	2.0%		-0.3%			
2013-06-21	mean	**41.05**	**0.01**	**0.01**	**7.35**	**0.11**	**0.32**	**51.02**	**0.01**	**99.88**	EPS1 Fo93 std
	SD	0.12	0.00	0.01	0.02	0.00	0.07	0.14	0.00	0.20	
Hofmeister	Balsam Gap	**40.85**	**0.13**		**7.17**	**0.07**	**0.30**	**51.63**			
	accuracy	0.5%	-90.6%		2.5%	55.7%	7.4%	-1.2%			
2014-02-12	mean	**41.23**	**0.01**	**0.01**	**7.35**	**0.11**	**0.39**	**51.99**	**0.01**	**101.09**	EPS1 Fo93
	SD	0.05	0.01	0.01	0.04	0.01	0.01	0.14	0.01	0.18	
Hofmeister	Balsam Gap	**40.85**	**0.13**		**7.17**	**0.07**	**0.30**	**51.63**			
	accuracy	0.9%	-89.9%		2.5%	58.6%	28.8%	0.7%			
2014-07-28	mean	**39.34**	**0.03**	**0.02**	**0.33**	**16.70**	**0.00**	**44.84**	**0.01**	**101.26**	EPS1 Fo83
	SD	0.12	0.00	0.01	0.01	0.04	0.01	0.07	0.00	0.18	
Jarosewich 1980	Fo83	**38.95**		**0.02**	**0.3**	**16.62**		**43.58**			
	accuracy	1.0%		-4.2%	8.6%	0.5%		2.9%			

Session	Chromite	SiO_2	TiO_2	Al_2O_3	Cr_2O_3	MnO	FeO	NiO	MgO	CaO	Total	Comment
2013-06-21	mean	**0.13**	**0.70**	**12.37**	**40.52**	**0.25**	**34.62**	**0.12**	**8.83**	**0.01**	**97.54**	639 chromite std
	SD	0.02	0.01	0.03	0.08	0.01	0.03	0.02	0.03	0.00	0.12	
in-house	Stillwater	**0.18**	**0.80**	**12.62**	**40.70**	**0.16**	**35.29**	**0.13**	**8.46**	**0.07**		
	accuracy	-27.4%	-12.0%	-2.0%	-0.5%	55.0%	-1.9%	-7.1%	4.4%	-81.1%		
2013-11-14	mean	**0.04**	**0.70**	**14.30**	**41.25**	**0.19**	**34.66**	**0.13**	**8.79**			639 chromite
	SD	0.01	0.01	0.04	0.14	0.01	0.03	0.02	0.05			
in-house	Stillwater	**0.18**	**0.80**	**12.62**	**40.70**	**0.16**	**35.29**	**0.13**	**8.46**			
	accuracy	-77.2%	-12.3%	13.3%	1.3%	19.4%	-1.8%	-0.5%	3.9%			
2014-02-12	mean	**0.04**	**0.11**	**10.83**	**60.38**	**0.18**	**12.71**	**0.17**	**16.27**		**100.70**	EPS1 NC-chromite
	SD	0.01	0.01	0.05	0.10	0.01	0.04	0.01	0.04		0.13	
Jarosewich 1980	Chromite NC			**9.92**	**60.50**	**0.11**	**13.04**		**15.20**			
	accuracy			9.2%	-0.2%	60.2%	-2.5%		7.1%			
2014-07-28	mean	**0.06**	**0.73**	**13.11**	**41.01**	**0.21**	**33.98**	**0.12**	**9.42**		**98.65**	639 chromite
	SD	0.03	0.01	0.08	0.07	0.01	0.09	0.01	0.06		0.14	
in-house	Stillwater	**0.18**	**0.80**	**12.62**	**40.70**	**0.16**	**35.29**	**0.13**	**8.46**			
	accuracy	-64.5%	-9.1%	3.9%	0.8%	33.8%	-3.7%	-6.8%	11.3%			

Session	Mica	SiO_2	TiO_2	Al_2O_3	MnO	FeO	MgO	CaO	BaO	Na_2O	K_2O	F	Cl	Total
2013-06-26	mean	**35.18**	**2.97**	**13.88**	**0.36**	**30.28**	**4.66**	**0.01**	**0.09**	**0.08**	**9.23**	**0.71**	**0.35**	**97.79**
	SD	0.12	0.06	0.11	0.03	0.12	0.05	0.01	0.02	0.02	0.09	0.10	0.01	0.26
in-house	biotite	**34.40**	**3.06**	**13.30**	**0.38**	**29.72**	**4.67**	**0.02**	**0.18**	**0.17**	**9.21**	**0.66**		
	accuracy	2.26%	-2.87%	4.34%	-4.47%	1.87%	-0.12%	-52.22%	-48.02%	-55.10%	0.18%	7.34%		
2013-08-28	mean	**34.07**	**2.86**	**13.48**	**0.34**	**30.01**	**4.74**	**0.04**	**0.13**	**0.05**	**8.84**	**0.19**	**0.35**	**95.12**
	SD	0.13	0.09	0.04	0.03	0.29	0.03	0.02	0.06	0.00	0.27	0.33	0.02	0.40
in-house	biotite	**34.40**	**3.06**	**13.30**	**0.38**	**29.72**	**4.67**	**0.02**	**0.18**	**0.17**	**9.21**	**0.66**		
	accuracy	-0.96%	-6.43%	1.35%	-9.74%	0.99%	1.57%	90.00%	-27.04%	-69.80%	-3.98%	-70.86%		
2013-11-15	mean	**34.02**	**3.00**	**13.54**	**0.37**	**30.66**	**4.78**	**0.00**		**0.09**	**9.48**	**0.90**	**0.38**	**97.22**
	SD	0.31	0.06	0.10	0.03	0.09	0.06	0.00		0.02	0.15	0.06	0.02	0.49
in-house	biotite	**34.40**	**3.06**	**13.30**	**0.38**	**29.72**	**4.67**	**0.02**		**0.17**	**9.21**	**0.66**		
	accuracy	-1.1%	-1.9%	1.8%	-2.1%	3.2%	2.3%	-100.0%		-46.9%	3.0%	36.7%		
2014-02-13	mean	**35.13**	**2.94**	**13.57**	**0.38**	**30.68**	**4.79**	**0.00**	**0.17**	**0.09**	**9.26**	**0.66**	**0.35**	**98.02**
	SD	0.29	0.08	0.09	0.03	0.21	0.10	0.00	0.11	0.02	0.10	0.02	0.02	0.49
in-house	biotite	**34.40**	**3.06**	**13.30**	**0.38**	**29.72**	**4.67**	**0.02**	**0.18**	**0.17**	**9.21**	**0.66**		
accuracy		2.1%	-3.8%	2.0%	-0.9%	3.2%	2.7%	-90.0%	-5.9%	-50.0%	0.5%	-0.5%		

A2.3. LA-ICP-MS Analytical Conditions

Mineral	Laser energy [mJ]	Transmission [%]	Fluene [J/cm^2]	Repetition rate [Hz]	Background time [s]	Ablation time [s]	Calibration material	Internal standard	Secondary standards
Phlogopite	120	44	~7	10	60	60	NIST SRM 612	^{29}Si	NIST SRM 614, BIR-1G
Isotopes analyzed:	^{43}Ca, ^{45}Sc, ^{51}V, ^{52}Cr, ^{55}Mn, ^{59}Co, ^{60}Ni, ^{85}Rb, ^{88}Sr, ^{90}Zr, ^{93}Nb, ^{133}Cs, ^{137}Ba, ^{140}Ce, ^{178}Hf, ^{181}Ta								

A2.4. LA-ICP-MS Secondary Standards

Session	Standard	Ca	Sc	V	Cr	Mn	Co	Ni	Rb	Sr	Zr	Nb	Cs	Ba	Ce	Hf	Ta
11/06/2014	BIR-1G	77820	34.9	258	303	1138	54.5	186	0.16	85.9	10.3	0.37	b.d.l.	5.2	1.49	0.38	0.025
11/06/2014	BIR-1G	80860	35.7	264	313	1160	55.4	186	0.14	89.3	10.7	0.39	b.d.l.	5.5	1.49	0.38	0.021
11/06/2014	BIR-1G	83110	36.4	275	321	1203	57.8	194	0.20	91.3	10.8	0.40	b.d.l.	5.3	1.55	0.47	0.021
11/06/2014	BIR-1G	81970	36.8	274	322	1200	59.0	199	0.23	91.9	11.4	0.35	b.d.l.	5.6	1.52	0.45	0.031
mean		**80940**	**35.9**	**268**	**315**	**1175**	**56.7**	**191**	**0.18**	**89.6**	**10.8**	**0.38**		**5.4**	**1.51**	**0.42**	**0.025**
SD		2274	0.8	8	9	32	2.1	7	0.04	2.7	0.4	0.02		0.2	0.03	0.04	0.005
Average detection limit		124	0.2	0.1	0.5	0.2	0.2	0.2	0.1	0.04	0.01	0.003	0.01	0.07	0.003	0.005	0.005
GeoRem		**95000**	**43.0**	**326**	**392**	**1471**	**52.0**	**166**	**0.20**	**109.0**	**14.0**	**0.55**	**0.007**	**7.1**	**1.89**	**0.57**	**0.036**
Accuracy		-15%	-16%	-18%	-20%	-20%	9%	15%	-11%	-18%	-23%	-31%		-25%	-20%	-26%	-31%
17/07/2014	BIR-1G	77400	33.4	276	332	1273	54.1	182	0.14	83.9	9.8	0.43	0.009	5.3	1.44	0.46	0.022
17/07/2014	BIR-1G	76700	33.2	273	329	1277	53.6	178	0.19	84.4	9.9	0.35	b.d.l.	5.4	1.46	0.48	0.021
17/07/2014	BIR-1G	79000	35.3	293	360	1336	57.1	191	0.19	92.0	10.7	0.44	b.d.l.	5.4	1.60	0.47	0.030
17/07/2014	BIR-1G	79400	35.3	293	353	1359	57.2	190	0.25	91.6	10.8	0.49	b.d.l.	5.5	1.57	0.43	0.022
mean		**78125**	**34.3**	**284**	**343**	**1311**	**55.5**	**185**	**0.19**	**88.0**	**10.3**	**0.43**	**0.009**	**5.4**	**1.52**	**0.46**	**0.024**
SD		1284	1.2	11	15	43	1.9	6	0.04	4.4	0.5	0.06		0.1	0.08	0.02	0.004
Average detection limit		91	0.1	0.1	0.4	0.2	0.1	0.2	0.1	0.02	0.01	0.002	0.008	0.04	0.002	0.007	0.003
GeoRem		**95000**	**43.0**	**326**	**392**	**1471**	**52.0**	**166**	**0.20**	**109.0**	**14.0**	**0.55**	**0.007**	**7.1**	**1.89**	**0.57**	**0.036**
Accuracy		-18%	-20%	-13%	-12%	-11%	7%	11%	-4%	-19%	-26%	-23%	31%	-25%	-20%	-20%	-33%
17/07/2014	NIST SRM614	86200	1.40	0.96	1.62	1.32	0.69	1.0	0.82	44.8	0.87	0.80	0.65	3.0	0.77	0.68	0.71
17/07/2014	NIST SRM614	87010	1.51	0.91	0.29	1.41	0.72	0.9	0.81	44.8	0.74	0.80	0.66	3.2	0.73	0.70	0.76
17/07/2014	NIST SRM614	86750	1.56	1.09	3.40	1.24	0.71	0.9	0.92	46.7	0.90	0.81	0.68	3.1	0.77	0.74	0.77
17/07/2014	NIST SRM614	86740	1.64	1.00	0.50	1.51	0.70	0.8	0.84	47.1	0.83	0.82	0.70	3.3	0.79	0.67	0.79
mean		**86675**	**1.53**	**0.99**	**1.45**	**1.37**	**0.70**	**0.9**	**0.84**	**45.8**	**0.83**	**0.81**	**0.67**	**3.1**	**0.77**	**0.70**	**0.76**
SD		340	0.10	0.08	1.42	0.12	0.01	0.1	0.05	1.2	0.07	0.01	0.02	0.1	0.02	0.03	0.03
Average detection limit		76	0.1	0.1	0.3	0.1	0.1	0.1	0.05	0.02	0.01	0.003	0.01	0.04	0.002	0.002	0.003
GeoRem		**85048**	**0.74**	**1.01**	**1.19**	**1.42**	**0.79**	**1.1**	**0.86**	**45.8**	**0.85**	**0.82**	**0.66**	**3.2**	**0.81**	**0.71**	**0.81**
Accuracy		2%	106%	-2%	22%	-4%	-11%	-17%	-1%	0%	-2%	-2%	1%	-2%	-6%	-2%	-6%

A2.5. EPMA Megacryst Hosts

Clinopyroxene

Location	Diavik - A154N									
Sample	DVK_CD_01		DVK_CD_02B		DVK_CD_04B		DVK_CD_6A		DVK_CD_6B	
Zone	clear	spongy rim	clear	spongy rim	clear	spongy rim	clear	spongy rim	clear	spongy rim
Major element analyses (wt.%)										
SiO_2	55.01	54.51	54.96	54.65	55.30	54.09	55.25	54.37	55.42	53.69
TiO_2	0.20	0.38	0.21	0.35	0.16	0.53	0.16	0.33	0.17	0.69
Al_2O_3	1.42	0.39	1.13	0.42	1.66	0.73	1.67	0.51	1.69	0.66
Cr_2O_3	0.79	0.83	1.51	1.30	1.78	1.77	1.37	1.09	1.37	1.17
FeO	2.62	2.08	2.40	1.97	2.48	2.21	2.63	2.28	2.63	2.42
MnO	0.09	0.08	0.09	0.07	0.09	0.08	0.12	0.10	0.11	0.07
NiO	0.05	0.03	0.03	0.03	0.03	0.05	0.00	0.01	0.00	0.00
MgO	16.63	16.89	16.63	16.95	17.20	16.89	16.86	16.99	16.74	16.07
CaO	22.06	24.54	21.47	24.06	19.74	23.63	20.57	23.84	20.40	24.91
Na_2O	1.07	0.34	1.47	0.54	1.82	0.76	1.46	0.61	1.46	0.35
K_2O	0.04	0.01	0.03	0.01	0.05	0.03	0.05	0.01	0.04	0.00
Total	99.98	100.09	99.93	100.35	100.31	100.76	100.13	100.13	100.04	100.03
Number of cations (apfu) on the basis of 6 oxygen atoms and 4 cations										
Si	1.993	1.983	1.994	1.982	1.991	1.960	1.994	1.978	2.000	1.964
Ti	0.005	0.010	0.006	0.010	0.004	0.014	0.004	0.009	0.005	0.019
Al	0.061	0.017	0.048	0.018	0.071	0.031	0.071	0.022	0.072	0.028
Cr	0.023	0.024	0.043	0.037	0.051	0.051	0.039	0.031	0.039	0.034
Fe	0.079	0.063	0.073	0.060	0.075	0.067	0.079	0.069	0.079	0.074
Mn	0.003	0.003	0.003	0.002	0.003	0.002	0.004	0.003	0.003	0.002
Ni	0.001	0.001	0.001	0.001	0.001	0.001	0.000	0.000	0.000	0.000
Mg	0.898	0.916	0.899	0.917	0.923	0.912	0.907	0.922	0.901	0.876
Ca	0.857	0.957	0.835	0.935	0.761	0.918	0.795	0.929	0.789	0.976
Na	0.075	0.024	0.103	0.038	0.127	0.053	0.102	0.043	0.102	0.025
K	0.002	0.000	0.001	0.001	0.002	0.002	0.002	0.001	0.002	0.000
sum	3.998	3.998	4.007	4.000	4.009	4.012	3.999	4.008	3.992	3.999
Mg/(Mg+Fe)	0.919	0.935	0.925	0.939	0.925	0.932	0.920	0.930	0.919	0.922
Ca/(Ca+Mg)	0.488	0.511	0.481	0.505	0.452	0.501	0.467	0.502	0.467	0.527

Clinopyroxene continued

Ekati - Point lake																			
PL_CD_03 (In01 - 04)		PL_CD_03 (In05)		PL_CD_0 3	PL_CD_0 3	PL_CD_03 (In09)		PL_CD_03 (In10)		PL_CD_06 (In01, 04)		PL_CD_06 (In02, 02b)		PL_CD_06 (In03)		PL_CD_07 (In01 - 03)		PL_CD_07 (In04 - 06)	
clear	spongy rim	clear	spongy rim	clear	clear	clear	spongy rim	clear	spongy rim	clear	spongy rim	clear	spongy rim	clear	spongy rim	clear	spongy rim	clear	spongy rim
54.52	53.54	54.08	53.94	54.34	53.89	54.27	51.46	54.41	53.63	55.47	55.18	54.78	54.21	54.56	53.47	55.02	53.78	54.85	54.49
0.17	0.36	0.22	0.35	0.17	0.15	0.21	0.28	0.14	0.30	0.16	0.35	0.17	0.15	0.13	0.18	0.16	0.27	0.15	0.35
1.62	0.43	1.71	0.62	1.65	1.67	1.37	0.34	1.74	0.30	1.69	0.39	1.66	0.94	1.62	0.79	1.71	0.64	1.67	0.40
0.58	0.60	0.70	0.63	1.12	1.17	1.24	0.74	1.35	1.05	1.26	0.96	1.25	1.19	1.28	1.38	1.22	1.10	1.27	1.34
2.75	2.49	2.64	2.64	2.67	2.62	2.50	2.00	2.71	2.13	2.65	2.20	2.64	2.67	2.58	2.64	2.65	2.47	2.52	2.33
0.11	0.08	0.09	0.10	0.10	0.09	0.09	0.07	0.10	0.09	0.10	0.07	0.09	0.11	0.11	0.12	0.10	0.08	0.08	0.09
0.04	0.01	0.04	0.03	0.04	0.05	0.04	0.04	0.04	0.03	0.05	0.02	0.03	0.03	0.04	0.03	0.03	0.03	0.04	0.02
17.87	17.52	17.54	17.20	17.77	17.53	17.45	18.34	17.70	18.87	16.52	16.86	16.67	16.20	16.71	16.30	16.74	16.14	16.77	17.40
21.06	24.64	21.23	24.12	20.53	20.36	21.44	24.32	20.26	23.09	20.63	23.97	20.38	23.31	20.63	23.13	20.25	24.31	20.53	23.13
1.09	0.20	1.15	0.31	1.28	1.33	1.20	0.31	1.40	0.42	1.38	0.50	1.43	0.71	1.33	0.65	1.40	0.42	1.38	0.63
0.04	0.01	0.04	0.01	0.04	0.04	0.03	0.00	0.04	0.01	0.04	0.00	0.04	0.00	0.05	0.03	0.04	0.00	0.04	0.03
99.85	99.89	99.44	99.95	99.70	98.90	99.83	97.89	99.89	99.90	99.95	100.51	99.14	99.52	99.02	98.72	99.32	99.23	99.31	100.22
1.976	1.959	1.970	1.969	1.973	1.973	1.972	1.926	1.972	1.954	2.004	1.995	1.996	1.985	1.993	1.977	1.999	1.979	1.995	1.979
0.005	0.010	0.006	0.010	0.005	0.004	0.006	0.008	0.004	0.008	0.004	0.009	0.005	0.004	0.003	0.005	0.004	0.007	0.004	0.010
0.069	0.019	0.073	0.027	0.071	0.072	0.059	0.015	0.074	0.013	0.072	0.017	0.071	0.040	0.070	0.034	0.073	0.028	0.072	0.017
0.017	0.017	0.020	0.018	0.032	0.034	0.036	0.022	0.039	0.030	0.036	0.028	0.036	0.034	0.037	0.040	0.035	0.032	0.037	0.039
0.083	0.076	0.080	0.081	0.081	0.080	0.076	0.063	0.082	0.065	0.080	0.067	0.080	0.082	0.079	0.082	0.081	0.076	0.077	0.071
0.003	0.003	0.003	0.003	0.003	0.003	0.003	0.002	0.003	0.003	0.003	0.002	0.003	0.003	0.003	0.004	0.003	0.003	0.003	0.003
0.001	0.000	0.001	0.001	0.001	0.002	0.001	0.001	0.001	0.001	0.001	0.001	0.001	0.001	0.001	0.001	0.001	0.001	0.001	0.001
0.965	0.956	0.953	0.936	0.962	0.957	0.945	1.024	0.956	1.025	0.890	0.909	0.906	0.884	0.910	0.898	0.907	0.885	0.909	0.942
0.818	0.966	0.829	0.943	0.799	0.799	0.835	0.976	0.787	0.902	0.798	0.929	0.796	0.914	0.807	0.916	0.788	0.958	0.800	0.900
0.077	0.014	0.081	0.022	0.090	0.094	0.084	0.022	0.098	0.029	0.097	0.035	0.101	0.051	0.094	0.047	0.099	0.030	0.097	0.045
0.002	0.000	0.002	0.000	0.002	0.002	0.001	0.000	0.002	0.000	0.002	0.000	0.002	0.000	0.002	0.001	0.002	0.000	0.002	0.001
4.016	4.020	4.019	4.010	4.017	4.019	4.018	4.059	4.018	4.031	3.987	3.991	3.997	3.999	3.999	4.005	3.992	3.999	3.996	4.007
0.921	0.926	0.922	0.921	0.922	0.923	0.926	0.942	0.921	0.940	0.917	0.932	0.918	0.915	0.920	0.917	0.918	0.921	0.922	0.930
0.459	0.503	0.465	0.502	0.454	0.455	0.469	0.488	0.451	0.468	0.473	0.505	0.468	0.508	0.470	0.505	0.465	0.520	0.468	0.489

Garnet

Location	Diavik - A154N	Diavik - A154N	Diavik - A154N	Diavik - A154N	Diavik - A154N	Diavik - A154N	Diavik - A154N	Diavik - A154N	Diavik - A154N	Diavik - A154N	Diavik - A154N	Diavik - A154N
Sample	DVK_GRT_01	DVK_GRT_01	DVK_GRT_01	DVK_GRT_02	DVK_GRT_02	DVK_GRT_02	DVK_GRT_03	DVK_GRT_03	DVK_GRT_03	DVK_GRT_04	DVK_GRT_04	DVK_GRT_04
	(In01 - 06)	(In07 - 12)	(In13)	(In01 - 02)	(In03 - 06)	(In07 - 10)	(In01 -02)	(In03 - 05)	(In06)	(In01)	(In02 - 08)	(In09)
Class	G11	G10	G1	G9	G10	G1	G9	G10	G3	G9	G9	G11
Major element analyses (wt.%)												
SiO_2	41.22	41.26	41.57	41.36	40.78	41.18	40.73	40.95	39.74	41.13	41.70	41.24
TiO_2	0.67	0.00	0.41	0.27	0.21	0.47	0.34	0.04	0.25	0.31	0.29	0.77
Al_2O_3	19.45	18.19	21.71	19.18	15.94	19.97	17.35	17.90	22.24	19.14	20.59	18.69
Cr_2O_3	4.08	7.65	1.73	5.42	9.91	3.86	7.82	7.86	0.05	5.51	3.32	4.54
FeO	8.29	7.28	7.99	6.99	6.86	7.82	7.12	7.53	14.69	6.80	7.57	7.77
MnO	0.38	0.50	0.37	0.33	0.39	0.43	0.37	0.47	0.26	0.37	0.33	0.32
NiO	0.01	0.00	0.00	0.02	0.01	0.00	0.02	0.00	0.00	0.02	0.00	0.01
MgO	19.43	21.45	20.71	20.35	19.68	19.78	19.46	19.54	8.46	20.55	20.82	20.55
CaO	6.08	3.62	4.41	5.36	5.77	5.49	5.78	5.18	13.84	5.00	4.95	5.29
Na_2O	0.06	0.02	0.07	0.04	0.05	0.10	0.07	0.02	0.09	0.06	0.08	0.06
P_2O_5	0.04	0.02	0.03	0.02	0.03	0.04	0.04	0.01	0.03	0.01	0.04	0.01
Total	99.71	99.99	99.00	99.33	99.63	99.14	99.09	99.51	99.65	98.89	99.70	99.25
Number of cations (apfu) on the basis of 12 oxygen atoms and 8 cations												
Si	2.988	2.979	2.989	2.994	2.993	2.988	2.988	2.990	2.993	2.988	2.991	2.995
Ti	0.037	0.000	0.022	0.015	0.011	0.026	0.018	0.002	0.014	0.017	0.016	0.042
Al	1.662	1.548	1.840	1.637	1.379	1.708	1.500	1.540	1.974	1.639	1.741	1.600
Cr	0.234	0.437	0.098	0.310	0.575	0.221	0.454	0.454	0.003	0.316	0.188	0.261
Fe	0.503	0.440	0.480	0.423	0.421	0.474	0.437	0.460	0.925	0.413	0.454	0.472
Mn	0.023	0.031	0.022	0.020	0.024	0.026	0.023	0.029	0.017	0.022	0.020	0.019
Ni	0.001	0.000	0.000	0.001	0.001	0.000	0.001	0.000	0.000	0.001	0.000	0.001
Mg	2.099	2.309	2.220	2.196	2.153	2.139	2.129	2.127	0.950	2.226	2.226	2.225
Ca	0.472	0.280	0.340	0.416	0.454	0.427	0.454	0.405	1.117	0.389	0.380	0.412
Na	0.008	0.002	0.010	0.005	0.007	0.015	0.010	0.003	0.014	0.008	0.011	0.009
P	0.003	0.001	0.002	0.001	0.002	0.002	0.002	0.001	0.002	0.001	0.002	0.001
sum	8.028	8.027	8.022	8.019	8.020	8.026	8.017	8.011	8.009	8.021	8.030	8.036
Mg/(Mg+Fe)	0.807	0.840	0.822	0.838	0.836	0.818	0.830	0.822	0.507	0.843	0.831	0.825

Garnet continued

Diavik - A154N DVK_GRT_05	Diavik - A154N DVK_GRT_06 (In01 - 02)	Diavik - A154N DVK_GRT_06 (In03)	Diavik - A154N DVK_GRT_06 (In04 - 06)	Diavik - A154N DVK_GRT_06 (In07 - 08)	Ekati - Wolverine WI7_GRT_03 (In01)	WI7_GRT_03 (In02 - 03)	WI7_GRT_03 (In04 - 05)	WI7_GRT_03 (In06 - 07)	WI7_GRT_03 (In08 - 11)	WI7_GRT_03 (In12 - 13)
G1/G9	G9	G9	G9	G10	G10	G11	G11	G9	G11	G11
41.52	40.47	41.22	41.12	40.79	41.48	41.17	41.28	41.57	41.76	42.01
0.43	0.21	0.28	0.33	0.04	0.03	0.68	0.62	0.35	0.49	0.46
21.29	17.46	20.12	18.99	16.69	18.14	18.96	18.47	20.92	19.15	19.05
2.07	7.67	3.93	5.52	9.21	7.88	4.61	5.55	3.25	5.44	5.47
8.14	8.00	7.46	6.81	6.65	7.27	8.77	7.91	7.93	7.92	7.76
0.36	0.50	0.39	0.35	0.37	0.49	0.43	0.37	0.38	0.35	0.32
0.00	0.00	0.01	0.00	0.00	0.00	0.00	0.02	0.01	0.02	0.03
20.42	18.82	20.85	21.00	20.45	20.50	17.07	19.11	19.89	19.40	19.41
4.90	6.20	4.76	5.27	5.32	3.80	8.14	5.92	4.58	5.79	6.04
0.05	0.06	0.08	0.05	0.02	0.03	0.04	0.05	0.07	0.05	0.05
0.03	0.07	0.03	0.01	0.03	0.04	0.04	0.01	0.02	0.04	0.02
99.20	99.45	99.14	99.46	99.56	99.65	99.91	99.31	98.96	100.41	100.63
2.989	2.975	2.980	2.975	2.981	3.005	3.006	3.010	3.003	3.005	3.016
0.023	0.012	0.015	0.018	0.002	0.002	0.037	0.034	0.019	0.026	0.025
1.806	1.513	1.714	1.619	1.438	1.549	1.632	1.587	1.781	1.624	1.612
0.118	0.446	0.225	0.316	0.532	0.451	0.266	0.320	0.186	0.310	0.310
0.490	0.492	0.451	0.412	0.406	0.440	0.536	0.482	0.479	0.477	0.466
0.022	0.031	0.024	0.022	0.023	0.030	0.026	0.023	0.023	0.022	0.020
0.000	0.000	0.000	0.000	0.000	0.000	0.000	0.001	0.000	0.001	0.002
2.192	2.062	2.247	2.265	2.228	2.214	1.858	2.077	2.142	2.081	2.077
0.378	0.488	0.369	0.408	0.417	0.295	0.637	0.462	0.354	0.446	0.465
0.006	0.008	0.011	0.007	0.002	0.004	0.006	0.007	0.009	0.007	0.007
0.002	0.005	0.002	0.001	0.002	0.002	0.002	0.001	0.001	0.002	0.001
8.026	8.031	8.038	8.042	8.031	7.992	8.007	8.005	7.998	8.002	8.000
0.817	0.807	0.833	0.846	0.846	0.834	0.776	0.812	0.817	0.814	0.817

Garnet continued

Ekati - Point lake										
PL_GRT_01 (In01 - 04) G11	PL_GRT_01 (In05 - 06) G9	PL_GRT_01 (In07) G9	PL_GRT_01 (In08) G9	PL_GRT_01 (In09) G1	PL_GRT_01 (In10 - 11) G9/G11	PL_GRT_01 (In12) G4	PL_GRT_02 (In01 - 02) G9	PL_GRT_02 (In03) G9	PL_GRT_02 (In04) G1	PL_GRT_02 (In05) G1
41.43	42.09	42.56	41.95	42.28	42.42	42.66	41.37	42.03	42.06	42.09
0.43	0.30	0.35	0.27	0.55	0.38	0.40	0.30	0.18	0.52	0.51
17.43	21.96	19.34	21.30	22.35	21.09	23.45	17.42	19.74	20.91	20.94
8.06	2.04	5.79	2.99	0.59	3.42	0.14	8.34	5.65	3.63	2.78
7.36	7.85	6.95	7.82	8.01	6.87	8.72	6.97	6.62	7.42	9.28
0.35	0.32	0.33	0.37	0.31	0.29	0.30	0.37	0.32	0.36	0.37
0.01	0.01	0.02	0.00	0.02	0.02	0.00	0.00	0.00	0.01	0.01
19.67	20.11	20.00	20.17	20.57	20.99	19.95	19.89	21.05	21.19	20.07
5.38	4.47	5.27	4.44	4.36	4.63	4.42	5.89	5.26	4.47	4.88
0.04	0.04	0.04	0.05	0.05	0.05	0.06	0.04	0.03	0.09	0.06
0.02	0.00	0.03	0.04	0.02	0.02	0.01	0.02	0.04	0.02	0.02
100.17	99.19	100.68	99.40	99.10	100.19	100.11	100.61	100.93	100.68	101.00
3.004	3.015	3.033	3.009	3.020	3.010	3.017	2.990	2.987	2.983	2.996
0.023	0.016	0.019	0.014	0.029	0.020	0.021	0.016	0.010	0.028	0.027
1.490	1.854	1.624	1.800	1.882	1.764	1.955	1.484	1.653	1.748	1.757
0.462	0.116	0.326	0.170	0.034	0.192	0.008	0.477	0.317	0.204	0.156
0.446	0.470	0.414	0.469	0.478	0.408	0.516	0.421	0.393	0.440	0.552
0.021	0.019	0.020	0.023	0.019	0.018	0.018	0.023	0.019	0.022	0.022
0.001	0.001	0.001	0.000	0.001	0.001	0.000	0.000	0.000	0.001	0.001
2.126	2.148	2.125	2.156	2.190	2.220	2.104	2.143	2.230	2.240	2.130
0.418	0.343	0.402	0.341	0.334	0.352	0.335	0.456	0.400	0.340	0.372
0.006	0.006	0.006	0.007	0.007	0.007	0.008	0.006	0.005	0.012	0.008
0.001	0.000	0.002	0.003	0.001	0.001	0.001	0.001	0.002	0.001	0.001
7.998	7.987	7.973	7.992	7.995	7.994	7.983	8.016	8.017	8.017	8.022
0.827	0.820	0.837	0.821	0.821	0.845	0.803	0.836	0.850	0.836	0.794

Garnet continued

Ekati - Point lake

PL_GRT_02 (In06) G9	PL_GRT_03 (In01 - 02) G1/G11	PL_GRT_03 (In03 - 04) G11	PL_GRT_04 (In01 - 03) G9/G11	PL_GRT_04 (In04 - 07) G9	PL_GRT_04 (In08 - 09) G11	PL_GRT_04 (In10) G9	PL_GRT_04 (In11) G9	PL_GRT_04 (In12) G9	PL_GRT_04 (In13 - 14) G1
42.32	42.28	41.84	41.98	42.48	41.87	41.88	41.54	42.15	41.97
0.27	0.37	0.55	0.38	0.21	0.59	0.28	0.30	0.37	0.58
19.91	21.71	19.15	19.02	21.36	20.02	21.31	18.56	21.96	20.67
5.29	2.71	5.39	5.87	3.42	4.23	2.84	6.58	2.12	2.50
7.35	6.90	7.55	7.16	7.17	6.29	7.53	6.23	8.03	7.71
0.35	0.31	0.34	0.34	0.34	0.29	0.32	0.31	0.36	0.31
0.01	0.01	0.03	0.01	0.01	0.00	0.00	0.02	0.01	0.02
21.01	21.96	20.71	20.12	20.28	21.15	20.58	20.24	20.38	20.56
4.99	4.13	5.05	5.39	4.75	4.85	4.56	5.42	4.24	4.78
0.04	0.06	0.07	0.06	0.04	0.07	0.05	0.06	0.06	0.05
0.03	0.02	0.01	0.04	0.02	0.03	0.03	0.01	0.04	0.01
101.57	100.45	100.68	100.37	100.09	99.39	99.38	99.27	99.72	99.16
2.992	2.984	2.993	3.011	3.020	3.001	3.001	3.008	3.006	3.018
0.015	0.020	0.030	0.020	0.011	0.032	0.015	0.016	0.020	0.031
1.659	1.806	1.615	1.608	1.790	1.691	1.800	1.584	1.846	1.752
0.296	0.151	0.305	0.333	0.192	0.240	0.161	0.377	0.120	0.142
0.435	0.407	0.452	0.429	0.426	0.377	0.451	0.377	0.479	0.464
0.021	0.018	0.020	0.021	0.021	0.017	0.019	0.019	0.022	0.019
0.000	0.001	0.001	0.001	0.001	0.000	0.000	0.001	0.001	0.001
2.214	2.311	2.209	2.151	2.149	2.260	2.198	2.185	2.166	2.204
0.378	0.312	0.387	0.414	0.362	0.373	0.350	0.421	0.324	0.368
0.006	0.008	0.009	0.009	0.006	0.010	0.007	0.008	0.008	0.007
0.002	0.001	0.001	0.002	0.001	0.002	0.002	0.001	0.002	0.001
8.017	8.020	8.021	8.000	7.979	8.004	8.005	7.998	7.993	8.006
0.836	0.850	0.830	0.834	0.834	0.857	0.830	0.853	0.819	0.826

A2.6. Megacryst Hosts Thermobarometry

P-T results for Cr-diopside megacryst hosts using single-cpx thermobarometry (Nimis and Taylor, 2000)

Location	Diavik - A154N		
Sample	DVK_CD_04B	DVK_CD_06A	DVK_CD_06B
T [°C]	1043	1009	1031
P [GPa]	5.3	4.6	4.7

Location	Ekati - Point lake										
Sample	PL_CD_03 (In01 - 04)	PL_CD_03 (In05)	PL_CD_03 (In06)	PL_CD_03 (In07 - 08)	PL_CD_03 (In09)	PL_CD_03 (In10)	PL_CD_06 (In01, 04)	PL_CD_06 (In02, 02b)	PL_CD_06 (In03)	PL_CD_07 (In01 - 03)	PL_CD_07 (In04 - 06)
T [°C]	1025	965	1040	1025	938	1046	1017	1014	997	1043	1011
P [GPa]	4.5	4.2	4.6	4.6	4.4	4.5	4.5	4.7	4.5	4.7	4.5

A2.7. EPMA Olivine

	Olivine in polymineralic inclusions in clinopyroxene										
Location	Diavik - A154N								Ekati - Point lake		
Sample	DVK_CD_01 _In01	DVK_CD_01 _In02	DVK_CD_01 _In02-2	DVK_CD_01 _In03	DVK_CD_01 _In04	DVK_CD_01 _In04-2	DVK_CD_01 _In08	DVK_CD_01 _In08-2	PL_CD_03 _In01	PL_CD_03 _In01-2	PL_CD_07 _In03
Inclusion type	cc-rich	cc-rich	cc-rich	cc-rich	cc-rich	cc-rich	cc-rich	cc-rich	cc-rich	cc-rich	si-rich
Major element analyses (wt.%)											
SiO_2	40.08	39.94	40.34	40.11	40.78	40.52	39.81	39.75	39.49	39.66	40.58
TiO_2	0.02	0.20	0.02	0.23	0.03	0.07	0.27	0.66	0.43	0.16	0.17
Al_2O_3	0.02	0.01	0.01	0.02	0.01	0.01	0.01	0.02	0.02	0.01	0.02
Cr_2O_3	0.18	0.39	0.20	0.32	0.23	0.31	0.38	0.31	0.20	0.31	0.37
FeO	10.86	9.81	9.25	9.25	8.47	9.00	9.10	9.46	10.03	10.15	9.19
MnO	0.31	0.21	0.20	0.22	0.20	0.20	0.22	0.20	0.26	0.27	0.20
NiO	0.10	0.08	0.08	0.13	0.10	0.13	0.14	0.17	0.12	0.09	0.21
MgO	47.08	47.70	48.63	48.46	49.24	49.00	48.44	48.15	47.07	47.29	47.85
CaO	0.79	0.47	0.31	0.50	0.40	0.41	0.66	0.59	0.78	0.66	0.38
Na_2O	n.a.	0.02	0.01	0.03	0.02	0.02	0.02	0.03	0.03	0.02	0.03
P_2O_5	n.a.	n.a.	n.a.	n.a.	n.a.	n.a.	n.a.	n.a.	0.30	0.14	0.22
Total	99.44	98.83	99.05	99.27	99.48	99.67	99.05	99.34	98.72	98.77	99.22
Number of cations (apfu) on the basis of 4 oxygen atoms and 3 cations											
Si	0.996	0.994	0.997	0.992	1.000	0.995	0.987	0.984	0.986	0.990	1.001
Ti	0.000	0.004	0.000	0.004	0.001	0.001	0.005	0.012	0.008	0.003	0.003
Al	0.000	0.000	0.000	0.001	0.000	0.000	0.000	0.001	0.001	0.000	0.001
Cr	0.004	0.008	0.004	0.006	0.004	0.006	0.007	0.006	0.004	0.006	0.007
Fe	0.226	0.204	0.191	0.191	0.174	0.185	0.189	0.196	0.209	0.212	0.190
Mn	0.007	0.004	0.004	0.005	0.004	0.004	0.005	0.004	0.005	0.006	0.004
Ni	0.002	0.002	0.002	0.003	0.002	0.003	0.003	0.003	0.002	0.002	0.004
Mg	1.745	1.770	1.793	1.786	1.800	1.794	1.790	1.777	1.751	1.760	1.760
Ca	0.021	0.013	0.008	0.013	0.011	0.011	0.018	0.016	0.021	0.018	0.010
Na	0.000	0.001	0.000	0.001	0.001	0.001	0.001	0.001	0.001	0.001	0.002
P	0.000	0.000	0.000	0.000	0.000	0.000	0.000	0.000	0.006	0.003	0.004
sum	3.001	2.999	3.000	3.002	2.997	3.001	3.005	3.001	2.995	3.000	2.986
Mg/(Mg+Fe)	0.885	0.897	0.904	0.903	0.912	0.907	0.905	0.901	0.893	0.893	0.903

Olivine continued

Olivine in polymineralic inclusions in garnet							
Diavik - A154N							
DVK_GRT_02_In09 si-rich	DVK_GRT_02_In9-2 si-rich	DVK_GRT_04_In07 si-rich	DVK_GRT_04_In07-2 si-rich	DVK_GRT_05_In01 cc-rich	DVK_GRT_05_In01-2 cc-rich	DVK_GRT_05_In02 cc-rich	DVK_GRT_05_In02-2 cc-rich
40.22	39.18	39.58	39.66	40.41	40.21	39.86	39.69
0.01	0.25	0.03	0.00	0.08	0.10	0.02	0.02
0.04	0.17	0.05	0.04	0.04	0.05	0.04	0.05
0.11	0.28	0.17	0.12	0.07	0.05	0.03	0.06
11.05	10.89	12.64	12.50	10.44	10.48	12.57	12.78
0.45	0.34	0.39	0.46	0.25	0.27	0.36	0.35
0.04	0.04	0.00	0.01	0.06	0.04	0.02	0.02
48.27	47.74	46.85	46.93	48.58	48.34	47.10	46.95
0.11	0.14	0.19	0.19	0.13	0.14	0.15	0.16
0.02	0.02	0.03	0.02	0.00	0.01	0.01	0.01
0.04	0.64	0.05	0.03	0.03	0.05	0.03	0.04
100.35	99.69	99.97	99.96	100.10	99.76	100.19	100.14
0.990	0.970	0.986	0.988	0.993	0.992	0.990	0.987
0.000	0.005	0.000	0.000	0.001	0.002	0.000	0.000
0.001	0.005	0.002	0.001	0.001	0.001	0.001	0.002
0.002	0.005	0.003	0.002	0.001	0.001	0.001	0.001
0.227	0.226	0.263	0.260	0.215	0.216	0.261	0.266
0.009	0.007	0.008	0.010	0.005	0.006	0.008	0.007
0.001	0.001	0.000	0.000	0.001	0.001	0.000	0.000
1.771	1.763	1.740	1.742	1.780	1.778	1.743	1.741
0.003	0.004	0.005	0.005	0.003	0.004	0.004	0.004
0.001	0.001	0.001	0.001	0.000	0.000	0.000	0.000
0.001	0.013	0.001	0.001	0.001	0.001	0.001	0.001
3.007	3.000	3.010	3.010	3.003	3.003	3.009	3.010
0.886	0.887	0.869	0.870	0.892	0.892	0.870	0.868

Olivine continued

Olivine in kimberlite rinds attached to garnet grains

Diavik - A154N

DVK_GRT_01_In08	DVK_GRT_01_In10	DVK_GRT_01_In10-2	DVK_GRT_01_In13	DVK_GRT_02_In01	DVK_GRT_02_In01-2	DVK_GRT_02_In03	DVK_GRT_02_In03-2	DVK_GRT_06_In07	DVK_GRT_06_In07-2
40.28	40.45	41.12	40.32	40.84	40.73	40.49	40.40	40.19	40.11
0.02	0.04	0.13	0.03	0.01	0.00	0.02	0.02	0.02	0.04
0.03	0.02	0.06	0.03	0.02	0.02	0.03	0.02	0.03	0.01
0.08	0.06	0.06	0.07	0.02	0.03	0.06	0.01	0.03	0.04
8.60	8.83	5.63	9.36	8.07	7.05	8.97	8.15	9.14	8.94
0.11	0.14	0.28	0.12	0.09	0.11	0.12	0.10	0.10	0.15
0.38	0.34	0.04	0.35	0.35	0.36	0.37	0.40	0.38	0.13
50.54	50.31	52.60	49.69	50.34	51.26	49.74	50.40	50.19	50.72
0.06	0.04	0.42	0.08	0.04	0.04	0.07	0.03	0.06	0.09
0.02	0.01	0.01	0.03	0.05	0.01	0.02	0.03	0.03	0.01
0.00	0.00	0.04	0.00	0.01	0.03	0.00	0.01	0.01	0.01
100.13	100.23	100.38	100.09	99.85	99.63	99.89	99.56	100.17	100.25
0.984	0.987	0.988	0.988	0.996	0.991	0.992	0.990	0.983	0.980
0.000	0.001	0.002	0.001	0.000	0.000	0.000	0.000	0.000	0.001
0.001	0.000	0.002	0.001	0.001	0.000	0.001	0.001	0.001	0.000
0.002	0.001	0.001	0.001	0.000	0.001	0.001	0.000	0.001	0.001
0.176	0.180	0.113	0.192	0.165	0.144	0.184	0.167	0.187	0.183
0.002	0.003	0.006	0.003	0.002	0.002	0.002	0.002	0.002	0.003
0.007	0.007	0.001	0.007	0.007	0.007	0.007	0.008	0.007	0.003
1.840	1.831	1.883	1.815	1.830	1.860	1.816	1.840	1.831	1.846
0.002	0.001	0.011	0.002	0.001	0.001	0.002	0.001	0.002	0.002
0.001	0.001	0.001	0.002	0.002	0.000	0.001	0.001	0.001	0.000
0.000	0.000	0.001	0.000	0.000	0.001	0.000	0.000	0.000	0.000
3.015	3.011	3.008	3.011	3.004	3.007	3.007	3.010	3.016	3.019
0.913	0.910	0.943	0.904	0.917	0.928	0.908	0.917	0.907	0.910

Olivine continued

(Altered) olivine mineral inclusions in garnet

Diavik - A154N

DVK_GRT_01_In07	DVK_GRT_01_In09	DVK_GRT_01_In11	DVK_GRT_02_In04	DVK_GRT_03_In02	DVK_GRT_03_In05	DVK_GRT_06_In04	DVK_GRT_06_In05	DVK_GRT_06_In07	DVK_GRT_06_In02
40.83	40.80	40.70	40.58	40.63	40.68	40.52	40.43	40.57	40.61
0.00	0.00	0.01	0.00	0.01	0.00	0.02	0.01	0.00	0.01
0.01	0.02	0.01	0.03	0.02	0.01	0.02	0.01	0.01	0.01
0.01	0.02	0.01	0.05	0.02	0.00	0.03	0.02	0.04	0.02
6.71	6.71	6.65	7.55	7.60	6.84	7.28	7.34	7.13	7.24
0.10	0.11	0.10	0.11	0.10	0.10	0.09	0.11	0.10	0.09
0.38	0.40	0.37	0.37	0.39	0.38	0.39	0.38	0.36	0.35
51.79	51.86	51.85	50.55	50.22	51.18	51.53	51.47	51.69	51.74
0.06	0.02	0.04	0.03	0.03	0.01	0.04	0.03	0.03	0.02
0.00	0.01	0.02	0.03	0.02	0.01	0.01	0.02	0.02	0.03
0.00	0.00	0.00	0.01	0.00	0.01	0.02	0.00	0.00	0.02
99.88	99.95	99.75	99.31	99.04	99.23	99.95	99.82	99.95	100.14
0.990	0.989	0.988	0.993	0.997	0.993	0.985	0.985	0.986	0.985
0.000	0.000	0.000	0.000	0.000	0.000	0.000	0.000	0.000	0.000
0.000	0.000	0.000	0.001	0.001	0.000	0.001	0.000	0.000	0.000
0.000	0.000	0.000	0.001	0.000	0.000	0.000	0.000	0.001	0.000
0.136	0.136	0.135	0.155	0.156	0.140	0.148	0.150	0.145	0.147
0.002	0.002	0.002	0.002	0.002	0.002	0.002	0.002	0.002	0.002
0.007	0.008	0.007	0.007	0.008	0.008	0.008	0.007	0.007	0.007
1.872	1.874	1.877	1.845	1.837	1.863	1.868	1.869	1.872	1.871
0.001	0.000	0.001	0.001	0.001	0.000	0.001	0.001	0.001	0.000
0.000	0.001	0.001	0.001	0.001	0.000	0.001	0.001	0.001	0.001
0.000	0.000	0.000	0.000	0.000	0.000	0.000	0.000	0.000	0.000
3.010	3.011	3.012	3.006	3.003	3.007	3.014	3.015	3.014	3.014
0.932	0.932	0.933	0.923	0.922	0.930	0.927	0.926	0.928	0.927

A2.8. EPMA Phlogopite

	Phlogopite in polymineralic inclusions in clinopyroxene							
Location	Diavik - A154N							
Sample	DVK_CD_01 _In01	DVK_CD_01 _In03	DVK_CD_01 _In04	DVK_CD_01 _In05	DVK_CD_01 _In07	DVK_CD_01 _In08	DVK_CD_02B _In01	DVK_CD_04B _In01
Inclusion type	cc-rich	cc-rich	cc-rich	cc-rich	cc-rich	cc-rich	si-rich	cc-rich
Major element analyses (wt.%)								
SiO_2	40.82	40.61	40.65	40.81	42.61	40.63	39.71	39.92
TiO_2	1.51	1.80	1.63	1.54	0.80	1.47	1.90	2.26
Al_2O_3	12.28	12.23	12.35	12.20	7.74	12.33	12.13	11.82
Cr_2O_3	1.24	1.28	1.24	1.32	0.39	1.23	1.32	1.74
MnO	0.03	0.05	0.05	0.02	0.02	0.03	0.08	0.05
FeO	4.23	3.63	4.25	4.20	5.86	4.30	4.22	3.90
NiO	0.19	0.16	0.20	0.21	0.26	0.07	0.00	0.00
MgO	24.23	24.41	23.99	24.19	25.98	23.74	23.77	23.82
CaO	0.05	0.06	0.00	0.08	0.08	0.14	0.05	0.04
BaO	0.16	0.14	0.13	0.13	0.11	0.09	0.18	0.15
Na_2O	0.09	0.10	0.18	0.18	0.16	0.16	0.33	0.17
K_2O	10.43	10.33	10.37	10.45	10.51	10.35	10.12	10.33
F	0.47	0.46	0.41	0.47	0.84	0.45	0.50	0.51
Cl	0.00	0.01	0.01	0.01	0.00	0.03	0.00	0.01
Total	95.74	95.26	95.46	95.83	95.36	95.03	94.31	94.71
Number of cations (apfu) on the basis of 11 oxygen atoms and 8 cations								
Si	2.920	2.911	2.915	2.918	3.096	2.926	2.889	2.892
Ti	0.081	0.097	0.088	0.083	0.044	0.080	0.104	0.123
Al	1.035	1.033	1.044	1.028	0.663	1.046	1.040	1.009
Cr	0.070	0.073	0.071	0.075	0.022	0.070	0.076	0.100
Mn	0.002	0.003	0.003	0.001	0.001	0.002	0.005	0.003
Fe	0.253	0.218	0.255	0.251	0.356	0.259	0.257	0.236
Ni	0.011	0.009	0.012	0.012	0.015	0.004	0.000	0.000
Mg	2.584	2.608	2.564	2.579	2.814	2.549	2.578	2.572
Ca	0.004	0.004	0.000	0.006	0.006	0.011	0.004	0.003
Ba	0.005	0.004	0.004	0.004	0.003	0.003	0.005	0.004
Na	0.013	0.013	0.025	0.026	0.023	0.022	0.046	0.024
K	0.952	0.945	0.949	0.953	0.974	0.951	0.939	0.955
sum	7.929	7.918	7.927	7.936	8.017	7.923	7.942	7.920
Mg/(Mg+Fe)	0.911	0.923	0.910	0.911	0.888	0.908	0.909	0.916

Phlogopite continued

Phlogopite in polymineralic inclusions in clinopyroxene

Diavik - A154N

DVK_CD_04B _In04 cc-rich	DVK_CD_06A _In01 si-rich	DVK_CD_06A _In02 si-rich	DVK_CD_06A _In03 si-rich	DVK_CD_06A _In04 si-rich	DVK_CD_06A _In05 si-rich	DVK_CD_06A _In06 si-rich	DVK_CD_06A _In07 si-rich
40.74	41.27	42.15	41.44	41.47	42.35	41.99	42.10
1.00	1.46	1.22	1.76	1.42	1.60	1.46	1.11
11.55	11.66	11.82	11.71	11.64	11.12	11.66	10.55
1.37	1.27	1.25	1.36	1.25	1.46	1.68	1.00
0.06	0.00	0.04	0.03	0.07	0.04	0.03	0.02
3.80	4.17	3.52	4.02	4.04	3.59	3.56	3.38
0.10	0.09	0.17	0.20	0.13	0.20	0.12	0.19
24.93	23.82	24.37	24.12	24.28	24.18	24.31	26.23
0.07	0.00	0.00	0.07	0.23	0.00	0.00	0.00
0.07	0.06	0.05	0.08	0.08	0.03	0.06	0.04
0.34	0.24	0.11	0.20	0.22	0.29	0.15	0.16
10.16	10.41	10.52	10.26	10.23	10.56	10.18	9.21
0.56	0.41	0.38	0.44	0.40	0.42	0.39	0.40
0.00	0.01	0.03	0.01	0.01	0.04	0.03	0.02
94.76	94.88	95.62	95.70	95.47	95.87	95.60	94.41
2.940	2.970	2.995	2.956	2.964	3.010	2.984	3.010
0.054	0.079	0.065	0.094	0.076	0.086	0.078	0.059
0.982	0.989	0.990	0.985	0.981	0.931	0.977	0.889
0.078	0.072	0.070	0.077	0.071	0.082	0.094	0.056
0.003	0.000	0.002	0.002	0.004	0.002	0.002	0.001
0.229	0.251	0.209	0.240	0.242	0.213	0.212	0.202
0.006	0.005	0.010	0.011	0.007	0.011	0.007	0.011
2.682	2.556	2.582	2.565	2.587	2.562	2.576	2.796
0.006	0.000	0.000	0.005	0.018	0.000	0.000	0.000
0.002	0.002	0.001	0.002	0.002	0.001	0.002	0.001
0.048	0.033	0.015	0.028	0.030	0.039	0.021	0.023
0.935	0.956	0.954	0.934	0.933	0.957	0.923	0.840
7.967	7.914	7.894	7.899	7.915	7.896	7.874	7.889
0.921	0.911	0.925	0.914	0.915	0.923	0.924	0.933

Phlogopite continued

Phlogopite in polymineralic inclusions in clinopyroxene

Diavik - A154N

DVK_CD_06A_In08 si-rich	DVK_CD_06A_In10 si-rich	DVK_CD_06A_In12 si-rich	DVK_CD_06B_In01 si-rich	DVK_CD_06B_In02 si-rich	DVK_CD_06B_In03 si-rich	DVK_CD_06B_In05 si-rich	DVK_CD_06B_In06 si-rich
41.94	41.85	42.25	41.18	42.01	41.55	41.23	41.84
1.53	1.36	1.55	1.56	1.28	1.73	1.23	1.15
12.04	11.50	11.74	11.77	11.79	11.75	9.16	11.79
1.44	1.18	1.46	1.52	1.45	1.44	0.97	1.28
0.02	0.02	0.03	0.03	0.01	0.05	0.06	0.04
3.54	3.39	3.43	4.01	3.65	3.82	3.35	3.53
0.26	0.19	0.28	0.12	0.28	0.16	0.23	0.20
24.19	24.77	24.12	23.78	24.17	24.27	27.65	24.35
0.00	0.22	0.00	0.00	0.00	0.00	0.01	0.00
0.00	0.01	0.06	0.08	0.10	0.05	0.07	0.00
0.11	0.19	0.18	0.24	0.16	0.21	0.20	0.13
10.64	10.13	10.43	10.51	10.60	10.53	7.72	10.74
0.38	0.43	0.38	0.42	0.46	0.45	0.35	0.39
0.03	0.03	0.04	0.00	0.02	0.01	0.00	0.03
96.12	95.27	95.93	95.21	95.98	96.02	92.22	95.46
2.970	2.984	2.994	2.957	2.986	2.955	3.002	2.985
0.081	0.073	0.083	0.084	0.068	0.093	0.067	0.062
1.005	0.966	0.980	0.996	0.988	0.985	0.786	0.991
0.081	0.067	0.082	0.086	0.082	0.081	0.056	0.072
0.001	0.001	0.002	0.002	0.001	0.003	0.004	0.003
0.210	0.202	0.203	0.241	0.217	0.227	0.204	0.211
0.015	0.011	0.016	0.007	0.016	0.009	0.013	0.011
2.554	2.633	2.548	2.545	2.561	2.573	3.002	2.590
0.000	0.017	0.000	0.000	0.000	0.000	0.001	0.000
0.000	0.000	0.002	0.002	0.003	0.001	0.002	0.000
0.015	0.027	0.025	0.033	0.022	0.029	0.028	0.018
0.961	0.921	0.943	0.963	0.961	0.955	0.717	0.977
7.894	7.901	7.876	7.916	7.903	7.912	7.882	7.919
0.924	0.929	0.926	0.914	0.922	0.919	0.936	0.925

Phlogopite continued

Phlogopite in polymineralic inclusions in clinopyroxene

Diavik - A154N					Ekati - Point lake			
DVK_CD_06B _In07 si-rich	DVK_CD_06B _In08 si-rich	DVK_CD_06B _In09 si-rich	DVK_CD_06B _In10 si-rich	DVK_CD_06B _In11 si-rich	PL_CD_03 _In01 cc-rich	PL_CD_03 _In04 cc-rich	PL_CD_03 _In05 cc-rich	PL_CD_03 _In07 cc-rich
42.34	42.14	41.94	41.83	41.81	39.53	41.15	40.38	41.04
1.09	1.36	1.70	1.71	1.27	1.40	0.91	1.20	0.96
11.06	11.77	11.62	12.06	9.40	11.19	11.94	12.05	11.49
0.90	1.42	1.53	1.83	1.18	0.77	0.62	0.46	0.56
0.05	0.04	0.00	0.03	0.06	0.05	0.05	0.01	0.06
3.42	3.52	3.49	3.56	3.78	4.45	4.68	3.48	3.58
0.24	0.18	0.29	0.25	0.12	n.a.	n.a.	n.a.	n.a.
25.44	24.34	24.02	23.92	27.40	25.31	24.55	25.09	25.51
0.00	0.00	0.00	0.00	0.01	0.03	0.75	0.02	0.11
0.05	0.01	0.06	0.02	0.05	n.a.	n.a.	n.a.	n.a.
0.12	0.15	0.13	0.13	0.15	0.18	0.23	0.18	0.57
9.99	10.62	10.67	10.59	8.38	10.34	10.14	10.88	10.02
0.39	0.39	0.42	0.41	0.35	0.39	0.26	0.30	0.40
0.03	0.03	0.04	0.02	0.01	0.02	0.01	0.07	0.05
95.11	95.96	95.90	96.35	93.95	93.66	95.29	94.12	94.34
3.015	2.988	2.982	2.960	3.002	2.896	2.948	2.925	2.958
0.058	0.073	0.091	0.091	0.068	0.077	0.049	0.065	0.052
0.928	0.984	0.974	1.006	0.795	0.966	1.008	1.029	0.976
0.050	0.079	0.086	0.102	0.067	0.044	0.035	0.026	0.032
0.003	0.002	0.000	0.002	0.003	0.003	0.003	0.001	0.004
0.204	0.209	0.208	0.211	0.227	0.273	0.280	0.211	0.216
0.014	0.010	0.016	0.014	0.007				
2.701	2.573	2.546	2.523	2.933	2.764	2.622	2.709	2.741
0.000	0.000	0.000	0.000	0.001	0.002	0.058	0.001	0.009
0.001	0.000	0.002	0.000	0.001				
0.016	0.020	0.018	0.018	0.021	0.026	0.032	0.025	0.079
0.908	0.961	0.968	0.956	0.768	0.966	0.927	1.005	0.921
7.899	7.899	7.890	7.882	7.893	8.018	7.961	7.998	7.987
0.930	0.925	0.925	0.923	0.928	0.910	0.903	0.928	0.927

Phlogopite continued

Phlogopite in polymineralic inclusions in clinopyroxene

Ekati - Point lake

PL_CD_03 _In09	PL_CD_03 _In10	PL_CD_06 _In02b	PL_CD_06 _In04	PL_CD_07 _In02	PL_CD_07 _In03	PL_CD_07 _In04	PL_CD_07 _In05	PL_CD_07 _In06	PL_CD_06 _In03	PL_CD_07 _In01
si-rich	si-rich	si-rich	si-rich	si-rich	si-rich	si-rich	si-rich	si-rich	si-rich	si-rich
40.33	40.72	40.08	41.02	41.27	42.17	40.67	42.61	41.26	41.16	41.40
1.03	0.95	1.09	1.51	1.19	1.07	1.60	0.86	2.09	1.59	1.83
12.07	9.61	12.07	11.32	11.78	9.21	12.31	9.22	11.65	11.77	11.50
0.62	0.96	1.35	1.20	0.57	1.08	1.68	1.20	2.03	1.76	1.84
0.05	0.05	0.05	0.01	0.04	0.06	0.00	0.04	0.03	0.00	0.01
3.59	4.07	4.14	4.22	3.65	4.49	4.11	3.90	3.27	3.24	3.51
n.a.	n.a.	n.a.	n.a.	n.a.	n.a.	n.a.	n.a.	n.a.	n.a.	n.a.
25.24	27.34	24.07	24.69	24.63	25.12	24.42	23.90	23.36	23.94	24.04
0.08	0.03	0.13	0.10	0.01	1.91	0.07	3.01	0.02	0.00	0.04
n.a.	n.a.	0.27	0.19	0.04	0.00	0.33	0.19	0.23	0.08	0.08
0.13	0.13	0.35	0.23	0.13	0.24	0.36	0.48	0.25	0.19	0.22
11.01	8.70	10.25	10.47	10.63	7.45	10.28	8.07	10.20	10.64	10.31
0.34	0.15	0.37	0.33	0.29	0.28	0.34	0.31	0.34	0.23	0.35
0.07	0.03	0.02	0.02	0.10	0.03	0.03	0.02	0.03	0.04	0.04
94.56	92.73	94.24	95.31	94.33	93.12	96.21	93.82	94.75	94.64	95.16
2.915	2.968	2.915	2.946	2.976	3.056	2.897	3.082	2.964	2.959	2.963
0.056	0.052	0.060	0.081	0.065	0.058	0.085	0.047	0.113	0.086	0.099
1.028	0.826	1.035	0.958	1.001	0.787	1.033	0.786	0.986	0.997	0.970
0.035	0.055	0.078	0.068	0.032	0.062	0.095	0.069	0.115	0.100	0.104
0.003	0.003	0.003	0.001	0.002	0.004	0.000	0.003	0.002	0.000	0.001
0.217	0.248	0.252	0.253	0.220	0.272	0.245	0.236	0.196	0.195	0.210
2.720	2.971	2.610	2.643	2.647	2.714	2.593	2.577	2.502	2.566	2.565
0.006	0.002	0.010	0.008	0.001	0.148	0.005	0.233	0.002	0.000	0.003
		0.008	0.005	0.001	0.000	0.009	0.005	0.006	0.002	0.002
0.019	0.019	0.049	0.032	0.018	0.034	0.050	0.067	0.035	0.026	0.030
1.015	0.809	0.951	0.959	0.978	0.689	0.934	0.745	0.935	0.976	0.941
8.014	7.953	7.969	7.956	7.941	7.823	7.946	7.850	7.857	7.907	7.887
0.926	0.923	0.912	0.913	0.923	0.909	0.914	0.916	0.927	0.929	0.924

Phlogopite continued

Phlogopite in polymineralic inclusions in garnet

Diavik - A154N

DVK_GRT_01 _In06 si-rich	DVK_GRT_02 _In01 cc-rich	DVK_GRT_02 _In02 cc-rich	DVK_GRT_02 _In09 si-rich	DVK_GRT_04 _In02 si-rich	DVK_GRT_04 _In03 si-rich	DVK_GRT_04 _In04 si-rich	DVK_GRT_04 _In06 si-rich
36.62	37.82	38.29	37.42	35.04	37.22	37.13	35.94
1.00	0.96	1.94	1.62	1.02	1.22	1.38	0.35
15.78	15.00	14.37	15.38	17.54	13.73	15.46	16.91
3.73	3.48	3.46	1.84	2.53	2.53	1.99	2.57
0.05	0.04	0.07	0.02	0.06	0.08	0.04	0.10
5.26	4.21	3.87	4.06	4.94	4.60	4.53	6.19
0.05	0.02	0.08	0.06	0.00	0.06	0.05	0.00
20.53	21.44	21.75	22.83	20.73	21.99	21.50	20.00
0.05	0.02	0.01	0.10	0.59	0.04	0.01	0.04
0.61	0.21	0.19	0.72	1.41	0.46	0.49	0.00
0.23	0.31	0.19	0.33	1.58	0.41	0.38	0.51
9.54	9.98	10.13	9.50	7.33	9.43	9.94	9.64
n.a.	n.a.	n.a.	n.a.	n.a.	n.a.	n.a.	n.a.
0.04	0.05	0.03	0.02	0.02	0.04	0.06	0.03
93.49	93.53	94.37	93.88	92.79	91.81	92.93	92.29
2.706	2.771	2.777	2.726	2.600	2.784	2.742	2.685
0.056	0.053	0.106	0.089	0.057	0.069	0.077	0.020
1.374	1.296	1.228	1.320	1.534	1.211	1.346	1.489
0.218	0.202	0.198	0.106	0.149	0.149	0.116	0.152
0.003	0.002	0.004	0.001	0.004	0.005	0.002	0.007
0.325	0.258	0.235	0.248	0.307	0.288	0.280	0.387
0.003	0.001	0.004	0.003	0.000	0.004	0.003	0.000
2.261	2.341	2.352	2.479	2.293	2.453	2.367	2.228
0.004	0.002	0.000	0.007	0.047	0.003	0.000	0.004
0.018	0.006	0.006	0.020	0.041	0.013	0.014	0.000
0.033	0.044	0.027	0.046	0.227	0.059	0.054	0.074
0.899	0.933	0.937	0.883	0.694	0.900	0.936	0.919
7.899	7.908	7.875	7.929	7.951	7.938	7.938	7.963
0.874	0.901	0.909	0.909	0.882	0.895	0.894	0.852

Phlogopite continued

Phlogopite in polymineralic inclusions in garnet

Diavik - A154N					Ekati - Point lake			
DVK_GRT_04_In07 si-rich	DVK_GRT_05_In01 si-rich	DVK_GRT_05_In02 si-rich	DVK_GRT_05_In03 si-rich	DVK_GRT_05_In05 si-rich	PL_GRT_01_In01 si-rich	PL_GRT_01_In02 si-rich	PL_GRT_01_In03 si-rich	PL_GRT_01_In05 si-rich
37.03	37.43	39.52	36.86	37.94	37.36	39.30	38.82	38.38
1.07	1.83	1.78	1.80	2.15	0.95	1.52	1.29	0.91
15.70	16.14	13.22	16.71	14.57	14.44	12.36	13.90	13.28
1.96	1.54	1.38	1.48	1.41	3.66	3.74	3.06	1.16
0.08	0.01	0.04	0.06	0.06	0.02	0.07	0.01	0.03
4.86	4.77	3.83	4.99	4.71	4.35	3.74	4.11	4.44
0.01	0.01	0.14	0.02	0.08	n.a.	n.a.	n.a.	n.a.
22.10	21.18	23.30	20.92	21.76	21.77	23.60	22.14	23.56
0.00	0.00	0.01	0.00	0.02	0.01	0.02	0.00	0.00
0.59	0.37	0.19	0.44	0.23	n.a.	n.a.	n.a.	n.a.
0.41	0.32	0.11	0.32	0.22	0.42	0.17	0.12	0.12
9.60	10.12	10.44	10.03	10.18	9.72	10.39	10.32	10.33
n.a.	n.a.	n.a.	n.a.	n.a.	0.36	0.33	0.29	0.26
0.04	0.04	0.05	0.05	0.05	0.07	0.06	0.05	0.06
93.45	93.75	94.00	93.66	93.37	93.14	95.29	94.11	92.52
2.721	2.735	2.865	2.701	2.783	2.763	2.838	2.829	2.842
0.059	0.101	0.097	0.099	0.118	0.053	0.083	0.071	0.050
1.360	1.390	1.129	1.443	1.259	1.258	1.052	1.194	1.159
0.114	0.089	0.079	0.086	0.082	0.214	0.214	0.176	0.068
0.005	0.001	0.002	0.003	0.004	0.001	0.004	0.001	0.002
0.299	0.291	0.232	0.306	0.289	0.269	0.226	0.250	0.275
0.000	0.000	0.008	0.001	0.005				
2.421	2.307	2.518	2.286	2.380	2.400	2.540	2.405	2.601
0.000	0.000	0.001	0.000	0.002	0.001	0.001	0.000	0.000
0.017	0.011	0.005	0.013	0.006				
0.058	0.045	0.015	0.045	0.032	0.060	0.023	0.018	0.018
0.900	0.944	0.965	0.938	0.952	0.917	0.957	0.959	0.976
7.954	7.912	7.917	7.920	7.912	7.936	7.937	7.904	7.991
0.890	0.888	0.916	0.882	0.892	0.899	0.918	0.906	0.904

Phlogopite continued

Phlogopite in polymineralic inclusions in garnet

Ekati - Point lake

PL_GRT_01 _In07 si-rich	PL_GRT_01 _In09 cc-rich	PL_GRT_02 _In01 si-rich	PL_GRT_02 _In02 si-rich	PL_GRT_02 _In04 si-rich	PL_GRT_02 _In05 si-rich	PL_GRT_02 _In06 si-rich	PL_GRT_03 _In03 si-rich	PL_GRT_04 _In04 si-rich	PL_GRT_04 _In05 si-rich
38.81	38.41	40.67	41.11	37.74	37.25	39.34	36.90	37.11	36.50
0.78	1.43	1.19	1.24	0.94	0.90	0.95	0.90	0.79	0.82
12.99	13.80	11.31	12.22	15.67	17.54	13.16	16.78	16.52	16.90
2.90	0.94	4.18	1.96	2.25	2.39	2.82	2.63	2.29	2.61
0.04	0.01	0.10	0.03	0.02	0.06	0.04	0.11	0.01	0.05
3.78	3.81	4.42	3.90	4.68	5.42	4.16	4.75	4.59	4.56
n.a.	n.a.	n.a.	n.a.	n.a.	n.a.	n.a.	n.a.	n.a.	n.a.
24.00	23.89	22.93	23.53	21.98	20.32	23.30	22.98	21.68	21.56
0.03	0.00	0.26	0.01	0.00	0.00	0.04	0.09	0.00	0.02
n.a.	n.a.	0.34	0.06	0.56	0.37	0.17	0.56	n.a.	n.a.
0.12	0.08	0.16	0.12	0.53	0.35	0.10	0.83	0.26	0.34
9.59	10.79	8.05	9.75	9.24	9.74	9.66	8.07	10.51	10.38
0.33	0.27	0.18	0.20	0.25	0.14	0.16	0.22	0.28	0.23
0.07	0.08	0.01	0.10	0.04	0.02	0.01	0.04	0.06	0.04
93.44	93.51	93.79	94.23	93.90	94.50	93.90	94.85	94.10	94.02
2.838	2.812	2.948	2.960	2.756	2.709	2.860	2.661	2.713	2.674
0.043	0.079	0.065	0.067	0.052	0.049	0.052	0.049	0.044	0.045
1.119	1.191	0.966	1.037	1.349	1.503	1.127	1.426	1.424	1.459
0.168	0.054	0.240	0.112	0.130	0.137	0.162	0.150	0.132	0.151
0.002	0.001	0.006	0.002	0.001	0.004	0.002	0.006	0.001	0.003
0.231	0.233	0.268	0.235	0.286	0.330	0.253	0.286	0.281	0.279
2.616	2.607	2.478	2.526	2.393	2.203	2.525	2.470	2.363	2.354
0.002	0.000	0.020	0.001	0.000	0.000	0.003	0.007	0.000	0.002
		0.010	0.002	0.016	0.011	0.005	0.016		
0.018	0.011	0.023	0.017	0.076	0.049	0.014	0.115	0.036	0.048
0.895	1.008	0.744	0.896	0.861	0.904	0.896	0.742	0.980	0.970
7.932	7.996	7.768	7.854	7.920	7.898	7.898	7.929	7.974	7.985
0.919	0.918	0.902	0.915	0.893	0.870	0.909	0.896	0.894	0.894

Phlogopite continued

Phlogopite in polymineralic inclusions in garnet

Ekati - Point lake							Ekati - Wolverine	
PL_GRT_04 _In06 si-rich	PL_GRT_04 _In07 si-rich	PL_GRT_04 _In09 si-rich	PL_GRT_04 _In10 si-rich	PL_GRT_04 _In11 si-rich	PL_GRT_04 _In13 cc-rich	PL_GRT_04 _In14 si-rich	WI7_GRT_03 _In01 si-rich	WI7_GRT_03 _In02 si-rich
35.45	37.31	35.73	37.71	36.64	37.66	38.99	38.40	37.07
0.32	0.73	1.63	1.36	0.91	1.62	1.23	0.86	1.76
17.68	16.97	15.69	15.27	14.60	13.73	12.57	12.73	15.30
2.28	2.33	3.47	3.02	4.47	1.84	1.68	2.59	2.18
0.07	0.05	0.07	0.02	0.06	0.07	0.05	0.06	0.09
6.19	4.83	4.35	4.39	3.90	4.88	3.70	3.87	4.93
n.a.	n.a.	n.a.	n.a.	n.a.	n.a.	n.a.	n.a.	n.a.
22.54	21.24	21.68	22.00	22.24	22.81	24.10	24.11	21.38
0.07	0.00	0.04	0.00	0.00	0.02	0.00	0.00	0.03
n.a.	n.a.	n.a.	n.a.	n.a.	n.a.	n.a.	n.a.	n.a.
0.29	0.25	0.36	0.08	0.35	0.18	0.09	0.32	0.01
8.99	10.49	9.60	10.34	9.73	10.13	10.60	10.26	10.18
0.13	0.20	0.37	0.30	0.20	0.20	0.30	0.25	0.39
0.03	0.03	0.04	0.05	0.04	0.05	0.04	0.04	0.02
94.04	94.42	93.03	94.54	93.14	93.19	93.35	93.48	93.34
2.595	2.715	2.650	2.743	2.709	2.780	2.860	2.821	2.736
0.018	0.040	0.091	0.074	0.051	0.090	0.068	0.047	0.098
1.525	1.455	1.372	1.309	1.272	1.195	1.087	1.102	1.331
0.132	0.134	0.203	0.174	0.261	0.107	0.097	0.150	0.127
0.004	0.003	0.005	0.001	0.004	0.004	0.003	0.003	0.006
0.379	0.294	0.270	0.267	0.241	0.301	0.227	0.238	0.304
2.460	2.304	2.397	2.386	2.451	2.510	2.635	2.640	2.353
0.005	0.000	0.003	0.000	0.000	0.001	0.000	0.000	0.002
0.041	0.035	0.052	0.012	0.050	0.025	0.012	0.045	0.002
0.840	0.974	0.908	0.960	0.918	0.954	0.992	0.962	0.959
7.999	7.955	7.951	7.926	7.957	7.969	7.982	8.009	7.917
0.867	0.887	0.899	0.899	0.910	0.893	0.921	0.917	0.885

Phlogopite continued

Phlogopite in polymineralic inclusions in garnet
Ekati - Wolverine

WI7_GRT_03_In04 si-rich	WI7_GRT_03_In05 si-rich	WI7_GRT_03_In07 si-rich	WI7_GRT_03_In08 si-rich	WI7_GRT_03_In08-2 si-rich	WI7_GRT_03_In09 si-rich	WI7_GRT_03_In10 si-rich	WI7_GRT_03_In12 si-rich	WI7_GRT_03_In13 si-rich
37.67	39.93	36.38	42.25	41.08	37.40	37.34	36.76	37.10
2.45	1.49	1.85	0.85	1.04	1.51	1.32	0.98	0.98
13.30	11.55	16.02	10.12	11.85	13.69	14.18	14.21	14.95
3.36	1.29	1.38	1.84	1.74	3.24	3.76	4.23	3.72
0.01	0.02	0.06	0.14	0.08	0.06	0.07	0.06	0.03
5.03	4.52	5.18	5.88	6.14	4.76	5.17	4.60	4.71
n.a.	n.a.	n.a.	n.a.	n.a.	n.a.	n.a.	n.a.	n.a.
21.65	23.82	22.02	24.37	22.69	22.49	21.95	21.96	21.90
0.07	0.00	0.02	0.97	0.50	0.00	0.07	0.22	0.01
n.a.	n.a.	n.a.	n.a.	n.a.	n.a.	n.a.	n.a.	n.a.
0.26	0.15	1.35	0.13	0.24	0.14	0.14	0.37	0.21
10.40	10.72	8.55	5.57	6.13	10.29	9.29	9.59	10.24
0.34	0.34	0.27	0.22	0.22	0.25	0.26	0.22	0.34
0.04	0.03	0.05	0.02	0.03	0.01	0.03	0.01	0.00
94.58	93.86	93.13	92.37	91.74	93.84	93.58	93.21	94.19
2.763	2.922	2.677	3.059	3.003	2.754	2.749	2.723	2.723
0.135	0.082	0.102	0.046	0.057	0.084	0.073	0.055	0.054
1.150	0.996	1.389	0.864	1.021	1.188	1.230	1.241	1.293
0.195	0.075	0.080	0.105	0.101	0.189	0.219	0.248	0.216
0.001	0.001	0.004	0.009	0.005	0.004	0.005	0.004	0.002
0.309	0.277	0.319	0.356	0.375	0.293	0.318	0.285	0.289
2.367	2.598	2.415	2.630	2.473	2.469	2.409	2.425	2.396
0.006	0.000	0.001	0.075	0.039	0.000	0.005	0.017	0.001
0.037	0.021	0.193	0.018	0.035	0.021	0.020	0.053	0.029
0.973	1.001	0.803	0.514	0.572	0.967	0.872	0.906	0.959
7.935	7.972	7.984	7.677	7.681	7.967	7.900	7.958	7.963
0.885	0.904	0.883	0.881	0.868	0.894	0.883	0.895	0.892

A2.9. LA-ICP-MS Phlogopite

Phlogopite in polymineralic inclusions in clinopyroxene

Location	Diavik - A154N								
Sample	DVK_CD_06B Incl02-1	DVK_CD_06B Incl02-2	DVK_CD_06B Incl03-1	DVK_CD_06B Incl03-2	DVK_CD_06B Incl03-3	DVK_CD_06B Incl06-1	DVK_CD_06B Incl06-2	DVK_CD_06B Incl07-1	DVK_CD_06B Incl08-1
Inclusion type	si-rich	si-rich	si-rich	si-rich	si-rich	si-rich	si-rich	si-rich	si-rich
Element concentrations in ppm									
Ca	168	132	228	b.d.l.	b.d.l.	173	162	171	119
Sc	1.62	1.62	1.18	1.59	1.40	1.44	1.34	1.27	1.46
V	102	107	97	94	95	94	93	95	113
Cr	9220	8300	7091	7430	7380	7081	6671	6278	8276
Mn	146	154	151	146	148	151	148	156	148
Co	59.8	60.4	57.7	57.4	59.3	59.7	58.8	57.6	58.1
Ni	1480	1494	1435	1408	1425	1490	1485	1384	1450
Rb	861	839	800	898	850	927	852	874	892
Sr	3.4	3.8	6.5	3.6	3.9	4.4	4.6	4.5	3.9
Zr	1.22	1.10	1.01	1.00	0.97	0.97	0.98	1.01	1.32
Nb	19.3	20.2	21.2	15.7	19.2	16.8	19.8	18.0	17.2
Cs	3.82	3.37	3.03	3.87	3.52	3.92	3.42	3.43	3.75
Ba	274	298	392	297	356	315	364	304	265
Ce	0.020	0.143	0.750	0.027	0.010	0.030	0.160	0.054	0.080
Hf	0.042	0.018	0.016	0.043	0.011	0.027	0.023	0.043	0.035
Ta	1.86	2.12	2.27	1.45	1.87	1.58	1.96	1.72	1.63

b.d.l. = below detection limit

Phlogopite continued

Phlogopite in polymineralic inclusions in clinopyroxene					Phlogopite in polymineralic inclusions in garnet					
Diavik - A154N					Ekati - Point lake					Ekati - Wolver
DVK_CD_06B	DVK_CD_06B	DVK_CD_06B	DVK_CD_06B	DVK_CD_06B	PL_GRT_01	PL_GRT_01	PL_GRT_01	PL_GRT_01	PL_GRT_01	WI7_GRT_03
Incl09-2	Incl09-4	Incl09-5	Incl10-1	Incl10-2	Incl3-1	Incl3-2	Incl3-3	Incl9-1	Incl9-2	Incl1-1
si-rich	si-rich	si-rich	si-rich	si-rich	si-rich	si-rich	si-rich	cc-rich	cc-rich	si-rich
304	b.d.l.	192	b.d.l.	176	1100	420	12000	1320	154	4000
1.40	1.42	1.41	1.70	1.50	6.74	10.80	19.90	5.68	3.82	44.90
113	107	95	128	130	150	229	162	295	249	149
8800	6720	7640	10104	10060	13340	19420	19600	4910	5710	18990
172	180	243	144	142	399	323	777	244	186	650
55.3	53.4	44.3	62.3	62.8	36.4	46.9	33.4	59.8	62.9	48.5
1260	1339	1041	1481	1530	163	227	131	567	879	521
814	830	692	926	919	291	411	335	536	759	372
4.3	6.4	7.9	3.4	3.4	23.5	20.8	199.0	26.9	13.8	31.9
1.31	0.98	1.08	1.37	1.32	4.28	6.7	13.9	3.6	2.076	8.9
19.9	15.6	15.3	20.0	20.0	46.7	65.1	97	64.1	42.24	27.69
3.33	3.57	3.11	4.02	4.00	4	3.81	3.61	4.331	4.54	2.91
295	319	225	290	280	1210	1241	6710	1612	1015	772
0.121	0.180	0.419	b.d.l.	b.d.l.	0.41	0.91	5.9	0.39	b.d.l.	5.1
0.049	0.029	0.027	0.039	0.028	0.179	0.271	0.293	0.167	0.069	0.235
1.97	1.28	1.31	1.87	1.83	4.34	7.06	8.1	6.39	3.99	1.93

Phlogopite continued

Phlogopite in polymineralic inclusions in garnet

Ekati - Wolverine

WI7_GRT_03 Incl4-1 si-rich	WI7_GRT_03 Incl4-2 si-rich	WI7_GRT_03 Incl5-1 si-rich	WI7_GRT_03 Incl5-2 si-rich	WI7_GRT_03 Incl5-3 si-rich	WI7_GRT_03 Incl9-1 si-rich
1860	1960	490	2600	610	5440
12.20	9.65	6.50	14.00	11.31	38.50
309	305	168	246	303	191
18600	19030	10190	10390	13420	7590
302	359	266	457	347	606
53.7	57.5	61.4	58.3	55.1	26.9
386	478	555	372	245	171
388	448	704	554	342	162
75.0	55.0	13.3	44.0	28.1	82.7
7.1	4.86	3.84	5.35	5.47	34
48.5	40.8	19.44	36.2	49	33.8
3.91	3.81	4.31	4.205	3.539	2.64
1683	1413	578	999	1800	1740
15.4	2.5	1.56	4.8	1.74	1.46
0.303	0.232	0.139	0.259	0.244	1.04
4.59	4.059	1.73	3.01	4.75	3.2

A2.10. EPMA Carbonates

	Carbonate in polymineralic inclusions in clinopyroxene								
Location	DVK - A154N								
Sample	DVK_CD_01 _In01	DVK_CD_01 _In02	DVK_CD_01 _In03	DVK_CD_01 _In03-2	DVK_CD_01 _In04	DVK_CD_01 _In05	DVK_CD_01 _In05-2	DVK_CD_01 _In06	DVK_CD_01 _In07
Inclusion type	cc-rich	cc-rich	cc-rich	cc-rich	cc-rich	cc-rich	cc-rich	si-rich	cc-rich
Major element analyses (wt.%)									
CaO	55.81	53.55	54.63	55.06	52.80	53.81	55.70	50.46	51.03
MgO	0.23	1.73	2.61	0.02	3.19	1.61	0.00	4.87	0.06
FeO	0.02	0.11	0.05	0.05	0.04	0.04	0.03	0.16	0.11
MnO	0.09	0.11	0.02	0.13	0.08	0.03	0.03	0.09	0.00
SrO	0.03	0.20	0.13	0.15	0.09	0.06	0.01	0.09	1.82
BaO	0.05	0.00	0.06	1.09	0.00	0.00	0.00	0.00	3.02
F	n.a.	n.a.	n.a.	n.a.	n.a.	n.a.	n.a.	n.a.	n.a.
CO_2*	43.77	44.30	42.52	43.50	43.80	44.44	44.23	44.34	43.96
Total	56.23	55.70	57.48	56.50	56.20	55.56	55.77	55.66	56.04
Number of cations (apfu) on the basis of 6 oxygen atoms and 2 cations									
Ca	1.996	1.900	1.966	1.983	1.874	1.906	1.984	1.776	1.852
Mg	0.011	0.085	0.131	0.001	0.158	0.080	0.000	0.238	0.003
Fe	0.001	0.003	0.001	0.001	0.001	0.001	0.001	0.004	0.003
Mn	0.003	0.003	0.001	0.004	0.002	0.001	0.001	0.003	0.000
Sr	0.001	0.004	0.002	0.003	0.002	0.001	0.000	0.002	0.036
Ba	0.001	0.000	0.001	0.014	0.000	0.000	0.000	0.000	0.040
sum	2.011	1.995	2.101	2.007	2.037	1.989	1.986	2.023	1.934
Ca/(Ca+Mg+Fe)	0.994	0.956	0.937	0.999	0.922	0.959	1.000	0.880	0.997

**by subtracting total from 100 wt.%*

Carbonates continued

Carbonate in polymineralic inclusions in clinopyroxene

DVK - A154N

DVK_CD_01_In08	DVK_CD_2B_In01	DVK_CD_2B_In03	DVK_CD_2B_In04	DVK_CD_04B_In01	DVK_CD_04B_In02	DVK_CD_04B_In04	DVK_CD_4B_In05	DVK_CD_06A_In01	DVK_CD_06A_In02
cc-rich	si-rich	si-rich	si-rich	cc-rich	cc-rich	cc-rich	si-rich	si-rich	si-rich
54.20	56.54	55.52	56.98	57.79	57.40	57.28	56.94	56.03	56.08
1.28	0.38	0.63	0.03	0.01	0.02	0.02	0.00	0.07	0.06
0.12	0.11	0.20	0.04	0.00	0.00	0.04	0.11	0.01	0.06
0.46	0.61	0.01	0.05	0.00	0.05	0.00	0.02	0.19	0.09
0.14	0.02	0.20	0.03	0.02	0.00	0.00	0.01	0.04	0.07
0.00	0.00	0.00	0.00	0.03	0.03	0.00	0.00	0.07	0.02
n.a.	n.a.	n.a.	n.a.	n.a.	n.a.	n.a.	n.a.	n.a.	n.a.
43.81	42.34	43.34	42.86	42.15	42.50	42.65	42.92	43.59	43.63
56.19	57.66	56.66	57.14	57.85	57.50	57.36	57.08	56.41	56.37
1.934	2.049	1.992	2.055	2.098	2.077	2.070	2.053	2.008	2.009
0.063	0.019	0.031	0.001	0.001	0.001	0.001	0.000	0.003	0.003
0.003	0.003	0.005	0.001	0.000	0.000	0.001	0.003	0.000	0.002
0.013	0.017	0.000	0.001	0.000	0.001	0.000	0.000	0.005	0.003
0.003	0.000	0.004	0.001	0.000	0.000	0.000	0.000	0.001	0.001
0.000	0.000	0.000	0.000	0.000	0.000	0.000	0.000	0.001	0.000
2.016	2.089	2.040	2.060	2.100	2.081	2.073	2.057	2.019	2.017
0.967	0.989	0.982	0.999	1.000	0.999	0.999	0.999	0.998	0.998

Carbonates continued

Carbonate in polymineralic inclusions in clinopyroxene

DVK - A154N

DVK_CD_06A_In03	DVK_CD_06A_In04	DVK_CD_06A_In04-2	DVK_CD_06A_In05	DVK_CD_06A_In06	DVK_CD_06A_In07	DVK_CD_06A_In08	DVK_CD_06A_In09	DVK_CD_06A_In10
si-rich	si-rich	si-rich	si-rich	si-rich	si-rich	si-rich	si-rich	si-rich
54.14	53.33	55.54	58.39	56.60	55.00	56.14	54.84	55.10
0.08	1.45	0.11	0.20	0.35	0.49	0.01	0.22	0.12
0.12	0.21	0.00	0.23	0.19	0.11	0.05	0.11	0.09
0.18	0.02	0.06	0.33	0.15	0.01	0.03	0.21	0.16
0.51	0.77	0.61	0.54	0.49	0.33	0.02	0.34	0.36
1.22	0.05	0.00	0.40	0.34	0.06	0.06	0.04	0.18
n.a.	n.a.	n.a.	n.a.	n.a.	n.a.	n.a.	n.a.	n.a.
43.75	44.17	43.68	39.92	41.88	44.01	43.70	44.24	43.99
56.25	55.83	56.32	60.08	58.12	55.99	56.30	55.76	56.01
1.949	1.899	1.991	2.172	2.065	1.963	2.010	1.955	1.970
0.004	0.072	0.006	0.010	0.018	0.024	0.000	0.011	0.006
0.003	0.006	0.000	0.007	0.005	0.003	0.001	0.003	0.003
0.005	0.001	0.002	0.010	0.004	0.000	0.001	0.006	0.004
0.010	0.015	0.012	0.011	0.010	0.006	0.000	0.007	0.007
0.016	0.001	0.000	0.005	0.005	0.001	0.001	0.000	0.002
1.987	1.992	2.010	2.215	2.106	1.997	2.013	1.982	1.992
0.996	0.961	0.997	0.992	0.989	0.986	0.999	0.993	0.996

Carbonates continued

Carbonate in polymineralic inclusions in clinopyroxene

DVK - A154N

DVK_CD_06A_In12	DVK_CD_06B_In01	DVK_CD_06B_In02	DVK_CD_06B_In03	DVK_CD_06B_In04	DVK_CD_06B_In05	DVK_CD_06B_In06	DVK_CD_06B_In07	DVK_CD_06B_In09	DVK_CD_06B_In10
si-rich	si-rich	si-rich	si-rich	si-rich	si-rich	si-rich	si-rich	si-rich	si-rich
55.93	54.28	55.09	55.79	55.49	54.66	56.60	54.41	54.09	54.42
0.02	0.18	0.09	0.02	0.01	0.08	0.01	0.41	0.24	0.91
0.14	0.15	0.05	0.09	0.05	0.09	0.00	0.23	0.09	0.21
0.00	0.21	0.00	0.04	0.04	0.01	0.02	0.34	0.60	0.01
0.46	0.45	0.66	0.68	0.63	0.44	0.26	0.32	0.25	0.56
0.08	0.43	0.12	0.08	0.01	0.67	0.00	0.00	0.22	0.05
n.a.	n.a.	n.a.	n.a.	n.a.	n.a.	n.a.	n.a.	n.a.	n.a.
43.38	44.30	43.99	43.31	43.77	44.05	43.11	44.29	44.51	43.84
56.62	55.70	56.02	56.69	56.23	55.95	56.89	55.71	55.49	56.16
2.011	1.937	1.970	2.008	1.988	1.957	2.038	1.938	1.925	1.945
0.001	0.009	0.004	0.001	0.000	0.004	0.001	0.020	0.012	0.045
0.004	0.004	0.001	0.002	0.001	0.003	0.000	0.006	0.002	0.006
0.000	0.006	0.000	0.001	0.001	0.000	0.000	0.010	0.017	0.000
0.009	0.009	0.013	0.013	0.012	0.008	0.005	0.006	0.005	0.011
0.001	0.006	0.002	0.001	0.000	0.009	0.000	0.000	0.003	0.001
2.026	1.970	1.991	2.027	2.004	1.981	2.044	1.980	1.964	2.008
0.998	0.993	0.997	0.998	0.999	0.997	1.000	0.986	0.993	0.974

Carbonates continued

Carbonate in polymineralic inclusions in clinopyroxene								Carbonate in polymineralic inclusions in garn		
DVK - A154N	Ekati - Point lake							DVK - A154N		
DVK_CD_06B_In11	PL_CD_03_Incl01	PL_CD_03_Incl02	PL_CD_03_Incl03	PL_CD_03_Incl04	PL_CD_07_In01	PL_CD_07_In02	PL_CD_07_In04	DVK_GRT_02_In09	DVK_GRT_04_In02	DVK_GRT_04_In03
si-rich	cc-rich	cc-rich	cc-rich	cc-rich	si-rich	si-rich	si-rich	si-rich	si-rich	si-rich
55.68	56.36	57.83	57.36	57.37	50.58	50.93	56.49	52.27	56.19	53.40
0.08	0.00	0.00	0.00	0.00	1.72	0.90	0.00	0.00	0.00	0.00
0.11	0.03	0.07	0.07	0.08	0.61	0.56	0.08	0.37	0.28	0.39
0.10	0.35	0.05	0.05	0.11	0.13	0.50	0.11	0.69	0.61	0.86
0.51	0.18	0.12	0.27	0.09	0.43	0.76	0.80	2.06	0.35	0.05
0.06	n.a.	n.a.	n.a.	n.a.	0.77	0.87	0.13	4.74	0.54	0.38
n.a.	0.54	0.32	0.46	0.58	0.20	0.10	0.08	n.a.	n.a.	n.a.
43.47	42.55	41.61	41.77	41.77	45.40	45.34	42.31	39.88	42.03	44.92
56.53	57.45	58.39	58.23	58.23	54.60	54.66	57.69	60.12	57.97	55.08
2.000	2.047	2.116	2.098	2.099	1.786	1.805	2.055	1.992	2.053	1.896
0.004	0.000	0.000	0.000	0.000	0.085	0.044	0.000	0.000	0.000	0.000
0.003	0.001	0.002	0.002	0.002	0.017	0.015	0.002	0.011	0.008	0.011
0.003	0.010	0.001	0.002	0.003	0.004	0.014	0.003	0.021	0.018	0.024
0.010	0.003	0.002	0.005	0.002	0.008	0.015	0.016	0.042	0.007	0.001
0.001					0.010	0.011	0.002	0.066	0.007	0.005
2.021	2.062	2.121	2.107	2.106	1.919	1.907	2.078	2.132	2.092	1.937
0.997	1.000	0.999	0.999	0.999	0.946	0.968	0.999	0.995	0.996	0.994

Carbonates continued

Carbonate in polymineralic inclusions in garnet

DVK - A154N

DVK_GRT_04_In03-2	DVK_GRT_04_In03-3	DVK_GRT_04_In04	DVK_GRT_04_In05	DVK_GRT_04_In06	DVK_GRT_04_In06-2	DVK_GRT_04_In07	DVK_GRT_04_In07-2	DVK_GRT_05_In01	DVK_GRT_05_In02
si-rich	si-rich	si-rich	si-rich	si-rich	si-rich	si-rich	si-rich	cc-rich	cc-rich
29.77	30.75	30.06	54.85	54.96	29.22	55.26	31.01	55.20	54.83
17.81	16.82	17.95	0.00	0.00	18.20	0.00	18.83	0.00	0.00
2.30	2.35	1.89	0.21	0.29	2.73	0.14	1.38	0.00	0.03
1.04	1.03	1.10	1.59	0.25	0.86	0.80	0.82	0.24	0.30
0.08	0.10	0.49	0.42	0.15	0.22	0.03	0.47	0.05	0.10
0.10	0.24	0.54	0.59	0.09	0.34	0.10	0.67	0.19	0.12
n.a.	n.a.	n.a.	n.a.	n.a.	n.a.	n.a.	n.a.	n.a.	n.a.
48.91	48.71	47.97	42.34	44.25	48.44	43.68	46.82	44.32	44.63
51.09	51.29	52.03	57.67	55.75	51.56	56.33	53.18	55.68	55.37
0.984	1.021	1.003	2.000	1.960	0.971	1.982	1.043	1.966	1.948
0.819	0.777	0.833	0.000	0.000	0.842	0.000	0.882	0.000	0.000
0.059	0.061	0.049	0.006	0.008	0.071	0.004	0.036	0.000	0.001
0.027	0.027	0.029	0.046	0.007	0.023	0.023	0.022	0.007	0.008
0.001	0.002	0.009	0.008	0.003	0.004	0.001	0.009	0.001	0.002
0.001	0.003	0.007	0.008	0.001	0.004	0.001	0.008	0.002	0.002
1.892	1.890	1.930	2.068	1.979	1.915	2.010	2.000	1.977	1.961
0.528	0.549	0.532	0.997	0.996	0.516	0.998	0.532	1.000	1.000

Carbonates continued

Carbonate in polymineralic inclusions in garnet										
DVK - A154N		Ekati - Point lake								
DVK_GRT_05_In03	DVK_GRT_05_In05	PL_GRT_01_In02	PL_GRT_01_In03	PL_GRT_01_In07	PL_GRT_01_In08	PL_GRT_01_In09	PL_GRT_01_In12	PL_GRT_02_In03	PL_GRT_04_In01	PL_GRT_04_In04
si-rich	si-rich	si-rich	si-rich	si-rich	si-rich	cc-rich	si-rich	cc-rich	si-rich	si-rich
56.38	56.89	55.92	55.24	52.60	56.21	56.60	53.86	57.57	57.67	32.00
0.00	0.00	0.00	0.00	0.92	0.00	0.00	0.54	0.00	0.00	17.73
0.24	0.20	0.35	0.19	0.45	0.54	0.11	0.23	0.16	0.05	3.33
0.47	0.05	0.15	0.82	1.91	0.04	0.30	1.06	0.02	0.10	0.39
0.10	0.02	0.64	0.22	0.10	0.30	0.03	0.11	0.09	0.04	0.29
0.35	0.02	n.a.	n.a.	n.a.	n.a.	n.a.	n.a.	0.08	n.a.	n.a.
n.a.	n.a.	0.56	0.51	0.47	0.53	0.53	0.54	0.09	0.51	0.29
42.45	42.83	42.38	43.03	43.56	42.38	42.43	43.67	42.00	41.64	45.98
57.55	57.17	57.62	56.97	56.44	57.62	57.57	56.34	58.00	58.36	54.03
2.046	2.054	2.038	1.999	1.892	2.047	2.057	1.936	2.097	2.111	1.088
0.000	0.000	0.000	0.000	0.046	0.000	0.000	0.027	0.000	0.000	0.838
0.007	0.006	0.010	0.005	0.013	0.015	0.003	0.006	0.005	0.001	0.088
0.014	0.001	0.004	0.023	0.054	0.001	0.009	0.030	0.001	0.003	0.010
0.002	0.000	0.013	0.004	0.002	0.006	0.001	0.002	0.002	0.001	0.005
0.005	0.000	0.000	0.000	0.000	0.000	0.000	0.000	0.001	0.000	0.000
2.073	2.061	2.065	2.032	2.007	2.069	2.070	2.001	2.105	2.116	2.030
0.997	0.997	0.995	0.997	0.970	0.993	0.998	0.983	0.998	0.999	0.540

Carbonates continued

Carbonate in polymineralic inclusions in garnet

Ekati - Point lake					Ekati - Wolverine	
PL_GRT_04_In05	PL_GRT_04_In06	PL_GRT_04_In08	PL_GRT_04_In13	PL_GRT_04_In14	WI7_GRT_03_In05	WI7_GRT_03_In05-2
si-rich	si-rich	si-rich	cc-rich	si-rich	si-rich	si-rich
27.22	31.53	52.27	57.43	55.58	55.62	55.28
22.45	18.77	1.35	0.00	0.00	0.00	0.24
2.03	1.37	0.51	0.02	0.30	0.30	0.26
1.19	1.57	1.68	0.00	0.05	0.10	0.07
0.18	0.42	0.50	0.02	0.80	0.40	0.41
n.a.	n.a.	n.a.	n.a.	n.a.	n.a.	n.a.
0.18	0.15	0.56	0.56	0.47	0.34	0.50
46.76	46.19	43.13	41.98	42.79	43.23	43.24
53.24	53.82	56.87	58.03	57.21	56.77	56.76
0.908	1.064	1.889	2.096	2.018	2.007	1.996
1.042	0.881	0.068	0.000	0.000	0.000	0.012
0.053	0.036	0.014	0.001	0.009	0.008	0.007
0.031	0.042	0.048	0.000	0.001	0.003	0.002
0.003	0.008	0.010	0.000	0.016	0.008	0.008
0.000	0.000	0.000	0.000	0.000	0.000	0.000
2.037	2.031	2.028	2.097	2.043	2.026	2.025
0.453	0.537	0.958	1.000	0.996	0.996	0.990

A2.11. EPMA Chromite and Spinel

	Chromite in polymineralic inclusions in clinopyroxene					
Location	DVK - A154N					
Sample	DVK_CD_01_In01	DVK_CD_01_In02	DVK_CD_01_In04	DVK_CD_01_In06	DVK_CD_01_In07	DVK_CD_02B_In03
Type	cc-rich	cc-rich	cc-rich	si-rich	cc-rich	si-rich
Mineral	chr	chr	chr	chr	chr	chr
Major element analyses (wt.%)						
SiO_2	0.08	0.08	0.78	0.09	0.14	0.06
TiO_2	6.09	6.60	3.87	5.77	4.15	3.87
Al_2O_3	2.01	1.85	4.75	2.17	3.14	2.94
Cr_2O_3	49.05	47.54	28.69	52.21	48.70	51.60
MnO	0.40	0.39	0.58	0.43	0.62	0.45
FeO	27.18	28.92	46.92	24.96	28.73	25.88
NiO	0.22	0.21	0.19	0.25	0.07	0.09
MgO	13.50	12.86	10.44	13.05	11.17	13.33
CaO	0.98	0.75	0.72	0.36	0.50	0.64
Total	99.58	99.23	97.03	99.35	97.38	98.99
Number of cations (apfu) on the basis of 4 oxygen atoms and 3 cations						
Ti	0.159	0.174	0.111	0.150	0.112	0.101
Al	0.082	0.076	0.214	0.088	0.133	0.121
Cr	1.345	1.316	0.869	1.427	1.383	1.421
Mn	0.012	0.011	0.019	0.013	0.019	0.013
Fe	0.789	0.847	1.503	0.722	0.863	0.754
Ni	0.006	0.006	0.006	0.007	0.002	0.003
Mg	0.698	0.671	0.596	0.673	0.598	0.692
Ca	0.036	0.028	0.029	0.013	0.019	0.024
Sum	3.127	3.130	3.347	3.092	3.130	3.128
Fe^{3+}	0.326	0.332	0.829	0.239	0.332	0.327
Normalized cation values according to Droop et al. (1987)						
T/S	0.959	0.958	0.896	0.970	0.959	0.959
Ti	0.152	0.167	0.100	0.146	0.108	0.097
Al	0.079	0.073	0.192	0.086	0.127	0.116
Cr	1.290	1.261	0.779	1.384	1.326	1.363
Mn	0.011	0.011	0.017	0.012	0.018	0.013
Fe (total)	0.756	0.812	1.347	0.700	0.827	0.723
Ni	0.006	0.006	0.005	0.007	0.002	0.002
Mg	0.670	0.643	0.534	0.652	0.573	0.664
Ca	0.035	0.027	0.026	0.013	0.018	0.023
Fe^{3+}	0.326	0.332	0.829	0.239	0.332	0.327
Fe^{2+}	0.431	0.479	0.517	0.461	0.496	0.396
$Mg/(Mg+Fe^{2+})$	0.609	0.573	0.508	0.586	0.536	0.627
Cr/(Cr+Al)	0.942	0.945	0.802	0.942	0.912	0.922

Chromite and spinel continued

Chromite in polymineralic inclusions in clinopyroxene

DVK - A154N

DVK_CD_04B_In02 cc-rich chr	DVK_CD_04B_In04 cc-rich chr	DVK_CD_04B_In05 si-rich chr	DVK_CD_06A_In01 si-rich chr	DVK_CD_06A_In02 si-rich chr	DVK_CD_06A_In03 si-rich chr	DVK_CD_06A_In04 si-rich chr
0.08	0.08	0.07	0.14	0.11	0.08	0.11
4.02	3.54	3.08	5.46	3.85	4.06	4.28
1.89	2.05	4.02	1.88	2.12	1.65	1.69
56.14	58.60	59.08	46.97	49.09	53.16	53.77
0.39	0.38	0.36	0.53	0.55	0.48	0.47
23.57	21.54	20.46	30.51	30.65	27.15	26.93
0.16	0.20	0.11	0.10	0.03	0.15	0.17
13.42	13.50	13.14	11.43	10.99	11.77	11.74
0.32	0.48	0.14	0.76	0.09	0.73	0.29
100.05	100.41	100.53	97.86	97.54	99.41	99.52
0.104	0.091	0.078	0.148	0.105	0.108	0.113
0.076	0.082	0.159	0.080	0.091	0.069	0.070
1.524	1.576	1.570	1.337	1.407	1.479	1.491
0.011	0.011	0.010	0.016	0.017	0.014	0.014
0.677	0.613	0.575	0.918	0.929	0.799	0.790
0.004	0.005	0.003	0.003	0.001	0.004	0.005
0.687	0.685	0.658	0.613	0.594	0.618	0.614
0.012	0.018	0.005	0.029	0.004	0.028	0.011
3.096	3.080	3.058	3.144	3.146	3.118	3.107
0.248	0.208	0.151	0.367	0.372	0.304	0.275
0.969	0.974	0.981	0.954	0.953	0.962	0.966
0.101	0.088	0.076	0.141	0.100	0.103	0.109
0.074	0.080	0.156	0.076	0.086	0.066	0.067
1.477	1.535	1.540	1.275	1.341	1.423	1.440
0.011	0.011	0.010	0.015	0.016	0.014	0.013
0.656	0.597	0.564	0.876	0.886	0.769	0.763
0.004	0.005	0.003	0.003	0.001	0.004	0.005
0.666	0.667	0.646	0.585	0.566	0.594	0.593
0.012	0.017	0.005	0.028	0.003	0.027	0.011
0.248	0.208	0.151	0.367	0.372	0.304	0.275
0.408	0.388	0.413	0.510	0.514	0.465	0.488
0.620	0.632	0.610	0.534	0.524	0.561	0.549
0.952	0.950	0.908	0.944	0.940	0.956	0.955

Chromite and spinel continued

Chromite in polymineralic inclusions in clinopyroxene

DVK - A154N

DVK_CD_06A_In05 si-rich chr	DVK_CD_06A_In07 si-rich chr	DVK_CD_06A_In08 si-rich chr	DVK_CD_06A_In12 si-rich chr	DVK_CD_06B_In01 si-rich chr	DVK_CD_06B_In02 si-rich chr	DVK_CD_06B_In03 si-rich chr
0.09	0.08	0.06	0.08	0.30	0.09	0.13
5.22	5.10	4.34	4.14	4.26	4.80	4.45
2.05	1.76	2.55	2.77	2.59	1.93	2.43
52.55	52.60	54.32	53.43	42.23	52.02	48.93
0.37	0.39	0.37	0.52	0.60	0.34	0.46
25.60	26.83	24.99	26.48	36.27	26.38	30.55
0.21	0.22	0.15	0.08	0.10	0.21	0.08
12.87	12.92	12.35	11.63	10.69	12.58	11.55
0.12	0.03	0.70	0.02	0.57	0.06	0.38
99.14	99.96	99.87	99.21	97.66	98.63	99.02
0.137	0.133	0.113	0.109	0.118	0.127	0.119
0.084	0.072	0.104	0.114	0.113	0.080	0.102
1.445	1.442	1.482	1.476	1.231	1.447	1.374
0.011	0.011	0.011	0.015	0.019	0.010	0.014
0.745	0.778	0.721	0.774	1.118	0.776	0.907
0.006	0.006	0.004	0.002	0.003	0.006	0.002
0.667	0.668	0.635	0.606	0.587	0.660	0.611
0.005	0.001	0.026	0.001	0.022	0.002	0.014
3.099	3.110	3.095	3.096	3.210	3.109	3.143
0.255	0.284	0.245	0.249	0.524	0.281	0.365
0.968	0.965	0.969	0.969	0.934	0.965	0.954
0.132	0.128	0.109	0.105	0.110	0.123	0.113
0.081	0.069	0.101	0.111	0.105	0.077	0.097
1.399	1.391	1.436	1.430	1.150	1.396	1.311
0.011	0.011	0.010	0.015	0.017	0.010	0.013
0.721	0.750	0.699	0.750	1.045	0.749	0.866
0.006	0.006	0.004	0.002	0.003	0.006	0.002
0.646	0.644	0.616	0.587	0.549	0.637	0.584
0.004	0.001	0.025	0.001	0.021	0.002	0.014
0.255	0.284	0.245	0.249	0.524	0.281	0.365
0.465	0.466	0.454	0.501	0.521	0.468	0.501
0.581	0.580	0.576	0.540	0.513	0.576	0.538
0.945	0.953	0.935	0.928	0.916	0.948	0.931

Chromite and spinel continued

Chromite in polymineralic inclusions in clinopyroxene

DVK - A154N						Ekati - Poin
DVK_CD_06B_In04	DVK_CD_06B_In06	DVK_CD_06B_In07	DVK_CD_06B_In08	DVK_CD_06B_In09	DVK_CD_06B_In10	PL_CD_07_In01
si-rich chr	si-rich chr	si-rich chr	si-rich chr	si-rich chr	si-rich chr	si-rich chr
0.07	0.07	0.09	0.12	0.08	0.08	0.17
4.44	5.39	5.34	3.98	4.71	4.58	3.64
1.85	2.03	1.77	2.38	2.54	2.48	3.56
54.69	51.44	51.66	45.51	53.23	54.25	54.31
0.40	0.38	0.36	0.50	0.40	0.32	0.47
25.75	27.24	27.33	33.70	26.18	25.27	25.15
0.17	0.22	0.20	0.13	0.06	0.11	0.06
12.35	12.65	12.49	10.81	12.47	12.45	11.74
0.03	0.12	0.03	0.03	0.03	0.05	0.11
99.80	99.57	99.32	97.23	99.78	99.65	99.22
0.116	0.141	0.140	0.110	0.123	0.119	0.095
0.076	0.083	0.073	0.103	0.104	0.101	0.146
1.501	1.415	1.428	1.320	1.456	1.483	1.490
0.012	0.011	0.011	0.016	0.012	0.009	0.014
0.747	0.793	0.799	1.034	0.758	0.731	0.730
0.005	0.006	0.006	0.004	0.002	0.003	0.002
0.639	0.656	0.651	0.591	0.643	0.642	0.607
0.001	0.004	0.001	0.001	0.001	0.002	0.004
3.096	3.110	3.109	3.179	3.098	3.089	3.087
0.248	0.282	0.280	0.450	0.252	0.231	0.226
0.969	0.965	0.965	0.944	0.969	0.971	0.972
0.112	0.136	0.136	0.104	0.119	0.116	0.092
0.073	0.080	0.071	0.097	0.100	0.098	0.141
1.454	1.365	1.378	1.246	1.410	1.440	1.448
0.011	0.011	0.010	0.015	0.011	0.009	0.013
0.724	0.765	0.771	0.976	0.734	0.710	0.709
0.005	0.006	0.005	0.004	0.002	0.003	0.002
0.619	0.633	0.628	0.558	0.623	0.623	0.590
0.001	0.004	0.001	0.001	0.001	0.002	0.004
0.248	0.282	0.280	0.450	0.252	0.231	0.226
0.476	0.482	0.491	0.526	0.482	0.479	0.483
0.565	0.568	0.561	0.515	0.564	0.565	0.550
0.952	0.944	0.951	0.928	0.934	0.936	0.911

Chromite and spinel continued

Chromite/spinel in polymineralic inclusions in garnet

Diavik - A154N

DVK_GRT_01_In06	DVK_GRT_01_In06-2	DVK_GRT_02_In01	DVK_GRT_02_In07	DVK_GRT_02_In09	DVK_GRT_03_In03	DVK_GRT_04_In02
si-rich spl	si-rich spl	si-rich spl	si-rich spl	si-rich spl	si-rich spl	si-rich spl
0.43	1.64	0.25	0.33	0.26	0.16	0.56
0.62	1.07	0.69	0.49	0.76	0.07	0.49
24.33	38.91	38.05	46.71	43.71	40.01	44.58
36.03	14.70	15.37	12.30	16.36	22.55	13.78
0.44	0.35	0.22	0.54	0.39	0.40	0.46
22.24	20.29	23.38	17.28	15.45	15.09	17.73
0.02	0.01	0.04	0.01	0.02	0.04	0.02
13.80	19.00	17.99	18.32	18.62	17.85	18.41
0.34	0.18	0.19	0.03	0.03	0.16	0.11
98.25	96.15	96.18	96.01	95.59	96.33	96.13
0.015	0.024	0.016	0.010	0.016	0.001	0.011
0.906	1.373	1.345	1.571	1.484	1.373	1.515
0.900	0.348	0.365	0.278	0.373	0.519	0.314
0.012	0.009	0.006	0.013	0.009	0.010	0.011
0.588	0.508	0.587	0.412	0.372	0.368	0.428
0.001	0.000	0.001	0.000	0.001	0.001	0.001
0.650	0.848	0.805	0.779	0.800	0.775	0.792
0.011	0.006	0.006	0.001	0.001	0.005	0.003
3.082	3.116	3.129	3.065	3.055	3.052	3.075
0.213	0.297	0.331	0.170	0.145	0.137	0.194
0.973	0.963	0.959	0.979	0.982	0.983	0.976
0.014	0.023	0.015	0.010	0.016	0.001	0.010
0.882	1.322	1.290	1.538	1.457	1.350	1.479
0.876	0.335	0.350	0.272	0.366	0.510	0.307
0.011	0.009	0.005	0.013	0.009	0.010	0.011
0.572	0.489	0.562	0.404	0.365	0.361	0.417
0.001	0.000	0.001	0.000	0.001	0.001	0.000
0.633	0.816	0.771	0.763	0.785	0.762	0.772
0.011	0.005	0.006	0.001	0.001	0.005	0.003
0.213	0.297	0.331	0.170	0.145	0.137	0.194
0.359	0.192	0.231	0.233	0.220	0.224	0.223
0.638	0.809	0.769	0.766	0.781	0.773	0.776
0.498	0.202	0.213	0.150	0.201	0.274	0.172

Chromite and spinel continued

Chromite/spinel in polymineralic inclusions in garnet

Diavik - A154N					Ekati - Point lake		
DVK_GRT_04_In04	DVK_GRT_04_In07	DVK_GRT_04_In09	DVK_GRT_05_In02	DVK_GRT_05_In03	PL_GRT_02_In01	PL_GRT_02_In02	PL_GRT_02_In04
si-rich chr	si-rich spl	si-rich spl	cc-rich chr	si-rich spl	si-rich spl	si-rich spl	si-rich spl
0.19	0.72	0.26	0.12	0.22	1.14	0.19	3.78
4.43	0.75	1.04	11.65	0.29	0.47	1.02	1.08
10.47	47.32	46.02	13.57	48.32	53.21	18.53	38.64
45.74	9.05	14.44	4.04	11.76	15.65	46.63	15.09
0.28	0.32	0.19	0.82	0.33	0.42	0.34	0.30
23.86	19.20	14.17	52.82	15.94	15.83	21.15	20.98
0.17	0.01	0.04	0.04	0.02	0.04	0.13	0.02
13.73	18.45	19.31	12.78	18.71	20.56	13.29	21.11
0.05	0.10	0.08	0.41	0.10	0.07	0.04	0.08
98.92	95.92	95.55	96.24	95.68	107.38	101.31	101.08
0.111	0.016	0.022	0.317	0.006	0.009	0.024	0.024
0.410	1.600	1.539	0.578	1.611	1.591	0.685	1.328
1.203	0.205	0.324	0.115	0.263	0.314	1.156	0.348
0.008	0.008	0.005	0.025	0.008	0.009	0.009	0.007
0.664	0.461	0.336	1.596	0.377	0.336	0.555	0.512
0.005	0.000	0.001	0.001	0.000	0.001	0.003	0.000
0.681	0.789	0.817	0.688	0.789	0.778	0.621	0.917
0.002	0.003	0.003	0.016	0.003	0.002	0.001	0.002
3.083	3.081	3.046	3.337	3.057	3.039	3.055	3.138
0.214	0.211	0.121	0.807	0.149	0.102	0.145	0.353
0.973	0.974	0.985	0.899	0.981	0.987	0.982	0.956
0.108	0.016	0.022	0.285	0.006	0.009	0.024	0.023
0.399	1.557	1.516	0.520	1.581	1.571	0.673	1.269
1.170	0.200	0.319	0.104	0.258	0.310	1.135	0.332
0.008	0.008	0.005	0.023	0.008	0.009	0.009	0.007
0.646	0.448	0.331	1.435	0.370	0.332	0.545	0.489
0.005	0.000	0.001	0.001	0.000	0.001	0.003	0.000
0.662	0.768	0.804	0.619	0.774	0.768	0.610	0.877
0.002	0.003	0.002	0.014	0.003	0.002	0.001	0.002
0.214	0.211	0.121	0.807	0.149	0.102	0.145	0.353
0.431	0.237	0.210	0.628	0.221	0.230	0.400	0.136
0.606	0.764	0.793	0.496	0.778	0.770	0.604	0.866
0.746	0.114	0.174	0.166	0.140	0.165	0.628	0.208

Chromite and spinel continued

Chromite/spinel in polymineralic inclusions in garnet

Ekati - Point lake							Ekati - Wolveri
PL_GRT_02_In05	PL_GRT_03_In03	PL_GRT_04_In04	PL_GRT_04_In13-2	PL_GRT_04_In14	PL_GRT_04_In14-2	PL_GRT_04_In13	WI7_GRT_03_In02
si-rich spl	si-rich chr	si-rich chr	cc-rich spl	si-rich chr	si-rich chr	cc-rich spl	si-rich spl
0.21	0.52	0.18	0.22	0.11	0.16	0.11	1.58
0.30	4.99	0.10	0.54	2.07	6.81	1.47	1.46
52.67	30.28	50.01	54.14	6.29	38.67	25.37	38.48
11.37	20.48	14.91	7.71	56.00	7.21	32.53	20.68
0.34	0.40	0.22	0.21	0.23	0.23	0.24	0.20
18.78	29.82	17.21	19.61	20.42	24.63	25.62	18.60
0.01	0.12	0.03	0.06	0.13	0.21	0.07	0.16
17.51	15.33	17.69	17.75	13.13	21.31	13.26	18.03
0.08	0.24	0.03	0.14	0.16	0.04	0.30	0.06
101.27	102.18	100.40	100.39	98.59	99.28	99.02	99.71
0.006	0.112	0.002	0.011	0.053	0.146	0.035	0.032
1.664	1.067	1.601	1.714	0.252	1.303	0.939	1.319
0.241	0.484	0.320	0.164	1.504	0.163	0.807	0.475
0.008	0.010	0.005	0.005	0.007	0.006	0.006	0.005
0.421	0.746	0.391	0.441	0.580	0.589	0.673	0.452
0.000	0.003	0.001	0.001	0.004	0.005	0.002	0.004
0.700	0.683	0.716	0.711	0.665	0.908	0.621	0.782
0.002	0.008	0.001	0.004	0.006	0.001	0.010	0.002
3.042	3.112	3.037	3.050	3.069	3.121	3.092	3.071
0.109	0.289	0.098	0.132	0.181	0.309	0.239	0.185
0.986	0.964	0.988	0.984	0.977	0.961	0.970	0.977
0.006	0.108	0.002	0.011	0.052	0.141	0.034	0.031
1.641	1.028	1.581	1.686	0.246	1.252	0.911	1.288
0.238	0.467	0.316	0.161	1.470	0.157	0.783	0.464
0.008	0.010	0.005	0.005	0.007	0.005	0.006	0.005
0.415	0.719	0.386	0.433	0.567	0.566	0.653	0.442
0.000	0.003	0.001	0.001	0.004	0.005	0.002	0.004
0.690	0.659	0.708	0.699	0.650	0.873	0.602	0.764
0.002	0.007	0.001	0.004	0.006	0.001	0.010	0.002
0.109	0.289	0.098	0.132	0.181	0.309	0.239	0.185
0.306	0.430	0.288	0.302	0.386	0.257	0.414	0.257
0.693	0.605	0.711	0.699	0.627	0.773	0.593	0.748
0.126	0.312	0.167	0.087	0.857	0.111	0.462	0.265

Chromite and spinel continued

Chromite/spinel in polymineralic inclusions in garnet

Ekati - Wolverine

WI7_GRT_03_In05	WI7_GRT_03_In09	WI7_GRT_03_In12	WI7_GRT_03_In12-2
si-rich spl	si-rich spl	si-rich chr	si-rich spl
0.09	0.99	0.12	2.37
1.46	1.15	4.68	1.15
20.36	43.54	8.68	24.50
38.62	17.26	46.56	32.01
0.33	0.35	0.28	0.30
27.42	19.74	24.66	21.91
0.03	0.03	0.19	0.04
11.18	18.39	13.86	15.92
0.11	0.07	0.08	0.39
99.64	101.55	99.15	99.29
0.035	0.024	0.118	0.028
0.774	1.431	0.343	0.918
0.985	0.380	1.234	0.805
0.009	0.008	0.008	0.008
0.740	0.460	0.691	0.583
0.001	0.001	0.005	0.001
0.538	0.764	0.692	0.755
0.004	0.002	0.003	0.013
3.085	3.070	3.094	3.111
0.221	0.184	0.243	0.285
0.972	0.977	0.970	0.964
0.034	0.023	0.114	0.027
0.753	1.398	0.332	0.886
0.958	0.372	1.196	0.776
0.009	0.008	0.008	0.008
0.719	0.450	0.670	0.562
0.001	0.001	0.005	0.001
0.523	0.747	0.671	0.728
0.004	0.002	0.003	0.013
0.221	0.184	0.243	0.285
0.498	0.266	0.427	0.277
0.512	0.737	0.611	0.724
0.560	0.210	0.783	0.467

A2.12. EPMA Serpentine and Chlorite

	Serpentine/chlorite in polymineralic inclusions in clinopyroxene								
Location	Diavik - A154N								
Sample	DVK_CD_01 _In01	DVK_CD_01 _In05	DVK_CD_01 _In06	DVK_CD_01 _In07	DVK_CD_01 _In08	DVK_CD_06A _In01	DVK_CD_06A _In02	DVK_CD_06A _In03	DVK_CD_06A _In04
Type	cc-rich	cc-rich	si-rich	cc-rich	cc-rich	si-rich	si-rich	si-rich	si-rich
Major element analyses (wt.%)									
SiO_2	45.63	47.75	42.19	44.01	41.54	41.58	40.84	41.65	41.51
TiO_2	0.44	0.39	0.22	0.05	0.38	0.19	0.18	0.15	0.18
Al_2O_3	1.64	0.59	0.97	3.06	1.29	0.91	2.23	0.99	1.60
Cr_2O_3	0.62	0.96	0.21	0.10	0.26	0.22	0.13	0.19	0.21
FeO	3.95	4.78	3.01	6.12	4.37	5.16	4.26	4.20	5.80
MnO	0.03	0.13	0.06	0.14	0.03	0.19	0.07	0.15	0.14
NiO	0.00	0.05	0.00	0.00	0.07	0.00	0.00	0.00	0.00
MgO	33.05	29.67	36.44	32.02	31.84	36.19	36.02	35.65	33.96
CaO	0.35	0.40	0.07	0.13	0.47	0.05	0.05	0.08	0.38
Na_2O	0.10	0.10	0.04	0.06	0.09	0.00	0.02	0.05	0.03
K_2O	0.07	0.45	0.01	0.41	0.05	0.02	0.04	0.03	0.03
H_2O*	14.12	14.73	16.78	13.90	19.61	15.49	16.16	16.86	16.16
Total	85.88	85.27	83.22	86.10	80.39	84.51	83.84	83.14	83.84
Number of cations (apfu) on the basis of 9 oxygen atoms									
Si	2.098	2.186	1.902	2.048	1.837	1.914	1.862	1.887	1.903
Ti	0.015	0.013	0.007	0.002	0.013	0.007	0.006	0.005	0.006
Al	0.089	0.032	0.052	0.168	0.067	0.049	0.120	0.053	0.086
Cr	0.023	0.035	0.007	0.004	0.009	0.008	0.005	0.007	0.008
Fe	0.152	0.183	0.113	0.238	0.162	0.199	0.162	0.159	0.222
Mn	0.001	0.005	0.002	0.006	0.001	0.007	0.003	0.006	0.005
Ni	0.000	0.002	0.000	0.000	0.002	0.000	0.000	0.000	0.000
Mg	2.265	2.025	2.449	2.221	2.100	2.484	2.449	2.408	2.321
Ca	0.017	0.020	0.003	0.006	0.022	0.002	0.002	0.004	0.019
Na	0.009	0.009	0.003	0.005	0.008	0.000	0.002	0.004	0.003
K	0.004	0.026	0.001	0.024	0.003	0.001	0.002	0.002	0.002
sum	4.673	4.536	4.540	4.722	4.224	4.672	4.613	4.534	4.575
Mg/(Mg+Fe)	0.937	0.917	0.956	0.903	0.929	0.926	0.938	0.938	0.913

Serpentine/Chlorite continued

Serpentine/chlorite in polymineralic inclusions in clinopyroxene

Diavik - A154N

DVK_CD_06A_In05 si-rich	DVK_CD_06A_In06 si-rich	DVK_CD_06A_In07 si-rich	DVK_CD_06A_In08 si-rich	DVK_CD_06A_In09 si-rich	DVK_CD_06A_In10 si-rich	DVK_CD_06A_In12 si-rich	DVK_CD_06B_In01 si-rich	DVK_CD_06B_In02 si-rich	DVK_CD_06B_In03 si-rich
42.25	41.94	41.91	41.03	41.54	42.15	39.56	40.92	40.76	41.43
0.17	0.15	0.13	0.34	0.13	0.13	0.10	0.19	0.16	0.17
1.57	1.04	0.56	2.24	1.23	1.67	4.25	2.86	2.57	2.15
0.15	0.16	0.14	0.10	0.27	0.28	0.05	0.16	0.10	0.10
4.47	4.34	3.49	5.98	4.88	4.43	4.38	5.25	4.82	4.17
0.14	0.18	0.18	0.17	0.11	0.14	0.08	0.09	0.09	0.09
0.00	0.00	0.00	0.00	0.00	0.00	0.00	0.00	0.00	0.00
36.73	35.13	34.67	34.31	35.80	35.18	35.51	34.83	36.18	35.74
0.04	0.05	0.06	0.08	0.05	0.05	0.11	0.04	0.19	0.05
0.04	0.04	0.03	0.02	0.05	0.03	0.02	0.04	0.02	0.03
0.07	0.08	0.05	0.07	0.04	0.04	0.10	0.07	0.05	0.05
14.37	16.89	18.78	15.66	15.90	15.90	15.84	15.55	15.06	16.02
85.63	83.11	81.22	84.34	84.10	84.10	84.16	84.45	84.94	83.98
1.956	1.899	1.861	1.891	1.903	1.924	1.812	1.881	1.882	1.889
0.006	0.005	0.004	0.012	0.004	0.004	0.003	0.007	0.006	0.006
0.086	0.056	0.029	0.122	0.066	0.090	0.229	0.155	0.140	0.116
0.005	0.006	0.005	0.004	0.010	0.010	0.002	0.006	0.004	0.004
0.173	0.164	0.130	0.230	0.187	0.169	0.168	0.202	0.186	0.159
0.005	0.007	0.007	0.007	0.004	0.005	0.003	0.004	0.004	0.003
0.000	0.000	0.000	0.000	0.000	0.000	0.000	0.000	0.000	0.000
2.535	2.371	2.295	2.357	2.445	2.394	2.424	2.387	2.490	2.429
0.002	0.002	0.003	0.004	0.002	0.002	0.005	0.002	0.009	0.002
0.004	0.004	0.003	0.002	0.004	0.003	0.002	0.004	0.002	0.003
0.004	0.005	0.003	0.004	0.002	0.002	0.006	0.004	0.003	0.003
4.777	4.519	4.339	4.631	4.629	4.604	4.654	4.651	4.725	4.613
0.936	0.935	0.947	0.911	0.929	0.934	0.935	0.922	0.930	0.939

Serpentine/Chlorite continued

Serpentine/chlorite in polymineralic inclusions in clinopyroxene						Serpentine/chlorite in polymineralic inclusions in garnet						
Diavik - A154N			Ekati - Point lake			Ekati - Point lake						
DVK_CD_06B_In04 si-rich	DVK_CD_06B_In10 si-rich	DVK_CD_06B_In11 si-rich	PL_CD_07_In02 si-rich	PL_CD_07_In03 si-rich	PL_CD_07_In04 si-rich	PL_GRT_02_In01 si-rich	PL_GRT_02_In02 si-rich	PL_GRT_02_In03 cc-rich	PL_GRT_02_In04 si-rich	PL_GRT_02_In05 si-rich	PL_GRT_02_In06 si-rich	PL_GRT_03_In03 si-rich
41.44	41.62	42.44	42.79	38.90	43.92	42.60	44.43	39.32	46.20	46.71	37.65	38.39
0.15	0.40	0.13	0.10	0.10	0.04	0.20	0.04	0.13	0.03	0.02	0.03	0.35
1.55	2.00	0.75	2.23	2.04	4.85	2.97	1.07	3.01	5.64	5.25	7.81	8.31
0.12	0.08	0.19	0.17	0.48	0.16	0.50	0.15	0.73	0.09	0.23	0.40	0.37
4.24	4.82	4.10	7.12	5.90	4.94	6.04	4.91	19.61	3.39	1.87	7.28	8.74
0.11	0.15	0.12	0.07	0.05	0.10	0.19	0.13	0.09	0.24	0.11	0.21	0.13
0.00	0.00	0.00	0.03	0.04	0.06	0.00	0.23	0.92	0.01	0.01	0.01	0.01
35.54	33.86	36.52	34.58	26.39	23.64	19.21	23.64	22.71	22.20	25.15	26.17	22.87
0.03	0.12	0.09	0.24	0.28	0.99	1.32	0.64	0.43	1.13	1.57	0.78	0.51
0.02	0.02	0.03	0.08	0.11	0.07	0.11	0.06	0.17	0.10	0.17	0.16	0.11
0.03	0.07	0.05	0.06	0.08	0.07	0.30	0.14	0.14	0.10	0.04	0.08	0.08
16.77	16.86	15.58	12.55	25.63	21.15	26.56	24.56	12.74	20.86	18.87	19.43	20.14
83.23	83.14	84.42	87.46	74.37	78.85	73.44	75.44	87.26	79.14	81.13	80.57	79.87
1.878	1.887	1.942	2.031	1.648	1.901	1.779	1.874	1.974	1.984	2.031	1.688	1.712
0.005	0.014	0.004	0.003	0.003	0.001	0.006	0.001	0.005	0.001	0.001	0.001	0.012
0.083	0.107	0.040	0.125	0.102	0.247	0.146	0.053	0.178	0.285	0.269	0.413	0.437
0.004	0.003	0.007	0.006	0.016	0.006	0.016	0.005	0.029	0.003	0.008	0.014	0.013
0.161	0.183	0.157	0.283	0.209	0.179	0.211	0.173	0.823	0.122	0.068	0.273	0.326
0.004	0.006	0.005	0.003	0.002	0.004	0.007	0.005	0.004	0.009	0.004	0.008	0.005
0.000	0.000	0.000	0.001	0.001	0.002	0.000	0.008	0.037	0.000	0.000	0.000	0.000
2.401	2.288	2.491	2.446	1.667	1.526	1.196	1.486	1.699	1.421	1.630	1.749	1.520
0.001	0.006	0.004	0.012	0.013	0.046	0.059	0.029	0.023	0.052	0.073	0.037	0.024
0.002	0.002	0.003	0.007	0.009	0.006	0.009	0.005	0.016	0.008	0.014	0.013	0.009
0.002	0.004	0.003	0.004	0.004	0.004	0.016	0.007	0.009	0.005	0.002	0.004	0.004
4.541	4.499	4.656	4.920	3.675	3.922	3.446	3.647	4.798	3.890	4.101	4.201	4.063
0.937	0.926	0.941	0.896	0.889	0.895	0.850	0.896	0.674	0.921	0.960	0.865	0.823

A2.13. EPMA Clinopyroxene in Polymineralic Inclusions within Garnet

Location	Diavik - A154N						Ekati - Point lake				
	DVK_GRT_01	DVK_GRT_02	DVK_GRT_03	DVK_GRT_04	DVK_GRT_04	DVK_GRT_05	PL_GRT_01	PL_GRT_01	PL_GRT_01	PL_GRT_04	PL_GRT_04
Comment	_In06	_In04	_In03	_In02	_In03	_In03-2	_In01	_In03	_In04	_In03b	_In04
Type	si-rich	alt. ol	si-rich	si-rich	si-rich	si-rich	si-rich	si-rich	si-rich	si-rich	si-rich
Major element analyses (wt.%)											
SiO_2	50.60	51.68	54.45	50.18	50.39	46.94	50.16	49.12	51.43	51.42	47.46
TiO_2	0.54	0.33	0.04	0.37	0.46	0.83	0.34	0.51	0.30	0.38	0.45
Al_2O_3	6.09	5.77	2.72	5.49	6.27	12.29	5.54	7.44	5.29	5.55	9.68
Cr_2O_3	0.64	1.72	2.15	0.64	0.48	0.96	1.89	2.02	1.51	0.68	1.28
FeO	5.09	3.54	2.68	4.63	4.08	4.62	3.77	3.93	4.12	3.94	4.41
MnO	0.32	0.26	0.16	0.29	0.23	0.24	0.26	0.25	0.35	0.28	0.27
NiO	0.01	0.01	0.06	0.01	0.02	0.00	0.01	0.01	0.00	0.00	0.00
MgO	17.71	15.89	15.28	16.10	14.84	12.15	16.76	14.74	18.36	16.96	13.74
CaO	18.78	20.15	20.13	20.85	22.75	21.75	20.21	20.30	18.07	20.28	21.36
Na_2O	0.55	1.14	2.22	0.53	0.59	0.86	0.74	0.84	0.64	0.49	0.64
K_2O	0.02	0.01	0.01	0.01	0.02	0.05	0.01	0.01	0.01	0.01	0.03
Total	100.34	100.50	99.89	99.09	100.13	100.68	99.69	99.17	100.08	99.99	99.33
Number of cations (apfu) on the basis of 6 oxygen atoms and 4 cations											
Si	1.839	1.872	1.977	1.854	1.845	1.714	1.839	1.812	1.864	1.869	1.756
Ti	0.015	0.009	0.001	0.010	0.013	0.023	0.009	0.014	0.008	0.010	0.012
Al	0.261	0.246	0.116	0.239	0.271	0.529	0.239	0.324	0.226	0.238	0.422
Cr	0.018	0.049	0.062	0.019	0.014	0.028	0.055	0.059	0.043	0.020	0.037
Fe	0.155	0.107	0.081	0.143	0.125	0.141	0.116	0.121	0.125	0.120	0.136
Mn	0.010	0.008	0.005	0.009	0.007	0.007	0.008	0.008	0.011	0.009	0.009
Ni	0.000	0.000	0.002	0.000	0.001	0.000	0.000	0.000	0.000	0.000	0.000
Mg	0.959	0.858	0.827	0.887	0.810	0.661	0.916	0.811	0.992	0.919	0.758
Ca	0.731	0.782	0.783	0.826	0.893	0.851	0.794	0.803	0.702	0.790	0.847
Na	0.039	0.080	0.156	0.038	0.042	0.061	0.052	0.060	0.045	0.035	0.046
K	0.001	0.001	0.000	0.000	0.001	0.002	0.000	0.000	0.001	0.000	0.001
sum	4.027	4.012	4.011	4.026	4.021	4.017	4.030	4.012	4.016	4.009	4.025
Mg/(Mg+Fe)	0.861	0.889	0.910	0.861	0.866	0.824	0.888	0.870	0.888	0.885	0.847

Clinopyroxene in Polymineralic Inclusions within Garnet continued

Ekati - Point lake				Ekati - Wolverine							
PL_GRT_04_In05 si-rich	PL_GRT_04_In08 si-rich	PL_GRT_04_In09 si-rich	PL_GRT_02_In05 si-rich	WI7_GRT_03_In02 si-rich	WI7_GRT_03_In04 si-rich	WI7_GRT_03_In04-2 si-rich	WI7_GRT_03_In08 si-rich	WI7_GRT_03_In09 si-rich	WI7_GRT_03_In11B si-rich	WI7_GRT_03_In012 si-rich	WI7_GRT_03_In012-2 si-rich
50.39	45.65	51.38	47.15	50.14	46.83	50.32	53.51	50.19	51.91	51.12	51.06
0.24	0.72	0.88	0.71	0.49	0.78	0.52	0.21	0.54	0.42	0.33	0.35
6.25	11.70	5.69	10.22	6.65	7.54	5.70	2.05	5.54	4.65	5.19	5.54
0.55	2.48	0.63	0.61	1.15	0.77	0.72	0.43	1.05	0.57	1.16	1.61
4.37	3.69	3.73	5.08	6.63	5.23	6.34	4.40	4.31	4.15	4.19	4.69
0.29	0.24	0.24	0.26	0.56	0.27	0.33	0.43	0.36	0.38	0.35	0.38
0.01	0.01	0.04	0.00	0.00	0.01	0.00	0.00	0.00	0.02	0.00	0.00
17.36	12.57	19.98	12.70	19.73	20.56	24.20	22.96	17.51	18.29	18.16	19.09
20.89	22.40	20.34	21.57	14.20	13.41	10.05	16.24	19.49	19.24	19.15	17.54
0.35	0.59	0.57	0.66	0.50	1.23	0.39	0.21	0.48	0.55	0.46	0.50
0.03	0.00	0.37	0.08	0.00	0.22	0.13	0.24	0.02	0.06	0.01	0.02
100.73	100.04	103.84	99.04	100.06	96.84	98.69	100.68	99.49	100.23	100.10	100.77
1.828	1.684	1.807	1.753	1.820	1.756	1.827	1.917	1.841	1.881	1.858	1.842
0.007	0.020	0.023	0.020	0.013	0.022	0.014	0.006	0.015	0.011	0.009	0.009
0.267	0.509	0.236	0.448	0.285	0.333	0.244	0.087	0.239	0.199	0.222	0.236
0.016	0.072	0.017	0.018	0.033	0.023	0.021	0.012	0.030	0.016	0.033	0.046
0.133	0.114	0.110	0.158	0.201	0.164	0.193	0.132	0.132	0.126	0.127	0.141
0.009	0.008	0.007	0.008	0.017	0.009	0.010	0.013	0.011	0.012	0.011	0.012
0.000	0.000	0.001	0.000	0.000	0.000	0.000	0.000	0.000	0.000	0.000	0.000
0.939	0.691	1.048	0.704	1.068	1.149	1.310	1.226	0.957	0.988	0.984	1.027
0.812	0.886	0.766	0.859	0.552	0.539	0.391	0.623	0.766	0.747	0.746	0.678
0.025	0.042	0.039	0.048	0.035	0.089	0.027	0.014	0.034	0.038	0.032	0.035
0.001	0.000	0.016	0.004	0.000	0.010	0.006	0.011	0.001	0.003	0.000	0.001
4.037	4.026	4.071	4.020	4.025	4.094	4.043	4.041	4.027	4.021	4.022	4.026
0.876	0.859	0.905	0.817	0.841	0.875	0.872	0.903	0.879	0.887	0.885	0.879

A2.14. Reconstructed Bulk Compositions of Polymineralic Inclusions

	Polymineralic inclusions in clinopyroxene															
Location	Diavik - A154N															
Sample	DVK_CD_01 _In07		DVK_CD_01 _In04		DVK_CD_01 _In02		DVK_CD_01 _In01		DVK_CD_01 _In08		DVK_CD_01 _In03		DVK_CD_01 _In05		DVK_CD_6A _In05	
Type	cc-rich		cc-rich		cc-rich		cc-rich		cc-rich		cc-rich		cc-rich		si-rich	
		1σ		1σ		1σ		1σ		1σ		1σ		1σ		1σ
SiO_2	14.8	1.66	14.5	1.63	13.4	1.50	12.2	1.37	9.2	1.03	9.1	1.02	7.6	0.85	40.9	4.57
TiO_2	0.2	0.02	0.2	0.02	0.1	0.01	0.2	0.02	0.1	0.01	0.1	0.01	0.2	0.02	0.3	0.03
Al_2O_3	1.6	0.18	3.1	0.34	0.2	0.02	0.7	0.07	0.4	0.05	0.7	0.08	1.9	0.21	2.0	0.22
Cr_2O_3	1.1	0.13	0.4	0.05	0.6	0.07	0.7	0.08	0.1	0.01	0.1	0.01	0.2	0.02	0.5	0.06
MnO	0.1	0.01	0.1	0.01	0.5	0.06	1.1	0.12	0.3	0.03	-		-		0.1	0.02
FeO	2.5	0.28	2.5	0.28	2.4	0.27	0.4	0.05	1.9	0.21	1.0	0.11	0.8	0.09	4.5	0.50
NiO	-		-		-		-		-		-		-		-	
MgO	10.8	1.21	12.5	1.40	15.0	1.68	11.5	1.28	11.6	1.29	9.1	1.02	5.2	0.59	35.4	3.96
CaO	33.7	3.77	34.1	3.81	37.5	4.19	37.3	4.17	41.3	4.62	42.1	4.71	44.8	5.01	1.2	0.13
BaO	1.3	0.14	-		-		-		-		0.1	0.01	0.1	0.01	-	
Na_2O	-		0.1	0.01	-		-		-		-		-		-	
K_2O	0.7	0.08	2.8	0.31	-		0.2	0.03	0.3	0.03	0.5	0.06	1.6	0.18	0.7	0.08
SrO	0.8	0.09	0.1	0.01	0.1	0.01	0.1	0.01	0.1	0.01	0.1	0.01	0.1	0.01	-	
F	-		0.1	0.01	-		-		-		-		0.1	0.01	-	
Cl	-		-		-		-		-		-		-		-	
Total	67.6		70.3		69.9		64.4		65.4		63.0		62.5		85.6	
Mg/(Mg+Fe)	0.88		0.90		0.92		0.98		0.92		0.94		0.92		0.93	

*overall uncertainty is ~11% and includes uncertainty on modal proportions obtained by QEMSCAN (~5%) and variability of mineral compositions of inclusion phases obtained by EPMA (~10%).

Reconstructed Bulk Compositions continued

Polymineralic inclusions in clinopyroxene														**Polymineralic inclusions in garne**			
Diavik - A154N												Ekati - Point lake		Ekati - Point lake			
DVK_CD_6A_In06		DVK_CD_6A_In03		DVK_CD_01_In06		DVK_CD_6A_In02		DVK_CD_6A_In01		DVK_CD_6A_In04		PL_CD_03_In01		PL_GRT_04_In14		PL_GRT_04_In7	
si-rich		si-rich		si-rich		si-rich		si-rich		si-rich		cc-rich		si-rich		si-rich	
	1σ		1σ		1σ		1σ		1σ		1σ		1σ		1σ		1σ
40.4	4.52	38.9	4.35	37.4	4.18	33.9	3.79	27.4	3.06	21.6	2.41	13.5	1.51	37.6	4.20	37.1	4.15
0.4	0.05	0.2	0.02	0.2	0.02	0.2	0.03	0.5	0.05	0.2	0.02	0.4	0.04	0.6	0.06	0.4	0.05
2.5	0.28	1.2	0.14	0.8	0.09	2.2	0.24	3.4	0.38	1.5	0.17	2.5	0.28	8.3	0.93	9.5	1.06
0.3	0.03	0.7	0.07	0.1	0.01	0.4	0.04	0.4	0.05	0.9	0.10	0.8	0.08	1.6	0.18	1.4	0.15
0.1	0.01	0.1	0.02	0.1	0.01	0.1	0.01	0.1	0.01	0.1	0.01	0.3	0.04	0.1	0.01	0.1	0.01
3.3	0.37	4.2	0.47	2.4	0.27	3.7	0.42	3.3	0.37	3.6	0.40	2.5	0.28	5.0	0.56	9.7	1.08
-		-		-		-		-		-		-		0.1	0.01	0.4	0.04
33.8	3.78	33.9	3.79	34.1	3.81	28.7	3.20	21.0	2.35	18.8	2.11	11.4	1.27	22.2	2.48	20.0	2.24
1.7	0.19	2.8	0.31	5.0	0.56	10.1	1.13	18.9	2.11	25.4	2.84	36.5	4.08	2.7	0.30	0.5	0.06
-		-		-		-		0.1	0.01	-		-		-		-	
0.1	0.01	0.1	0.01	-		-		0.1	0.01	-		-		0.1	0.01	0.1	0.02
1.3	0.15	0.3	0.04	0.2	0.02	0.8	0.08	2.7	0.30	0.5	0.06	2.3	0.25	3.2	0.36	5.1	0.57
-		-		-		0.1	0.01	0.1	0.01	0.2	0.02	0.1	0.02	-		-	
-		-		-		-		0.1	0.01	-		0.4	0.05	0.1	0.01	0.1	0.01
-		-		-		-		-		-		-		-		-	
84.0		82.4		80.1		80.0		77.9		72.9		70.6		81.5		84.4	
0.95		0.93		0.96		0.93		0.92		0.90		0.89		0.89		0.79	

Reconstructed Bulk Compositions continued

Polymineralic inclusions in garnet

Ekati - Point lake

PL_GRT_04_In04 si-rich	1σ	PL_GRT_04_In05 si-rich	1σ	PL_GRT_04_In03 si-rich	1σ	PL_GRT_04_In13 si-rich	1σ
33.9	3.80	32.5	3.63	30.9	3.46	20.9	2.34
0.5	0.05	0.2	0.03	0.3	0.04	0.6	0.06
10.8	1.21	9.4	1.05	10.9	1.22	6.2	0.69
1.9	0.21	1.6	0.18	4.3	0.48	0.9	0.10
0.1	0.01	0.1	0.02	0.1	0.02	0.1	0.01
7.9	0.88	8.9	1.00	10.7	1.20	5.1	0.57
0.3	0.03	0.4	0.04	0.3	0.03	0.2	0.02
19.6	2.19	19.7	2.20	19.5	2.18	12.2	1.36
2.5	0.28	2.5	0.28	2.4	0.26	24.3	2.71
-		-		-		-	
0.2	0.02	0.3	0.04	0.4	0.04	0.1	0.01
5.1	0.57	2.9	0.33	1.5	0.17	3.1	0.35
-		-		-		-	
0.1	0.02	0.1	0.01	-		0.3	0.03
-		-		-		-	
82.8		78.6		81.3		73.9	
0.82		0.80		0.76		0.81	

A3.1. LA-ICP-MS Analytical Conditions

Mineral	Laser energy [mJ]	Transmission [%]	Fluence [J/m^2]	Spot size [µm]	Repitition rate [Hz]	Back-ground time [s]	Ablation time [s]	Calibration material	Internal standard	Secondary standard
cpx	120	11.4	~ 3	33	10	80	80	NIST SRM 612	^{29}Si	NIST SRM 614
grt	120	26	~ 3	33	10	60	60	NIST SRM 612	^{43}Ca, ^{29}Si	NIST SRM 614

Isotopes analyzed: ^{43}Ca, ^{29}Si, ^{47}Ti, ^{49}Ti, ^{60}Ni, ^{85}Rb, ^{88}Sr, ^{89}Y, ^{90}Zr, ^{93}Nb, ^{137}Ba, ^{139}La, ^{140}Ce, ^{141}Pr, ^{146}Nd, ^{147}Sm, ^{153}Eu, ^{157}Gd, ^{159}Tb, ^{163}Dy, ^{165}Ho, ^{166}Er, ^{169}Tm, ^{172}Yb, ^{175}Lu, ^{178}Hf, ^{181}Ta, ^{232}Th, ^{238}U

A3.2. LA-ICP-MS Clinopyroxene

Location	Diavik - A154N			
Sample	DVK_CD_01	DVK_CD_06A	DVK_CD_02B	DVK_CD_04B
LA-ICP-MS Trace element analyses (ppm)				
Ba	0.84	0.44	0.42	0.39
La	2.08	2.70	4.04	2.86
Ce	8.17	10.17	16.43	10.26
Pr	1.27	1.52	2.58	1.60
Nd	6.04	6.82	11.83	7.40
Sm	1.07	1.08	1.93	1.33
Eu	0.28	0.31	0.52	0.37
Gd	0.63	0.64	1.11	0.84
Tb	0.06	0.06	0.12	0.09
Dy	0.27	0.28	0.48	0.38
Ho	0.03	0.04	0.07	0.05
Er	0.06	0.07	0.14	0.09
Tm	0.01	0.01	0.01	0.01
Yb	0.03	0.03	0.08	0.04
Lu	0.002	0.004	0.009	0.004

A3.3. LA-ICP-MS Garnet

Location	EKATI - Point lake															
Sample	PLGRT1-1	PLGRT1-2	PLGRT1-3	PLGRT1-4	PLGRT1-5	PLGRT1-6	PLGRT1-7	PLGRT1-8	PLGRT1-9	PLGRT1-10	PLGRT1-11	PLGRT1-12	PLGRT1-13	PLGRT1-14	PLGRT1-15	
	Incl01 clear	Incl01 rim	Incl07 clear	Incl07 rim	Incl08 clear	Incl08 rim	Incl09 clear	Incl09 rim	Incl09 rim	Incl10 clear	Incl10 rim	Incl10 rim	Incl12 clear	Incl12 rim	Incl12 rim	
Type	G11	G11	G9	G9	G9	G9	G1	G1	G1	G9/G11	G9/G11	G9/G11	G4	G4	G4	
LA-ICP-MS Trace element analyses (ppm)																
La	0.04	8.60	0.04	0.05	0.03	0.03	0.03	0.83	0.05	<0.018	4.20	0.05	<0.0133	0.05	0.19	
Ce	0.45	19.50	0.29	0.35	0.32	0.26	0.27	1.65	0.31	0.28	12.20	0.19	0.23	0.21	0.57	
Pr	0.15	2.13	0.12	0.11	0.14	0.12	0.12	0.24	0.14	0.09	1.50	0.07	0.07	0.09	0.11	
Nd	1.44	8.50	0.95	1.01	1.37	1.24	0.82	1.24	0.96	0.94	5.20	0.86	0.59	0.52	0.62	
Sm	0.81	1.70	0.76	0.76	1.11	1.01	0.59	0.80	0.66	0.67	1.74	0.89	0.41	0.51	0.37	
Eu	0.49	0.47	0.37	0.33	0.40	0.49	0.27	0.34	0.32	0.43	0.50	0.42	0.26	0.25	0.27	
Gd	1.72	1.34	1.41	1.39	2.06	1.85	1.54	1.39	1.27	1.93	1.90	1.59	1.06	0.72	0.91	
Tb	0.28	0.24	0.27	0.22	0.41	0.46	0.27	0.29	0.25	0.27	0.32	0.29	0.23	0.19	0.22	
Dy	2.16	1.73	1.91	1.67	2.82	3.26	2.23	2.35	2.22	2.34	2.10	2.64	1.69	1.70	1.66	
Ho	0.48	0.30	0.41	0.41	0.69	0.79	0.58	0.65	0.52	0.52	0.46	0.51	0.41	0.35	0.38	
Er	1.10	0.69	1.34	1.31	2.42	2.65	1.88	1.94	1.95	1.65	1.45	1.66	1.16	1.08	1.09	
Tm	0.11	0.08	0.14	0.20	0.35	0.37	0.29	0.31	0.28	0.23	0.23	0.22	0.16	0.13	0.14	
Yb	0.65	0.41	1.33	1.26	2.41	2.98	2.30	2.28	2.30	1.80	1.33	1.71	1.24	0.92	1.21	
Lu	0.10	0.05	0.18	0.20	0.35	0.45	0.39	0.33	0.34	0.32	0.22	0.27	0.19	0.15	0.20	

A4.1. List of Experimental Samples

	Brey et al. (1990)			*This study*		
Run	**P [kb]**	**T [ºC]**	**Starting Material**	**SEM sample ID**	**SIMS mount**	**SIMS sample ID**
P2/2	28	1000	J4	m1336_A	M1349	S3331A
			SC1	m1336_B		S3331B
P3	28	1150	J4	m1332_A	M1349	S3321A
			SC1	m1332_B		S3321B
			n.a.*	m1332_C		S3321C
406	40	1200	SC1	m1334_A	M1350	S3326A
			SCS	m1334_B		S3326B
			J4	m1334_C		S3326C
249	50	1100	SCS	m1329_C	M1348	S3310C
320b	50	1200	n.a.*	m1330_D	M1348	S3313D
407	50	1300	J4	m1337_A	M1350	S3333A
			SC1	m1337_B		S3333B
418	60	1300	J4	m1340_A	M1351	S3338A
			SC1	m1340_B		S3338B

*Starting material could not be reliably identified.

A4.2. Al concentrations in experimental olivines measured by SIMS (screened)

Brey et al. (1990)				*This study*			
Run	**P [kb]**	**T [ºC]**	**Starting Material**	**SIMS sample ID**	**Measuring point**	**Al [ppm]**	**2σ [ppm]**
P2/2	28	1000	J4	S3331A	S3331A_OL_1	42	2
					S3331A_OL_2	40	1
					S3331A_OL_3	41	1
					S3331A_OL_4	42	1
					S3331A_OL_6	33	1
					S3331A_OL_7	35	1
					S3331A_OL_8	43	2
			SC1	S3331B	S3331B_OL_1	74	3
					S3331B_OL_2	75	5
					S3331B_OL_3	63	2
					S3331B_OL_4	62	2
					S3331B_OL_5	77	7
					S3331B_OL_7	51	3
					S3331B_OL_8	63	3
P3	28	1150	J4	S3321A	S3321A_OL_1	102	4
					S3321A_OL_3	104	3
					S3321A_OL_4	149	5
					S3321A_OL_5	94	3
					S3321A_OL_6	89	3
					S3321A_OL_7	86	3
					S3321A_OL_8	140	5
					S3321A_OL_9	103	3
			SC1	S3321B	S3321B_OL_1	136	5
					S3321B_OL_3	138	5
					S3321B_OL_4	133	5
					S3321B_OL_5	130	5
					S3321B_OL_6	132	4
					S3321B_OL_8	144	5
					S3321B_OL_9	141	5
			n.a.*	S3321C	S3321C_OL_1	146	7
					S3321C_OL_2	143	5
					S3321C_OL_3	138	5
					S3321C_OL_4	173	6
					S3321C_OL_5	171	6
					S3321C_OL_7	191	6
					S3321C_OL_8	171	6
					S3321C_OL_10	167	5
					S3321C_OL_11	137	5

406	40	1200	SC1	S3326A	S3326A_OL_1	98	3
					S3326A_OL_2	118	5
					S3326A_OL_3	119	5
					S3326A_OL_5	104	4
					S3326A_OL_6	101	4
					S3326A_OL_7	86	3
					S3326A_OL_8	98	3
					S3326A_OL_9	95	4
					S3326A_OL_10	102	3
			SCS	S3326B	S3326B_OL_1	110	4
					S3326B_OL_2	115	4
					S3326B_OL_3	102	3
					S3326B_OL_4	103	3
					S3326B_OL_5	101	3
					S3326B_OL_6	100	4
			J4	S3326C	S3326C_OL_1	153	6
					S3326C_OL_2	149	8
					S3326C_OL_3	119	4
					S3326C_OL_4	108	4
					S3326C_OL_5	104	3
249	50	1100	SCS	S3310C	S3310C_OL_1	43	1
					S3310C_OL_2	45	1
					S3310C_OL_3	55	2
320b	50	1200	n.a.*	S3313D	S3313D_OL_1	79	2
					S3313D_OL_3	85	3
					S3313D_OL_4	96	4
					S3313D_OL_6	84	3
					S3313D_OL_8	92	5
					S3313D_OL_10	83	3
407	50	1300	J4	S3333A	S3333A_OL_1	143	5
					S3333A_OL_3	171	6
					S3333A_OL_5	155	5
					S3333A_OL_6	171	6
					S3333A_OL_7	185	7
					S3333A_OL_8	160	5
					S3333A_OL_9	159	5
			SC1	S3333B	S3333B_OL_1	148	5
					S3333B_OL_2	145	5
					S3333B_OL_3	156	5
					S3333B_OL_4	167	5
					S3333B_OL_5	142	5
					S3333B_OL_6	163	5
					S3333B_OL_7	162	6
					S3333B_OL_8	148	5
					S3333B_OL_9	141	5

				S3338A_OL_1	134	6
				S3338A_OL_2	144	6
				S3338A_OL_2	136	6
			J4	S3338A	S3338A_OL_3	135	6
					S3338A_OL_4	127	5
					S3338A_OL_4	113	5
418	60	1300			S3338A_OL_5	140	7
					S3338B_OL_1	118	5
					S3338B_OL_2	135	6
					S3338B_OL_4	136	6
			SC1	S3338B	S3338B_OL_5	124	6
					S3338B_OL_6	131	6
					S3338B_OL_7	121	6
					S3338B_OL_8	123	6

*Starting material could not be reliably identified.

A4.3. Equilibrium Al values and Cr# for the different experimental runs

Run	P [kb]	T [°C]	Al [ppm]	2σ [ppm]	Cr#*
P2/2	28	1000	47	3	0.63
P3	28	1150	141	5	0.60
406	40	1200	109	4	0.56
249	50	1100	47	2	0.63
320b	50	1200	86	5	0.53
407	50	1300	155	5	0.50
418	60	1300	127	6	0.50

*Calculated with average Cr concentrations published by Brey et al. (1990).

A4.4. Mineral compositions for mantle xenolith samples from Diavik, Somerset Island, and Kimberley and thermobarometry results (following 2 pages)

Location	Diavik	Diavik	Diavik	Diavik	Diavik	Diavik	Diavik	Somerset	Somerset	Somerset	Somerset	Somerset	Somerset
Sample	DDM_327	DDM_360	DDM_367A	DDM_368	DDM_335	DDM_366	MX5023	K11A1-2	K11A3	K11A7-4	K11A9	K11A15-4	K11A16-2
Type	gt lhz	gt lhz	gt lhz	gt lhz	gt lhz	gt lhz	gt hrz	gt lhz	gt lhz	gt lhz	gt lhz	gt lhz	gt lhz
Major and minor element analyses by EPMA (wt%) [a]													
Olivine													
Na_2O	-	0.00	0.00	0.00	0.00	0.00	0.01	-	-	-	-	-	-
CaO	0.05	0.04	0.05	0.04	0.05	0.05	0.02	0.08	0.03	0.05	0.04	0.09	0.05
FeO	9.25	8.98	8.70	8.49	8.70	8.69	7.21	7.35	7.93	7.58	8.21	7.99	7.58
SiO_2	41.5	41.2	40.8	41.3	40.8	41.3	42.0	40.8	41.3	41.3	41.3	41.4	41.8
K_2O	-	0.00	0.00	0.00	0.00	0.00	0.01	n.a.	n.a.	n.a.	n.a.	n.a.	n.a.
MgO	50.3	50.8	50.5	51.0	50.6	50.6	50.1	50.8	50.3	50.1	50.1	50.3	50.6
TiO_2	0.02	0.01	0.02	0.01	0.02	0.02	0.00	0.04	0.01	0	0.02	0.05	0
Cr_2O_3	0.04	0.02	0.05	0.04	0.05	0.05	0.03	0.07	0.09	0.04	0.06	0.08	0.07
MnO	0.13	0.12	0.12	0.10	0.12	0.12	0.08	0.08	0.12	0.11	0.14	0.1	0.07
NiO	0.39	0.43	0.38	0.40	0.38	0.39	0.34	0.4	0.34	0.37	0.36	0.33	0.39
Total	101.7	101.6	100.6	101.4	100.7	101.2	99.8	99.6	100.1	99.5	100.2	100.3	100.6
Trace elements in olivine measured by LA-ICP-MS (ppm) [b]													
Al	95	82	61	81	79	88	47	91	70	64	78	82	78
V	9.08	7.35	7.93	7.51	8.70	8.89	7.05	7.59	6.42	6.24	7.17	5.99	7.23
Cr#	0.60	0.46	0.75	0.64	0.69	0.67	0.70	0.73	0.82	0.69	0.73	0.78	0.76
Orthopyroxene													
Na_2O	-	0.00	0.00	0.00	0.00	0.00	0.11	0.13	0.17	0.16	0.14	0.14	0.14
CaO	0.99	0.80	0.79	0.77	0.91	0.92	0.61	0.84	0.66	0.77	0.81	0.8	0.8
Al_2O_3	0.71	0.64	0.59	0.60	0.67	0.68	0.51	1.19	1.06	1.21	1.21	1.19	1.07
FeO	5.72	5.44	5.36	5.18	5.22	5.25	4.37	4.6	4.73	4.77	4.89	4.87	4.62
SiO_2	58.4	58.6	57.8	58.1	57.5	58.0	58.5	57.8	58.4	58.2	57.5	58.0	58.4
K_2O	-	0.00	0.00	0.00	0.00	0.00	0.01	n.a.	n.a.	n.a.	n.a.	n.a.	n.a.
MgO	35.1	35.5	35.6	35.9	35.3	35.1	35.5	35.1	34.8	35.1	34.7	34.9	34.8
TiO_2	0.13	0.06	0.12	0.07	0.13	0.12	0.06	0.09	0.08	0.04	0.18	0.09	0.06
Cr_2O_3	0.22	0.17	0.38	0.35	0.34	0.33	0.31	0.73	0.51	0.65	0.42	0.57	0.58
MnO	0.13	0.12	0.13	0.12	0.13	0.13	0.17	0.09	0.13	0.11	0.09	0.1	0.15
NiO	0.14	0.13	0.12	0.12	0.11	0.13	0.00	0.1	0.1	0.11	0.09	0.1	0.11
Total	101.5	101.5	100.9	101.2	100.3	100.7	100.1	100.6	100.6	101.1	100.1	100.7	100.7
Clinopyroxene													
Na_2O	1.42	1.37	1.47	1.44	1.51	1.50	-	1.53	1.91	1.68	1.63	1.57	1.61
CaO	17.8	18.9	18.8	19.1	17.9	17.8	-	19.4	19.3	19.3	19.0	19.5	19.3
Al_2O_3	1.72	1.75	1.38	1.44	1.61	1.60	-	2.05	2.34	2.09	2.49	2.06	1.99
FeO	3.48	3.13	2.97	2.79	3.08	3.06	-	2.3	2.48	2.27	2.65	2.4	2.17
SiO_2	55.9	56.3	55.3	55.7	55.2	55.1	-	54.0	55.2	55.5	55.0	55.2	55.0
K_2O	0.06	0.05	0.06	0.05	0.04	0.04	-	n.a.	n.a.	n.a.	n.a.	n.a.	n.a.
MgO	19.3	19.0	18.7	18.6	19.0	19.0	-	17.0	16.4	17.1	17.3	17.2	17.2
TiO_2	0.22	0.11	0.18	0.11	0.21	0.20	-	0.07	0.13	0.08	0.28	0.15	0.08
Cr_2O_3	0.75	0.74	1.60	1.51	1.41	1.41	-	2.35	2.4	2.31	1.28	1.85	2.29
MnO	0.14	0.10	0.11	0.12	0.12	0.12	-	0.08	0.09	0.11	0.08	0.1	0.09
NiO	0.04	0.06	0.06	0.05	0.07	0.06	-	0.07	0.06	0.06	0.07	0.05	0.07
Total	100.8	101.5	100.6	100.9	100.1	99.9		98.9	100.4	100.4	99.8	100.0	99.8
Garnet													
Na_2O	0.03	0.00	0.00	0.02	0.00	0.00	0.03	0.01	0.03	0.02	0.06	0.02	0.03
CaO	4.80	4.60	6.53	5.82	5.80	5.60	6.23	6.38	5.76	6.22	5.14	6.28	6.26
Al_2O_3	20.2	21.2	16.2	18.0	17.5	17.9	17.6	17.5	18.2	17.6	20.2	18.1	17.4
FeO	7.82	7.72	7.61	7.35	7.32	7.25	6.42	6.39	7.13	6.4	6.95	6.47	6.45
SiO_2	42.4	42.3	41.0	41.7	41.4	41.6	41.6	41.5	41.8	41.6	42.0	41.7	41.8
K_2O	0.00	0.00	0.00	0.00	0.00	0.00	0.01	n.a.	n.a.	n.a.	n.a.	n.a.	n.a.
MgO	21.5	21.6	19.6	20.4	20.7	20.7	19.9	19.8	20.1	19.5	20.9	19.6	19.6
TiO_2	0.77	0.37	0.76	0.42	0.80	0.71	0.41	0.21	0.31	0.14	0.39	0.29	0.18
Cr_2O_3	2.75	2.73	8.96	6.04	7.07	6.70	8.10	6.81	6.07	7.25	3.4	6.66	7.59
MnO	0.36	0.31	0.36	0.40	0.33	0.34	0.36	0.32	0.38	0.3	0.4	0.29	0.35
NiO	0.00	0.00	0.00	0.00	0.00	0.00	0.01	0.03	0.02	0.13	0.01	0	0.08
Total	100.6	100.8	101.0	100.1	100.9	100.8	100.7	99.0	99.7	99.1	99.4	99.4	99.7
Thermobarometry results for xenoliths													
	DDM_327	DDM_360	DDM_367A	DDM_368	DDM_335	DDM_366	MX5023	K11A1-2	K11A3	K11A7-4	K11A9	K11A15-4	K11A16-2
T (2px;BK1990)	1365	1297	1296	1276	1343	1344	-	1146	1125	1161	1195	1155	1161
P (Al-opx;BK1990)	79	70	79	74	77	76	-	44	41	41	48	42	43
T (Al-ol-Cr#;Eqn2)	1323	1307	1215	1270	1261	1279	-	1125	1052	1080	1121	1090	1092
T (Al-ol;Eqn3)	1362	1293	1289	1312	1322	1335	-	1177	1124	1108	1173	1152	1149
T (cpx;NT2000)	1323	1261	1250	1235	1297	1300	-	1089	1047	1103	1130	1099	1106
P (Al-opx;BK1990)	78	69	78	73	76	75	-	42	39	39	46	41	42
T (Al-ol;Eqn3)	1356	1289	1283	1307	1316	1329	-	1169	1113	1100	1164	1145	1142
T (opx-gt;Harley1984)	1299	1183	1167	1167	1203	1223	1025	1014	927	1000	1038	1034	995
P (Al-opx;BK1990)	74	62	68	66	66	67	47	38	31	33	39	36	35
T (Al-ol;Eqn3)	1334	1249	1238	1269	1267	1287	1088	1144	1070	1070	1127	1122	1109

[a] EPMA data for Diavik samples from Mather (2012), for Somerset Island samples from Kjarsgaard and Peterson (1992), for Kimberley from Creighton et al. (2009)

[b] LA-ICP-MS data for olivines from Diavik and Somerset Island was collected at the Geological Survey of Canada, for olivines from Kimberley at the University of Alberta (see Supplementary Material)

Somerset K12A3 gt lhz	Somerset K12A4-5 gt lhz	Somerset K12A7 gt lhz	Somerset K12A8 gt lhz	Somerset K13B5-4 gt lhz	Somerset K14A1-4 gt lhz	Somerset K15A2-2 gt lhz	Somerset K15A7-4 gt lhz	Somerset K16A2-2 gt lhz	Somerset K16A3-1 gt lhz	Somerset K11A4 gt-sp lhz	Somerset K11A5-1 gt-sp lhz	Somerset K11A14 gt-sp lhz	Somerset K13B3-4 gt-sp lhz	Kimberley Bo-02 gt-hrz	Kimberley Bo-20 gt-hrz
-	-	-	-	-	-	-	-	-	-	-	-	-	-	0.02	0.03
0.05	0.05	0.07	0.07	0.05	0.06	0.04	0.09	0.06	0.06	0.12	0.03	0.04	0.03	0.01	0.03
7.41	7.58	7.2	7.8	6.76	8.46	7.89	8.02	7.53	7.66	8.34	7.94	7.86	7.47	6.55	6.81
41.7	41.3	41.4	41.5	41.6	41.7	41.0	41.5	41.2	41.0	40.4	41.7	41.8	41.6	40.6	39.8
n.a.	n.a.	n.a.	n.a.	n.a.	n.a.	n.a.	n.a.	n.a.	n.a.	n.a.	n.a.	n.a.	n.a.	n.a.	n.a.
50.9	49.6	50.7	49.4	49.8	49.9	49.7	49.8	49.6	50.2	50.3	50.5	50.3	50.3	51.5	51.1
0.03	0.01	0.03	0.07	0.03	0.04	0.03	0.04	0.02	0.02	0.05	0.03	0.02	0.02	-	-
0.07	0.01	0.09	0.06	0.07	0.1	0.08	0.06	0.05	0.05	0.03	0.05	0.01	-	0.02	0.03
0.12	0.12	0.12	0.11	0.11	0.08	0.17	0.1	0.17	0.08	0.1	0.12	0.09	0.11	0.09	0.09
0.37	0.39	0.36	0.4	0.45		0.38	0.35	0.37	0.44	0.36	0.41	0.33	0.41	0.42	0.41
100.6	99.1	99.9	99.4	98.9	100.3	99.3	99.9	99.0	99.5	99.6	100.7	100.5	99.9	99.2	98.3
110	35	114	114	57	72	79	114	59	57	6	6	5	8	27	43
8.84	3.75	8.83	9.29	5.53	7.08	5.93	9.10	6.03	5.27	0.77	0.76	0.74	1.07	4.92	4.75
0.69	0.50	0.74	0.65	0.81	0.83	0.78	0.65	0.75	0.76	0.95	0.97	0.87	-	0.76	0.70
0.23	0.15	0.16	0.16	0.16	0.17	0.17	0.15	0.14	0.13	0.16	0.14	0.12	0.03	0.10	0.18
0.95	0.43	0.95	1.00	0.63	0.73	0.7	1.00	0.62	0.67	0.99	0.61	0.64	0.17	0.28	0.44
1.33	0.96	1.31	1.32	1.06	1.17	1.24	1.37	1.05	1.00	1.39	1.08	1.1	1.13	0.80	0.81
4.34	5.32	4.52	4.6	4.17	4.95	4.45	4.85	4.86	4.51	5.18	4.76	4.85	4.22	3.98	4.14
57.7	58.6	57.6	57.7	58.3	58.4	57.3	57.7	57.2	58.3	57.1	58.1	58.3	58.3	57.3	56.4
n.a.	n.a.	n.a.	n.a.	n.a.	n.a.	n.a.	n.a.	n.a.	n.a.	n.a.	n.a.	n.a.	n.a.	n.a.	n.a.
34.9	34.7	34.5	33.8	34.3	34.7	34.2	34.3	34.1	34.8	34.4	35.2	34.9	35.4	36.1	35.2
0.2	0.08	0.23	0.31	0.06	0.22	0.08	0.33	0.11	0.04	0.28	0.1	0.14	0.04	-	0.01
0.56	0.3	0.53	0.41	0.47	0.69	0.44	0.53	0.5	0.46	0.43	0.54	0.61	0.23	0.38	0.39
0.08	0.08	0.13	0.1	0.11	0.12	0.16	0.11	0.13	0.09	0.14	0.13	0.14	0.12	0.10	0.10
0.12	0.09	0.12	0.14	0.13	0.06	0.12	0.12	0.09	0.13	0.12	0.11	0.1	0.09	0.11	0.11
100.4	100.7	100.1	99.5	99.5	101.2	98.8	100.5	98.9	100.1	100.2	100.7	100.9	99.7	99.2	97.8
1.62	2.62	1.68	1.39	1.95	2.02	1.97	1.64	1.7	1.37	1.56	2.24	1.78	2.14	-	-
18.8	19.1	18.7	18.8	19.5	18.6	18.8	18.4	20.0	20.8	18.7	18.7	19.3	20.7	-	-
2.37	3.06	2.43	2.38	2.23	2.39	2.67	2.36	1.45	1.66	2.61	2.53	2.27	3.53	-	-
2.28	2.69	2.4	2.72	2.05	2.7	2.45	2.66	2.41	1.92	2.98	2.42	2.28	1.31	-	-
54.9	55.5	54.8	55.0	55.3	55.7	54.3	54.2	53.9	55.4	54.2	54.9	54.6	55.0	-	-
n.a.	n.a.	n.a.	n.a.	n.a.	n.a.	n.a.	n.a.	n.a.	n.a.	n.a.	n.a.	n.a.	n.a.	-	-
17.5	15.1	17.6	17.7	16.1	16.7	16.5	17.3	15.9	17.0	17.5	16.0	16.4	15.7	-	-
0.34	0.2	0.31	0.54	0.05	0.34	0.1	0.45	0.23	0.04	0.5	0.15	0.27	0.35	-	-
1.68	1.83	1.69	1.13	2.63	2.73	1.74	1.76	2.57	1.9	1.47	2.77	2.23	1.45	-	-
0.08	0.03	0.1	0.07	0.08	0.09	0.09	0.1	0.08	0.09	0.1	0.08	0.09	0.07	-	-
0.07	0.05	0.07	0.08	0.07	0.05	0.05	0.05	0.04	0.07	0.07	0.06	0.05	0	-	-
99.6	100.2	99.7	99.8	99.9	101.4	98.7	98.8	98.2	100.2	99.7	99.8	99.3	100.3		
0.05	0.02	0.05	0.03	0.01	0.07	0.04	0.02	0.05	0.02	0.04	0.03	0.03	0.02	0.03	0.05
5.93	4.94	5.71	4.88	6.14	6.33	4.79	5.69	5.76	6.73	4.87	5.95	6.52	5.75	4.04	4.87
18.1	21.0	18.5	20.8	17.1	17.2	20.1	17.6	17.8	16.7	20.6	17.8	16.8	19.6	20.7	18.9
5.8	7.97	5.83	6.12	5.92	7.1	6.72	6.55	6.68	6.32	6.75	6.86	6.88	7.08	6.27	6.02
42.2	42.4	42.0	42.8	41.8	41.9	42.0	42.0	42.0	41.6	41.5	41.6	41.7	42.2	41.9	41.1
n.a.	n.a.	n.a.	n.a.	n.a.	n.a.	n.a.	n.a.	n.a.	n.a.	n.a.	n.a.	n.a.	n.a.	n.a.	n.a.
21.0	20.2	20.7	21.3	19.1	19.2	21.0	20.3	19.7	19.0	21.5	19.7	19.4	18.9	22.0	21.0
0.53	0.09	0.53	0.37	0.13	0.7	0.22	0.27	0.3	0.07	0.04	0.29	0.36	0.18	-	-
5.46	2.92	5.62	2.38	6.79	6.88	3.89	6.34	6.98	7.28	3.42	6.96	7.47	3.63	4.78	6.16
0.26	0.4	0.3	0.34	0.41	0.38	0.32	0.31	0.31	0.36	0.3	0.32	0.4	0.46	0.33	0.32
0.02	0.01	0.02	0.01	0.02	0.08	0.01	0.02	0.02	0.01	0.01	0.06	0.02	0.00	-	-
99.4	99.9	99.3	99.0	97.4	99.9	99.1	99.1	99.6	98.1	99.1	99.6	99.6	97.8	100.0	98.4
K12A3-1208	K12A4-5 996	K12A7 1214	K12A8 1251	K13B5-4 1092	K14A1-4 1210	K15A2-2 1139	K15A7-4 1229	K16A2-2 1002	K16A3-1 1053	K11A4 1223	K11A5-1 1129	K11A14 1128	K13B3-4 864	Bo-02 -	Bo-20 -
44	37	46	53	38	50	41	48	35	38	48	42	44	28	-	-
1161	1041	1163	1219	1015	1088	1076	1198	1026	1031	709	679	702	-	-	-
1204	995	1223	1257	1077	1170	1138	1232	1067	1075	771	742	735	714	-	-
1140	881	1146	1189	1012	1124	1054	1157	928	1010	1152	1033	1057	777	-	-
42	34	44	51	36	48	38	46	33	37	46	40	42	25	-	-
1195	979	1214	1249	1067	1159	1127	1223	1057	1069	762	729	725	702	-	-
1081	945	1137	1192	962	976	957	1075	1024	969	1172	953	986	790	948	996
38	34	42	49	33	37	31	40	36	34	45	33	37	24	36	36
1174	979	1203	1239	1049	1104	1089	1190	1073	1057	756	695	698	695	948	1021

A5.1 EPMA measuring conditions for olivine

Oxide	Channel	Standard	Std Current (nA)	Lower bkgd (mm)	Upper bkgd (mm)	Peak time (s)	Bkg time (s)
MgO	TAP	Fo90.5	100	N/A	2	30	15
SiO_2	TAPJ	Fo90.5	100	N/A	3	30	15
FeO	LIFH	Fo90.5	50	5	5	30	30
NiO	LIFH	Ni_wire_CB1	20	1.5	1.5	60	60
MnO	LIFH	SpessartineSK	100	6	1.5	60	60
CaO	PETH	diopside	50	2	2	180	180
Cr_2O_3	PET	Cr2O3_CB1	50	1.9	3	120	120
Al_2O_3	TAPJ	FrankSmith_CB1	50	2.6	2	180	180
CoO	LIFH	Co_metal	20	6	3	90	90

A5.2.1. SC-GB results from University of Alberta

Sample	SC-GB																					
Lab	University of Alberta																					
Method	solution ICP-MS		EPMA		LA-ICP-MS, 10 Hz												LA-ICP-MS, 5 Hz					
Calibration	medium res.				NIST612, 29Si						GSD-1G, 25Mg		GSE-1G, 25Mg		GSD-1G, 25Mg		NIST612, 29Si					
Spot size [µm]					130		75		33		130		75		33		75		50		33	
	n = 3	SD		SD	n = 10	SD	n = 8	SD	n = 3	SD	n = 10	SD	n = 8	SD	n = 3	SD	n = 10	SD	n = 9	SD	n = 8	SD
7Li	1.53	0.06			1.58	0.04	n.a.		1.6	0.2	1.62	0.02	n.a.		1.6	0.2	1.5	0.2	1.5	0.2	b.d.l.	
23Na	46	0.3			49	3	55	3	65	5	51	1	49	2	55	4	40	6	39	7	57	27
27Al	86	1	83	10	85	2	89	4	73	2	71	3	75	3	67	2	76	2	78.8	0.9	84	5
P31					2.9	0.3	6.6	0.3	82	23	2.0	0.2	11.6	0.7	b.d.l.		4.7	0.5	7	1	12	9
43Ca	528	13	550	11	452	12	505	23	438	29	405	11	460	22	416	31	441	15	498	26	491	132
45Sc	2.6	0.1			3.2	0.1	3.5	0.1	2.64	0.03	3.0	0.1	3.0	0.1	2.85	0.02	2.7	0.2	2.8	0.1	1.9	0.4
49Ti	4.1	0.03			3.9	1.0	4.7	1.1	5.1	0.4	3.2	0.6	4.1	0.9	4.8	0.3	3.1	0.7	4.0	0.4	6.9	5.4
51V	3.72	0.04			3.4	0.1	3.9	0.1	3.0	0.1	3.3	0.05	3.45	0.08	3.20	0.05	3.57	0.04	3.4	0.1	3.3	0.1
53Cr	181	4	153	16	166	4	177	5	148.1	0.5	161	1	169	3	153	1	163	2	159	4	160	2
55Mn	1042	18	1065	21	1160	11	1236	22	980	6	1175	13	1158	21	1032	3	1036	8	1020	6	988	3
59Co	139	2	117	14	146	2	170	5	179	1	143	2	144	3	170	4	145	1	149	1	157	2
60Ni	3079	29	3081	60	3329	34	3922	96	4040	50	3074	37	3531	86	3863	110	3144	39	3390	49	3589	119
65Cu	1.04	0.02			0.99	0.06	0.74	0.10	1.33	0.09	0.96	0.01	0.65	0.08	1.3	0.1	0.31	0.08	1.08	0.06	1.1	0.2
66Zn					65	2	76	2	89	1	58	1	68	2	91	2	65	1	69	1	74	2
88Sr					0.003	0.001	0.015	0.008	b.d.l.		0.004	0.001	0.013	0.007	b.d.l.		0.028	0.010	0.026	0.005	b.d.l.	
89Y					0.04	0.01	0.046	0.004	0.04	0.01	0.04	0.01	0.038	0.004	0.04	0.01	0.04	0.00	0.04	0.01	0.05	0.01
90Zr					0.026	0.005	0.026	0.009	0.023	0.007	0.029	0.006	0.023	0.007	0.029	0.007	0.027	0.002	b.d.l.		b.d.l.	
93Nb					0.0020	0.0004	0.0023	0.0009	bd.l.		0.0016	0.0003	0.0021	0.0009	b.d.l.		b.d.l.		b.d.l.		b.d.l.	
140Ce					0.0003	0.0001	b.d.l.		b.d.l.		0.0004	0.0002	b.d.l.		0.0003	0.0003	b.d.l.		b.d.l.		b.d.l.	

A5.2.2. SC-GB results from University of Melbourne

Sample	**SC-GB**																	
Lab	**University of Melbourne**																	
Method	LA-ICP-MS, 5 Hz																	
Calibration	BHVO, 29Si						355OL, 29Si						NIST612, 29Si					
Spot size [µm]	104		40		26		104		40		26		104		40		26	
	n = 10	SD	n = 10	SD	n = 10	SD	n = 10	SD	n = 10	SD	n = 10	SD	n = 10	SD	n = 10	SD	n = 10	SD
7Li	1.75	0.05	1.7	0.2	1.7	0.4	1.54	0.03	1.53	0.09	1.42	0.09	1.67	0.04	1.62	0.09	1.4	0.3
23Na	49	1	55	2	54	3	47	1	48	2	50	2	43	1	48	2	52	2
27Al	93	4	92	7	93	6	94	3	95	3	96	3	84	3	84	3	80	4
P31	12	1	22	3	26	5	7	1	12	1	12	1	7	1	11	1	11	1
43Ca	538	5	540	15	547	22	603	4	597	12	605	12	493	5	496	8	475	5
45Sc	3.39	0.03	3.5	0.1	3.4	0.1	3.1	0.0	2.8	0.1	2.6	0.1	3.9	0.0	4.0	0.1	4.2	0.1
49Ti	4.4	1.6	4.4	1.8	4.5	1.7	4.6	1.6	5.0	1.7	5.0	1.7	4.6	1.6	4.9	1.7	5.0	2.0
51V	3.40	0.04	3.4	0.1	3.4	0.1	3.4	0.0	3.5	0.1	3.4	0.1	3.4	0.0	3.3	0.1	3.1	0.1
53Cr	174	1	172	3	173	3	165	1	164	2	164	2	160	2	156	1	149	2
55Mn	1076	3	1089	5	1093	4	1081	4	1071	6	1067	6	1029	7	1002	5	983	3
59Co	141.8	0.5	154	1	163	1	140.9	0.4	137.3	0.5	139.5	0.5	142.0	0.9	144.9	0.4	152.4	0.8
60Ni	2993	19	3280	28	3471	31	2912	6	2864	15	2893	15	3105	15	3237	16	3339	16
65Cu	0.92	0.01	1.06	0.12	1.08	0.12	1.20	0.04	1.21	0.11	1.26	0.11	0.94	0.03	1.02	0.09	1.08	0.09
66Zn	56.6	0.4	66	1	69	2	54.8	0.2	55.1	0.4	57.6	0.4	63.7	0.3	74.2	0.5	82	1
88Sr	0.01	0.02	0.002	0.007	b.d.l.		0.22	0.08	0.30	0.21	b.d.l.		0.004	0.001	0.004	0.003	0.003	0.003
89Y	0.03	0.01	0.02	0.01	b.d.l.		0.03	0.01	0.04	0.02	0.04	0.02	0.035	0.007	0.035	0.007	0.034	0.005
90Zr	0.006	0.007	b.d.l.		b.d.l.		0.0017	0.0018	0.003	0.001	b.d.l.		0.02	0.01	0.03	0.01	0.02	0.01
93Nb													0.003	0.004	0.003	0.001	b.d.l.	
140Ce	0.001	0.002																

A5.2.3. SC-GB results from Geological Survey of Canada

Sample	SC-GB												SC-BK			
Lab	Geological Survey of Canada															
Method	LA-ICP-MS, 10 Hz												LA-ICP-MS			
Calibration	NIST612, 29Si						GSD-1G, 25Mg						NIST612, 29Si		GSE-1G, 25Mg	
Spot size [µm]	135		65		30		135		65		30		86		86	
	n = 11	SD	n = 11	SD	n = 11	SD	n = 11	SD	n = 11	SD	n = 10	SD		SD		SD
7Li	1.66	0.06	1.67	0.08	1.7	0.3	1.77	0.03	1.60	0.05	1.7	0.2	1.77	0.06	1.59	0.06
23Na	48	4	46.8	0.9	41	3	52	1	44	6	42	2	47	1	45	2
27Al	87	1	94	2	84	3	82	1	87	1	88	1	86	2	80	2
P31	2.0	0.1	2.7	0.3	b.d.l.		1.7	0.2	2.8	0.8	6	3	2.0	0.3	1.5	0.3
43Ca	444	4	474	7	447	19	442	3	520	11	485	19	441	7	457	7
45Sc	3.9	0.1	4.6	0.2	3.7	0.1	4.17	0.09	3.97	0.05	5.8	0.6	3.35	0.05	3.6	0.1
49Ti	3.7	0.6	3.8	0.7	3.6	1.0	3.1	0.6	3.6	0.7	3.8	0.6	5.0	1.0	4.5	0.9
51V	3.6	0.1	3.41	0.07	3.2	0.1	3.97	0.03	3.56	0.07	3.5	0.1	3.4	0.1	3.39	0.05
53Cr	166	3	157	1	154	1	178	2	159.0	0.8	155	3	159	2	155	1
55Mn	1,094	16	1,017	6	997	8	1,186	15	1,080	7	1,062	11	1,043	4	1,066	7
59Co	138	2	138	1	156	1	152	1	144	4	154	8	140	1	139	1
60Ni	2,958	41	2,921	15	3,364	28	3,274	15	3,141	106	3,419	203	3,095	22	3,025	27
65Cu	0.9	0.1	0.84	0.03	0.9	0.1	1.1	0.2	1.1	0.3	1.0	0.2				
66Zn	61	5	59	2	69	2	54	2	59	3	64	4	66	1	68	2
88Sr	0.003	0.001	0.004	0.001	0.007	0.001	0.004	0.002	0.003	0.001	0.008	0.002	0.004	0.001	0.004	0.001
89Y	0.036	0.004	0.035	0.005	0.03	0.01	0.04	0.01	0.04	0.01	0.04	0.01	0.040	0.005	0.043	0.005
90Zr	0.02	0.01	0.02	0.01	0.022	0.005	0.02	0.01	0.02	0.01	0.025	0.009	0.03	0.01	0.03	0.01
93Nb	0.003	0.002	0.004	0.003	0.005	0.001	0.004	0.003	0.003	0.002	0.008	0.001	0.003	0.002	0.003	0.003
140Ce	0.0009	0.0008	0.0016	0.0020	0.0015	0.0012	0.0009	0.0011	0.0023	0.0013	b.d.l.		0.0009	0.0008	0.0012	0.0016

A5.3.1. 355OL results from University of Alberta

Sample	355OL															
Lab	University of Alberta															
Method	LA-ICP-MS, 10 Hz				LA-ICP-MS, 5 Hz											
Calibration	NIST612, 29Si		SC-GB, 29Si		NIST612, 29Si						SC-GB, 29Si					
Spot size [µm]	130		130		75		50		33		75		50		33	
	n = 12	SD	n = 12	SD	n = 5	SD	n = 3	SD	n = 3	SD	n = 5	SD	n = 3	SD	n = 3	SD
7Li	1.02	0.09	1.01	0.02	0.8	0.1	1.4	0.1	b.d.l.		1.0	0.1	1.8	0.4	b.d.l.	
23Na	96	13	107	34	91	8	87	4	121	52	104	16	104	16	150	15
27Al	45	2	47	1	41	3	42	1	48	3	46	5	46	2	49	3
P31	57	5	63	11	53	2	57	2	43	5	34	2	23	1	45	42
43Ca	99	18	152	18	192	11	136	3	b.d.l.		143	17	151	17	190	85
45Sc	1.0	0.2	1.0	0.10	0.7	0.1	0.5	0.1	b.d.l.		0.8	0.1	0.6	0.2	0.4	0.4
49Ti	9.8	0.9	10.7	0.9	10	1	11	2	10	9	13	3	19	15	b.d.l.	
51V	5.6	0.3	5.4	0.3	5.6	0.1	5.3	0.1	5.2	0.1	5.3	0.1	5.2	0.1	5.4	0.2
53Cr	209	11	205	5.3	203	5	199	5	196	2	207	4	207	1	205	3
55Mn	657	55	580	5	569	6	562	4	548	7	585	7	586	5	591	8
59Co	141	10	123	2	121	1	128	0	134	3	122.5	0.4	124.7	0.2	123.3	2.5
60Ni	3191	195	2791	29	2878	34	3067	27	3239	31	2805	21	2792	18	2781	47
65Cu	0.9	0.1	0.9	0.1	0.33	0.07	0.91	0.05	1.0	0.3	1.2	0.4	0.89	0.07	1.0	0.2
66Zn	50	3	48	1	47.1	0.8	49.6	0.9	51	3	46.6	0.5	46	1	45	2
88Sr	0.01	0.02	0.006	0.005	b.d.l.		b.d.l.		b.d.l.		0.01	0.02	0.11	0.15	0.014	0.016
89Y	0.002	0.001	0.002	0.001	0.008	0.003	b.d.l.		b.d.l.		0.006	0.001	b.d.l.		b.d.l.	
90Zr	0.14	0.06	0.13	0.06	0.10	0.01	0.11	0.00	b.d.l.		0.14	0.03	0.33	0.29	b.d.l.	
93Nb	0.43	0.12	0.41	0.25	0.25	0.02	0.32	0.02	0.33	0.05	0.76	0.71	0.21	0.13	0.18	0.07
140Ce	0.01	0.02	0.03	0.04	b.d.l.		b.d.l.		b.d.l.		0.03	0.04	b.d.l.		b.d.l.	

A5.3.2. 355OL results from University of Melbourne

Sample	**355OL**															
Lab	**University of Melbourne**															
Method	solution ICP-MS				EPMA		LA-ICP-MS, 5 Hz									
Calibration							BHVO, 25Mg				NIST612, 29Si					
Spot size [µm]							104		26		104		40		26	
		SD		SD	n = 9	SD	n = 11	SD	n = 10	SD	n = 4	SD	n = 4	SD	n = 3	SD
7Li	1.01		0.96				0.93	0.04	1.0	0.1	1.03	0.02	1.01	0.07	1.0	0.1
23Na			94				97	4	107	7	86	1	93	2	96	3
27Al			55		75	48	51.5	0.8	54	2	48.7	0.6	48	1	45.6	0.4
P31	57		61				48	7	58	7	57	4	56	1	53	6
43Ca	161		161		193	97	149	24	256	174	130	1	132	3	124	2
45Sc	0.6		1.3				1.23	0.02	2.1	0.1	1.6	0.1	1.8	0.1	2.1	0.1
49Ti	11.2		10.5				11.0	0.7	12.1	0.9	11.0	0.4	10.5	0.9	10.5	0.8
51V	5.5		5.3				5.50	0.04	5.3	0.1	5.38	0.05	5.2	0.1	4.8	0.1
53Cr	219		207		166	119	216	1	211	3	199	2	195	1	187	3
55Mn			563		647	135	599	3	599	4	564	6	555	2	547	3
59Co	120		109				119.3	0.4	128	1	120	1	125.3	0.5	131	1
60Ni	2679		2498		2876	226	2695	12	2978	21	2829	24	2993	28	3056	
65Cu	1.28		0.97				0.76	0.03	0.9	0.1	0.76	0.02	0.81	0.02	0.84	0.03
66Zn	41		35				41.1	0.5	51	1	47.2	0.4	54.7	0.4	58.5	1.4
88Sr	0.35		0.10				0.01	0.02	0.40	0.51	0.002	0.001	0.002	0.001	b.d.l.	
89Y											0.0005	0.0001	0.0004	0.0000	0.0007	0.0007
90Zr	0.14		0.16				0.11	0.01	0.63	1.02	0.105	0.005	0.093	0.003	0.09	0.02
93Nb	0.40		0.37				0.50	0.18	0.48	0.15	0.40	0.12	0.37	0.13	0.45	0.10
140Ce	0.02		0.03				0.0003	0.0002								

A5.3.3. 355OL results from Geological Survey of Canada

Sample	**355OL**											
Lab	**Geological Survey of Canada**											
Method	LA-ICP-MS, 10 Hz											
Calibration	NIST612, 29Si						GSD-1G, 25Mg					
Spot size [µm]	135		65		30		135		65		30	
	n = 6	SD	n = 6	SD	n = 6	SD	n = 6	SD	n = 6	SD	n = 6	SD
7Li	0.96	0.02	0.99	0.04	1.1	0.3	1.07	0.05	1.00	0.09	1.0	0.2
23Na	93	1	94.6	0.6	83	5	106	2	83.1	0.6	80	2
27Al	51.1	0.8	52.1	0.4	48	2	47.0	0.9	48.9	0.7	48	2
P31	54	6	53	2	46	5	45	5	40	4	37	5
43Ca	120	3	119	4	115	31	121	4	129	5	117	27
45Sc	1.52	0.03	1.85	0.06	1.47	0.04	1.73	0.02	1.45	0.02	2.2	0.1
49Ti	10.6	0.4	10.4	0.5	10.3	1.4	9.3	0.3	9.7	0.6	9.5	0.6
51V	5.7	0.1	5.32	0.04	5.3	0.1	6.31	0.04	5.52	0.05	5.46	0.08
53Cr	206	3	197	1	202	2	223	1	196	1	191	2
55Mn	600	8	564	4	571	2	665	2	588	1	583	4
59Co	116	1	118.3	0.5	118	1	130.7	0.7	120.1	0.4	116	2
60Ni	2707	26	2724	9	2717	16	3015	19	2774	8	2674	47
65Cu	0.71	0.01	0.69	0.05	0.6	0.2	0.84	0.08	0.82	0.07	0.7	0.2
66Zn	43.0	0.4	43.6	0.8	44	2	40.1	0.5	51.5	0.5	40	1
88Sr	0.01	0.03	0.003	0.002	0.31	0.35	0.04	0.09	0.003	0.001	b.d.l.	
89Y	0.0008	0.0003	0.0011	0.0003	b.d.l.		0.0008	0.0005	0.001	n.a.	0.004	0.001
90Zr	0.104	0.003	0.10	0.01	0.11	0.07	0.11	0.01	0.11	0.01	0.10	0.01
93Nb	0.47	0.15	0.43	0.16	0.50	0.20	0.42	0.12	0.45	0.17	0.42	0.13
140Ce	0.009	0.014	0.0023	0.0021	b.d.l.		0.016	0.034	0.0006	0.0003	b.d.l.	